The Pennsylvania State University

The Graduate School

College of Engineering

MULTI-SCALE TECHNIQUES IN

COMPUTATIONAL ELECTROMAGNETICS

A Dissertation in

Electrical Engineering

by

Jonathan Neil Bringuier

Submitted in Partial Fulfillment
of the Requirements
for the Degree of

Doctor of Philosophy

May 2010

The dissertation of Jonathan Neil Bringuier was reviewed and approved* by the following:

Raj Mittra
Professor of Electrical Engineering
Dissertation Advisor
Chair of Committee

James K. Breakall
Professor of Electrical Engineering

Randy Haupt
Senior Scientist

Michael T. Lanagan
Associate Professor of Engineering Science and Mechanics

W. Kenneth Jenkins
Professor of Electrical Engineering
Head of the Department of Electrical Engineering

*Signatures are on file in the Graduate School

ABSTRACT

The last several decades have experienced an extraordinarily focused effort on developing general-purpose numerical methods in computational electromagnetics (CEM) that can accurately model a wide variety of electromagnetic systems. In turn, this has led to a number of techniques, such as the Method of Moments (MoM), the Finite Element Method (FEM), and the Finite-Difference-Time-Domain (FDTD), each of which exhibits their own advantages and disadvantages. In particular, the FDTD has become a widely used tool for modeling electromagnetic systems, and since it solves Maxwell's equations directly—without having to derive Green's Functions or to solve a matrix equation or—it experiences little or no difficulties when handling complex inhomogeneous media. Furthermore, the FDTD has the additional advantage that it can be easily parallelized; and, hence, it can model large systems using supercomputing clusters. However, the FDTD method is not without its disadvantages when used on platforms with limited computational resources. For many problems, the domain size can be extremely large in terms of the operating wavelengths, whereas many of the objects have fine features (e.g., Body Area Networks). Since FDTD requires a meshing of the entire computational domain, presence of these fine features can significantly increase the computational burden; in fact, in many cases, it can render the problem either too time-consuming or altogether impractical to solve. This has served as the primary motivation in this thesis for developing multi-scale techniques that can circumvent many of the problems associated with CEM, and in particular with time domain methods, such as the FDTD.

Numerous multi-scale problems that frequently arise in CEM have been investigated in this work. These include: 1) The coupling problem between two conformal antennas systems on complex platforms; 2) Rigorous modeling of Body Area Networks (BANs), and some approximate human phantom models for path loss characterization; 3) Efficient modeling of fine

features in the FDTD method and the introduction of the dipole moment method for finite

methods; and, 4) Time domain scattering by thin wire structures using a novel Time-Domain-

Electric-Field-Integral-Equation (TD-EFIE) formulation. Furthermore, it is illustrated, via several

examples, that each problem requires a unique approach. Finally, the results obtained by each

technique have been compared with other existing numerical methods for the purpose of

validation.

TABLE OF CONTENTS

LIST OF FIGURES

LIST OF TABLES

ACKNOWLEDGEMENTS

I would like to dedicate this dissertation to my fiancée Katie, whose support and encouragement never waivered, even during those long nights and weekends in the laboratory. I am truly a lucky individual to have you in my life. To my family, I am often reminded of a famous saying that "a journey of a thousand miles begins with a single step." Without your guidance that first step would never have been possible.

I would be remiss if I did not express a tremendous amount of gratitude towards my advisor, Dr. Raj Mittra. The intellectual and personal growth that I have experienced under his supervision cannot be overstated. To my colleagues in the Electromagnetic Communications Laboratory, Dr. Wenhau Yu, Xialong (Bob) Yang, Yongjun Liu, Kadappan (Kip) Panayappan, Nikhil Mehta, Kyungho Yoo, Dr. Lai-Ching (Kit) Ma, Dr. Neng-Tien Huang, thank you for the technical support, without which this dissertation could not have been completed. Finally, I am truly appreciative of all my committee members, Dr. James K. Breakall, Dr. Randy Haupt, and Dr. Michael T. Lanagan, who set aside their busy schedules to review this work.

Chapter 1

Introduction

1.1 What is Multi-scale Electromagnetics?

The term multi-scale has become an increasingly popular but difficult topic amongst the computational electromagnetics community. In short, multi-scale electromagnetics pertains to those geometries in which both electrically large and small features are present, and they continue to push modern computational techniques to their limits. For finite methods (FDTD, FEM) the multi-scale nature of the problem exacerbates the difficulties in generating a good quality mesh that does not suffer from ill-conditioning behavior. In principle, finite methods can model an arbitrary geometry but the CPU time and memory requirements posed by multi-scale problems can quickly render these techniques either too time-consuming or altogether impractical. In many multi-scale problems the number of unknowns can reach billions and these problems quickly become unmanageable without sufficient computing power. The bottleneck is most often attributed to the fine features of the problem and many attempts have been made to circumvent the meshing requirements dictated by these geometries. However, most approaches have met with limited success, either because of instability problems arising in the FDTD or the matrix size in FEM. In contrast, the Method of Moments (MoM) has no difficulty when dealing with multi-scale structure because the approach does not require meshing the entire computational space. Although MoM avoids these meshing constraints altogether, it does require a knowledge of the Green's function for the medium. In many practical problems the Green's function is either unavailable or its computational implementation becomes overly complicated. Therefore, the

MoM is seldom used when complex inhomogeneous media are involved and finite methods are generally regarded as best suited for these types of problems.

1.2 Emerging research in Body Area Networks (BANs) and its electromagnetic Multi-scale nature

Recently, the need for accurate modeling of performance of antennas and sensors operating in the human body environment, and the challenges encountered when attempting to do this by using conventional numerical methods, have been widely recognized. The process of modeling on-body and in-body sensors truly brings to fore the problematic features of finite methods when applied to the simulation of objects with multi-scale inhomogeneous geometries such as the human body which is electrically large, whereas the antennas or sensors mounted on it are comparatively very small. The interaction between electromagnetic energy and biological media has long been a source of focused research and has drawn the attention of researchers in both the measurement and analytical communities. Since the early years of electromagnetic engineering, researchers have attempted to model and estimate the effects of human exposure to RF radiation. These early attempts where limited to simple measurement of dielectric properties of biological tissue samples and approximate calculations of specific absorption rates (SAR) by using simplified models that made the problem tractable even when available computing resources were limited. For example, prior to the development of the Geometrical Theory of Diffraction (GTD) by Keller *et al.*, estimates of the SAR were based on the solution of plane wave scattering for both spherical models of the human head and oblate spheroids for the torso. It has been recognized, however, that it is highly desirable to improve the accuracy of SAR calculations, since the measurements entails the probing of live specimens that not only may pose ethical problems, but may be highly costly as well. Despite these limitations, early researchers

relied on simple models in an attempt to understand scattering and absorption properties of biological media, involving scatterers, which will be referred to herein as anthropomorphic forms. Although these simple models did yield some useful data, they were often found to be much too crude when attempting to simulate the scattering properties of objects with anthropomorphic geometries. The GTD was first introduced for RCS (radar cross-section) computation of radar targets by utilizing combinations of canonical geometries to represent a fairly realistic model of the problem at hand. It is recognized, however, that despite its success in the area of RCS computation, the GTD is neither well suited for SAR calculations involving human bodies, nor is it commonly used to analyze radiating elements in the presence of an inhomogeneous scatterer except in limited cases. For instance, some researchers have used hybrid techniques to analyze the propagation of creeping waves in the asymptotic regions on the body to estimate the coupling between two antennas that are located close to the body. However, despite the extensive developments of the GTD and related asymptotic techniques over the last our decades, these methods have not rivaled the accuracy and versatility of the numerical techniques.

Thus far, many of the modeling tools mentioned above have primarily focused on scattering and absorption of electromagnetic waves from biological media; and, in fact this was the primary interest in the early days of radio communication. However, with the unabated growth of personal computing devices, cell phones, PDA's, medical implants, etc., a recent wave of interest has focused on *body-centric* communications or body area networks (BANs). The basis of this research is an attempt to implement the analogue of wireless land area networks (WLAN) in the human body environment. The standard operating band assigned to body-centric communications is 3-10 GHz. This poses a very difficult task for the engineer since the human body is a very complex platform in which to operate efficiently. Some unique features of the human body are: 1) it is very lossy and highly inhomogeneous; 2) it has non-Debye dispersion

properties; 3) it is electrically large; 4) it is a non-stationary environment. All these features make the study of BANs unique, complex and highly challenging.

To-date, most preliminary research related to BANs has focused on measurement efforts (Hall *et al.,* [7]). For example, much research has been dedicated to the mutual coupling between antenna elements mounted on the body. These studies have characterized the coupling coefficient as a function of the distance around the torso. Although these results are useful, they are limited to specific antenna configurations and fail to account for SAR within the body. Furthermore, these measurements cannot address the behavior of antennas inside the body, which is crucial information for medical implants. Nevertheless, these measurements do serve as a benchmark for numerical codes that attempt to model the same phenomenon.

The growing need to model electromagnetic radiation interacting with biological media along with the limitations of measurements have led most researchers to rely upon the numerous advances in numerical methods. Although several numerical techniques, such as MoM, FEM, and FDTD, are available for CEM modeling, the FDTD method has been viewed as the most desirable approach to modeling these types of problems. The major reason for this is that FDTD has many advantages over other methods, namely: 1) it is highly parallel; 2) it can handle highly inhomogeneous media; 3) it can handle dispersive media; and 4) it generates a wideband response. However, as with other numerical methods, the FDTD is not without its limitations. For instance, the conventional FDTD does not explicitly handle curved geometries. Typically, these types of structures require a modified version of the basic update equations usually referred to as the conformal FDTD or CFDTD [28] for short. This technique has been well tested and has been demonstrated to yield accurate results for many canonical geometries, e.g., spheres, for which an analytical solution is available for reference. Unfortunately, this embellishment of the conventional FDTD does not help address the problem of accurate modeling thin structures that neither fill the Yee cell only partially, nor lie on the cell grid. Additionally, wire structures that

are orientated at an angle with respect to the FDTD mesh cannot be conveniently handled by the FDTD. For example, it has difficulty in modeling thin curved wires, e.g., helical antennas, unless the cell size is made extremely small ($<< \lambda/20$) to accurately capture the nuances of the thin curved structure. Note that $\lambda/20$ is the well known nominal cell-size taken at the upper frequency limit of the source excitation and the largest dielectric contrast from free space. This inability to accurately handle thin, curved and arbitrarily oriented structures poses a formidable challenge to modeling antennas or scatterers in the FDTD simulation of BANs.

There are additional subtle points to be made about the limitations of FDTD specifically related to the problem of BANs. First, many of the antennas used in BANs can be geometrically thin and also electrically very small, whereas the human body is an electrically large object in the band 3-10 GHz. These two extreme conditions pose a problem for FDTD simulations. Obviously, the dimensions of the small antenna/scatterer will dictate the global cell size in the computational domain, and the computational cost can be high when this size is small. Secondly, in many cases the antenna can be significantly smaller than the required cell size needed to model the human body. The brute force approach to simultaneously modeling these antennas together with the entire human body can require simulation times that are several orders of magnitude larger than they would be if the antenna/scatterer had dimensions on the order of the nominal FDTD cell size. Therefore, if it is highly desirable to devise techniques that avoid the computational expense of using small cell sizes to model the antenna/human body composite, there are two approaches that may be proposed for doing this. The first is to model the local problem involving the radiating structure and its local environment. This essentially means that we only consider the local properties of the body and model the fine geometrical details of the antenna/scatterer with the required mesh size. This is a viable solution if only the terminal properties of the antenna, e.g., the impedance and the near-field behavior, are of interest.

However, if we are interested in estimating the coupling between two antennas, whose separation distance is large, and we wish to maintain the nominal FDTD cell size, with respect to the body, then we must seek alternative solutions. The techniques for handling these types of problems will be referred to herein as multi-scale methods.

Thus far, the limitations of FDTD have been identified in the context of the simulation of BANs or electromagnetic interaction with biological media. It should be recognized that there are a whole host of problems, with BANs being a special case, that exhibit multi-scale features that tax the conventional numerical approaches. In the next section we will present a summary of the multi-scale techniques developed in this thesis, as they relate to several issues alluded to above.

1.3 Thesis overview

Chapter two introduces some novel techniques that are capable of handling general planar complex multi-scale electromagnetic coupling problems, where they can be applied to many applications in addition to BANs. In many scenarios the antenna or array system is conformal to a surface and operating in the presence of multiple systems that are similar. This is typically the case for radar systems, and especially for the BANs. Often the separation distances are large compared to the operating wavelength — exceeding several or even tens of wavelengths — but the system is highly sensitive so that the coupling between two such systems is of great concern. For example, two array systems comprising of many elements with fine features conformal to a RAM material is commonplace in military applications. In BANs, the problem geometry usually consists of several sensors placed strategically around the body. Such a problem is electrically large and would require expensive computational resources if full-wave solvers, such as FDTD, were used. Furthermore, the antenna or array elements can have fine features which require high resolution meshing and thus exacerbate the difficulties encountered in the computational effort.

One approach that has been used in the past to circumvent this problem is to use a serial/parallel version of the FDTD. This approach decomposes the problem into subdomains and assumes that multiple reflections between the subdomains can be neglected at large distances. Each subdomain, starting with the domain containing the active elements, is rigorously solved by using the conventional FDTD. Subsequently, each subdomain is excited by the equivalent field sources saved on the boundary of the previous domain. The process marches on in time for each subdomain until the final receiving elements are excited. The method inherently saves the computational resources needed to model the entire problem, though not the simulation runtime. However, we can obtain a very accurate approximation to the full-wave solution and further limit the computational cost by reducing the problem into smaller parts using various techniques. Toward this end, we introduce a time-domain Green's function approach to solving these types of problems.

The time-domain Green's function method is a multi-step algorithm, each requiring special numerical techniques to arrive at the final coupling calculation between two radiating elements. The antenna or array system is assumed to lie on a planar complex substrate, which may be a RAM material for military-type array systems, and the human body is modeled as a locally planar, complex half-space for BANs. The half space problem for BANs is reasonable for antennas mounted on the same side of the torso, which is a common location for sensors. The method begins by rigorously simulating the excited elements in their respective local environment by using the conventional FDTD and storing the aperture field in a matrix. The aperture field is determined by setting a threshold level, say -20 dB, below which the fields can be neglected. These aperture field distributions subsequently act as equivalent sources radiating into the medium. It is important to point out that we have neglected the contribution of the equivalent sources residing on the surface inside the material due to the lossy nature of the substrate. Therefore, the equivalent sources exist only on the planar aperture above the antenna/array.

Once the aperture field is stored, we turn to the task of deriving a time-domain Green's function for both electric and magnetic sources so that we may simply use the convolution integral to find the total field anywhere in the domain. In the context of the reaction theorem, only the fields on the aperture of the receiving antenna/array would be needed and, hence, we choose the substrate surface as the observation point for numerically determining the time-domain Green's function.

The time-domain Green's function is calculated by a special version of the FDTD algorithm, known as the Body-of-Revolution FDTD (BOR-FDTD). The reason for using this version of the FDTD is that it removes the azimuthal behavior of the fields and yields only the Fourier coefficients that are functions of z and the radial distance, ρ. After obtaining a numerical solution for the time-domain Green's function well into the asymptotic regions, we can apply Prony's method to extrapolate these fields to arbitrary radial distances on the aperture surface of the receiving unit. The coupling between these two systems can now be computed in a straightforward manner via the use of the Reaction Theorem.

Chapter three deals with the rigorous full-wave solution, via the FDTD method, in an attempt to obtain realistic communications channel models for on-body communications in BANs. The problem of modeling the coupling between body mounted antennas is often not amenable to attack by hybrid techniques owing to the complex nature of the human body. For instance, the time-domain Green's function approach becomes more involved when the antennas are not conformal. Furthermore, the human body is irregular in shape and has dispersion properties that are unique. Therefore, it must be treated with a modified version of the basic FDTD algorithm, which will be introduced in Chapter 3. One consequence of this is that we must resort to modeling the antenna network mounted on the body in its entirety, and the number of degrees of freedom (DoFs) can be on the order of billions. Even so, this type of problem can still be modeled by employing a parallel version of the FDTD algorithm running on a cluster. Lastly,

we note that the results of rigorous simulation of BANs can serve as benchmarks for comparison with the abundance of measurement data.

Despite the capability of FDTD to model the complex human body in its original form, it is often desired to seek out good geometrical approximations. This has been documented in the literature for both measurement and simulation purposes. However, to-date a quantitative study that demonstrates the accuracy of the results using simplified models has not yet been reported. Therefore, it is highly desirable to carry out an in-depth study of these approximations and to see how well the results based on these approximations compare to the rigorous simulation of the human body. A detailed characterization of this comparison has been carried out and will be presented in Chapter 3.

Next, in Chapter 4 we will introduce an entirely new hybrid approach to modeling fine geometrical features in the FDTD without reducing the nominal cell size (typically taken to be $\lambda_{high}/20$), where λ_{high} is the wavelength at the highest simulation frequency. The general nature of the problems described thus far can be simply labeled as electrically large in nature as they relate to the inhomogeneous host medium, e.g. , for instance the human body. However, in most cases, the radiating or imbedded scattering structures have geometrically fine features so that they would be nonintrusive, and the size of these structures are typically smaller than the FDTD cell size, which is nominally chosen to be $\lambda_{high}/20$, as needed to remain nonintrusive. It is evident, therefore, that the problem at hand is multi-scale in nature. The computational burden to model both fine features and the large host medium remains a common problem in the simulation of BANs, as well as in the modeling of medical sensors of various types. Although attempts have been made by a number of researchers to incorporate multi-scale techniques in the FDTD — and it has been an active research area during the last decade — a robust approach to modeling the one or more small structures located in a host medium has yet to be reported. This has motivated

us to pursue the developments of a multi-scale method based on the dipole moment concept that will enable us to model these problems in the context of the FDTD.

The principal motivation for using the dipole moment (DM) approach is that the near-field behavior of the DM representation is quasi-static in nature. In fact, we show in this work that any small scatterer/antenna can be represented by a dipole moment representation, regardless of its geometrical shape, and it is this property that enables us to couple the quasi-static solution to the FDTD. Thus the problem at hand is to find a dipole moment representation for an arbitrary geometry which is electrically small. In Chapter 4 we describe how the scattered field of an electrically small structure can be computed by modeling it as a continuous chain of spheres each having an analytically known dipole moment. This approach has been validated for straight wires, bent wires, loops, etc., when used to compute the scattered field.

By expanding on the dipole moment concept it will be demonstrated how we can couple the scattered field of a sphere — or any known distribution of dipole moments for that matter — to FDTD for lossless and lossy media when the scatterer is contained either within a single or multiple FDTD cells. The scattering results for the sphere are compared with the Mie series to serve as a benchmark test to validate the approach.

Of course, in many applications there may be multiple small scatterers located near each other and it is desired to have an FDTD formulation than can account for this coupling. It has been demonstrated that the formulation given in Chapter 4 can accurately model the scattered fields of two small spheres located in adjacent FDTD cells.

Often the geometrical details may be fine in some regards but not in others. For instance, simulating a thin wire is problematic for FDTD not because of its length but due to the small radius desired to be modeled. Therefore, an approach that can apply the dipole moment formulation to structures that pass through multiple cells in the FDTD but posses some fine geometrical features, e.g., zig-zag, loop and helical antennas will be presented.

In Chapter 5 we will introduce a new approach to the Time-Domain-Electric-Field-Integral-Equation (TD-EFIE). This approach relies upon the known closed-form solution for a wire carrying an assumed sinusoidal current distribution. This closed-form solution for the electric field has been generalized in this work to account for bent wire geometries. Furthermore, it has many attractive features that make it amenable to formulating the TD-EFIE. Specifically, the electric field produced by a wire carrying the assumed current distribution is represented as a sum of complex exponential terms, which provide a simple representation of the fields in the time domain in terms of delays. By expanding on this result it is possible to construct a matrix equation for the current distribution in the time domain for a given geometry. The ability to construct a TD-EFIE has the potential for future hybridization with the FDTD in scenarios where the propagation along wire geometries must be considered. In contrast, the dipole moment approach cannot account for this behavior. Therefore, a novel formulation based on this concept along with some results for simple wire and loop geometries will be presented.

The results and contributions of this thesis will be summarized in Chapter 6. Finally, we will provide some avenues of future research that can apply the results of Chapter 5 towards a hybridization with the FDTD.

1.4 Background Material

The Finite Difference Time Domain (FDTD) technique is a very popular tool for analyzing many electromagnetic problems due to its flexibility in modeling complex media and suitability for parallelization in large computing clusters. In addition, it has the advantage over other methods in modeling planar antenna geometries with layered media. Furthermore, since the FDTD method is performed in the time domain, it has the benefit of generating wide-band frequency domain results from a single simulation via the Fourier transform.

The FDTD technique is based on Maxwell's curl equations, which quantify the fields for all time and space. Explicitly they are given by

$$
\nabla \times \vec{H} = \vec{J} + \frac{\partial \vec{D}}{\partial t}
$$
$$
\nabla \times \vec{E} = -\vec{M} - \frac{\partial \vec{B}}{\partial t}
$$

(1.1)

In the FDTD technique, central differences are used to approximate Maxwell's curl expressions in (1.1). The development of this approximation is based on the Yee algorithm, which uses central differences to relate the derivatives of the neighboring discrete fields. The unit cell in Fig. 1.1 graphically shows the spatial arrangement of the fields in the Yee algorithm and is known as a Yee cell. In order to accurately describe geometrical parameters, source excitations, and observation points, it is necessary to have a complete understanding of where the fields are located in the FDTD mesh.
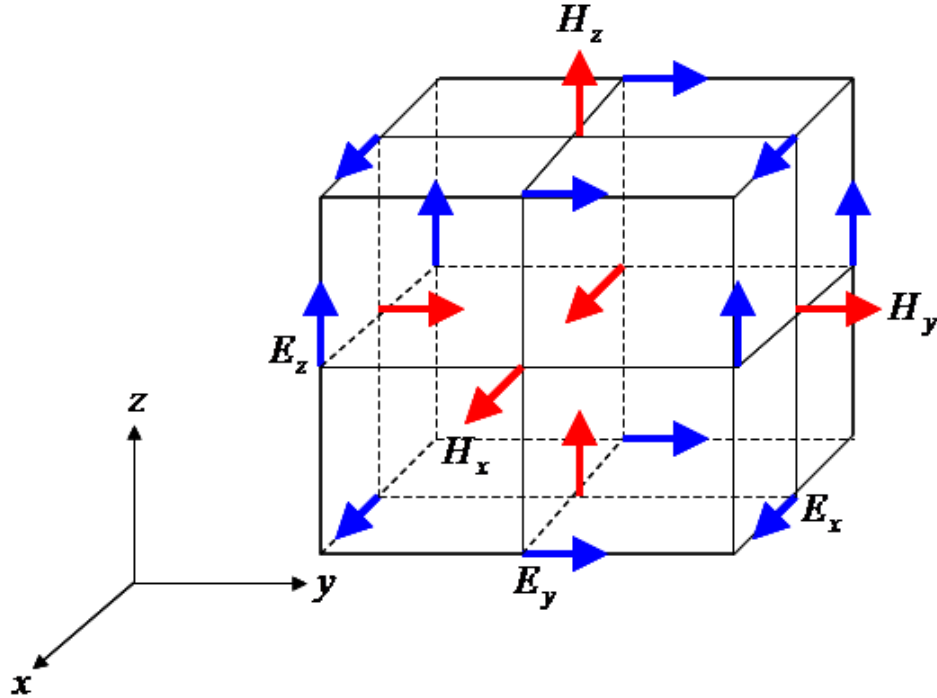
Fig. 1.1: The Yee cell used in FDTD.

Since the Yee algorithm centers the E-and H-field components in time, it is commonly termed a *leapfrog* scheme. The resulting update expressions for the three components of the E- and H-fields in a cubic lattice with $\Delta x = \Delta y = \Delta z = \Delta s$, each corresponding to the Cartesian coordinate system, are given by

$$
E_x\Big|_{i+1/2,j,k}^{n+1} = C_{aE_x}\Big|_{i+1/2,j,k} \cdot E_z\Big|_{i+1/2}^{n} + C_{bE_x}\Big|_{i+1/2,j,k}
$$
$$
\cdot \left(H_z\Big|_{i+1/2,j+1/2,k}^{n+1/2} - H_z\Big|_{i+1/2.j-1/2,k}^{n+1/2} + H_y\Big|_{i+1/2,j,k-1/2}^{n+1/2} - H_y\Big|_{i+1/2,j,k+1/2}^{n+1/2} \right)
$$
(1.2a)

$$
E_y\Big|_{i,j+1/2,k}^{n+1} = C_{aE_y}\Big|_{i,j+1/2,k} \cdot E_y\Big|_{i,j+1/2,k}^{n} + C_{bE_y}\Big|_{i,j+1/2,k}
$$
$$
\cdot \left(H_x\Big|_{i,j+1/2,k+1/2}^{n+1/2} - H_x\Big|_{i,j+1/2,k-1/2}^{n+1/2} + H_z\Big|_{i-1/2,j+1/2,k}^{n+1/2} - H_z\Big|_{i+1/2,j+1/2,k}^{n+1/2} \right)
$$
(1.2b)

$$
E_z\Big|_{i,j,k+1/2}^{n+1} = C_{aE_z}\Big|_{i,j,k+1/2} \cdot E_z\Big|_{i,j,k+1/2}^{n} + C_{bE_z}\Big|_{i,j,k+1/2}
$$
$$
\cdot \left(H_y\Big|_{i+1/2,,j,k+1/2}^{n+1/2} - H_y\Big|_{i-1/2,j,k+1/2}^{n+1/2} + H_x\Big|_{i,j-1/2,k+1/2}^{n+1/2} - H_x\Big|_{i,j+1/2,k+1/2}^{n+1/2} \right)
$$
(1.2c)

$$
H_x\Big|_{i,j+1/2,k+1/2}^{n+1/2} = D_{aH_x}\Big|_{i,j+1/2,k+1/2} \cdot H_x\Big|_{i,j+1/2,k+1/2}^{n-1/2} + D_{bH_x}\Big|_{i,j+1/2,k+1/2}
$$
$$
\cdot \left(E_y\Big|_{i,j+1/2,k+1}^{n} - E_y\Big|_{i,j+1/2,k}^{n} + E_z\Big|_{i,j,k+1/2}^{n} - E_z\Big|_{i,j+1,k+1/2}^{n} \right)
$$
(1.2d)

$$
H_y\Big|_{i+1/2,j,k+1/2}^{n+1/2} = D_{aH_y}\Big|_{i+1/2,j,k+1/2} \cdot H_y\Big|_{i+1/2,j,k+1/2}^{n-1/2} + D_{bH_y}\Big|_{i+1/2,j,k+1/2}
$$
$$
\cdot \left(E_z\Big|_{i+1,j,k+1/2}^{n} - E_z\Big|_{i,j,k+1/2}^{n} + E_x\Big|_{i+1/2,j,k}^{n} - E_x\Big|_{i+1/2,j,k+1}^{n} \right)
$$
(1.2e)

$$
H_z\Big|_{i+1/2,j+1/2,k}^{n+1/2} = D_{aH_z}\Big|_{i+1/2,j+1/2,k} \cdot H_z\Big|_{i+1/2,j+1/2,k}^{n-1/2} + D_{bH_z}\Big|_{i+1/2,j+1/2,k}
$$
$$
\cdot \left(E_x\Big|_{i+1/2,j+1,k}^{n} - E_x\Big|_{i+1/2,j,k}^{n} + E_y\Big|_{i,j+1/2,k}^{n} - E_y\Big|_{i+1,j+1/2,k}^{n} \right)
$$
(1.2f)

where (i,j,k) represent the spatial index and n is the time index, [51]. The electric and magnetic field coefficients at the point (i,j,k) are given by

$$C_a\big|_{i,j,k} = \frac{1 - \dfrac{\sigma_{i,j,k}\Delta t}{2\varepsilon_{i,j,k}}}{1 + \dfrac{\sigma_{i,j,k}\Delta t}{2\varepsilon_{i,j,k}}} \tag{1.3a}$$

$$C_b\big|_{i,j,k} = \frac{\dfrac{\Delta t}{\varepsilon_{i,j,k}\Delta s}}{1 + \dfrac{\sigma_{i,j,k}\Delta t}{2\varepsilon_{i,j,k}}} \tag{1.3b}$$

$$D_a\big|_{i,j,k} = \frac{1 - \dfrac{\rho'_{i,j,k}\Delta t}{2\mu_{i,j,k}}}{1 + \dfrac{\rho'_{i,j,k}\Delta t}{2\mu_{i,j,k}}} \tag{1.3c}$$

$$D_b\big|_{i,j,k} = \frac{\dfrac{\Delta t}{\mu_{i,j,k}\Delta s}}{1 + \dfrac{\rho'_{i,j,k}\Delta t}{2\mu_{i,j,k}}} \ . \tag{1.3d}$$

As the Yee algorithm indicates, the choice of spatial discretization is key to obtaining numerically stable and accurate results. It has been found that the choice of cell size should be no larger than approximately $\dfrac{\lambda}{20}$ to provide for sufficient sampling of the fields and to minimize the effects of numerical dispersion. Much smaller cell sizes are necessary in cases where the geometry has fine features. To guarantee numerical stability in the general case, it has been shown that the following condition must be satisfied [30]:

$$\Delta t \leq \frac{1}{c\sqrt{\dfrac{1}{(\Delta x)^2} + \dfrac{1}{(\Delta y)^2} + \dfrac{1}{(\Delta z)^2}}} \tag{1.4}$$

The expression in (1.4) is referred to as the Courant stability condition and is a necessary requirement when constructing the FDTD mesh for the geometry under analysis.

As for most finite methods, the FDTD algorithm meshes the entire computational space, and therefore requires proper treatment of the boundary truncation. Specifically, the finite computational domain boundaries should yield little or no reflections in order to accurately analyze open boundary radiation problems. Over the years, several absorbing boundary conditions (ABCs) have been proposed, and one of the simplest has been developed by Mur, [51]. The FDTD simulations presented in Chapter 4 utilize the Mur type ABC since it gave sufficiently low reflections while reducing the computational cost. However, for some cases the Mur ABC has been known to introduce reflections that can cause the simulation accuracy to suffer. In recent years, the ABC proposed by Berenger, [47], has become the most popular choice for handling the FDTD boundaries. This type of ABC is commonly referred to as the Perfectly Matched Layer (PML) in the literature. It has been demonstrated that this technique can lower reflections from the outer boundaries by several orders of magnitude when compared to other approaches. The PML formulation introduces an artificial anisotropic medium and uses a modified set of Maxwell's equations in which the fields are split into two components at the interface of the ABC and simulation space. In effect, the resulting wave impedance is perfectly matched to the simulation space and is independent of the incident angle. In principle, the outgoing waves are attenuated in a direction normal to the layers of the artificial medium as they impinge on the PML. Although accurate results can be achieved by placing as few as 4 or 5 cells between the radiating structure and the PML boundary, it is typically preferred to maintain a minimum of 10 cells. The FDTD simulations presented in Chapters 2 and 3 are based on a modified variation of Berenger's PML, which consists of six layers. This alternate approach has been shown to enhance the computational efficiency while obviating the need to modify the FDTD update equations for the split field formulation.

Chapter 2

A Numerically Efficient Technique for Determining the Coupling in Electrically Large Conformal Array Systems

In this chapter we provide a novel approach to finding the Green's function for layered media using the Body-of-Revolution-FDTD. From this information we can extrapolate the fields to electrically large distances using Prony's method. As an application of this approach we determine the coupling between two large Ku-band and X-band arrays using the reaction concept.

2.1 Methodology

Green's functions for layered media play an important role in RF and microwave circuit applications and they are time-consuming to construct because of the computationally intensive nature of the Sommerfeld integrals. Several techniques for expediting the construction of the layered-medium Green's functions have been proposed in the literature [1, 2], notable among them is the closed-form Green's function approach [2]. However, these techniques are still not as efficient as one would desire, especially when the source and observation points are not strictly located in the same plane. Furthermore, if the computational domain size is large and the observation points are many wavelengths away, the accuracy of the closed-form Green's function is known to suffer.

In this work we present a novel approach to constructing the layered medium Green's function using the BOR (body of revolution) version of the FDTD, which has several desirable attributes: (a) It poses no difficulty when handling n-layer problems, even when n is large; (b) it is easy to analyze lossy layers, including RAM materials; (c) the location of the observation point

can be arbitrary in terms of horizontal and vertical distances from the source; (d) the electric and magnetic fields (all six components) are computed directly at all observation points in the computational domain and, hence, they can be conveniently used to compute MoM matrix; (e) surface wave contributions, which play an important role at large distances from the source, can be obtained without any difficulty; (f) the dielectric layers can be truncated at an arbitrary *radial* distance from the source to estimate truncation effects and, (g) the mutual interaction between two sources (e.g., antennas) can be obtained by applying the Reaction concept once the field due to the first source at the location of the second one has been obtained. The Green's function results are then combined with superposition to construct the fields due to a distributed source.

To demonstrate the powerful efficiency of this method we have chosen to analyze the problem of EM I-type coupling between two arrays operating in the X- and Ku-bands, each with 18 elements. The arrays are mounted on a lossy RAM material over a ground plane that mimics the mast of a ship. The procedure for arriving at the solution is outlined as follows: (1) Simulate the antenna structure in isolation to obtain terminal parameters and fields on an aperture just above the conformal antenna; (2) Treat the fields in this aperture distribution as equivalent sources, J and M, in the analysis that follows. We assume that this information can either be obtained or given *a priori*; (3) Use the BOR-FDTD to simulate the problem of horizontal electric and magnetic incremental sources residing on the layered model, and construct the appropriate Green's functions for the layered media; (4) Use a Prony-type analysis of the fields at large distances from the source where only surface waves dominate; (5) Break up the obtained transmitting aperture into a discrete number of incremental sources (both magnetic and electric) and apply superposition to an arbitrary receive aperture size; (6) Apply the *Reaction concept* to compute the coupling between the two arrays by using the fields obtained on the receive aperture.

2.2 The Body-of-Revolution FDTD (BOR-FDTD)

The Body-of-Revolution Finite Difference Time Domain (BOR-FDTD) algorithm enables one to analytically extract the azimuthal behavior of fields that exhibit symmetric behavior around the axis of revolution. The BOR-FDTD is well suited for problems such as circular waveguides, corrugated circular horn antennas, and many other common geometries that posses circular symmetry. The formulation of the BOR-FDTD presented below closely follows that of [4]. It is based on the fact that the fields generated by these geometries and corresponding sources can be represented in a cylindrical coordinate system as follows:

$$\vec{E}(\rho,\phi,z,t) = \sum_{m=0}^{\infty} \left(\hat{\vec{E}}(\rho,m,z,t)_{even} \cos m\phi + \hat{\vec{E}}(\rho,m,z,t)_{odd} \sin m\phi \right) \tag{2.1}$$

$$\vec{H}(\rho,\phi,z,t) = \sum_{m=0}^{\infty} \left(\hat{\vec{H}}(\rho,m,z,t)_{even} \cos m\phi + \hat{\vec{H}}(\rho,m,z,t)_{odd} \sin m\phi \right) \tag{2.2}$$

where m is the index for the harmonics in the azimuthal plane. The even and odd modes are independent as long as the medium is isotropic. Therefore, we begin the analysis with Maxwell's equations in the time-domain

$$\vec{\nabla} \times \vec{H} = \varepsilon \frac{\partial \vec{E}}{\partial t} + \sigma_e \vec{E} \tag{2.3}$$

$$\vec{\nabla} \times \vec{E} = -\mu \frac{\partial \vec{H}}{\partial t} - \sigma_m \vec{H} \ . \tag{2.4}$$

Substituting (2.1) and (2.2) into (2.3) and (2.4) in addition to removing the cosine and sine parts of the field components yields

$$
\begin{bmatrix}
0 & -\partial_z & \pm\dfrac{m}{\rho} \\
\partial_z & 0 & -\partial_\rho \\
\mp\dfrac{m}{\rho} & \dfrac{1}{\rho}\left(\partial_\rho\rho\right) & 0
\end{bmatrix}
\begin{bmatrix}
\hat{E}_\rho \\
\hat{E}_\phi \\
\hat{E}_z
\end{bmatrix}
= -
\begin{bmatrix}
\left(\mu_0\mu_\rho\partial_t + \sigma_{m\rho}\right)\hat{H}_\rho \\
\left(\mu_0\mu_\phi\partial_t + \sigma_{m\phi}\right)\hat{H}_\phi \\
\left(\mu_0\mu_z\partial_t + \sigma_{mz}\right)\hat{H}_z
\end{bmatrix}
\tag{2.5}
$$

$$
\begin{bmatrix}
0 & -\partial_z & \mp\dfrac{m}{\rho} \\
\partial_z & 0 & -\partial_\rho \\
\pm\dfrac{m}{\rho} & \dfrac{1}{\rho}\left(\partial_\rho\rho\right) & 0
\end{bmatrix}
\begin{bmatrix}
\hat{H}_\rho \\
\hat{H}_\phi \\
\hat{H}_z
\end{bmatrix}
=
\begin{bmatrix}
\left(\varepsilon_0\varepsilon_\rho\partial_t + \sigma_{e\rho}\right)\hat{E}_\rho \\
\left(\varepsilon_0\varepsilon_\phi\partial_t + \sigma_{e\phi}\right)\hat{E}_\phi \\
\left(\varepsilon_0\varepsilon_z\partial_t + \sigma_{ez}\right)\hat{E}_z
\end{bmatrix}
\tag{2.6}
$$

where the field components represent the Fourier coefficients to the even or odd modal

expansions, respectively. In final form, the field components are then found as

$$
\begin{aligned}
E_\rho &= \hat{E}_\rho \begin{pmatrix} \sin m\phi \\ \cos m\phi \end{pmatrix} & H_\rho &= \hat{H}_\rho \begin{pmatrix} \cos m\phi \\ \sin m\phi \end{pmatrix} \\
E_\phi &= \hat{E}_\phi \begin{pmatrix} \cos m\phi \\ \sin m\phi \end{pmatrix} & H_\phi &= \hat{H}_\phi \begin{pmatrix} \sin m\phi \\ \cos m\phi \end{pmatrix} \\
E_z &= \hat{E}_z \begin{pmatrix} \sin m\phi \\ \cos m\phi \end{pmatrix} & H_z &= \hat{H}_z \begin{pmatrix} \cos m\phi \\ \sin m\phi \end{pmatrix}.
\end{aligned}
\tag{2.7}
$$

The cosine and sine expressions in the brackets are respective to the plus and minus signs

in (2.5) and (2.6). For brevity, we have omitted the t, ρ and z dependence in the Fourier

coefficients.

Equations (2.5) and (2.6) have now been reduced to a form with only two spatial

dependencies, namely, ρ and z. This serves as the motivation for using the BOR-FDTD

formulation, since it reduces the original 3D problem into an equivalent 2D version. Specifically,

the FDTD formulation of equations (2.5) and (2.6) substantially reduces the computational costs

in comparison to those of the conventional 3D FDTD analysis. To formulate the FDTD update

equations for the BOR problem, we refer to Fig. 2.1.
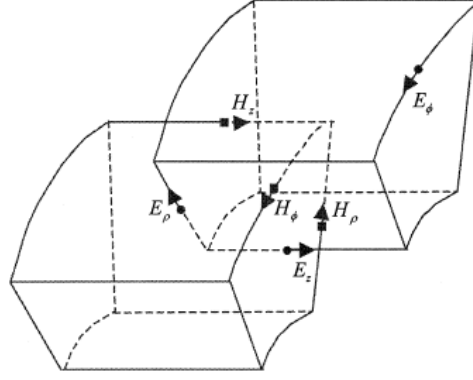
(a)
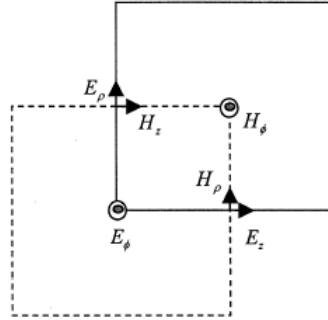
(b)

Fig. 2.1: Configuration of field locations: (a) field locations in 3-D and (b) field
locations in 2.5-D (source from [4]).

For nonmagnetic materials, the expressions for the $\hat{E}$ and $\hat{H}$ coefficients, resulting from an

application of the central-difference scheme (graphically shown in Fig. 2.1), are given by

equations (2.8a-f) below:

$$E_\rho^{n+1}\left(i+\tfrac{1}{2},j\right)=\frac{\varepsilon_\rho-0.5\sigma_\rho\Delta t}{\varepsilon_\rho+0.5\sigma_\rho\Delta t}\,E_\rho^n\left(i+\tfrac{1}{2},j\right)$$

$$-\frac{\Delta t}{\varepsilon_\rho+0.5\sigma_\rho\Delta t}\left[\frac{H_\phi^{n+\frac{1}{2}}\left(i+\tfrac{1}{2},j+\tfrac{1}{2}\right)-H_\phi^{n+\frac{1}{2}}\left(i+\tfrac{1}{2},j-\tfrac{1}{2}\right)}{\Delta z(j)}\right] \qquad (2.8a)$$

$$\mp\frac{m\Delta t}{\varepsilon_\rho+0.5\sigma_\rho\Delta t}\,\frac{H_z^{n+\frac{1}{2}}\left(i+\tfrac{1}{2},j\right)}{\rho\left(i+\tfrac{1}{2}\right)}$$

$$E_\phi^{n+1}\left(i,j\right)=\frac{\varepsilon_\phi-0.5\sigma_\phi\Delta t}{\varepsilon_\phi+0.5\sigma_\phi\Delta t}\,E_\phi^n\left(i,j\right)$$

$$+\frac{\Delta t}{\varepsilon_\phi+0.5\sigma_\phi\Delta t}\left[\frac{H_\rho^{n+\frac{1}{2}}\left(i+\tfrac{1}{2},j+\tfrac{1}{2}\right)-H_\rho^{n+\frac{1}{2}}\left(i+\tfrac{1}{2},j-\tfrac{1}{2}\right)}{\Delta z(j)}\right] \qquad (2.8b)$$

$$-\frac{\Delta t}{\varepsilon_\phi+0.5\sigma_\phi\Delta t}\left[\frac{H_z^{n+\frac{1}{2}}\left(i+\tfrac{1}{2},j\right)-H_z^{n+\frac{1}{2}}\left(i-\tfrac{1}{2},j\right)}{\Delta\rho(i)}\right]$$

$$E_z^{n+1}\left(i,j+\tfrac{1}{2}\right)=\frac{\varepsilon_z-0.5\sigma_z\Delta t}{\varepsilon_z+0.5\sigma_z\Delta t}\,E_z^n\left(i,j+\tfrac{1}{2}\right)$$

$$+\frac{\Delta t}{\varepsilon_z+0.5\sigma_z\Delta t}\left[\frac{\rho\left(i+\tfrac{1}{2}\right)H_\phi^{n+\frac{1}{2}}\left(i+\tfrac{1}{2},j+\tfrac{1}{2}\right)-\rho\left(i-\tfrac{1}{2}\right)H_\phi^{n+\frac{1}{2}}\left(i-\tfrac{1}{2},j+\tfrac{1}{2}\right)}{\rho(i)\Delta\rho(i)}\right] \qquad (2.8c)$$

$$\pm\frac{m\Delta t}{\varepsilon_z+0.5\sigma_z\Delta t}\,\frac{H_\rho^{n+\frac{1}{2}}\left(i,j+\tfrac{1}{2}\right)}{\rho(i)}$$

$$H_\rho^{n+\frac{1}{2}}\left(i, j + \frac{1}{2}\right) = H_\rho^{n-\frac{1}{2}}\left(i, j + \frac{1}{2}\right) \mp \frac{m\Delta t}{\mu_\rho \rho(i)} E_z^n\left(i, j + \frac{1}{2}\right)$$

$$+ \frac{\Delta t}{\mu_\rho}\left[\frac{E_\phi^n(i, j+1) - E_\phi^n(i, j)}{\Delta z(j)}\right] \tag{2.8d}$$

$$H_\phi^{n+\frac{1}{2}}\left(i + \frac{1}{2}, j + \frac{1}{2}\right) = H_\phi^{n-\frac{1}{2}}\left(i + \frac{1}{2}, j + \frac{1}{2}\right)$$

$$- \frac{\Delta t}{\mu_\phi \rho\left(i + \frac{1}{2}\right)}\left[\frac{E_\rho^n\left(i + \frac{1}{2}, j+1\right) - E_\rho^n\left(i + \frac{1}{2}, j\right)}{\Delta z(j)}\right] \tag{2.8e}$$

$$+ \frac{\Delta t}{\mu_\phi}\left[\frac{E_z^n\left(i+1, j + \frac{1}{2}\right) - E_z^n\left(i, j + \frac{1}{2}\right)}{\Delta \rho(j)}\right]$$

$$H_z^{n+\frac{1}{2}}\left(i + \frac{1}{2}, j\right) = H_z^{n-\frac{1}{2}}\left(i + \frac{1}{2}, j\right)$$

$$- \frac{\Delta t}{\mu_z \rho\left(i + \frac{1}{2}\right)}\left[\frac{\rho(i+1)E_\phi^n(i+1, j) - \rho(i)E_\phi^n(i, j)}{\Delta \rho(i)}\right] \tag{2.8f}$$

$$\pm \frac{m\Delta t}{\mu_z \rho\left(i + \frac{1}{2}\right)} E_\rho^n\left(i+1/2, j\right)$$

The plus and minus signs in the above equations are related to which basis function has been chosen in (2.1) and (2.2), respectively. A problematic feature in the above equations is the point where $\rho \to 0$. It has been suggested that the most suitable way to deal with this singular point is to force the H_z component to align with the z-axis. Consequently, the first cell in the ρ-direction will be offset by a half-cell inside the computational domain.

2.3 Dipole Sources in BOR-FDTD

For rectangular-shaped conformal antennas, as well as for aperture sources, the equivalent problem is most conveniently represented by *x*- and *y*-oriented electric and magnetic sources. However, the BOR-FDTD can only represent sources with azimuthal harmonic symmetry, which the x- and y-oriented sources do not posses. This apparent obstacle to using the BOR analysis can be overcome by decomposing these Cartesian sources into their corresponding cylindrical components, namely, $\rho-$ and $\phi-$oriented sources. Specifically, let us consider an impressed electric field source, $E_x^{source} = E_0$, in the FDTD. This source can be represented in cylindrical coordinates as

$$E_\rho^{source} = E_o \cos\phi$$

$$E_\phi^{source} = -E_o \sin\phi$$

$$E_x^{source} = E_\rho^{source} \cos\phi - E_\phi^{source} \sin\phi = E_o \qquad (2.9)$$

Also note that the corresponding harmonic variations to each field component automatically satisfies (2.7). Therefore, we have a method for implementing x and y-oriented sources in BOR-FDTD.

In reality, the equivalent sources are $J_x^{source}, J_y^{source}, M_x^{source}, \; and \; M_y^{source}$. Since the FDTD primarily deals with Electric and Magnetic fields, the source excitations it works with are $E_x^{source}, E_y^{source}, H_x^{source}, \; and \; H_y^{source}$. Therefore, the relationship between the FDTD sources and the physical sources will involve a normalization constant that must be determined in order for the two results agree. If E_x^{source} is an incremental source in free space, the normalization constant

will be the dipole moment of the corresponding electric current source as shown in Fig. 2.2. In a

similar manner, the dipole moment can be found for a magnetic current source from H_x^{source} .
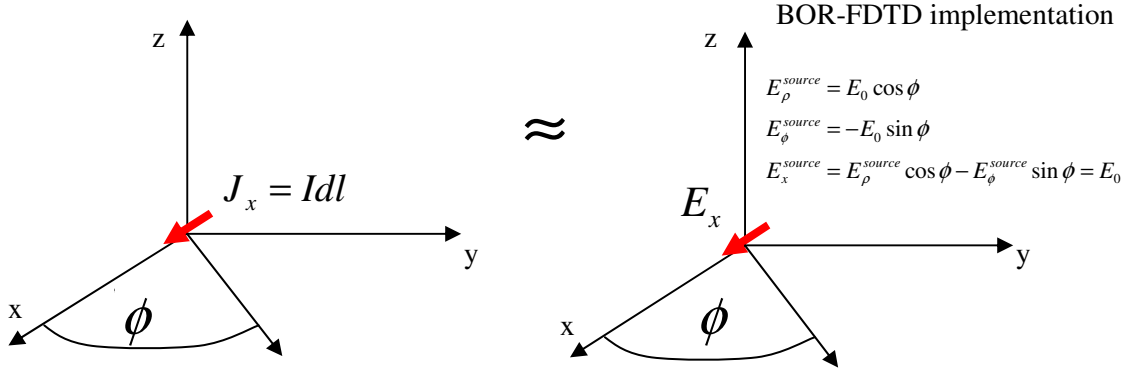
Fig.2.2: Simulating Horizontal Electric dipoles (HED) in Free-Space using BOR- FDTD.

To demonstrate that these BOR-FDTD sources behave as the physical ones mentioned in

the previous paragraph, we have simulated a point source excitation, $E_x^{source} = E_0 = 1$, at the

origin for 10 GHz, and have compared it to the radial variation of the analytical expressions for a

unit dipole moment in the $\theta = \dfrac{\pi}{2}$ plane. In Fig. 2.3 we observe a near-perfect agreement

between the analytical and numerical results in the qualitative behavior of the magnitude.

However, we also note that we need to utilize a normalization factor in the magnitude of the

numerical results for it to agree with the analytical one. For convenience, we choose to normalize

the fields to those that represent a unit dipole moment excitation throughout subsequent

simulations. In Fig. 2.4, we present a comparison between the analytical and numerical results,

for both the magnitude and phase, after they have been normalized.
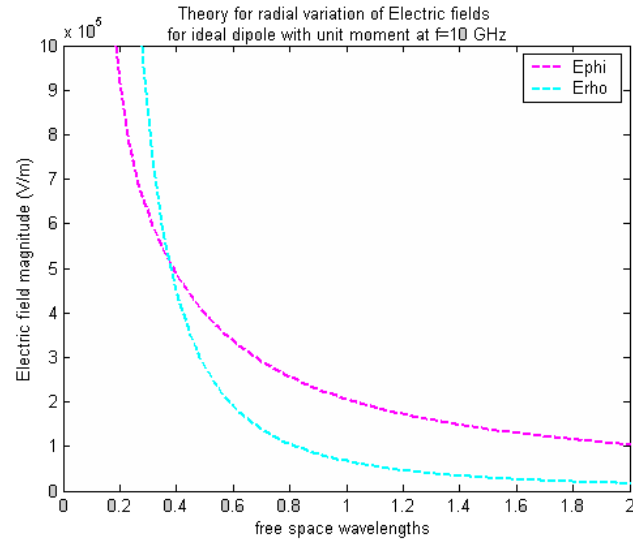
(a)
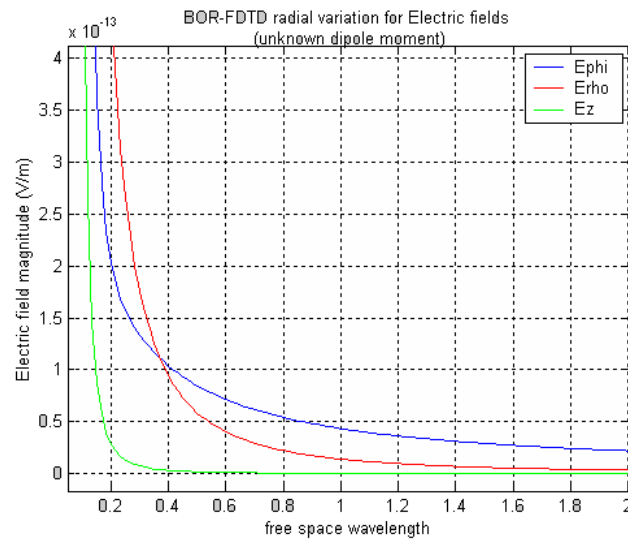
(b)

Fig. 2.3: Electric field from an x-oriented HED (a) Analytical results (b) Numerical results for magnitude along radial.
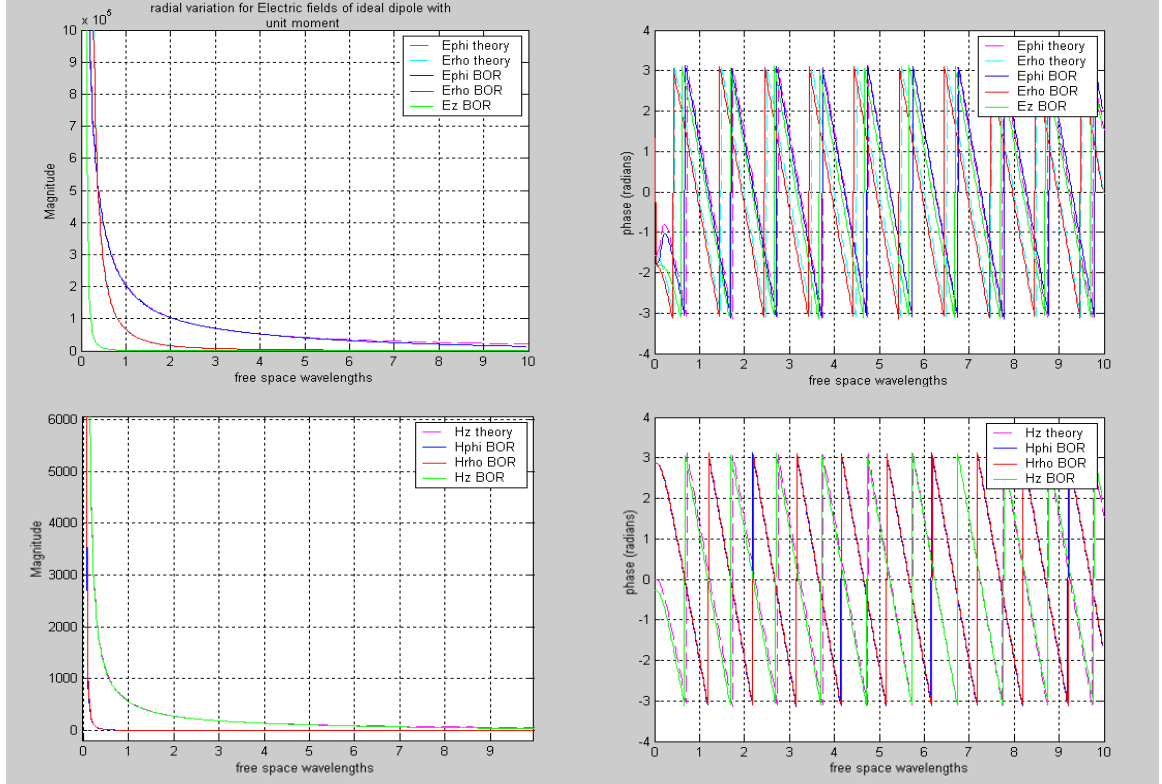
Fig. 2.4: Analytical and numerical results for magnitude and phase after normalization.

At this point it is important as well as worthwhile to relate the purpose for the preceding analysis to the problem at hand. Recall that the Green's function represents the fields generated by a point source of unit strength radiating in the medium under consideration, which can be possibly inhomogeneous. To numerically perform the convolution integral of an aperture source distribution with the Green's function, it is necessary to approximate the distribution as a summation of weighted incremental *x* and *y*-oriented electric and magnetic sources, which is precisely what has been simulated here. Therefore, the BOR-FDTD can be used as a tool to directly determine the Green's function of an inhomogeneous medium throughout the entire volume of the computational domain, and it enables us to calculate the fields generated by an arbitrary aperture source distribution via superposition.

2.4 Prony's Method and the Time Domain Green's Function

The BOR-FDTD has the distinct advantage in that it allows us to reduce the computational space from 3D to 2D when simulating point sources. However, if we wish to compute the fields at some very large distance, e.g., 30λ, the computational cost can become prohibitive. In order to circumvent this problem, we have used Prony's method to extrapolate the behavior of the fields in the asymptotic region, to arbitrarily large distances, by using the Prony parameters that we have extracted.

A full discussion of Prony's method is provided in Appendix A and excellent references can be found in [3]. In summary, Prony's method is a powerful tool that estimates the field behavior as a weighted some of complex exponentials given by

$$g(\rho) = \sum_n^N \hat{A}_n e^{\hat{k}_n \rho} \ .$$

(2.10)

For our purposes of estimating the coupling between two widely-spaced antenna arrays, we are interested in extrapolating the fields generated by the arrays in the asymptotic region. A graphical illustration of how we use Prony's method to address this problem is shown in Fig. 2.5. Also, a numerical example is presented in Figs. 2.6 and 2.7 for a horizontal electric dipole source, located at the origin of the BOR-FDTD computational domain and radiating at the interface between free space and a RAM material backed by a ground plane.

Field
Magnitude

FDTD result

Only propagating surface waves
Remain in the asymptotic region.

$f(\rho)$

$g(\rho)$

$f(\rho) = g(\rho - \rho_0)$

Sample region

Data used in Prony anaylsis

ρ_0

$$f(\rho) = \sum_{n}^{N} \hat{A}_n e^{\hat{k}_n (\rho - \rho_0)}$$
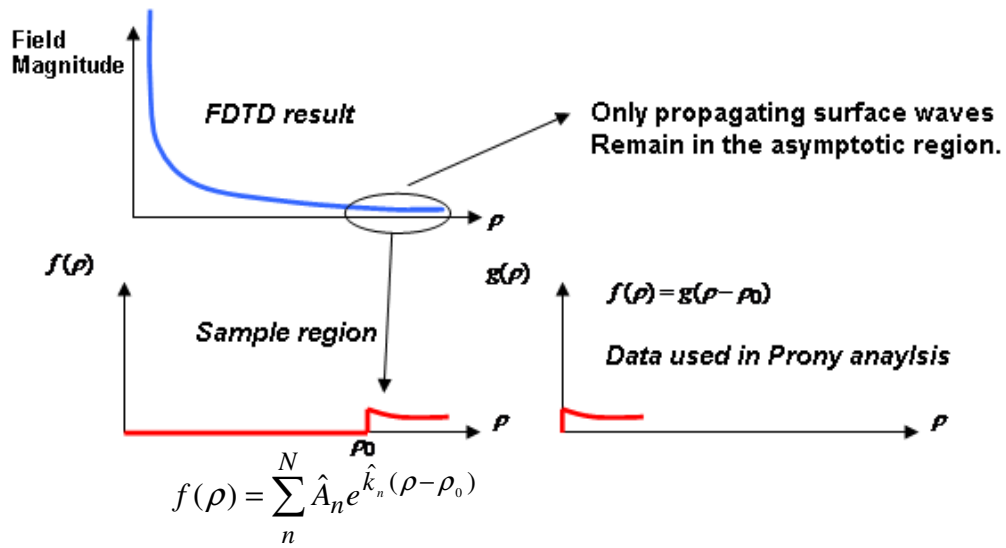
Fig. 2.5: Illustration of Prony's method for fields in the asymptotic region.

z

300 cells

Source position: cell index=50

Field observation plane

$\varepsilon_{r1} = 2.4$

$\varepsilon_{r2} = 10$

1200 cells

ρ

gnd
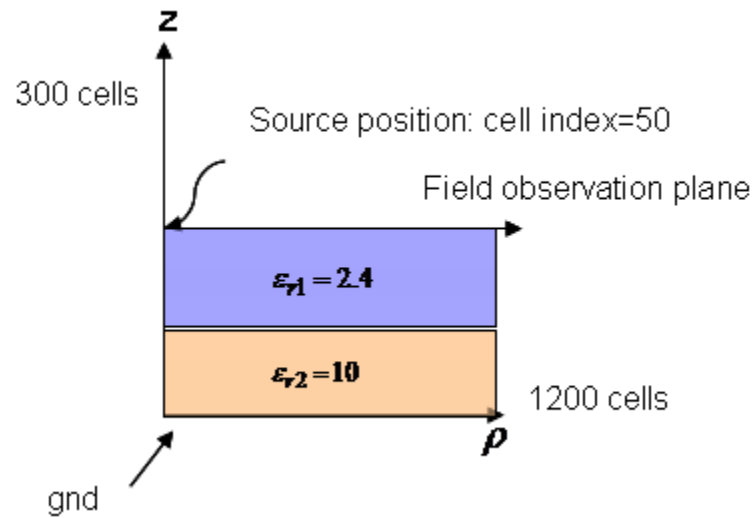
Fig. 2.6: A horizontal electric dipole (HED) located at the interface of free space and a RAM material backed by a ground plane.
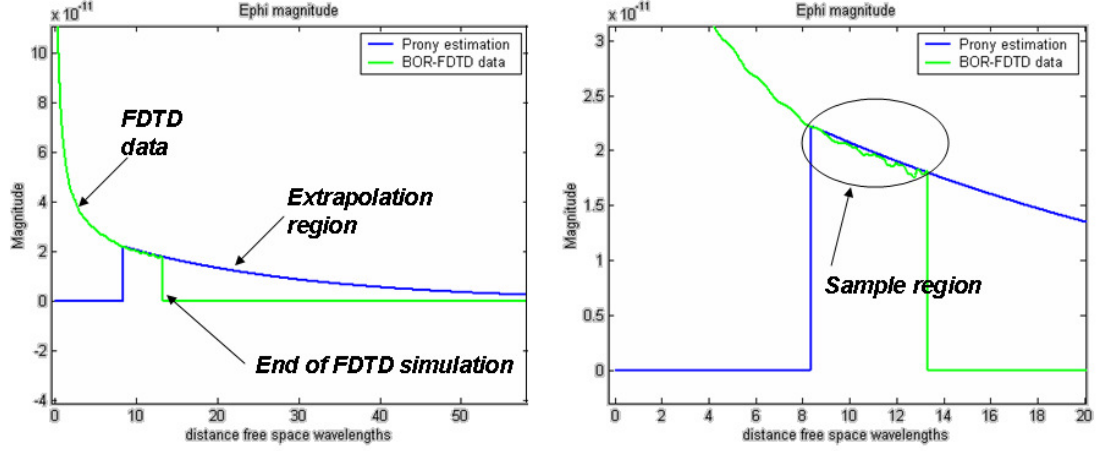
Fig. 2.7: Numerical example of Prony's method for a horizontal dipole source at the interface between free space and a RAM material backed by a ground plane.

For our purposes it was desired to find the Green's function for a RAM material with parameters given by $\varepsilon_r = 3.1, \quad \sigma = 0.134$, whose height is $0.34\,\lambda_0$, and backed by a ground plane. The BOR-FDTD computational domain extends to a length of $15\,\lambda_0$ along the radial direction, and $1.7\,\lambda_0$ along the vertical. The sources were placed at the air-dielectric interface and the Green's function was computed in the same plane as in Fig. 2.7 (i.e., the source plane). The data used for the Prony algorithm was derived in the asymptotic region, beginning at $13.33\,\lambda_0$ (see Fig. 2.9), after all fields were normalized by the dipole moment determined in the previous section. The Green's function for E_z is shown in Fig. 2.8 for a vertical cut plane with $\phi = 0$ excited by an x-oriented magnetic point source resting on the surface. It can be observed that a surface wave along the air-dielectric interface is indeed present and is the primary contributor to the planar antenna coupling. For increasing vertical distances, the behavior tends towards that of a space-wave.
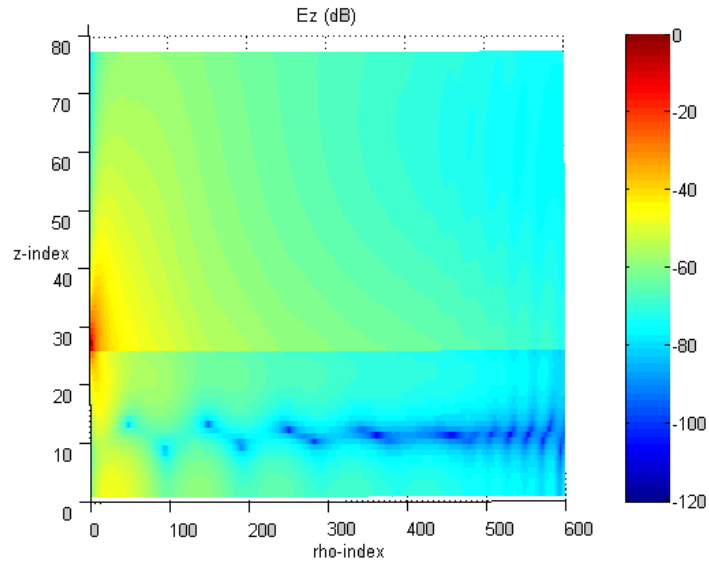
Fig. 2.8: E_z magnitude (dB) for x-oriented magnetic point source.
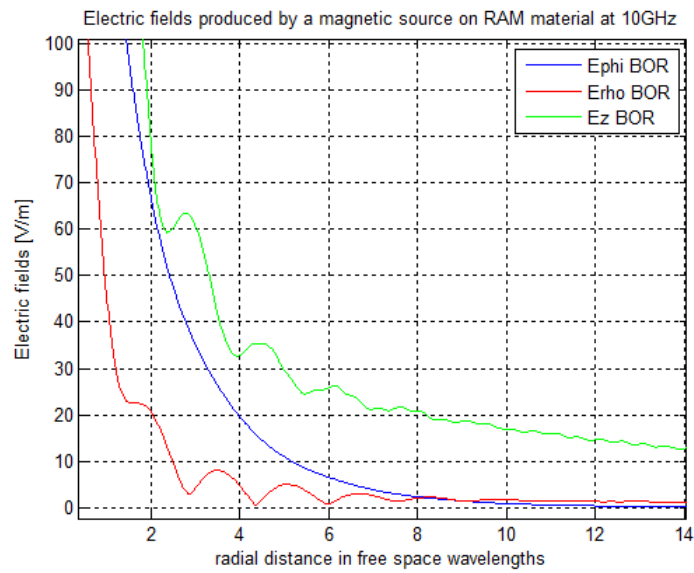
Fig. 2.9: Normalized Green's function and surface wave behavior along the air-dielectric interface for x-oriented magnetic point source.

2.5 Coupling Analysis Using the Time Domain Green's Function and the Reaction Concept

The numerically-determined Green's function, used in conjunction with Prony's approach to extrapolating the fields to large radial distances, enables us to determine the fields generated by an arbitrary aperture-type source via simple superposition. First, consider the system shown in Fig. 2.10, where an 18-element X-band spiral array is placed on the same RAM material described in the preceding section, and is separated by a distance of approximately 30 free-space wavelengths at 10 GHz from a spiral Ku-band array. At 10 GHz, the X-band array is operating in a transmit mode for the non-scanning case and the Ku-band array has only the center element excited. The problem consists of determining the surface wave coupling to the center element of the Ku-band array. Although trivial, it is still important to note that any contribution of the incident power reradiated by the Ku-band array is negligible, insofar as the estimation of coupling level is concerned, and can be ignored in the coupling calculation.
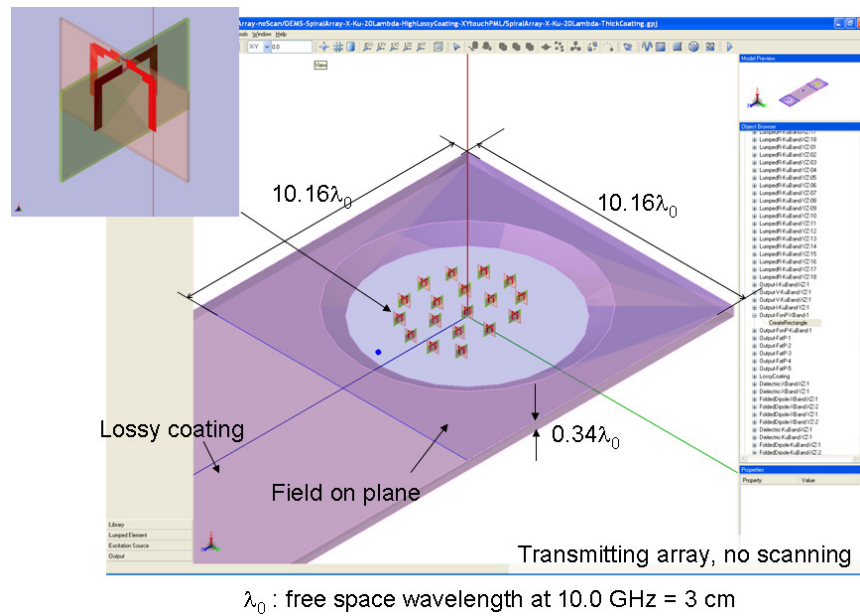
Fig. 2.10: An 18 element spiral X-band array separated by 30 free space wavelengths at 10 GHz from a similar spiral Ku-band array.

To formulate the equivalent problem we construct a planar surface just above each array. From the equivalence principle, we know that the fields generated by a particular source distribution are exactly those obtained by an equivalent distribution of sources on a surface enclosing the original sources and satisfying the boundary conditions. Furthermore, the excitation sources can be removed from the original problem and the material within the surface can be chosen arbitrarily provided that the boundary conditions are satisfied. To obtain the equivalent sources on the aperture, each array must be simulated in isolation and the fields calculated by any numerical method of choice. For our analysis, the fields obtained on the aperture of each array were obtained by using the conventional 3D FDTD. Although, induced equivalence is mathematically satisfied only when the surface is closed, for planar conformal antennas it is sufficient to work with a surface that is not closed but large enough to satisfy the condition that the contributions from the side surfaces be essentially negligible. This point is further illustrated in Figs. 2.11 and 2.12 where it can be seen that for a large planar surface the equivalent problem can be accurately defined, and is pictorially represented in Fig. 2.13.
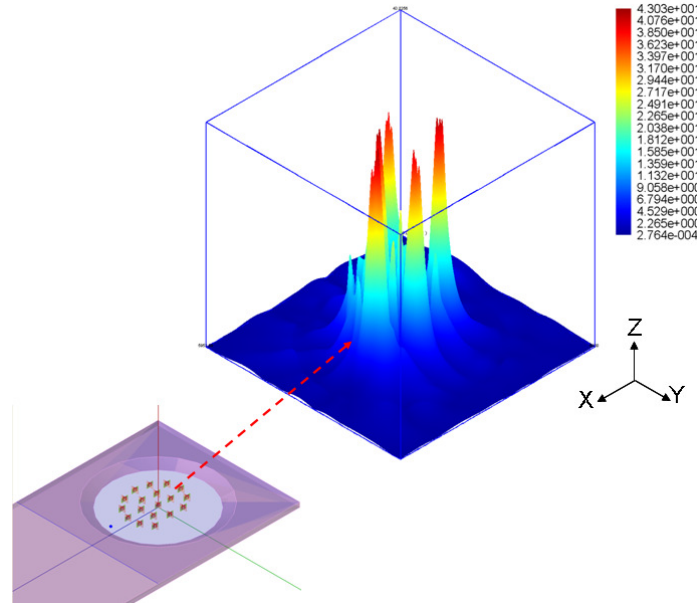
Fig. 2.11: E_x for the X-band spiral array in transmit mode non-scanning at 10 GHz.
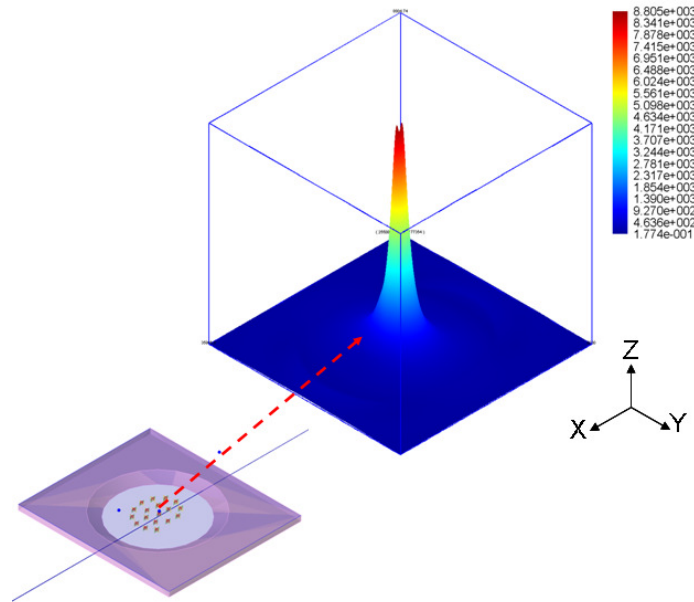
Fig. 2.12: E_x for the Ku-band spiral array with only center element active at 10 GHz.
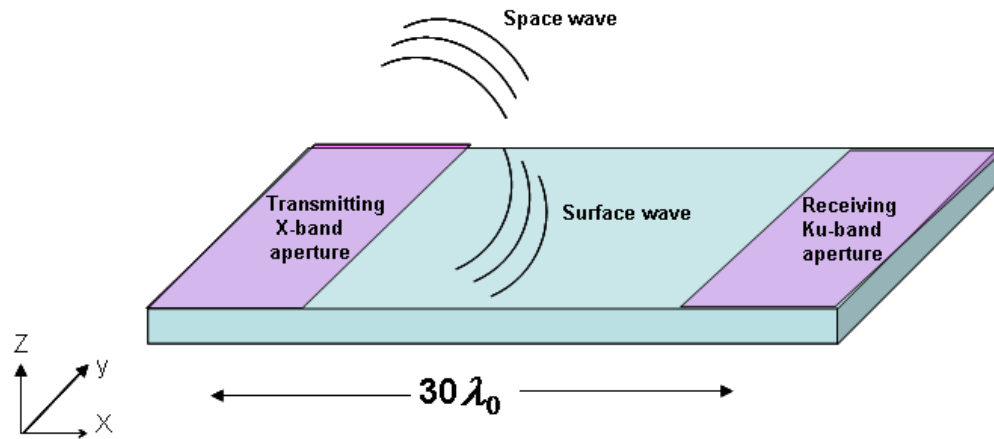
Fig. 2.13: Representation of the equivalent problem for the two array system.

Once we have obtained the equivalent source distribution on the X-band array aperture, as well the Ku-band equivalent sources when a single element of the latter array is excited, we can determine the fields induced by the X-band array on the aperture of the Ku-band array in the absence of its own equivalent sources. The reason for performing this calculation would be evident when we introduce the *reaction* concept. The fields from the X-band array that are induced on the Ku-band array aperture can be easily determined from the Green's function via the convolution integral. To perform this integration we first note how the sources are numerically calculated on the FDTD grid, as depicted in Fig. 2.14 for electric current sources.
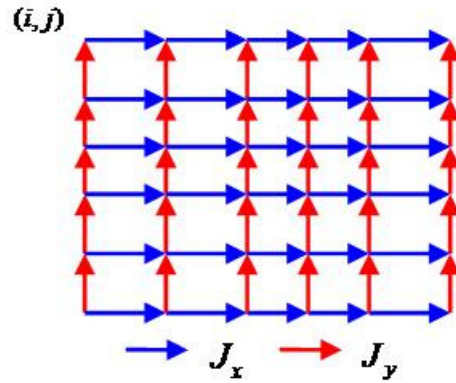
Fig. 2.14: Equivalent electric sources on aperture FDTD mesh.

It important to note that, in general, the FDTD computational mesh is non-uniform; as a consequence, it yields an equivalent surface mesh that also has non-uniform sampling. This is especially true for the case of each array because the individual array elements possess very fine features that can require cell sizes on the order of $\lambda_0/80$ or smaller to accurately compute mutual interaction between elements. However, the aperture fields used to form the equivalent surface do not vary nearly as rapidly and, hence, we can down-sample the mesh—while still retaining its

non-uniform nature—by a factor of 4 or even 8 without significant loss of accuracy. The down-sampling can significantly reduce the computational cost, in view of the fact that the number of computations required to perform the superposition of each source on a receiving aperture mesh can be quite large.

In performing the convolution integral, we note that the FDTD results are spatially sampled points and therefore the equivalent sources may be treated as a planar array of equivalent incremental sources. A key point to note is that both apertures (with dimensions of approximately $10\lambda_o$ on each side at 10 GHz), which are separated by approximately $30\lambda_0$, are *not* in the far-field of each other; therefore, we cannot use far-field approximations. This, in turn, leads to the convolution sum of the Green's function obtained and the array distribution of the aperture.

$$F(\rho,\phi) = \sum_n \sum_l^{L_y} \sum_m^{L_x} \begin{Bmatrix} \cos\phi_{ml} \\ \sin\phi_{ml} \end{Bmatrix} \cdot \hat{C}_n(|\rho-\rho_{ml}|) \cdot e^{-j\beta_n(|\rho-\rho_{ml}|-\rho_0)} \cdot \hat{S}_{ml} \qquad (2.11)$$

where $\phi_{ml} = \tan^{-1}\left(\dfrac{\rho\sin\phi - y_{ml}}{\rho\cos\phi - x_{ml}}\right)$ and $F(\rho,\phi)$ can be any one of the six field components. The bracketed cosine and sine terms are results of the BOR-FDTD formulation and the first summation corresponds to the Prony parameters obtained in order to estimate the Green's function in the asymptotic region. The second double summation is the weighting distribution of the transmitting array aperture. The term $\hat{S}_{ml}$ corresponds to the dipole moment of each equivalent incremental source and is defined as $J_{ml}\Delta y_m\Delta x_l$ for electric (magnetic) current sources both x- or y-orientations.

2.6 The Serial-Parallel FDTD

One approach to circumventing the difficulties that arise when attempting to solve electrically large problems with limited computer resources is to use the FDTD method with domain decomposition\serial-parallel processing. This method is based on dividing the computational domain into relatively small sub-regions along one direction and applying the parallel FDTD serially in each of these sub-regions with parallelization along the transverse directions, if desired. The tangential E-field is stored at the interface between each adjacent subdomain and is used as a boundary condition for the following subregion. The FDTD algorithm is then continued serially along the computational domain until the last subdomain is reached and the induced voltage and currents on the receive element can be calculated. This method is pictorially shown in Fig. 2.15 and it has been validated for many geometries [46]. Therefore, we have used it to simulate the X-band and Ku-band array coupling and field distributions as a benchmark comparison with the Green's function method.
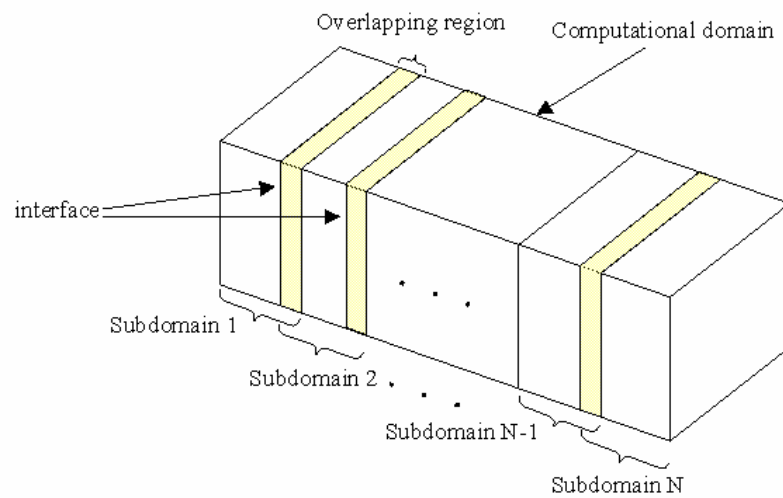
Fig. 2.15: Illustration of domain decomposition\ serial-parallel processing.

2.7 Results and Discussion

Constructing the equivalent problem by using the E_x fields from Fig. 2.11, as well as the

other tangential components, namely, E_y, H_x and H_y (not shown here) along with (2.11) forms

the basis for performing the calculation of the fields over the Ku-band aperture. To reiterate that

the FDTD mesh of the Ku-band aperture, over which we are performing the superposition, is non-

uniform we have again shown the single element excitation on the Ku-band array along with the

spatial discretization in Fig. 2.16. The resulting tangential electric field distribution (magnetic

fields not shown here) induced from the X-band array observed over the Ku-band array aperture

are shown in Figs. 2.17-2.18 where they have been compared with the results obtained using the

Serial-Parallel FDTD. For the purpose of comparison, the results from the two different

approaches were normalized to unity. Clearly, the field distribution generated by the Serial-

Parallel FDTD and the Green's function approach are in close agreement.
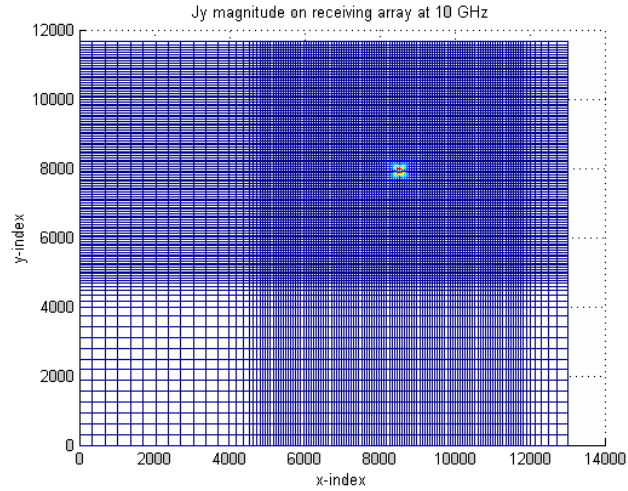
Fig. 2.16: Single active element and the spatial discretization of the Ku-band equivalent
surface.

(a)

(b)
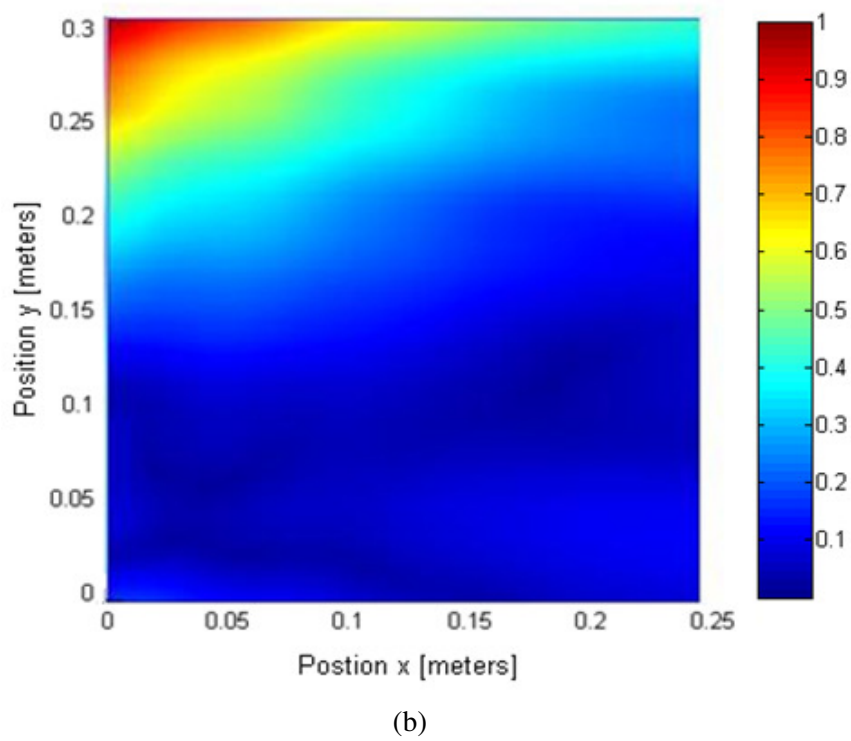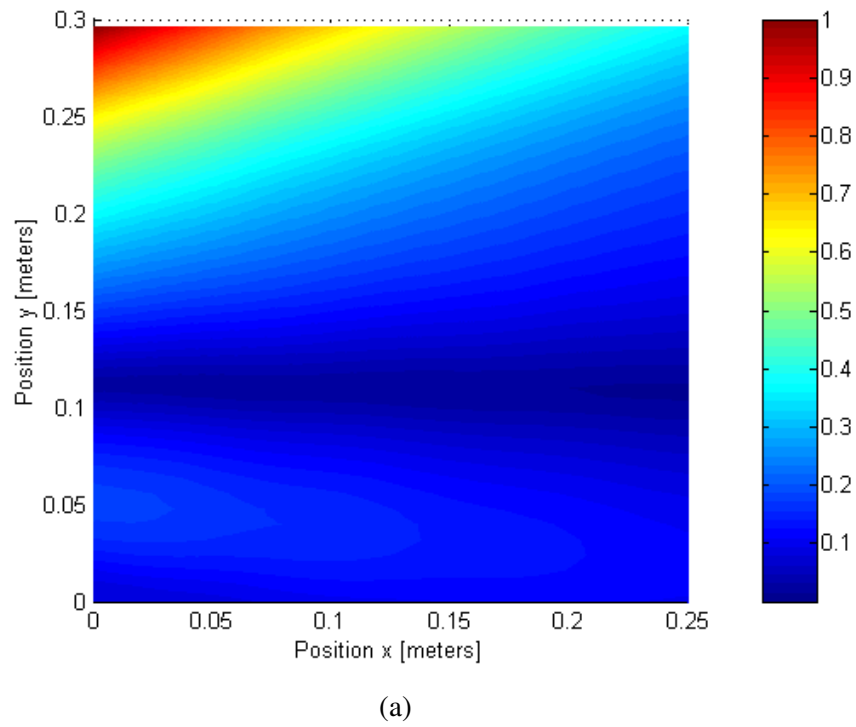
Fig. 2.17: Field distribution on the receiving aperture (a) E_y Green's function approach (b) E_y Serial-Parallel FDTD.

(a)

(b)
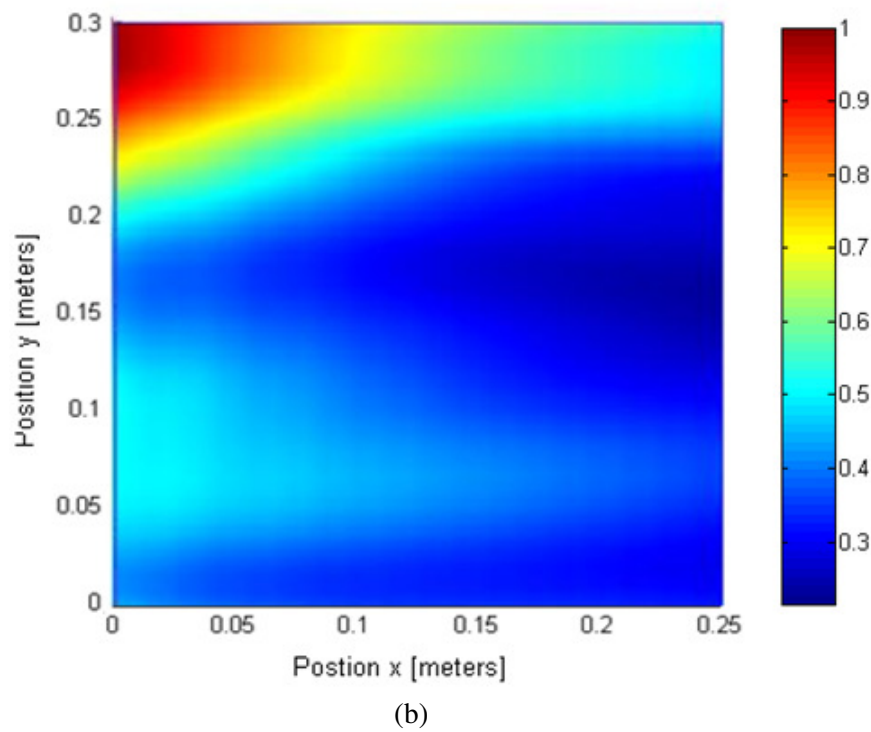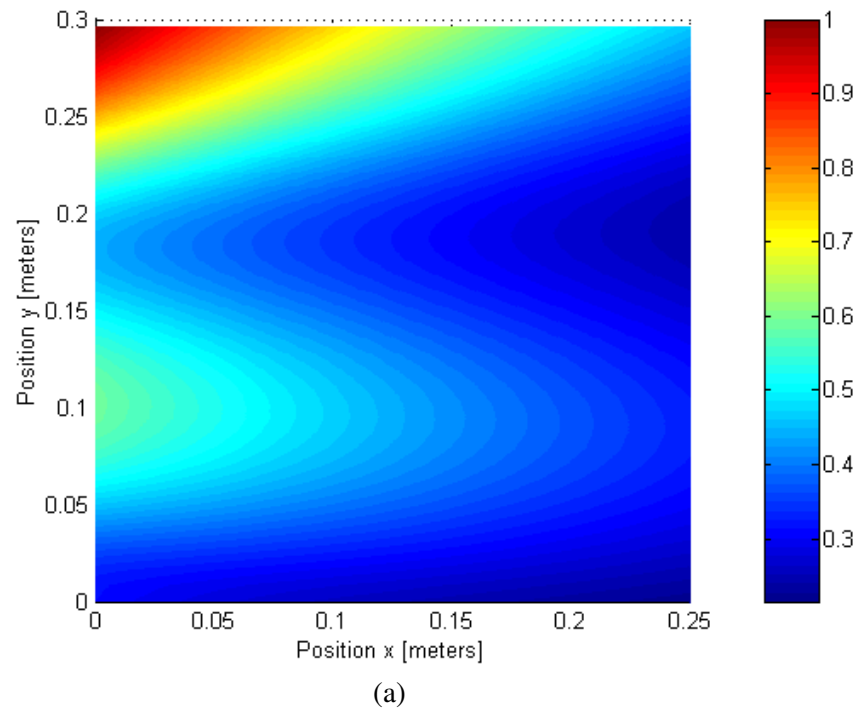
Fig. 2.18: Field distribution on the receiving aperture (a) E_x Green's function approach (b) E_x Serial-Parallel FDTD.

At this point we proceed to demonstrate how the results of Figs. 2.17-2.18 are used in the context of the reaction concept to calculate the coupling between the two arrays. First, we briefly summarize the reaction theorem as it applies to our problem. It can be shown from Maxwell's equations that for a closed region containing two sources (electric and magnetic) a and b that

$$-\oiint\left(\bar{E}^a \times \bar{H}^b - \bar{E}^b \times \bar{H}^a\right)\cdot d\bar{s} = \iiint\left(\bar{E}^a \cdot \bar{J}^b - \bar{H}^a \cdot \bar{M}^b - \bar{E}^b \cdot \bar{J}^a + \bar{H}^b \cdot \bar{M}^a\right)dV . \quad (2.12)$$

However, if we extend the radius of the surface $r \to \infty$ we know that for each source the fields are related as

$$E_\theta = \eta H_\phi \qquad E_\phi = -\eta H_\theta \qquad\qquad (2.13)$$

and the integral in (2.12) reduces to

$$\iiint\left(\bar{E}^a \cdot \bar{J}^b - \bar{H}^a \cdot \bar{M}^b\right)dV = \iiint\left(\bar{E}^b \cdot \bar{J}^a - \bar{H}^b \cdot \bar{M}^a\right)dV . \qquad (2.14)$$

Equation (2.14) is one form of the reciprocity theorem and the integral

$$<a,b>= \iiint\left(\bar{E}^a \cdot \bar{J}^b - \bar{H}^a \cdot \bar{M}^b\right)dV \qquad\qquad (2.15)$$

has been given the name *reaction*.

In our problem, the sources are defined over a surface and the volume integral reduces to a surface type as follows:

$$<a,b>= \iint\left(\bar{E}^a \cdot \bar{J}^b - \bar{H}^a \cdot \bar{M}^b\right)ds . \qquad\qquad (2.16)$$

Since $\bar{J}^b$ and $\bar{M}^b$ form the equivalent sources on the aperture, it is necessary that the reaction of the equivalent problem be the same as that of the original one, consisting of a source current on a probe-feed and some unknown incident field. In mathematical form

$$< a,b >= \iint \left(\vec{E}^a \cdot \vec{J}^b - \vec{H}^a \cdot \vec{M}^b \right) ds = \tag{2.17}$$

$$\int \vec{E}^a_{feed} \cdot I^b_{feed} d\vec{l} = -V^a I^b \tag{2.18}$$

$$V^a = \frac{< a,b >}{-I^b}. \tag{2.19}$$

Equation (2.19) can be used to calculate the induced voltage. However, it is more convenient to use the power induced in the termination load. This requires a knowledge of the terminal input impedance of the antenna, as well as of the source impedance. For our case, the source impedance was assumed to be 50Ω and the input impedance of the single active element on the Ku-band array was found to be $9.28 - j44.3\Omega$. Therefore, the power delivered to the single Ku-band active element can be found by using the expressions

$$P_d = \frac{1}{2} \text{Re} \left\{ V^a I^{ind*} \right\} = \frac{\left| V^a \right|^2}{2} \frac{R_L}{(R_L + R_{rad})^2 + (X_{rad})^2}$$

$$P_d = \frac{\left| < a,b > \right|^2}{2\left| I^b \right|^2} \frac{R_L}{(R_L + R_{rad})^2 + (X_{rad})^2} \tag{2.20}$$

where I^{ind} is the induced current in the receiving load. Using the results shown in Fig. 2.12 and the other corresponding equivalent sources on the Ku-band aperture (not shown) along with the results of Figs. 2.17-2.18, the reaction integral in (2.16) was computed in order find the power delivered to the victim array.

To find the power radiated by the X-band array we do not use the sources of the original problem, but follow a simpler approach instead. We calculate the surface integral of the Poynting vector for the equivalent problem given by

$$P_{inc} = \text{Re} \left\{ \iint_{\substack{aperture \\ surface}} \left(\vec{E}_{inc} \times \vec{H}_{inc} \right) \cdot d\vec{s} \right\}. \tag{2.21}$$

An electric field normalization factor is used so that (2.21) equals 1 Watt. This normalization does not affect the final coupling result. To show this we define the coupling as

$$S_{12} = 10\log\left(\frac{P_d}{P_{inc}}\right) = 10\log\left(\frac{\dfrac{\left|\iiint\left(\bar{E}^a \cdot \bar{J}^b - \bar{H}^a \cdot \bar{M}^b\right)ds\right|^2}{2\left|I^b\right|^2}\dfrac{R_L}{(R_L + R_{rad})^2 + (X_{rad})^2}}{\mathrm{Re}\left\{\displaystyle\iint_{\substack{aperture\\surface}}\left(\bar{E}_{inc} \times \bar{H}_{inc}\right)\cdot d\bar{s}\right\}}\right). \qquad (2.22)$$

From Maxwell's equations we know that

$$\nabla \times \bar{E} = -j\omega\mu\bar{H} \qquad (2.23)$$

where $\bar{E} = \bar{E}_{inc}$ at the transmitting aperture plane and $\bar{E} = \bar{E}^a$ at the receiving aperture plane. We know that both of these fields must satisfy (2.23) since they are produced by the same source. Therefore, if we let $\bar{E}'_{inc} = C\bar{E}_{inc}$ then $\bar{E}'^a = C\bar{E}'^a$, where C is some scale factor. Substituting (2.23) in (2.22) we obtain

$$S_{12} = 10\log\left(\frac{P_d}{P_{inc}}\right) = 10\log\left(\frac{\dfrac{\left|\iiint\left(\bar{E}^a \cdot \bar{J}^b - \dfrac{1}{-j\omega\mu}\nabla\times\bar{E}^a \cdot \bar{M}^b\right)ds\right|^2}{2\left|I^b\right|^2}\dfrac{R_L}{(R_L + R_{rad})^2 + (X_{rad})^2}}{\mathrm{Re}\left\{\displaystyle\iint_{\substack{aperture\\surface}}\left(\bar{E}_{inc} \times \dfrac{1}{-j\omega\mu}\nabla\times\bar{E}_{inc}\right)\cdot d\bar{s}\right\}}\right). \qquad (2.24)$$

From (2.24) it is evident that if we normalize $\bar{E}_{inc}$ by some value to force the surface integral to be 1 Watt, the corresponding $\bar{E}^a$ will scale by the same value and the result of (2.22) will be the same. Likewise, if we chose $I^b = 1$ A, the equivalent $\bar{J}^b$ and $\bar{M}^b$ sources will scale by the same amount. Therefore the coupling calculation is independent of different source values used in each array simulation and the final result of (2.22) gave a coupling value of about **-75.2 dB** for the non-scanning case.

The method which we have described here provides a systematic way in which the coupling in an electrically large problem, both in terms of array size and separation distances, can be solved with limited computational resources. For comparison, the coupling was determined through the use of the serial-parallel FDTD. The total simulation time to determine the array coupling using the serial-parallel FDTD (two stages) took about 192 hours using 64 3.2 GHz processors. However, by utilizing the Green's function method described in this chapter the total simulation time is about 97 hours (48 hours for each array in isolation and 1 hour for the convolution integrals). Therefore, we have substantially reduced the total simulation time and the results of both methods have been shown to be in good agreement and we can reliably apply this method to other similar problems, such as those that arise in the modeling of BANs.

In this chapter, we have demonstrated two new approaches and have discussed conventional ways that utilize the FDTD algorithm to obtain the coupling information of antennas and/or arrays on mounted on complex layered media. They have been termed the following: full-domain computation; domain decomposition\serial-parallel processing; and Green's function method. Each approach has distinct advantages and disadvantages, in terms of computational resources required and simulation time.

As an additional example we apply these various methods to a common scenario found in BANs, namely, the coupling between two antennas mounted on the same side of a human torso. The full-domain approach places the entire body geometry and all radiating elements in the FDTD computational domain (see Fig. 2.19). This approach is direct and leads to coupling results that are consistent with available measurements [7]. However, the amount of data contained in the entire human 3D-CT scan can place an extraordinarily heavy burden on the computational resources. Furthermore, simulating the entire human body can take an unreasonable amount of time owing to the electrically large nature of the problem. In most cases, using this approach is

not a viable option and other methods which break up the problem size into smaller ones must be

employed.
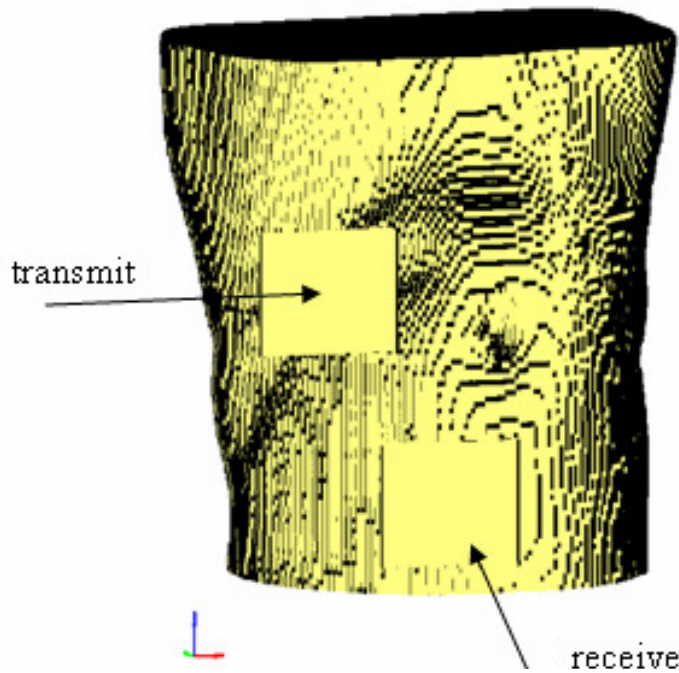
Fig. 2.19: FDTD human torso composite.

The Green's function method offers a more efficient strategy for determining coupling

effects than do the other approaches. First, we simulate the antenna structure with the body

present in isolation to obtain the terminal parameters and fields on an aperture just above the

conformal antenna. Then the aperture field distributions are represented in terms of equivalent

electric and magnetic sources. This information can either be obtained or given *a priori*. Using

FDTD, we simulate horizontal electric and magnetic ideal dipole sources resting on the human

body layered model to estimate the Green's function of the media. Since the coupling distances

can reach a large number of wavelengths, we use Prony's method yet again to approximate the

fields at distances from the source where only the surface waves are sustained and higher order

contributions are negligible. Furthermore, we break up the obtained transmitting aperture into a discrete number of ideal dipole sources (both magnetic and electric) and apply superposition to derive the fields on the receive aperture. Using the fields obtained on the receive aperture, we can apply the reaction concept in conjunction with the isolated port characteristics to calculate the coupling.

For our purposes we are interested in the coupling between two identical rectangular patches with dimensions 30 mm x 28 mm on a 2mm thick substrate with $\varepsilon_r = 4$ and separated by 24.5 cm (approximate distance from the chest to the waist). The patches are designed to operate at 2.45 GHz, and they rest on the human body represented by a layered medium model. The patch antenna was simulated via the conventional FDTD in isolation using a microstrip feed with a characteristic impedance of 50 Ohms. The input impedance was found to be 37 – j20 Ohms. In addition, we applied the conventional FDTD to determine the S_{21} and it is shown in Fig. 2.20 for the case when the body is present and absent. The total simulation time using the conventional FDTD for the entire geometry with the body present was approximately 48 hours.
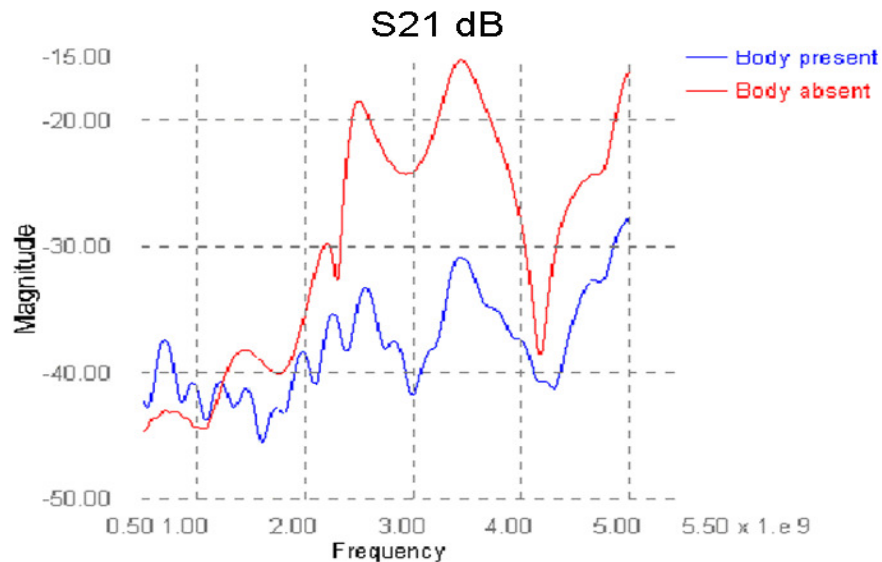
Fig. 2.20: Coupling for patch antenna system on the human body.

In the conventional FDTD the human body model was comprised of three tissue types. Specifically, they are muscle, fat, and skin and the electrical parameters of each tissue type is well documented in the literature [10]. Therefore, when applying the Green's function approach to this model, we approximated the human torso as a planar slab consisting of these three materials, as shown in Figs. 2.21and 2.22.
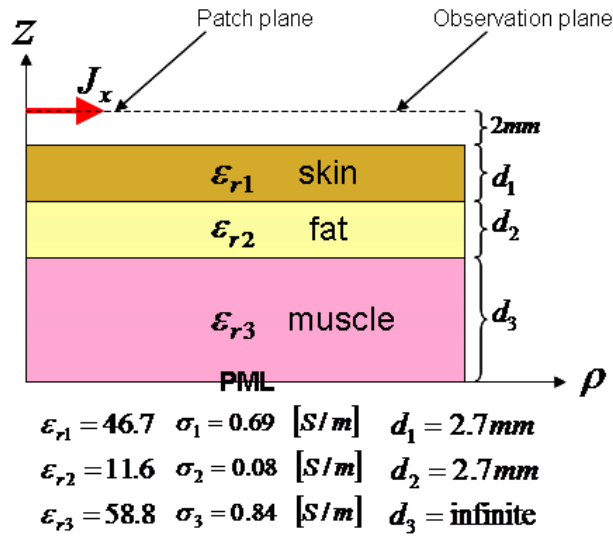
Fig. 2.21: Horizontal electric dipole (HED) resting on a 3-layer human body model.
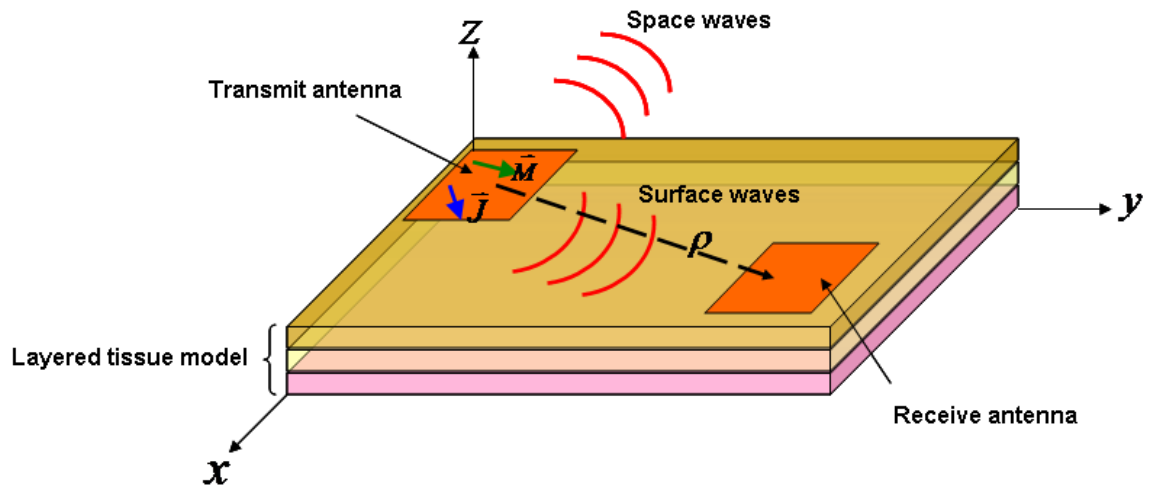
Fig. 2.22: Two patch antennas conformal to the human body layered model.

The computed Green's function was obtained by using the BOR-FDTD and the results for the electric and magnetic fields from an electric dipole on the source plane (i.e. patch plane) are shown in Figs. 2.23 and 2.24. The Prony algorithm was applied to these fields and the resulting electric field distributions on the receiving patch are shown in Fig. 2.25. Furthermore, since the electric current distribution is primarily responsible for the radiation of the rectangular patch operating with its dominant mode excited, it is only necessary to calculate the Green's function for electric dipole sources.
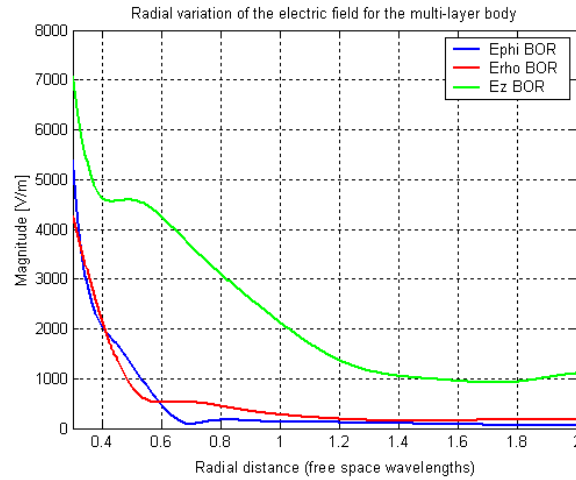
Fig. 2.23: E-field for an x-directed electric ideal dipole source 2 mm above the 3-layer body model observed on source plane.
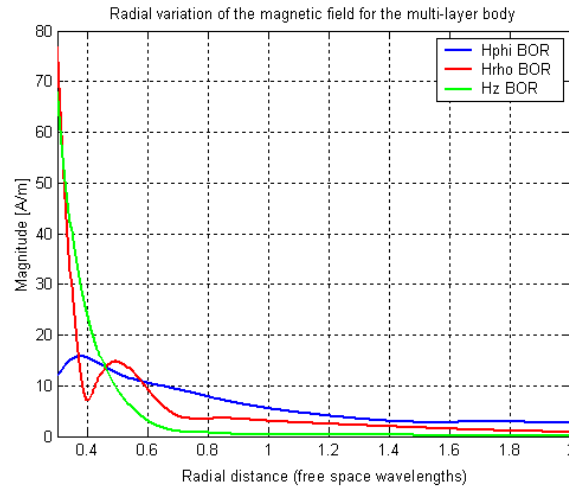
Fig. 2.24: H-field for an x-directed electric ideal dipole source 2 mm above the 3-layer body model observed on source plane.
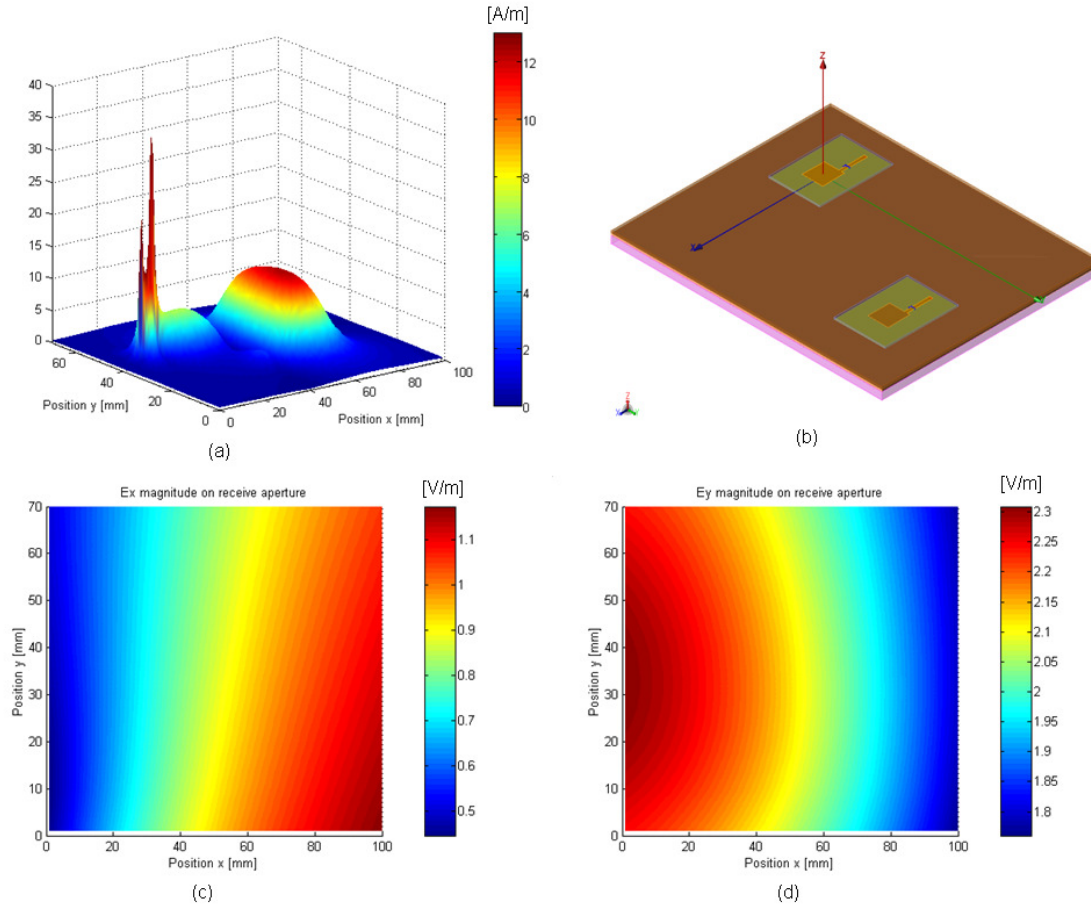
Fig. 2.25: (a) J_x electric current distribution on the transmitting patch (b) The MPA configuration to calculate the S_{21} (c) E_x on receive aperture (d) E_y on receive aperture.

By using the aforementioned approach, the final coupling value was found to be around -34.8 dB at 2.45 GHz and the total simulation was approximately 50 min., including all patch simulations and post-processing. For comparison purposes, the 3-layer planar tissue slab with the corresponding MPA configuration was simulated using the full-domain FDTD approach and the S_{21} was computed as shown in Fig. 2.26. The agreement between the results obtained by using the full–domain FDTD for the human body phantom, the full-domain FDTD for the planar 3-layer model, and the Green's function methods is seen to be excellent, and the shorter run time clearly demonstrates the advantages of the Green's function approach for estimating the coupling.
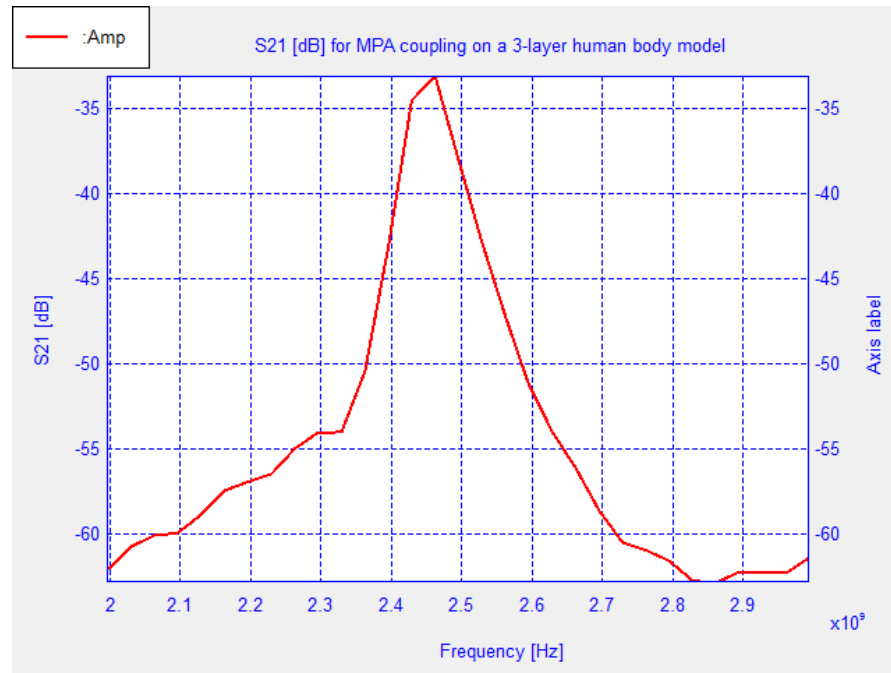
Fig. 2.26: The S_{21} using the full-domain FDTD for the MPA configuration on the 3-layer human body model.

In conclusion, the three approaches outlined in this chapter can be used to model and simulate the performance of antenna systems mounted on the human body. The full-domain approach offers a robust but computationally intensive way to obtain coupling information of body-centric networks. In contrast, the domain decomposition\serial-parallel method can alleviate much of burden on the computational resources required, but without any reduction in simulation time. Finally, the Green's function method requires relatively small computational resources and simulation time, but has several additional steps to generate the final result in comparison with the previous two. However, much of the post-FDTD processing is very simplistic in nature. Therefore, useful information pertaining to body-centric networks can be obtained by any one of the methods mentioned in this chapter, and the choice is left to the user.

Chapter 3

Electromagnetic Wave Propagation in Body Area Networks using the Finite-Difference-Time-Domain

As wireless technologies continue to evolve, the development of personalized devices which exchange data with unprecedented ease and efficiency is certain to grow unabated. Recently, such technologies have garnered much attention from those interested in biomedical sensing and Body-Area-Networks (BANs). However, the complexity of integrating efficient communication systems in the human body environment poses many challenges to the future of this emerging technology. The excitation of surface and space waves from radiating antennas mounted on the body can have a large impact on the performance of co-site body-centric antenna systems. Moreover, the presence of multiple antennas on the body can lead to unexpected coupling due to creeping wave interaction. Fortunately, recent developments in powerful numerical methods, such as the FDTD running on parallel platforms, has made it feasible for us to carry out a detailed study of these body-centric antenna systems.

3.1 Simple Models for BANs

For many years researchers have used simplified geometries to model the interaction of electromagnetic energy with biological tissue. Such geometries typically lend themselves to simple shapes, such as cylinders, ellipses and spheres for which past research has typically treated these as perfectly conducting objects. This type of treatment was convenient due to the availability of well known analytical methods used solve these problems, such as the uniform theory of diffraction (UTD), ray tracing (RT), and eigenfunction analysis. Indeed, these models

have been shown in recent years to yield reasonably good results for simple cases that compare well to those derived numerically rigorously with modern CEM techniques. However, the asymptotic techniques fail to perform well when the dielectric medium they deal with is arbitrarily shaped, inhomogeneous and lossy, and such problems must be handled by using general-purpose numerical methods, such as the FDTD. Nevertheless, these simple geometries can still provide a computationally efficient way to study the propagation around and through the human body. Therefore, these models remain useful for studying BANs.

In this section we provide the results of a simplified model for the human body torso. The proposed model is a 3-layer elliptical structure having major and minor axis of 150 cm and 120 cm, respectively. This model has been used in [6] to investigate the coupling around a 2-D ellipse using the sub-band FDTD, UTD/RT and measurement techniques at UWB frequencies. However, in that work the model was assumed to be perfectly conducting when applying the UTD/RT method while a homogeneous muscle phantom was employed for the sub-band FDTD analysis. Additionally, a conformal FDTD algorithm was not used to improve the accuracy of the curved surface whereas the author has done so in this work. Furthermore, it neither accounted for the multi-layer dielectric properties of the tissue in the human torso, nor did it simulate the actual radiating element, i.e., viz., the monopole antenna rigorously.

The 3-layer ellipse model incorporates the skin, fat, and muscle layers. In [24] simple 3-layer planar slab model using 3 mm skin layer, 5 mm fat layer and muscle was used to study the penetration depth of an incident plane wave for use in implantable medical devices. In this work we have used the same thickness for the skin and fat layers in the elliptical model.

Although the FDTD method enjoys a significant advantage over MoM in terms of its ability to simulate complex structures and lossy inhomogeneous materials, it has been known to require far more computational resources than are usually available to accurately model, simultaneously, the fine features of the radiating element, the layered structure of the geometry

and the electrically large size of the entire structure typically encountered in the study of BANs. To circumvent this problem, most research done on BANs by utilizing the FDTD have been carried out using a point source approximation. While such an approximation is adequate for directly estimating the path loss associated with the body, it does not rigorously account for a number of crucial antenna factors that affect the antenna performance, such as finite ground size, radiation pattern and efficiency. Furthermore, any field behavior in either the near or the intermediate region is inherently neglected in the point source approximation, whereas the physical structure of the radiating element must be included to properly model the physical system.

In this Chapter we have used a parallel version of FDTD that can handle such electrically large geometries as well as the fine features of the radiating element. To this end, we have used a quarter-wave monopole resonant at 2.45 GHz with a 75 mm x 75 mm square ground plane. Although other antennas could be used, the choice of the monopole antenna has the distinct advantage in that the radiation pattern in the plane azimuthal to the monopole is inherently stable across the bandwidth of interest. Thus, polarization and radiation pattern deviations of the transmitter across the frequency band can more or less be neglected when performing coupling calculations.

The setup used in the simulation is shown in Fig. 3.1 where the receiver is located first in the source plane and then displaced vertically by 210mm and 400mm, respectively, from the above plane. For each observation plane the receiver is moved around the elliptical trunk model and the S_{21} is recorded. The mode of propagation is known to be a creeping wave and the direct ray paths are shown. For each observation plane the S_{21} was calculated along the elliptical path in the level plane and plotted for frequencies between 0.8-6 GHz as shown in Figs. 3.2-3.4.
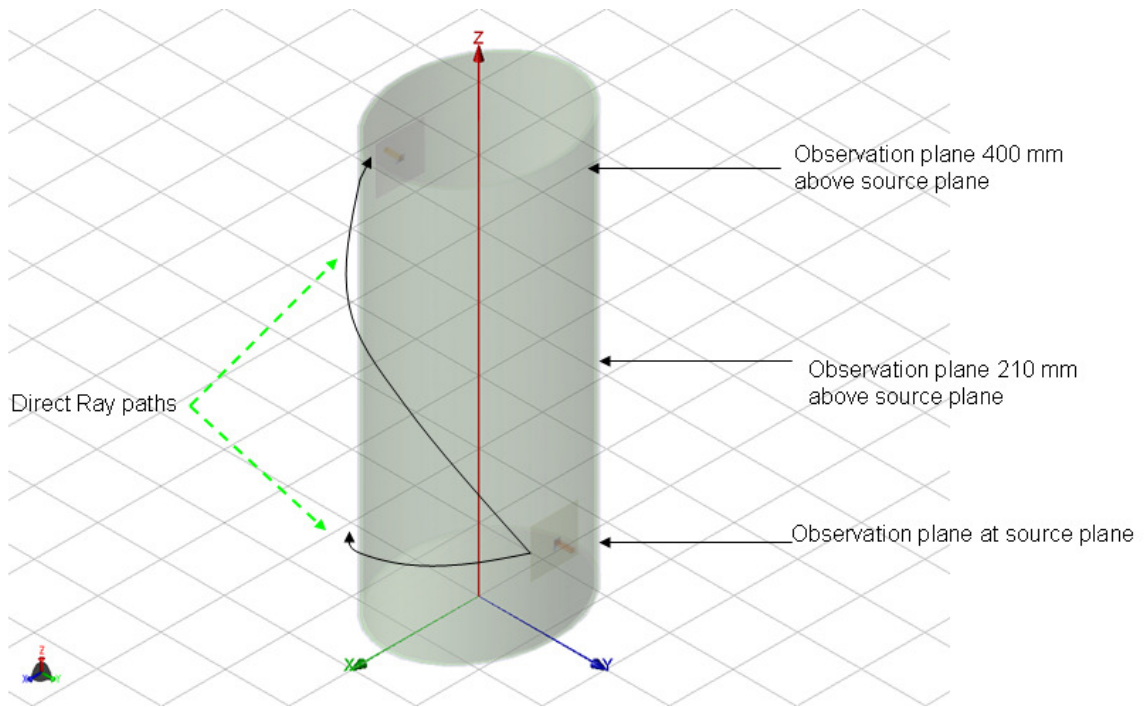
Fig. 3.1: 3-layer ellipse model of the human torso with transmitting antenna at the front and receiving antenna at the back.
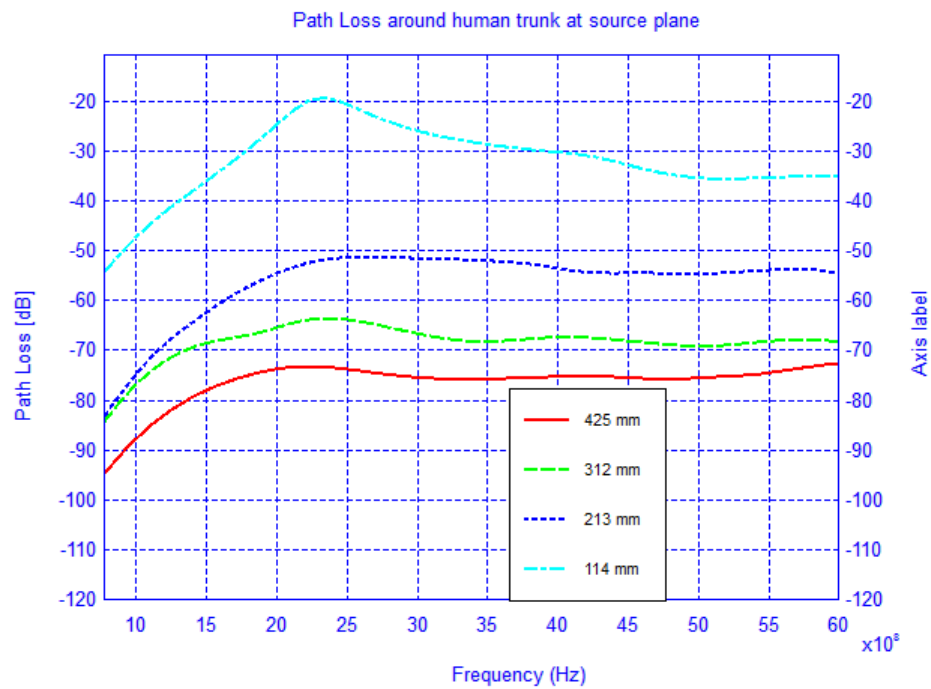
Fig. 3.2: Path loss around the cylindrical human trunk model at the source plane.
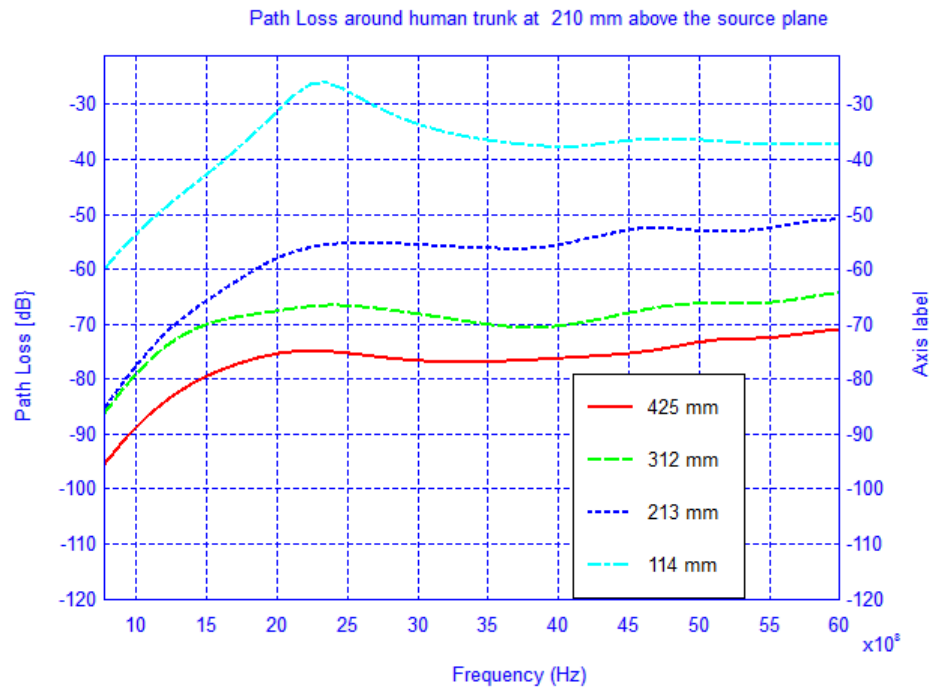
Fig. 3.3: Path loss around the cylindrical human trunk model 210 mm above source plane.
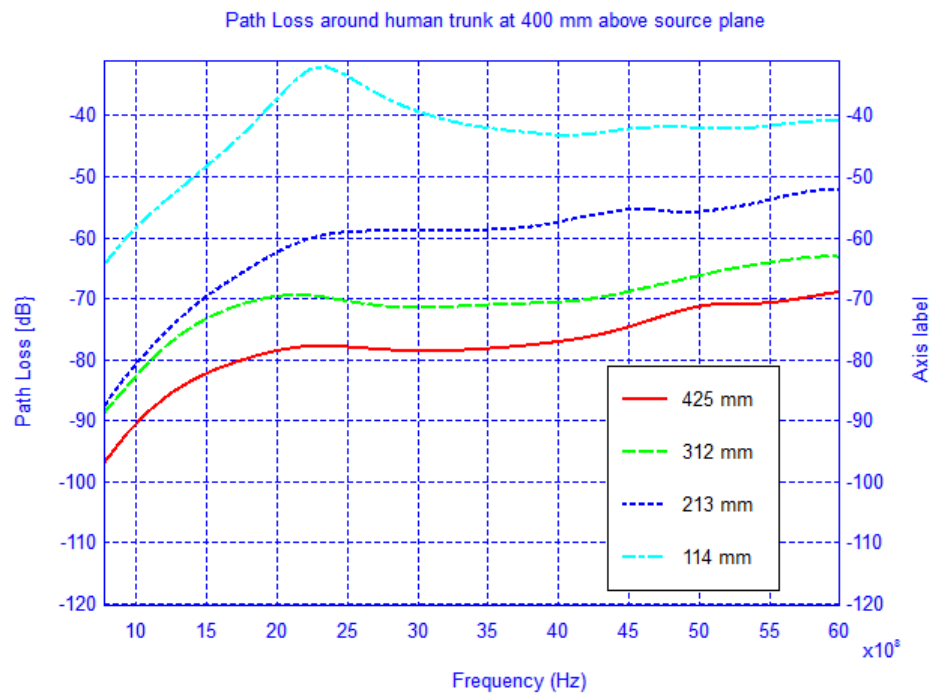
Fig. 3.4: Path loss around the cylindrical human trunk model 400 mm above source plane.

For BANs it is typically assumed that the wave propagation through the body is so attenuated that its contribution can be ignored. To verify this we have plotted the fields for the cross-section of the ellipse in the source plane as well as a vertical cross-section along the extent of the ellipse model. The electric field plots are shown in Figs. 3.5 and 3.6. From these figures it can be seen that the field magnitude inside the model is less than -100 dB and the main source of energy transfer is along the surface of the trunk in the form of a creeping wave.
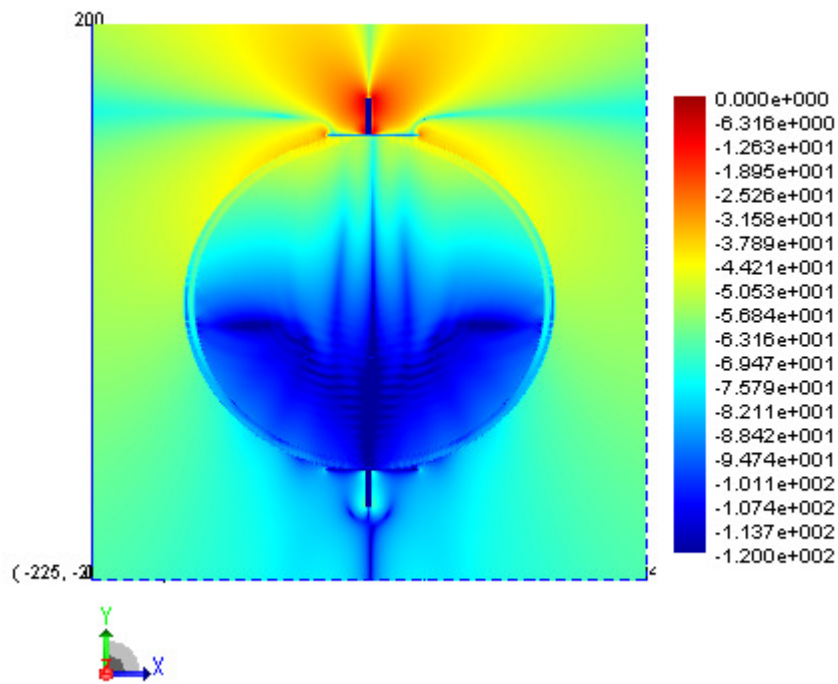
Fig. 3.5: Electric field distribution in the source plane.
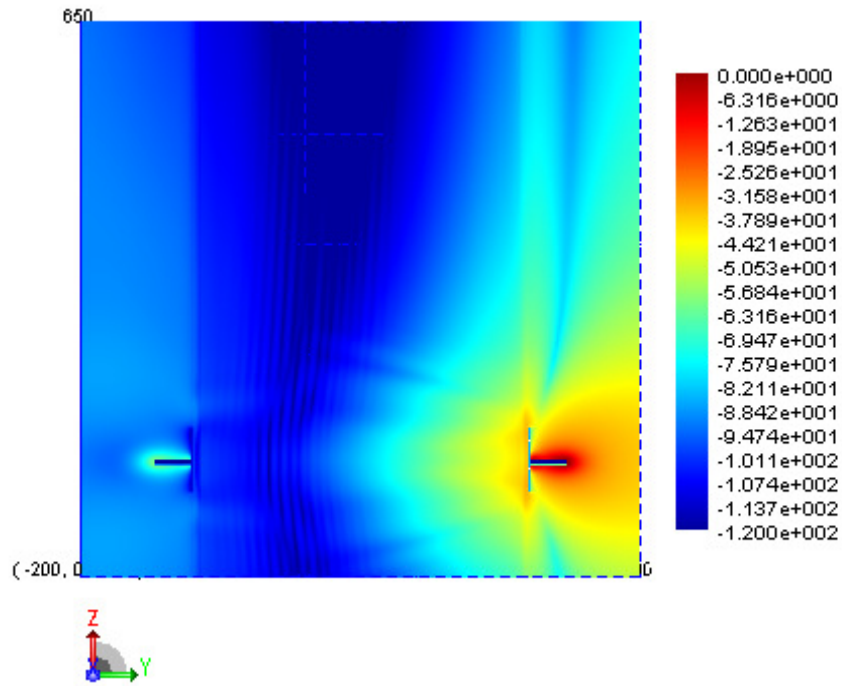
Fig. 3.6: Electric field distribution on a vertical cut plane bisecting the cylindrical model.

In Figs. 3.7-3.9 the path loss is plotted versus the distance around the elliptical model in each of the different observation planes. As shown in Fig. 3.7, which depicts the observations made in the source plane, the attenuation at higher frequencies exhibit a clear monotonic behavior and is characteristic of a creeping wave. The results in Fig. 3.7-3.9 have been found to agree closely with those in the literature for other body models [6]-[15]. These results can be useful as reference points when approximating the rate of attenuation along the trunk in body-centric network scenarios.
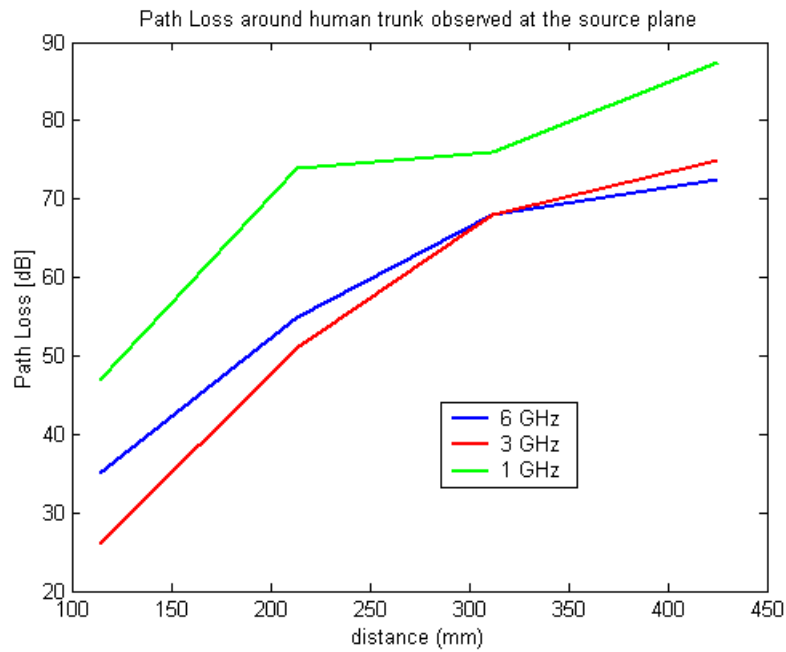
Fig. 3.7: Path loss versus separation distance with receiving antenna at the source plane.
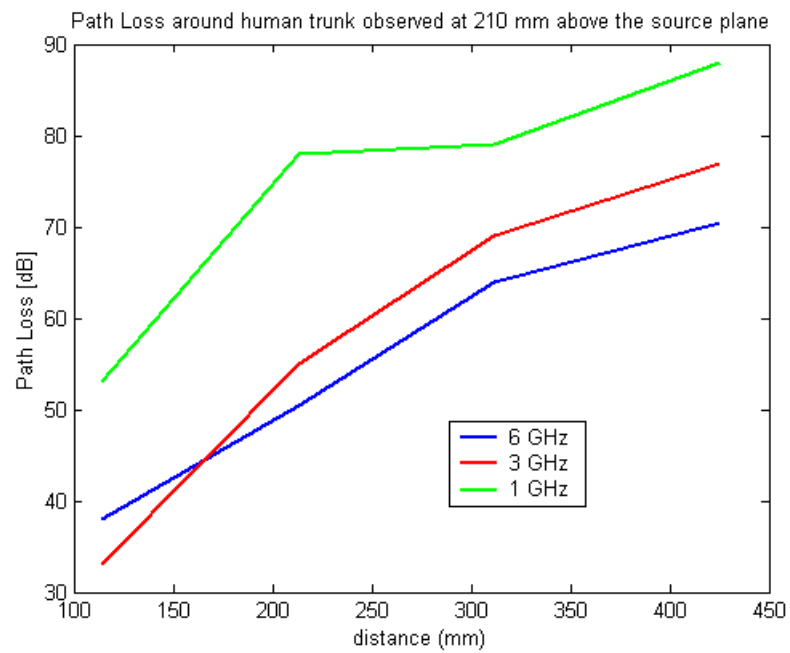
Fig. 3.8: Path loss versus separation distance with receiving antenna 210 mm above the source plane.
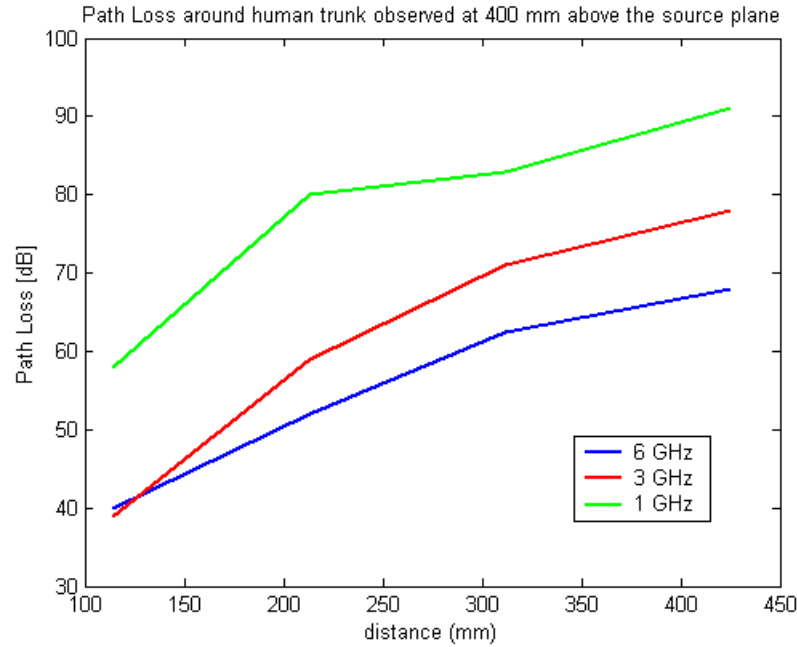
Fig. 3.9: Path loss versus separation distance with receiving antenna 400 mm above the source plane.

3.2 Numerical Phantoms for BANs

Although simplified geometries have their use in analyzing body-centric communication networks, the availability of realistic human body models enables us to use a more rigorous approach to understanding how the irregular shape of the body affects the performance of BANs. One of the most commonly used body models is shown in Fig. 3.10, where the original data set is comprised of voxels (i.e., 3D matrix data set). Furthermore, a hypothetical BAN configuration is shown with the transmitting and receiving antennas. To reduce the computational resources needed in the simulation, a lossy homogeneous model was used.

Additionally, the resolution of the original voxel data set, which is 1mm x 1mm x 1mm, was down-sampled to 3 mm x 3 mm x 3 mm. Even at this lower resolution the computational

resources needed are high, specifically 8 hours on 16 pentium 4 cpu's. Although this may seem too coarse for the conventional $\lambda/20$ cell size, the fields couple on or near the surface of the body, where the mesh can be coarser, and we are interested in separation distance well into the asymptotic region of the transmitting antenna. To demonstrate that the loss of accuracy is negligible in doing so, we have performed a simple experiment by computing the difference in field magnitude at 3 GHz —far away from the transmitting antenna on the same plane as shown in Fig. 3.11. It is evident from the results that in the asymptotic region there is little loss in accuracy by utilizing a down-sampled phantom model.
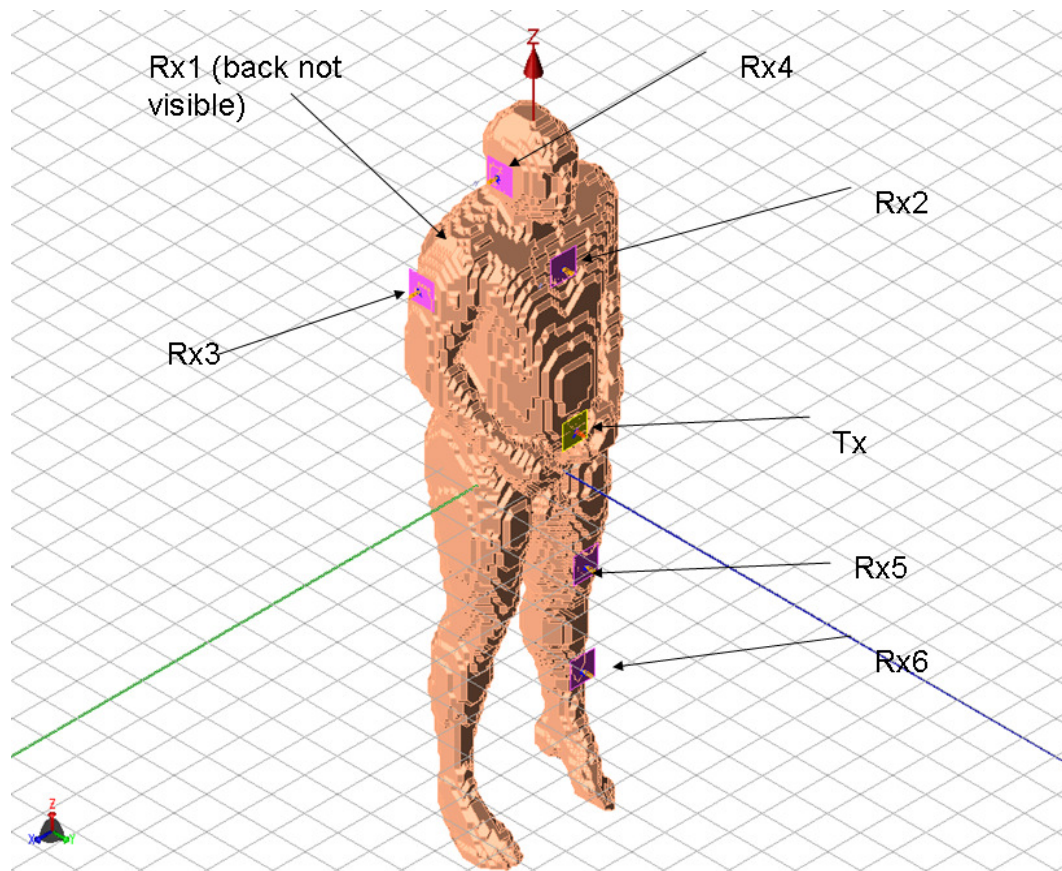
Fig. 3.10: Numerical human body phantom based on 3D CT scan voxel set with transmitting and receiving antennas in typical BAN scenario.
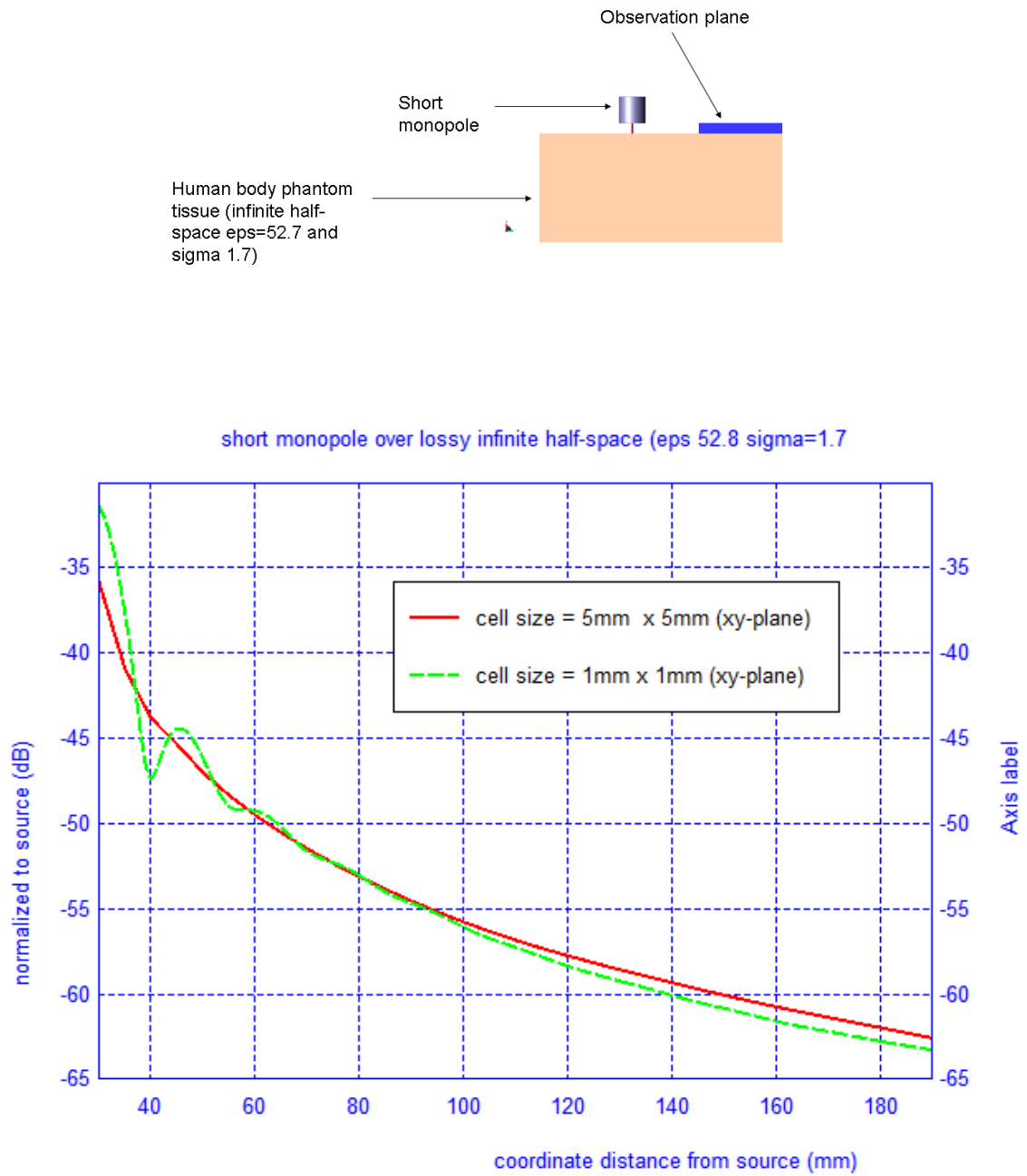
Fig. 3.11: Experiment to determine if the down-sampled human body voxel set causes numerical inaccuracies ($\lambda = 10cm$).

3.3 Dielectric Properties and Dispersion Models of Biological Tissue

It is commonly claimed in the literature that a good approximation for the body can be made by using a full muscle phantom or a two-thirds muscle equivalent phantom, the later being more commonly used in EMC analysis for SAR [25] , [26]. However, realistic biological tissues exhibit dispersion characteristics that are not of the traditional Debye type used in the FDTD model, whose spectral behavior is usually represented by the form

$$\hat{\varepsilon}(\omega) = \varepsilon_\infty + \sum_{n=1}^{N} \frac{\Delta\varepsilon_n}{1 + j\omega\tau_n} + \frac{\sigma_n}{j\omega\varepsilon_0} \tag{3.1}$$

where τ_n is the relaxation time constant $\Delta\varepsilon_n$ is the spectral coefficient and σ_n is the static ionic conductivity. This model can be handled in FDTD through a simple convolution extension of the basic FDTD algorithm. In general, biological tissue exhibit a broadened spectrum which is empirically accounted for by the parameter $0 \le \alpha_n < 1$, (see Gabriel *et al*. [27]) and is typically referred to as the Cole-Cole model. It is given by

$$\hat{\varepsilon}(\omega) = \varepsilon_\infty + \sum_{n=1}^{N} \frac{\Delta\varepsilon_n}{1 + (j\omega\tau_n)^{1-\alpha_n}} + \frac{\sigma_n}{j\omega\varepsilon_0} \tag{3.2}$$

The difficulty in this model lies in the fact that there are no simple closed form expression amenable to the FDTD algorithm due to the fact that the inverse Fourier transform is non-trivial.

3.3.1 Dielectic Spectrum Approximation

In this Section we will introduce a technique that can be used to implement the Cole-Cole model into the desired frequency band of interest for simple geometries relevant to BANs (e.g., planar human tissue phantoms) in FDTD. Since the static conductivity term can be handled easily

in the FDTD update equations we turn our attention to the term containing α_n. First we postulate

that each term in the Cole-Cole model can be rewritten as an integral representation of a Debye

spectrum as follows

$$\frac{\hat{\varepsilon}_i(\omega)}{\Delta\varepsilon_i} = \frac{1}{1+(j\omega)^{1-\alpha_i}} = \frac{1}{1+(j\omega)^{\beta_i}} = \int_0^\infty \frac{g_i(\lambda)}{\lambda+j\omega}d\lambda \tag{3.3}$$

Then the expression for the electric field density follow as

$$D(\omega) = \hat{\varepsilon}_i(\omega)E(\omega) \tag{3.4}$$

$$= \Delta\varepsilon_i \int_0^\infty \frac{E(\omega)g_i(\lambda)}{\lambda+j\omega}d\lambda \quad . \tag{3.5}$$

whereby the inverse Fourier transform yields

$$D(t) = F^{-1}\{\hat{\varepsilon}_i(\omega)E(\omega)\}(t) = \int_0^\infty E(t)\otimes e^{-\lambda t}g_i(\lambda)d\lambda \tag{3.6}$$

$$D(t) = E(t)\otimes L\{g_i(\lambda)\}(t) \tag{3.7}$$

Therefore, if it is possible to find a time domain representation for the Laplace transform

of the unknown spectrum $g_i(\lambda)$ and, hence, we may extend the basic convolutional FDTD to

implement non-Debye types of materials.

The problem at hand is to determine a suitable function for which we can derive the

Laplace transform. To do this we first rewrite the Debye integral representation as

$$\frac{\hat{\varepsilon}(\omega)}{\Delta\varepsilon} = \int_0^\infty \frac{g(\omega)}{\lambda+j\omega}d\lambda = \int_0^\infty g(\lambda)\int_{-\infty}^\infty e^{-j\omega\rho}e^{-\lambda\rho}u(\rho)d\rho d\lambda \tag{3.8}$$

$$= \int_0^\infty\int_0^\infty g(\lambda)e^{-\lambda\rho}e^{-j\omega\rho}d\lambda d\rho \tag{3.9}$$

where $u(\rho)$ is the Heaviside step function. Now by Fubini's Theorem

$$\frac{\hat{\varepsilon}(\omega)}{\Delta\varepsilon} = \int_0^\infty e^{-j\omega\rho}\left[\int_0^\infty g(\lambda)e^{-\lambda\rho}\,d\lambda\right]d\rho \tag{3.10}$$

To find $g(\lambda)$ we expand it in terms of some complete basis set for which we know the Laplace transform. Specifically, we chose Bessel functions of the first kind which form a complete set in $\Re : \lambda \in [0,\infty)$. Therefore, we have

$$g(\lambda) = \sum_{n=0}^\infty C_n J_n(a\lambda) \tag{3.11}$$

where a is a fitting parameter. Obviously we must truncate this infinite series for numerical purposes; hence we write

$$g(\lambda) \approx \sum_{n=0}^N C_n J_n(a\lambda) \tag{3.12}$$

Now we use the Laplace transform relation given by

$$\int_0^\infty J_n(a\lambda)e^{-\lambda\rho}\,d\lambda = \frac{1}{\sqrt{\rho^2 + a^2}}\frac{a^n}{\left(\rho + \sqrt{\rho^2 + a^2}\right)^n} \tag{3.13}$$

Of course, we could have used (3.13) directly in (3.5); however, we have found that the integral converges much more slowly than that of the reformulation given in (3.10). After inserting (3.13) into the equation given in (3.10) we have

$$\frac{\hat{\varepsilon}(\omega)}{\Delta\varepsilon} = \int_0^\infty e^{-j\omega\rho}\left(\sum_{n=0}^N C_n \frac{1}{\sqrt{\rho^2 + a^2}}\frac{a^n}{\left(\rho^2 + \sqrt{\rho^2 + a^2}\right)^n}\right)d\rho \tag{3.14}$$

Next, we can apply the method of least squares to find the coefficients C_n. However, from (3.7) it is obvious that we must require the C_n's to be real. Therefore we have a constrained least squares system of equations given by the following:

$$\bar{b}^T = \left[\operatorname{Re} \int_0^\infty \frac{\hat{\varepsilon}(\omega)}{\Delta\varepsilon} I_0 \, d\omega \quad \operatorname{Im} \int_0^\infty \frac{\hat{\varepsilon}(\omega)}{\Delta\varepsilon} I_0 \, d\omega \quad \operatorname{Re} \int_0^\infty \frac{\hat{\varepsilon}(\omega)}{\Delta\varepsilon} I_1 \, d\omega \quad \operatorname{Im} \int_0^\infty \frac{\hat{\varepsilon}(\omega)}{\Delta\varepsilon} I_1 \, d\omega \quad \bullet \quad \bullet \quad \operatorname{Im} \int_0^\infty \frac{\hat{\varepsilon}(\omega)}{\Delta\varepsilon} I_N \, d\omega \right]$$

(3.15)

$$\bar{x}^T = \begin{bmatrix} C_1 & C_2 & C_3 & \bullet & \bullet & \bullet & C_N \end{bmatrix}$$

(3.16)

$$\bar{\bar{A}} = \begin{bmatrix}
\operatorname{Re}\int_0^\infty I_0 I_0 d\omega & \operatorname{Re}\int_0^\infty I_0 I_1 d\omega & \operatorname{Re}\int_0^\infty I_0 I_2 d\omega & \bullet & \bullet & \bullet & \operatorname{Re}\int_0^\infty I_0 I_N d\omega \\
\operatorname{Im}\int_0^\infty I_0 I_0 d\omega & \operatorname{Im}\int_0^\infty I_0 I_1 d\omega & \operatorname{Im}\int_0^\infty I_0 I_2 d\omega & \bullet & \bullet & \bullet & \operatorname{Im}\int_0^\infty I_0 I_N d\omega \\
\operatorname{Re}\int_0^\infty I_1 I_0 d\omega & \operatorname{Re}\int_0^\infty I_1 I_1 d\omega & \bullet & & & & \\
\operatorname{Im}\int_0^\infty I_1 I_0 d\omega & \operatorname{Im}\int_0^\infty I_1 I_1 d\omega & & \bullet & & & \\
& \bullet & & & \bullet & & \\
\operatorname{Re}\int_0^\infty I_N I_0 d\omega & & & & & \bullet & \\
\operatorname{Im}\int_0^\infty I_N I_0 d\omega & & & & & & \operatorname{Im}\int_0^\infty I_N I_N d
\end{bmatrix}$$

(3.17)

where $\bar{\bar{A}}$ is 2NxN, $\bar{b}$ is 2Nx1, $\bar{x}$ is Nx1, $\bar{x} = \bar{\bar{A}}^+ \bar{b}$ and

$$I_n = \int_0^\infty \frac{e^{-j\omega\tau} a^n}{\sqrt{\tau^2 + a^2} \cdot \left(\tau^2 + \sqrt{\tau^2 + a^2} \right)^n} \, d\tau$$

(3.18)

In common with most over-constrained inverse problems, we must use the Moore-Penrose

pseudoinverse for $\bar{\bar{A}}^+$ to solve the system of equations. In practice, the integral cannot be

evaluated over all possible frequencies; hence, it is typically replaced by a discrete summation

over all frequencies of interest where the spectral match is desired.

As an illustrative example of this approach, the 4-term Cole-Cole model was taken for the tissue corresponding to the muscle. Although the preceding formulation corresponds to a single Cole-Cole term, the postulated Debye spectrum can equally well be applied to the entire summation of Cole-Cole terms. The parameters given by Gabriel [27] listed in Table 3.1.

Table 3.1: 4 term Cole-Cole model parameters for muscle.

$\Delta\varepsilon_1 = 50$	$\tau_1 = 7.23e - 12$	$\alpha_1 = 0.1$
$\Delta\varepsilon_2 = 7000$	$\tau_2 = 353.68e - 9$	$\alpha_2 = 0.1$
$\Delta\varepsilon_3 = 1.2e6$	$\tau_3 = 318.31e - 6$	$\alpha_3 = 0.1$
$\Delta\varepsilon_4 = 2.5e7$	$\tau_4 = 2.27e - 3$	$\alpha_4 = 0$

Using the proposed algorithm we have obtained the following coefficients for an 11th-order expansion that are listed in Table 3.2. In addition, we have found that a good match was achieved when the fitting parameter was chosen to be $a = 0.5e - 9$. Although initially the order of the expansion may seem to be large, the expansion is only 2.75 times that of the original 4-term Cole-Cole model. Figs. 3.12-3.13 show the magnitude and phase spectrum match for the band of interest, specifically 1-10 GHz. Furthermore, Fig. 3.14 shows that the relative error is less than 5 percent over the entire band, for both magnitude and phase, and this can be considered a very good match for simulation purposes.

Table 3.2: Calculated coefficients from the spectral approximation method.

C1	0.0002e6
C2	-0.0032e6
C3	0.0394e6

C4	-0.2759e6
C5	1.1027e6
C6	-2.4578e6
C7	2.7137e6
C8	-0.5489e6
C9	-1.7652e6
C10	1.6288e6
C11	-0.4334e6
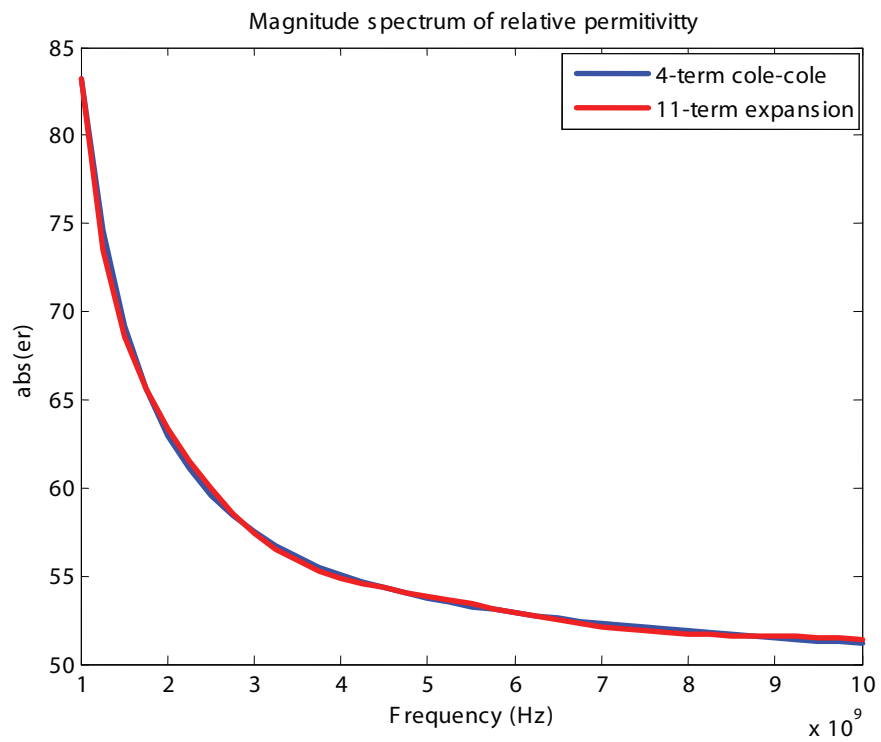
Fig. 3.12: Magnitude spectrum of the relative permittivity for the 4 term Cole-Cole model and the spectrum approximation.
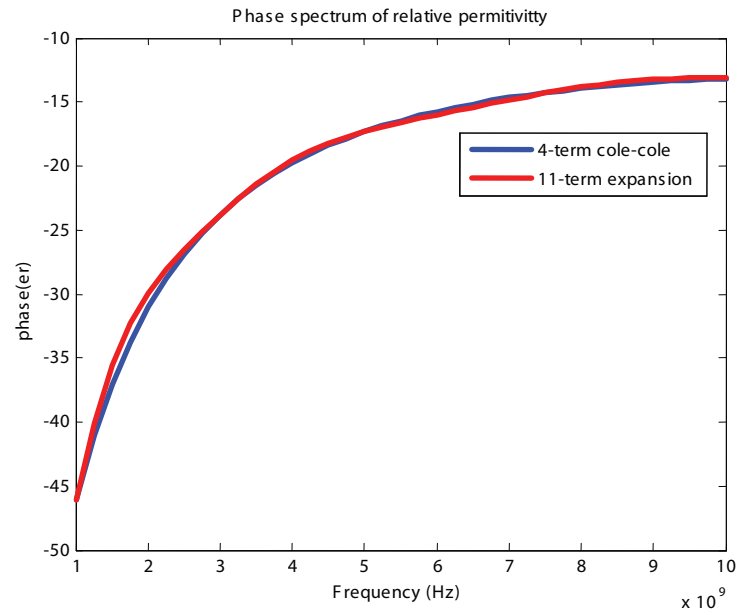
Fig. 3.13: Phase spectrum of the relative permittivity for the 4 term Cole-Cole model and the spectrum approximation.
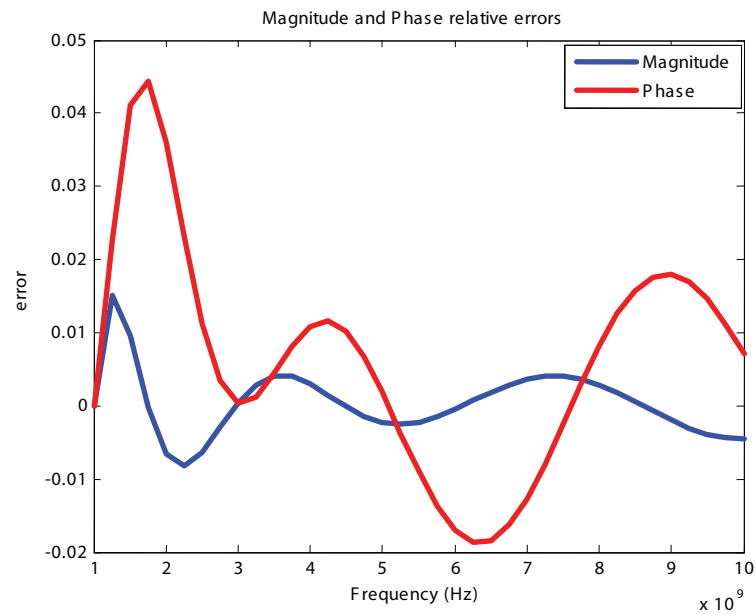
Fig. 3.14: Magnitude and Phase relative errors of the spectrum approximation and the 4 Cole-Cole model.

As an example, the calculated coefficients along with the fitting parameter were used to model the frequency response in a muscle medium. Using the convolution sum of (3.7) for a Gaussian pulse excitation in the medium yields the result shown in Fig. 3.15. It can be seen from Fig. 3.15 that the electric field density inside the muscle medium is influenced by its frequency domain characteristics as modeled by the proposed algorithm.
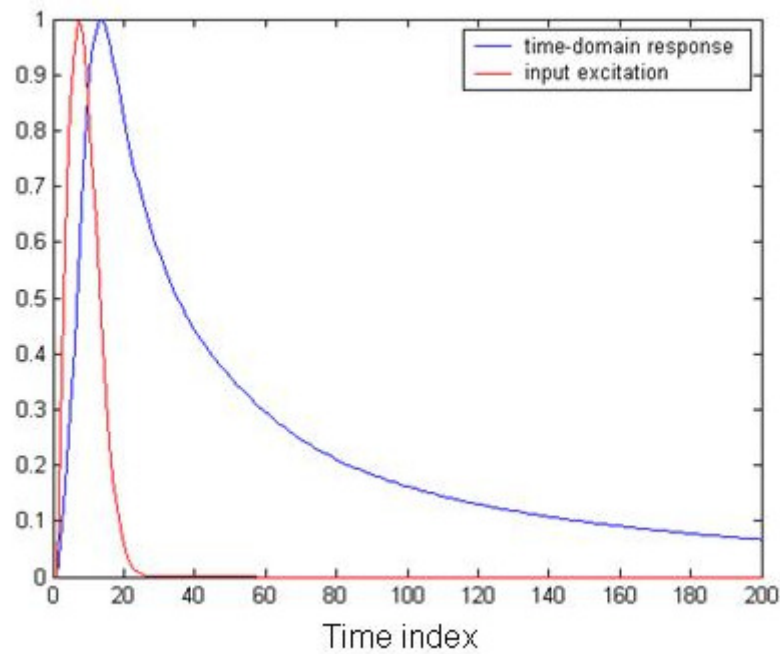
Fig. 3.15: Time domain response of the electric field density using the spectral approximation.

3.3.2 Recursive Convolution Method for Debye Materials

The problem with incorporating the spectral approximation algorithm proposed in the previous section is that FDTD requires a record-keeping of all past time values of the electric field components. If either the problem size is small, or reflection properties from an infinite planar slab are of interest then this approach may be feasible. However, for practical problems, the computational domain can become exceedingly large (e.g., upward of 1 billion unknowns for

realistic human body phantoms), and other approximation methods must be used. Often times, the dispersion properties of biological tissue can be approximated by a Debye model over a finite frequency bandwidth. In this case it is possible to formulate an FDTD updating scheme for dispersive materials that does not require keeping all past histories of the fields.

The recursive convolution FDTD is one such method and is discussed in [4]. The essential features of this method are based on the Debye dispersion model given by

$$\varepsilon(\omega) = \varepsilon_o \varepsilon_\infty + \varepsilon_o \chi(\omega) \tag{3.19}$$

where $\chi(\omega)$ is explicitly given as

$$\chi(\omega) = \sum_{p=1}^{P} \frac{A_p}{\omega - W_p} \quad . \tag{3.20}$$

After some extensive manipulations the final form of the FDTD updating equations for the electric field become

$$\vec{E}^{n+1} = \frac{\dfrac{\varepsilon_{eff}}{\Delta t} - \dfrac{\sigma_{eff}}{2}}{\dfrac{\varepsilon_{eff}}{\Delta t} + \dfrac{\sigma_{eff}}{2}} \vec{E}^n + \frac{1}{\dfrac{\varepsilon_{eff}}{\Delta t} + \dfrac{\sigma_{eff}}{2}} \vec{\nabla} \times \vec{H}^{n+\frac{1}{2}} + \frac{\dfrac{\varepsilon_o}{\Delta t}}{\dfrac{\varepsilon_{eff}}{\Delta t} + \dfrac{\sigma_{eff}}{2}} \sum_{p=1}^{P} \psi_p^n \tag{3.21}$$

and ψ_p^n is given by

$$\psi_p^n = \vec{E}^n \Delta \chi_p^0 + e^{jW_p \Delta t} \psi_p^{n-1} \quad . \tag{3.22}$$

The formulation given in (3.21) can be used to incorporate materials that exhibit Debye-type dispersive properties into the FDTD. If the geometry is simple (e.g., a dispersive sphere), this method has been shown to give improved accuracy. However, in the case of the human body, where the object has irregular features, and many dispersive dielectric layers, the CFDTD, combined with the recursive convolution method, can lead to unstable results. In fact, when using the parameters in Table 3.1 with $\alpha_i = 0$ to simulate the body shown in Fig. 3.10, the results were

found to diverge. This problem further demonstrates the difficulties when trying to rigorously

simulate a realistic human body. Therefore, we have used a common approximation [26] for the

human body as consisting of a non-dispersive muscle ($\varepsilon_r = 52.7$, $\sigma = 1.7$) or its two-thirds

equivalent phantom in the band of 0.8-3 GHz.

3.4 Simulations and Results

Using the muscle and the two-thirds muscle equivalent human body phantom, the

CFDTD algorithm was used to simulate the setup previously shown in Fig. 3.10. For each model,

the network configuration was simulated and the S_{21} was calculated. Additionally, the network

was also simulated in the absence of the body in order to understand the influence of its presence.

The free-space case (body absent) is shown in Fig. 3.16 and the results of the two body models

are shown in Figs. 3.17 and 3.18. To gain insight into the field distribution around the body the

electric field is shown in Fig. 3.19 at 3 GHz. It is evident from the results that the line-of-sight

(LOS) or near LOS paths are not greatly influenced by the presence of the body for monopole

antennas. However, for the non-line-of –sight (NLOS) there is a noticeable difference in the path

loss, especially at frequencies above 1 GHz, where the difference is approximately 35 dB

compared to the free-space case.
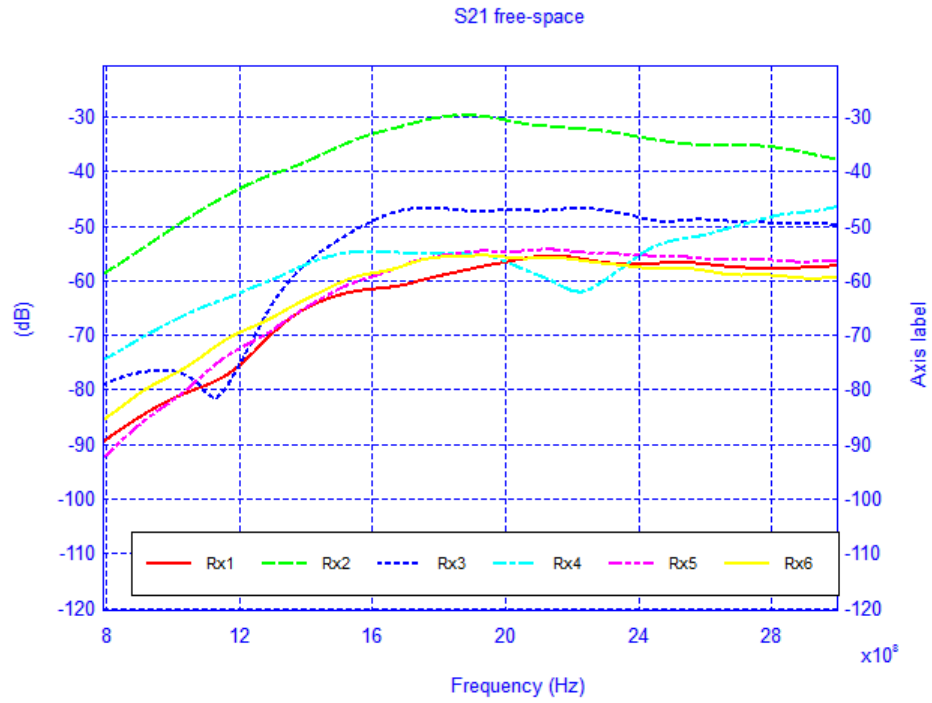
Fig. 3.16: S_{21} of the BAN network scenario with body absent.
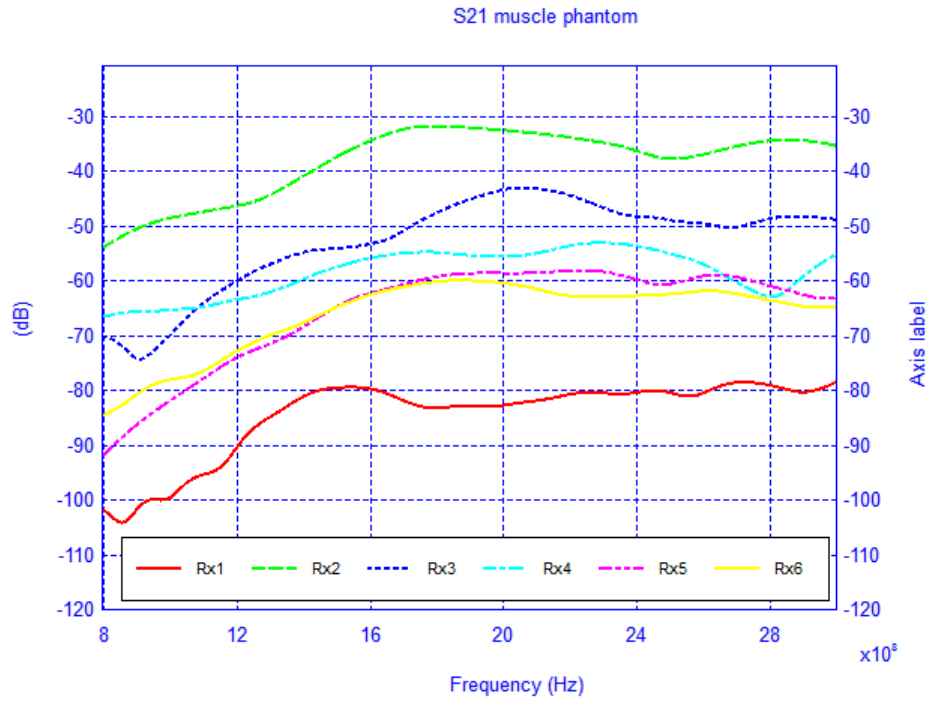
Fig. 3.17: S_{21} of the BAN network scenario with muscle phantom.
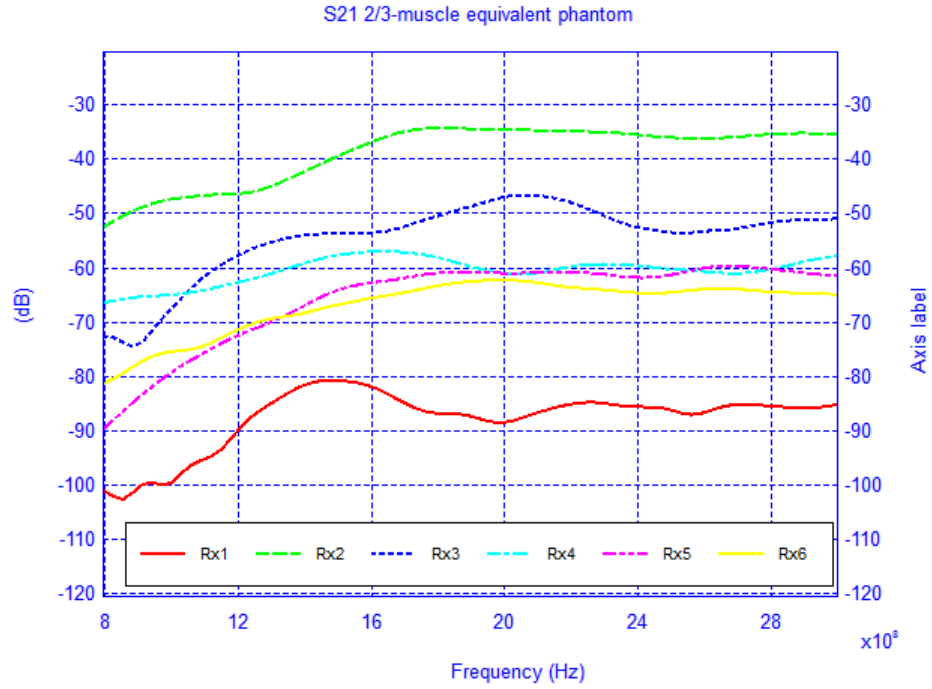
Fig. 3.18: S_{21} of the BAN network scenario with 2/3-muscle phantom.
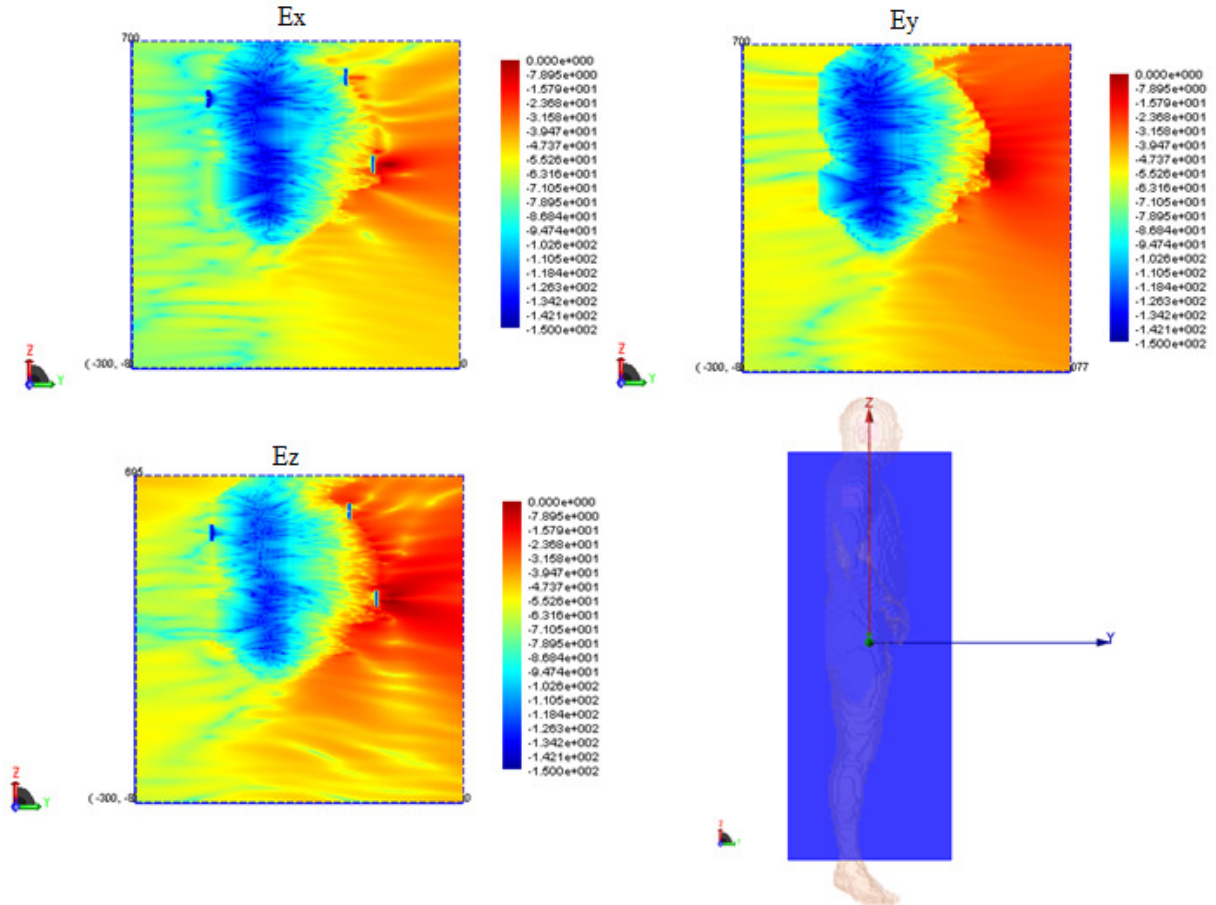
Fig. 3.19: Electric field distributions on a vertical cut plane bisecting the body.

To determine the accuracy of the elliptical model, we compare two cases, namely when the receiver is located on the back of the body and on the shoulder-side. Additionally, in order to improve the elliptical model from the previous section, two muscle tissue arms, composed of cylinders and spheres, were placed alongside the elliptical torso model and are shown superimposed on the actual physical model in Fig. 3.20. The results for the case when the receiver is located on the back of the body and on the shoulder-side are shown in Figs. 3.21 and 3.22. For the case when the receiver is located on the back of the body the addition of the arms improves the accuracy of the results when compared to the physical model. This indicates that the arms can have a significant effect on the coupling between antennas mounted on the body. However, for the case when the antenna is placed on the shoulder side of the body, neither the elliptical model nor the ellipse with arms yielded accurate results, and there was approximately a 10 dB discrepancy between the results obtained with these and the physical models. Therefore, we surmise that the addition of other scattering features such as the head, irregular arm position and shape — not exhibited in the simplified models —play a crucial role in accurately capturing the behaviors of the fields around the human body.
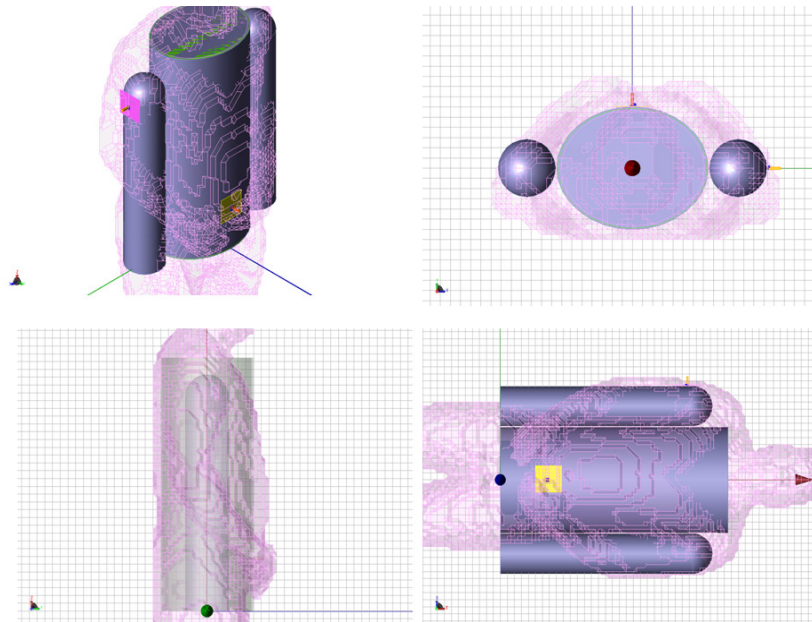
Fig. 3.20: Simplified model superimposed on the human body numerical phantom.
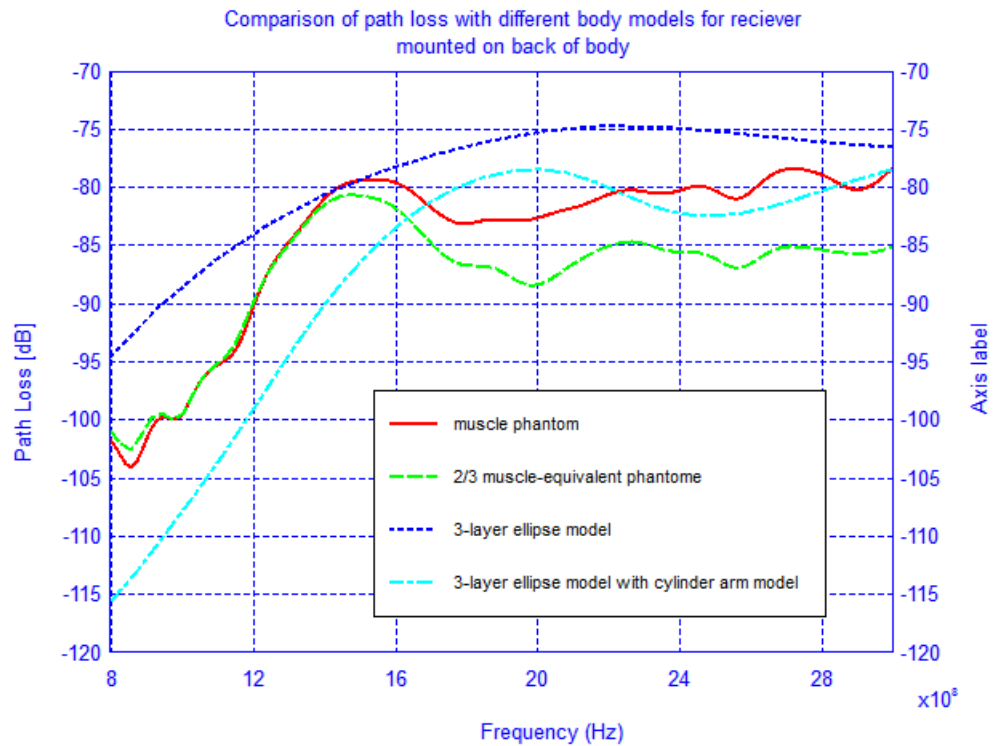
Fig. 3.21: Comparison of the path loss for different phantom models with receiving antenna on the back of the body and transmitting antenna at the waist.
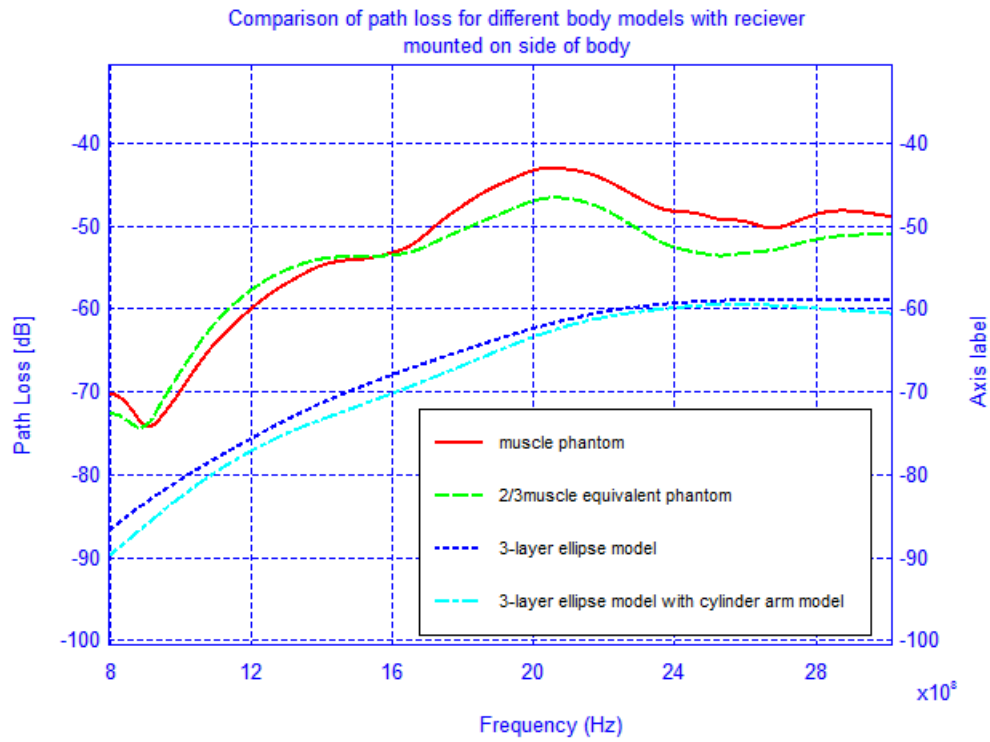
Fig. 3.22: Comparison of the path loss for different phantom models with receiving antenna on the shoulder side of the body and transmitting antenna at the waist.

Chapter 4

A New Hybrid Dipole Moment Based Approach for Handling Sub-Cellular Structures in FDTD

As emerging technologies have continued to provide us with increased computational power, the well established FDTD method has kept pace by enhancing its capabilities to rigorously simulate electromagnetic systems and devices with ever-increasing complexities. Of course, in principle most systems can be modeled via the FDTD method provided that the computational resources are available. Yet, in many cases the method can quickly become unattractive if the computational domain size is extremely large (on the order of tens of wavelengths) and several of the features within the model are much less than the wavelength (on the order of hundredths or thousandths of a wavelength). These scenarios frequently arise when we attempt to model BANs and other similar systems, and they continue to create a "bottleneck" effect in Finite Methods. This chapter will begin by reviewing some previous sub-cell approaches to the FDTD method and their shortcomings. Next, we will introduce a completely new approach to handling these sub-cellular features based on the dipole moment (DM) concept and provide some benchmark results for several canonical geometries, to validate the results and, also, to illustrate the computation efficiency both in terms of CPU memory and time.

4.1 Review of Previous Sub-Cell FDTD Methods

The attempt to model features whose dimensions do not coincide with the conventional Yee cell on a staggered Cartesian mesh has had a long history, ever since the FDTD method was adopted as a powerful computational approach in CEM. These attempts can be categorically

divided into two categories, namely, the contour-path approach and the auxiliary differential

equation model (ADE). Each approach is distinctly different in its respective formulations and

underlying assumptions that inherently limit the scope of problems that they can solve.

4.1.1 The Contour-Path FDTD Approach

By far the easiest and most simplest approach to modeling features that do not fill an

entire FDTD cell is based on a modification of the path integrals in Maxwell's equations. Since

the FDTD method can be viewed as a locally piece-wise constant approximation to the integral

form of Maxwell's equation, it is straightforward to visualize the computational domain as a

series of interlinked contour integrals. The contour-path modeling approach is then a modification

of these path integrals based on either a knowledge of the boundary conditions, or an assumed

local behavior of the fields.

In many cases, the object may occupy a significant portion of the computation domain

and partially fill several FDTD cells. If the structure is a PEC then the Yu-Mittra technique [28]

has been used as a stable, simple, and effective way to model these objects. The basis of this

method is to simply remove those portions of the path integral using Faraday's law where the

PEC has partially filled the cell. The geometry of a partially filled cell is show in Fig. 4.1, where

the object is assumed to extend several FDTD cells.
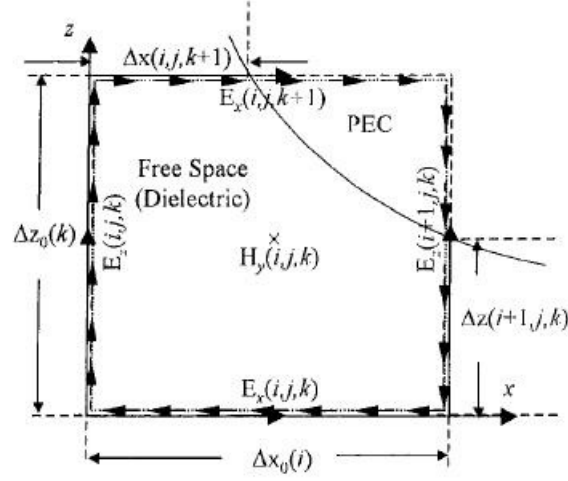
Fig. 4.1: The contour-path of the Conformal FDTD in a deformed cell (source from [28]]).

Clearly, the electric field inside the PEC is zero and only those portions of the path integral that are non-zero will enter into the update equations. Upon applying Faraday's law to the model shown in Fig. 4.1, we find the update equation for the H_y (other magnetic field components are found similarly) component in the partially filled cell given by equation (4.1) below.

$$H_y^{n+\frac{1}{2}}(i, j, k) = H_y^{n-\frac{1}{2}}(i, j, k)$$
$$+ \frac{\Delta t}{\mu_o \Delta x_o(i) \Delta z_o(k)} \left[\begin{array}{l} \Delta z(i, j, k) E_z^n(i, j, k) - \Delta z(i+1, j, k) E_z^n(i+1, j, k) \\ + \Delta x(i, j, k+1) E_x^n(i, j, k+1) - \Delta x(i, j, k) E_x^n(i, j, k) \end{array} \right] \quad (4.1)$$

The form of equation (4.1) shows that the only net effect on the conventional FDTD algorithm is a modification of the integral path lengths in front of each electric field component. To implement this approach we simply introduce a pre-calculated reduction factor for the electric field components affected by the partially filled cell, without making any other basic changes to the conventional updating scheme.

There are several key issues related to this method that become troublesome when one tries to generalize this approach to arbitrary structures. First, notice that only the magnetic field is updated without any regard to the effect of the partially filled cell on the electric field components. A simple example which demonstrates that neglecting the effect on the electric field will not give the correct results is that of a simple long straight wire— aligned with the grid and partially filling several FDTD cells. Using the aforementioned approach, the electric field is assumed to have no variation away from (but still within the partially filled FDTD cell) the wire along the radial path when computing the path integral. However, since it is well known that the electric field strength decays rapidly near the wire, this method would not be suitable for analyzing these types of geometries. Furthermore, any abrupt discontinuities or sharp corners in the geometry, at or near the partially filled cell, will not provide the correct fields near this location. Secondly, the approach obviously entirely neglects the actual curvature of the PEC structure inside the cell. Thus, all that matters in this formulation is the net effect on the path integrals and not the actual structure of the geometry itself. Therefore, any straight or curved wire structures passing through the cell cannot be modeled with this method.

A version of the contour-path approach can be applied to thin wires and enables a more accurate representation of wire geometries (thin slots can be similarly treated) and was first proposed by [29]. This formulation relies on the *a priori* assumption that we have a static-field spatial distribution for the electric and magnetic field components in the near vicinity of the wire and that it is aligned with the computational grid corresponding to any one of the three Cartesian electric field components. In turn, the relevant near-field components are essentially being generated by the currents and charges on the wire from which we have assumed the local static field behavior. According to [30], the method is simply described as follows:

- The circumferential *H* components immediately adjacent to the wire have spatial variation proportional to $1/r$.

- The radial *E* components immediately adjacent to the wire have spatial variation proportional to $1/r$.

- The axial *E* component on the wire is zero for all time as to satisfy the boundary condition.

The rest of the field components inside the computational domain are left unchanged in the updating scheme. The geometry under consideration is shown in Fig. 4.2 with all relevant field components.
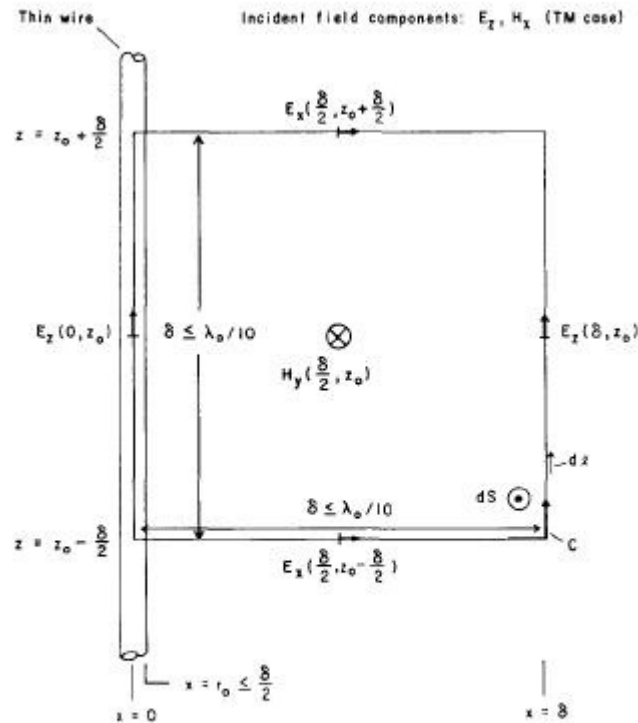
Fig. 4.2: Faraday's law contour path for thin wire (source from [29]).

Further improvements to this method are discussed in [30], and these additional

considerations into the near-field effects of the wire leads to the following modification to the

finite-difference update equations for the fields nearest the wire. The modifications for the

looping H_y and radial E_x component (other corresponding components can be obtained from a

simple permutation of the subscripts) as indicated by Fig. 4.2 are given by

$$
\begin{aligned}
H_y\big|_{\Delta x/2,y_o,z_o}^{n+\frac{1}{2}} &= H_y\big|_{\Delta x/2,y_o,z_o}^{n-\frac{1}{2}} + \frac{k_E \Delta t}{\mu_o \Delta z}\left(E_x\big|_{\Delta x/2,y_o,z_o-\Delta z/2}^{n} - E_x\big|_{\Delta x/2,y_o,z_o+\Delta z/2}^{n}\right) \\
&+ \frac{2\Delta t}{\mu_o \Delta x \ln(\Delta x/r_o)}E_z\big|_{\Delta x,y_o,z_o}^{n}
\end{aligned}
\tag{4.2}
$$

$$
\begin{aligned}
E_x\big|_{\Delta x/2,y_o,z_o-\Delta z/2}^{n+1} &= E_x\big|_{\Delta x/2,y_o,z_o-\Delta z/2}^{n} + \frac{k_H \Delta t}{\varepsilon_o \Delta z}\left(H_y\big|_{\Delta x/2,y_o,z_o-\Delta z}^{n+\frac{1}{2}} - H_y\big|_{\Delta x/2,y_o,z_o}^{n+\frac{1}{2}}\right) \\
&+ \frac{\Delta t}{\varepsilon_o \Delta y}\left(H_z\big|_{\Delta x/2,y_o+\Delta y/2,z_o-\Delta z/2}^{n+\frac{1}{2}} - H_z\big|_{\Delta x/2,y_o-\Delta y/2,z_o-\Delta z/2}^{n+\frac{1}{2}}\right)
\end{aligned}
\tag{4.3}
$$

where $k_E = \left[(\Delta x/\Delta y)\tan^{-1}(\Delta y/\Delta x)\right]^{-1}$ and $k_H = (\Delta x/\Delta y)\tan^{-1}(\Delta y/\Delta x)$. Furthermore, a special

treatment of the end open-circuited wire is available but the modifications to the update equations

are rather complex leading to the evaluation of the complete elliptic integrals of the first and

second kinds [30]. As such, the open-circuited treatment finds limited practical use as it requires a

significant change to the basic FDTD update equations.

The thin wire contour-path sub-cell technique has found some useful applications to

power surge analysis on transmission lines; but, to-date, it has not been utilized extensively in

most computational simulations with fine features. One major reason for this lies in the fact that it

is limited to straight wires that must coincide with the FDTD mesh at the electrical field nodal

points. Finally, the assumed $\frac{1}{r}$ variation is only valid for long wires; thus, short wires and objects within a single cell cannot be modeled accurately even when the open-circuit type of end condition is implemented.

4.1.2 The Auxiliary Differential Equation Method

The Auxiliary Differential Equation (ADE) method is an approach that allows for the treatment of thin wires or slots that are arbitrarily placed inside the FDTD mesh and was first proposed by Holland [31]. Many extensions and modifications have been made to the basic algorithm to improve its range of applications [32], [33]. In contrast to the contour-path model for thin wires, this method does not require the wires to lie on the FDTD grid. However, similar assumptions are made about the nature of the electric and magnetic fields near the wire, namely, that the fields near the wire have a $\frac{1}{r}$ spatial variation. The details of this method are more involved than the contour-path model and we only outline the basic principles of the approach as given by [31] in order to point out some of its features.

A typical straight wire parallel to the z-axis and passing through an FDTD cell is shown in Fig. 4.3. In this case the wire is shown off-center to the electric field grid points in the computational domain. The analysis begins by separating the electromagnetic fields into their incident and scattered counterparts as

$$\vec{E} = \vec{E}^{\,s} + \vec{E}^{\,i} \qquad\qquad (4.4)$$

$$\vec{H} = \vec{H}^{\,s} + \vec{H}^{\,i} \qquad\qquad (4.5)$$
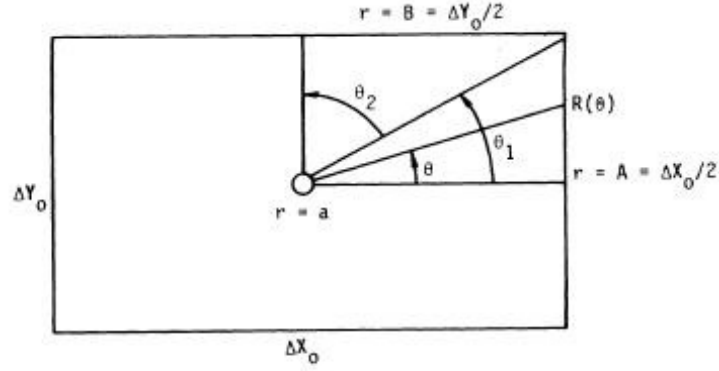
Fig. 4.3: Geometry of a wire inside a rectangular FDTD cell (source from [31]).

Naturally, for wire geometries it is easiest to work in polar coordinates and we proceed to write Maxwell's equations for the θ-component of the curl-$\bar{E}$ equation as

$$\frac{\partial E_r^s}{\partial z} + \frac{\partial E_r^i}{\partial z} - \frac{\partial E_z^s}{\partial r} - \frac{\partial E_z^i}{\partial r} = -\mu_o \left(\frac{\partial H_\theta^s}{\partial t} + \frac{\partial H_\theta^i}{\partial t} \right).$$ (4.6)

At $r = a$, we enforce the boundary condition

$$E_z^s + E_z^i = 0.$$ (4.7)

If we integrate out to an arbitrary radius r we have

$$E_z^s(r) + E_z^i(r) = \mu_o \frac{\partial}{\partial t} \int_a^r \left(H_\theta^s + H_\theta^i \right) d\rho$$
$$+ \frac{\partial}{\partial z} \int_a^r \left(E_r^s + E_r^i \right) d\rho$$ (4.8)

Since it is assumed that the FDTD cell size, and therefore the radii are small compared to the wavelength, we can write the expressions for the magnetic and electric fields in terms of currents and charge per unit length in average sense around θ. Specifically, these are given by

$$H_\theta^s + H_\theta^i = \frac{I^s + I^i}{2\pi r}$$

(4.9)

$$E_r^s + E_r^i = \frac{Q^s}{2\pi r \varepsilon_o}$$

(4.10)

where I^i is any locally injected current source in the model. In most cases, we would have either $I^i = 0$, or $E^i = 0$ because the scatterer is unlikely to be simultaneously illuminated by an incident field and driven by an injected current source. In the absence of any current injected sources, we assume that the incident fields are known *a priori*. Inserting (4.9) and (4.10) into (4.8) gives us an expression for the electric field in terms of currents and charges as

$$E_z^s(r) + E_z^i(r) = \frac{\partial(I^s + I^i)}{\partial t} \mu_o \frac{\ln(r/a)}{2\pi} + \frac{\partial Q^s}{\partial z} \frac{\ln(r/a)}{2\pi \varepsilon_o} \ .$$

(4.11)

A similar analysis for the r-component of the curl-$\bar{H}$ equation yields

$$\frac{\partial Q^s}{\partial t} + \frac{\partial I^s}{\partial z} = -\frac{\partial I^i}{\partial z} \ .$$

(4.12)

To remove the radial dependence on (4.11), it is typical to carry out an averaging operation. This process introduces a numerical factor known as the "in-cell" inductance of the wire, and is a key step that makes the accuracy of the method questionable. The result of this averaging process and its "in-cell" inductance are given by

$$L\left(\frac{\partial(I^s + I^i)}{\partial t} + \frac{1}{\varepsilon_o \mu_o} \frac{\partial Q^s}{\partial z}\right) = \langle E_z^s \rangle + \langle E_z^i \rangle$$

(4.13)

$$L = \frac{\mu_o}{2\pi} \frac{\int_a^R \ln(r/a)r\,dr}{\int_0^R r\,dr} = \frac{\mu_o}{2\pi}\left(\ln(R/a) - \frac{1}{2} + \frac{a^2}{2R^2}\right).$$

(4.14)

The choice of R is entirely arbitrary and its value for which the best results were obtained has empirically been found to be related to the area of the FDTD cell cross-section. Once all these

preliminary calculations have been carried out, a finite-differencing scheme consistent with the

FDTD is performed on (4.12) and (4.13), and the time-stepping process as described by [31]

begins as follows:

1) $\langle E^i \rangle$ and $\partial I^i / \partial t$ are calculated at the I^s mesh points.

2) $\langle E^s \rangle$ is calculated at the I^s mesh points.

3) Update I^s based on the conventional finite-differencing scheme.

4) Update H^s from the curl-$\bar{E}$ equations.

5) Increment time by $\Delta t / 2$.

6) Partition $I^s + I^i$ to the four nearest E_z^s mesh points. The partitioning is based on a weighting of the current density from the calculated current and its location within the cell.

7) Update $\bar{E}^s$ from the curl-$\bar{H}$ equations. In these equations an added source term $\bar{J}^s$ is included, which is found by the appropriate partitioning of $I^s + I^i$.

8) Update Q^s based on the conventional finite-differencing scheme.

9) Increment time by $\Delta t / 2$ and repeat step 1).

The additional update equations for the current and charge is the basis of the ADE

method, and it has garnered some success. Many researchers continue to modify and improve this

basic approach, including wires that are not aligned with the FDTD mesh. However, as in the thin

wire contour-path method, this approach has the underlying assumption of a $1/r$ spatial variation

for the fields near the wire. Furthermore, this spatial dependence behavior is only reliable if the

wire is sufficiently long, i.e., it spans several FDTD cells. Therefore, short wires or those that

have curvatures inside the cell — which do not exhibit this type of spatial variation—cannot be modeled by using this technique.

4.2 The Dipole Moment (DM) Method

The previous section presented an overview of most of the popular sub-cell techniques for handling either partially filled cells or long wire sections. It was frequently pointed out that the $\frac{1}{r}$ near field behavior is not an accurate representation of the fields if the wire is short, contained within a single FDTD cell, and exhibits curved features within the cell. All these features are becoming more commonplace in large systems that contain fine features. As an example, antennas and sensors in BANs invariably have some or all of these attributes. Some typical geometries are shown in Figs. 4.4 and 4.5 where it becomes rather obvious that many common sub-cell techniques would be totally inadequate if they attempted to handle these features. Currently, there are advanced techniques — referred to in the literature as sub-gridding methods—that attempt to address these issues. The most common is referred to as the Alternating Direction Implicit FDTD (ADI-FDTD) in which the region containing the fine features is sub-gridded to match the local feature resolution. This method is unconditionally stable, which has made it an attractive option for dealing with multi-scale problems. Unfortunately, the interface region between the local fine mesh and the global mesh size is known to introduce artificial numerical reflections and has rendered the method as inaccurate and unreliable. Additionally, despite eliminating the need to create a fine mesh throughout the entire computational domain, the fine mesh region still requires additional computational resources—need to invert a matrix for instance — whereas the aforementioned sub-cell techniques do not. Furthermore, many fine - featured structures that are integral parts of BANs and other complex systems have dimensions

that are smaller than the nominal FDTD cell size, taken to be $\lambda_{high}/20$, and it is these type of geometries that are of interest in many practical applications. This motivates us to develop a new technique that can handle these fine features without introducing any modifications to the FDTD grid structure.
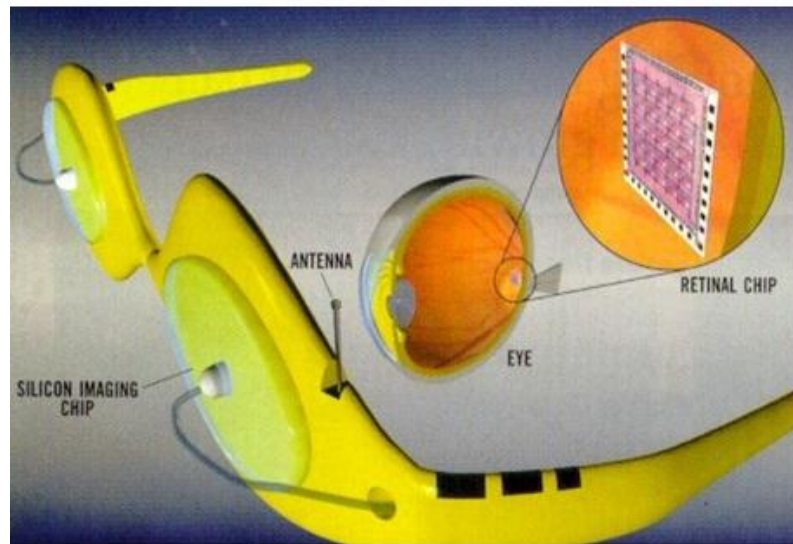
Fig. 4.4: A retinal implant with antenna sensor (source from [34]).
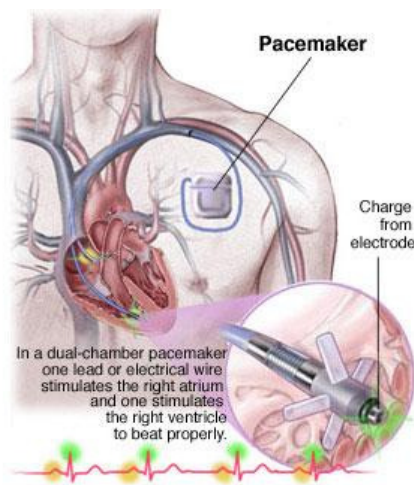
Fig. 4.5: Charge electrode from a pacemaker (source from [34]).

It is well known that the electromagnetic properties of objects that are significantly smaller than the wavelength (maximum dimension $<< \lambda/20$) can be accurately and conveniently characterized by a dipole moment representation. In fact, any arbitrary structure that is significantly smaller than the wavelength can in general be decomposed into three electric and three magnetic dipole moments along the principal axes. Furthermore, these dipole moments can be uniquely obtained by the fact that their far field patterns form a vector space. As an example, suppose we have a far field pattern $P(r,\phi,\theta)$ that is generated by the scattered field of a small object. If $P(r,\phi,\theta)$ belongs to the vector space of all possible functions having an electric dipole moment pattern, then we may form a basis for this finite 3-dimensional (not spatial but vector space dimension) space from the set $\{\vec{\phi}_x, \vec{\phi}_y, \vec{\phi}_z\}$, where $\vec{\phi}_\alpha$ is a dipole pattern with orientation α . A basis forms a Hilbert space if and only if $\langle \vec{\phi}_\alpha, \vec{\phi}_\beta^* \rangle = 0$ when $\alpha \neq \beta$, is non-zero otherwise, and is complete. To show that these dipole moment far field patterns satisfy this condition we consider the particular far fields produced by x- and z-oriented electric dipole moments (EDMs) without any loss of generality to the basic analysis when multiple EDMs are present. The far field for a z-oriented EDM is given by

$$\bar{E} = -\hat{\theta} \frac{j\omega\mu}{4\pi r} e^{jkr} Il_z \sin\theta \tag{4.15}$$

and that for an x-oriented EDM is given by

$$\bar{E} = \frac{j\omega\mu}{4\pi r} e^{jkr} Il_x \left(\hat{\theta} \cos\theta \cos\phi - \hat{\phi} \sin\phi \right) . \tag{4.16}$$

For this vector space a suitable inner product is defined as

$$\left\langle \vec{\phi}_\alpha, \vec{\phi}_\beta^* \right\rangle \equiv \oiint_S \vec{\phi}_\alpha * \vec{\phi}_\beta^* ds = \int_0^{2\pi} \int_0^\pi \vec{\phi}_\alpha * \vec{\phi}_\beta^* r^2 \sin\theta d\theta d\phi \tag{4.17}$$

By inserting (4.15) and (4.16) into the inner product given in (4.17) it is straightforward to show that the resulting inner product is

$$\left\langle \vec{\bar{\phi}}_z, \vec{\bar{\phi}}_x^* \right\rangle = 0 \,. \tag{4.18}$$

The same is true for the orthogonality between other dipole moment orientations, be they electric or magnetic. Therefore, we can write the far fields of any small object in terms of a superposition of three electric and three magnetic dipole moments and use the orthogonality properties similar to (4.18) to find their respective weights.

The problem with using the far fields to obtain the dipole moments is that it leaves us without any knowledge of the relationship between the induced dipole moments and the incident field. It can be shown [35] that finding an EDM (or MDM) representation amounts to solving three quasi-static near field problems with three orthogonal excitations, each having weights determined by the projection of the incident field polarization on the principal axes, and defining a phase center. This establishes an equivalency between proving the orthogonality of the far field patterns, and solving quasi-static problems with orthogonal incident field excitations. The later path is more advantageous to follow because it provides us with a means to relate the polarizibilty of the object with the incident field. However, solving these quasi-static problems can only be done analytically for a few cases and, hence, we typically rely on numerical solutions of the quasi-static problems to derive the charge distribution on the object. Furthermore, these numerical approaches use conventional integral equation methods that are cumbersome and not conveniently amenable to hybridization with the FDTD. It is for this reason that we introduce a new approach for solving these quasi-static problems, which is based on the dipole moment of a sphere, and its simple implementation into a hybrid FDTD scheme.

4.2.1 Dipole Moments and Scattering from a PEC Sphere

We begin our discussion by considering the problem of plane wave scattering by a small

PEC sphere of radius a illuminated by an incident wave traveling in the negative z-direction

whose electric field is polarized along the x-axis, and it is well known that the scattered far-field

for this small ($ka \to 0$) PEC sphere is given by the following equations:

$$E_\theta^s \underset{ka \to 0}{=} E_o \frac{e^{-jkr}}{kr}(ka)^3 \cos\phi\left(\cos\theta - \frac{1}{2}\right) \tag{4.19}$$

$$E_\phi^s \underset{ka \to 0}{=} E_o \frac{e^{-jkr}}{kr}(ka)^3 \sin\phi\left(\frac{1}{2}\cos\theta - 1\right) \tag{4.20}$$

where E_o is the magnitude of the incident electric field and k is the wavenumber in the medium.

When this result is compared with the radiated fields of a dipole whose electric and

magnetic moments are Il and kl, respectively, we find that the same fields, as those of the

original sphere, are produced with

$$\hat{a}_x Il = \hat{a}_x E_o \frac{4\pi j}{\eta k^2}(ka)^3 \tag{4.21}$$

$$\hat{a}_y kl = \hat{a}_y E_o \frac{2\pi}{jk^2}(ka)^3 \quad . \tag{4.22}$$

It is not surprising that, in the far-field region, the fields from any small scatterer can be

characterized by a superposition of those originating from electric and magnetic dipole moments

with appropriate weights. However, to the best of our knowledge, the question of whether or not

these dipole moment representations are valid equally well in the near-field region of the scatterer

has not been addressed in the literature. Furthermore, we may inquire about the limits of the DM

representation and ask the question of how close to the scatterer surface can we come before they

become inaccurate. To answer these questions we refer back to the Mie series representation of the scattered electric field for a small sphere. First we consider the θ-component of the electric field, which is of most interest because it is the dominant backscatter contribution in the near region and satisfies the boundary condition of the PEC sphere. It is expressed as:

$$E_\theta = \frac{E_o}{kr}\cos\phi\sum_{n=1}^{\infty}\left[jb_n\hat{H}_n'^{(2)}(kr)\sin\theta P_n'^1(\cos\theta) - c_n\hat{H}_n^{(2)}(kr)\frac{P_n^1(\cos\theta)}{\sin\theta}\right]$$ (4.23)

where b_n and c_n are given by

$$b_n = -\frac{n+1}{n}c_n$$ (4.24)

$$c_n = \frac{-2n}{j^{n+1}(n+1)}\left[\frac{2^{2n}(n-1)!}{(2n)!}\right]^2\left(\frac{ka}{2}\right)^{2n+1}, \qquad ka\to 0 .$$ (4.25)

Next we apply an asymptotic analysis to the Mie series solution by letting $kr\to 0$. The resulting expressions for the Hankel function and its derivatives take the form of

$$\hat{H}_n^{(2)} \approx j\frac{\Gamma\left(n+\tfrac{1}{2}\right)}{\sqrt{\pi}}\left(\frac{kr}{2}\right)^{-n}$$ (4.26)

$$\hat{H}_n'^{(2)} \approx \frac{-jn\Gamma\left(n+\tfrac{1}{2}\right)}{2\sqrt{\pi}}\left(\frac{kr}{2}\right)^{-n-1}$$ (4.27)

where the notation $' = \frac{\partial}{\partial(kr)}$ is used. Utilizing (4.24) and (4.26)-(4.27) in equation (4.23) we obtain the asymptotic form for the θ component given by

$$E_\theta = \frac{E_o}{2}\cos\phi\sum_{n=1}^{\infty}c_n\left[-\frac{n+1}{2}\frac{\Gamma\left(n+\tfrac{1}{2}\right)}{\sqrt{\pi}}\left(\frac{kr}{2}\right)^{-n-2}\sin\theta P_n'^1(\cos\theta) - j\frac{\Gamma\left(n+\tfrac{1}{2}\right)}{\sqrt{\pi}}\left(\frac{kr}{2}\right)^{-n-1}\frac{P_n^1(\cos\theta)}{\sin\theta}\right]$$ (4.28)

If we retain only the $n=1$ term in (4.28), note that $\Gamma(3/2)=\sqrt{\pi}/2$, $P_1^1(\cos\theta)=-\sin\theta$, $P_1'^1=\cot\theta$, and $c_1=4(ka/2)^3$ from (4.25), we obtain

$$E_\theta = E_o \cos\phi \left[\left(\frac{a}{r}\right)^3 \cos\theta + j\frac{ka^3}{2r^2}\right]$$ (4.29)

However, we observe that $(a/r)^3 \gg ka^3/2r^2$ since $r \to a$ and $a \to 0$. Therefore, the near field for the θ component is given by

$$E_\theta = -E_o \cos\phi\cos\theta\left(\frac{a}{r}\right)^3$$ (4.30)

and for $\theta=0, \phi=0$ we have shown that $E_\theta^s = -E^i\big|_{r=a}$ as required by the boundary conditions on the PEC sphere. The other near field components of the PEC sphere can be derived in a similar manner.

Now we turn to the expression for the θ-component of the electric fields produced by an x-oriented electric dipole moment. It is given by

$$E_\theta = \frac{Il_x}{4\pi}e^{-jkr}\left(\frac{j\omega\mu}{r}+\frac{\eta}{r^2}+\frac{1}{j\omega\varepsilon r^3}\right)\cos\phi\cos\theta$$ (4.31)

Substituting (4.21) into (4.31), and retaining only the $1/r^3$ term, yields exactly the same result as derived in (4.30). It then becomes clear that the electric dipole moment representation for the PEC sphere remains valid even in the near-field.

There are some key points which we need to make at this point. First, we have neglected to address how the magnetic dipole moment contributes to the electric field in the near region if we choose to use these representations. The result in (4.30) demonstrates that the electric dipole moment is sufficient to represent the near field for the θ-component. If the magnetic dipole moment were to contribute to the near-field it must produce TEy fields. Clearly, E_θ is TEy for $\theta=0, \phi=0$ and we have already shown that the electric dipole moment alone completely

represents this field for all θ and ϕ in the near region. In view of this, we conclude that the magnetic dipole moment contribution in the near-field is negligible for all the electric field components. Furthermore, the result of (4.30) can be alternatively derived from solving an electrostatics problem for the PEC sphere. Therefore, we conclude that the near-fields for a PEC sphere can be completely described by a single electric dipole moment.

4.2.2 The Dipole Moment Formulation for PEC Structures

Suppose the PEC sphere is located at the origin. Using the dipole moment equivalence for the scattered field we can write for the electric-dipole moment $\hat{z} - oriented$ (corresponding to Ez incident plane wave) as

$$E_r = \frac{Il}{2\pi} e^{-jkr} \left(\frac{\eta}{r^2} + \frac{1}{j\omega\varepsilon r^3} \right) \cos\theta \tag{4.32}$$

$$E_\theta = \frac{Il}{4\pi} e^{-jkr} \left(\frac{j\omega\mu}{r} + \frac{\eta}{r^2} + \frac{1}{j\omega\varepsilon r^3} \right) \sin\theta \tag{4.33}$$

where Il is given in (4.21).

In FDTD, we consider the sphere located within a cell, which is typically $\leq \dfrac{\lambda}{20}$ along each spatial dimension. In this case, the grid lines of the cell are located very close to the sphere and we can make the following quasi-static approximations:

1) $kr << 1$ so in the phase term $\rightarrow e^{-jkr} \approx 1$.

2) The $\dfrac{1}{r^3}$ term dominates close to the sphere and inside the unit FDTD cell.

   Therefore, by using the expression in (4.21) along with (4.32)-(4.33) it can be shown that

$$E_r = 2E_o \left(\frac{a}{r}\right)^3 \cos\theta \tag{4.34}$$

$$E_\theta = E_o \left(\frac{a}{r}\right)^3 \sin\theta \tag{4.35}$$

which shows that the fields close to sphere are *"time-independent"* and identical to those from a

static charge doublet (dipole). This result is necessary in order to implement the modified fields

into the FDTD algorithm, since the spatial variation of the fields cannot be frequency-dependent

if they are to be coupled to the FDTD, which we are planning to do.

When working with FDTD, it is convenient to describe the scattered fields produced by

the sphere(s) in Cartesian coordinates, to avoid the need to carry out coordinate transformations

between respective spherical origins of the multiple spheres. This approach is easily implemented

since we are only retaining the first term in the series expansion and the spatial variations can be

most conveniently described between the two different coordinates systems. By defining a global

origin in the FDTD, the respective fields produced by x, y, and z-oriented dipole moments in

Cartesian components can be written as

For x-oriented dipole-moment

$$E_x = E_x^{inc} a^3 \frac{2(x-x')^2 - (y-y')^2 - (z-z')^2}{\left[(x-x')^2 + (y-y')^2 + (z-z')^2\right]^{5/2}} \tag{4.36}$$

$$E_y = 3E_x^{inc} a^3 \frac{(y-y')(x-x')}{\left[(x-x')^2 + (y-y')^2 + (z-z')^2\right]^{5/2}}$$

$$E_z = 3E_x^{inc} a^3 \frac{(z-z')(x-x')}{\left[(x-x')^2 + (y-y')^2 + (z-z')^2\right]^{5/2}}$$

For y-oriented dipole-moment

$$E_y = E_y^{inc} a^3 \frac{2(y-y')^2 - (x-x')^2 - (z-z')^2}{\left[(x-x')^2 + (y-y')^2 + (z-z')^2\right]^{5/2}}$$

$$E_x = 3E_y^{inc} a^3 \frac{(y-y')(x-x')}{\left[(x-x')^2 + (y-y')^2 + (z-z')^2\right]^{5/2}}$$

$$E_z = 3E_y^{inc} a^3 \frac{(z-z')(y-y')}{\left[(x-x')^2 + (y-y')^2 + (z-z')^2\right]^{5/2}}$$

(4.37)

For z-oriented dipole-moment

$$E_z = E_z^{inc} a^3 \frac{2(z-z')^2 - (x-x')^2 - (y-y')^2}{\left[(x-x')^2 + (y-y')^2 + (z-z')^2\right]^{5/2}}$$

$$E_y = 3E_z^{inc} a^3 \frac{(y-y')(z-z')}{\left[(x-x')^2 + (y-y')^2 + (z-z')^2\right]^{5/2}}$$

$$E_x = 3E_z^{inc} a^3 \frac{(z-z')(x-x')}{\left[(x-x')^2 + (y-y')^2 + (z-z')^2\right]^{5/2}}$$

(4.38)

where the primed coordinates represent the spatial position of the sphere with respect to the

global FDTD origin.

In general, a single sphere will have a dipole moment in the direction coinciding with the

polarization of the incident field. However, if we cascade these spheres in such a way that they

provide a conducting path through which the current will flow, then we must enforce a criterion

of 'preferred direction,' and assume that the dipole-moments are all oriented along this direction.

This will provide a consistency between the direction of the dipole-moments calculated and that

of the current path through the network of cascaded spheres which comprise the conducting

structure. For a wire, each sphere will have a single associated 'preferred direction'

corresponding to the position of the adjacent sphere. For a surface-type structure, each sphere will

then have two associated 'preferred directions' corresponding to the two adjacent spheres. The

calculated 'preferred directions' are pictorially described in Fig. 4.6.
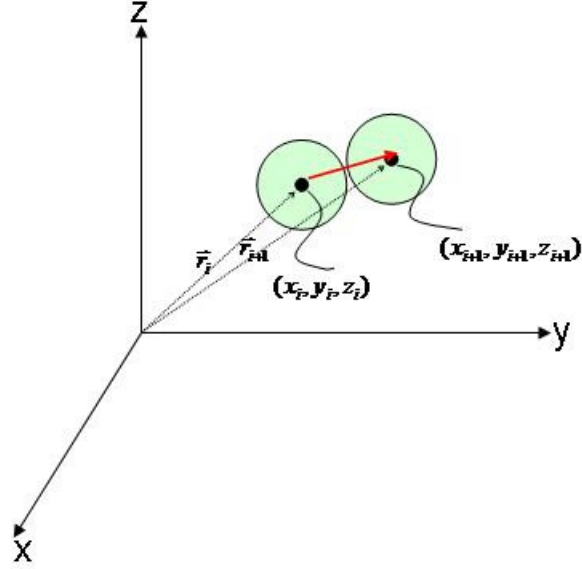
Fig. 4.6: Method for calculating the preferred direction of the dipole-moments.

From Fig.4.6, the corresponding unit vector of the preferred direction is seen to be

$$\hat{u}_i = \frac{1}{|L|}\left\{(x_{i+1} - x_i)\hat{a}_x + (y_{i+1} - y_i)\hat{a}_y + (z_{i+1} - z_i)\hat{a}_z\right\}$$ (4.39)

$$|L| = 2a = \left[(x_{i+1} - x_i)^2 + (y_{i+1} - y_i)^2 + (z_{i+1} - z_i)^2\right]^{1/2}$$

and we define

$$\alpha_i = \frac{(x_{i+1} - x_i)}{|L|}$$

$$\beta_i = \frac{(y_{i+1} - y_i)}{|L|}$$ (4.40)

$$\chi_i = \frac{(z_{i+1} - z_i)}{|L|}$$

The corresponding dipole moment is $Il_i \hat{u}_i = \alpha_i Il_i \hat{a}_x + \beta_i Il_i \hat{a}_y + \chi_i Il_i \hat{a}_z$, or in vector algebra notation

$$\bar{Il}_i = Il \begin{bmatrix} \alpha_i \\ \beta_i \\ \chi_i \end{bmatrix} \tag{4.41}$$

Next, we define the spatial Green's Dyadic, which relates the scattered fields in Cartesian components to those of the arbitrary directed dipole moments. This function describes our kernel in a manner analogous to the Moment Method matrix, and is entirely frequency independent —an attribute that is crucial for our hybridization of the DM formalism with the FDTD. In matrix form the Green's Dyadic is given by

$$\overline{\overline{G}}_i = \begin{bmatrix} \dfrac{2(x-x_i)^2 - (y-y_i)^2 - (z-z_i)^2}{|\vec{r}-\vec{r}|^5} & \dfrac{3(x-x_i)(y-y_i)}{|\vec{r}-\vec{r}|^5} & \dfrac{3(x-x_i)(z-z_i)}{|\vec{r}-\vec{r}|^5} \\ \dfrac{3(x-x_i)(y-y_i)}{|\vec{r}-\vec{r}|^5} & \dfrac{2(y-y_i)^2 - (x-x_i)^2 - (z-z_i)^2}{|\vec{r}-\vec{r}|^5} & \dfrac{3(y-y_i)(z-z_i)}{|\vec{r}-\vec{r}|^5} \\ \dfrac{3(x-x_i)(z-z_i)}{|\vec{r}-\vec{r}|^5} & \dfrac{3(y-y_i)(z-z_i)}{|\vec{r}-\vec{r}|^5} & \dfrac{2(z-z_i)^2 - (x-x_i)^2 - (y-y_i)^2}{|\vec{r}-\vec{r}|^5} \end{bmatrix} \tag{4.42}$$

where $|\vec{r}-\vec{r}_i| = \sqrt{(x-x_i)^2 - (y-y_i)^2 - (z-z_i)^2}$ and the subscripted coordinates are the locations of the ith dipole moment. The un-subscripted coordinates are arbitrary observation points provided that they are located in the near field region of the scatterer. In simple matrix notation we can now write the expression for the scattered field of a *single* sphere as

$$\overline{E}^{scat} = \begin{bmatrix} E_x^{scat} \\ E_y^{scat} \\ E_z^{scat} \end{bmatrix} = \overline{\overline{G}}_i \overline{Il}_i \tag{4.43}$$

Or equivalently

$$\overline{E}^{scat} = \underline{\underline{G}}_i \overline{Il}_i = \underline{\underline{G}}_i Il_i \begin{bmatrix} \alpha_i \\ \beta_i \\ \chi_i \end{bmatrix} \tag{4.44}$$

.

Now suppose that we wish to know the scattered field in some arbitrary $\vec{u}$-direction. Then the scattered field components in the direction of $\vec{u}$ is given by

$$\overline{u} \bullet \overline{E}^{scat} = \overline{u}^T \overline{E}^{scat} = Il_i \overline{u}^T \underline{\underline{G}}_i \overline{u}_i = E^{scat}\Big|_{u-direction} \tag{4.45}$$

where the superscript ^{T} denotes the transpose of the column vector.

Now, for a PEC structure we must impose the boundary condition that satisfies the total tangential electric field equal to zero. Suppose that for a single sphere we have forced the dipole moment to be orientated along some direction $\overline{u}_i$. Note that for either a single sphere, or a cluster of disjoint spheres this assumption is not generally accurate since the dipole moments will be directed in the same direction as the impinging wave. However, when the spheres are connected by using the directional constraint imposed on the dipole moments, then the formulation below is valid under this assumption. Therefore, assuming that the for a single sphere the dipole moment is directed in the $\overline{u}_i$ direction, we have

$$E^{scat}\Big|_{u_i-direction} = -E^{inc}\Big|_{u_i-direction} = -\overline{u}_i \bullet \overline{E}^{inc} = -\overline{u}_i^T \overline{E}^{inc} \tag{4.46}$$

and in terms of the dipole moment

$$-\overline{u}_i^T \overline{E}^{inc} = Il\overline{u}_i^T \underline{\underline{G}}_i \overline{u}_i = E_o a^3 \overline{u}_i^T \underline{\underline{G}}_i \overline{u}_i \tag{4.47}$$

where E_o is the solution to this equation and will satisfy the boundary condition under the assumption that the dipole moment is in the $\overline{u}_i$ direction. The constant a^3 is included as

convenience so that the quantity on the right hand side is unity when testing point is on the boundary and has the physical interpretation as being the radius of the sphere.

Again, we have stated that the above formulation for a single sphere is not generally accurate unless the impinging wave is in the same direction as the assumed dipole moment. However for a linear cluster of spheres that are electrically connected we can build on this formulation, which would indeed be correct since we would have an imposed the directional constraint on each of the dipole moments. Therefore, the scattered field at any spatial point (with the near field constraint) of a single sphere is given as

$$\overline{E}_i^{scat} = E_i a^3 \underline{\underline{G_i}} \overline{u}_i \qquad (4.48)$$

and for *N-spheres* we have

$$\overline{E}^{Total-scat} = \sum_{i=1}^{N} E_i a^3 \underline{\underline{G_i}} \overline{u}_i \qquad (4.49)$$

where the E_i's are the unknown constants to be determined by satisfying the boundary conditions in the same manner as before. If we wish to know the total scattered field at some point $\vec{r}_j$ on the PEC structure, then we can use

$$\overline{E}_j^{Total-scat} = \sum_{i=1}^{N} E_i a^3 \underline{\underline{G_{ij}}} \overline{u}_i \quad . \qquad (4.50)$$

Also, to satisfy the boundary conditions at this point, we must have

$$\overline{u}_j^T \overline{E}_j^{Total-scat} = \overline{u}_j^T \sum_{i=1}^{N} E_i a^3 \underline{\underline{G_{ij}}} \overline{u}_i = -\overline{u}_j^T \overline{E}_j^{inc} \qquad j = 1,2,3,.....,N . \qquad (4.51)$$

This sets up and $N \times N$ matrix equation for the unknown weight coefficients E_i's, with the $\overline{E}_j^{inc}$ assumed known from the specified incident field.

It is worth commenting on how the formulation embodied in (4.51) relates to approaches based on conventional integral equation methods. First, we note that we have chosen a dipole moment representation corresponding to the small PEC sphere for several points along a PEC structure. Although, this choice of representing a PEC structure out of a "string' of small PEC spheres may seem initially unusual, we will show how it closely resembles an alternative basis function for the electric field integral equation (EFIE) convenient for use in the FDTD. The equation constituting the starting point for solving (EFIE) is given in potential form by

$$- \bar{E}^{i}\left(\bar{r}\right) = -j\omega\bar{A} - \bar{\nabla}\phi \tag{4.52}$$

For all $\bar{r}$ on the surface of the PEC surface. Expressing [36] the potentials in terms of the electric currents on the PEC scatterer (4.52) can be written as

$$- \bar{E}^{i}\left(\bar{r}\right) = -\frac{j\omega\mu_{o}}{4\pi}\int_{S}\bar{J}_{S}\left(\bar{r}'\right)\frac{e^{-jk_{o}\left|\bar{r}-\bar{r}'\right|}}{\left|\bar{r}-\bar{r}'\right|}dS' + \nabla\frac{1}{4\pi j\omega\varepsilon_{o}}\int_{S}\nabla'\bullet\bar{J}_{S}\left(\bar{r}'\right)\frac{e^{-jk_{o}\left|\bar{r}-\bar{r}'\right|}}{\left|\bar{r}-\bar{r}'\right|}dS'. \tag{4.53}$$

The first term in (4.53) accounts for the magnetic or "inductive part" while the second one contributes to the electric or "capacitive part" of the field. For small PEC scatterers it becomes evident that the "capacitive part" dominates in the near field and thus only the contribution from the scalar potential is needed to approximate the field in this region. Furthermore, we note that the divergence of the current can be expressed as $\nabla' \bullet \bar{J}_{S} = j\omega\rho_{S}$ and the result is a static equation for the charge. It follows that the dipole moment formulation is then a quasi-static approximation to the EFIE in the near field with the delta basis functions with magnitude of (4.21) and point matching the fields at designated source points. Evidently, using a delta function representation

creates an uncertainty into how many delta functions we should use and what should be the

discretization size of the PEC scatterer. By relating the discretization to the radius of our small

PEC spheres, we have found that an optimal size is $\Delta = 0.5a$ for PEC wire structures and about

$\Delta = 0.75a$ for dielectrics. This has been validated for many wire geometries [37] and we will

therefore follow this guideline when hybridizing the dipole moment (DM) method with the

FDTD.

4.3 Hybridization with FDTD

Once we have found the dipole moment distribution the most effective approach to

coupling the scattered/radiated fields to the FDTD is to "collapse" the DM distribution to a single

DM located at the center of the Yee cell. Although this approach fails to model the fields in the

immediate vicinity of the scatterer, we have demonstrated that it nevertheless becomes quite

accurate within a few cells (typically two FDTD cells) from the scatterer. It is worthwhile to point

out that we can obtain the very near field accurately, any time we desire, directly from the DM

distribution. The reason for collapsing the DM distribution can be most easily understood by a

closer inspection of how the electric field is evaluated in the FDTD. As mentioned previously in

this chapter, the FDTD path integrals assume that the field is piece-wise constant at the nodal

points where the field is evaluated through finite differences. Assuming that we have accurately

determined the quasi-static near fields from the DM method it becomes clear that a static solution

coupled back to the FDTD must satisfy

$$\oint_C \vec{E} \cdot d\vec{l} = 0 \qquad (4.54)$$

which follows from the fact that the for static fields $\vec{E} = -\vec{\nabla}\phi$ and the potential function must be

a conservative field. Since, our quasi-static solution satisfies this conservative property it follows

that the updated electric fields at the nodal points must exhibit a symmetry for which the

evaluated fields are piece-wise constant. In an average sense, this can be done by collapsing the

DM solution to the center of the electric field cell, in the process defining a phase center. In

theory we know the quasi-static near fields exactly from their DM solution and a rigorous

integration of these fields in the FDTD would satisfy (4.54). However, we are seeking a method

that does not require any sophisticated modification of the basic FDTD algorithm and we have

found that this approach is best suited for our objective.

At first glance, it may seem that defining a phase center and solving a static problem are

contradictory. Furthermore, one may incorrectly conclude that introducing a quasi-static solution

into the FDTD at special points within the grid would yield a quasi-static solution throughout the

computational domain. In fact, a novel feature of this proposed hybrid scheme is that the FDTD

algorithm automatically performs the analytic continuation of the coupled quasi-static solution as

a consequence of the dynamic nature of Maxwell's curl-$\vec{E}$ and curl-$\vec{H}$ equations in the FDTD.

Additionally, the continual updating of the scattered field in the quasi-static near region, where

the DM method is used, gives rise to a dynamic response of the FDTD algorithm, which, in turn,

propagates the scattered field outwards, capturing all the nuances of this field, including its full

dynamic (as opposed to quasi-static) behavior. This characteristic of the FDTD has not been

previously reported in the literature and we have exploited this feature to incorporate the

hybridization of small features into an unmodified FDTD grid structure.

The dipole moment formulation mentioned in the previous section has some features that

require a slight modification of the basic update equations in the FDTD algorithm. In the dipole

moment formulation it is the incident field that allows us to set up the matrix equation for

satisfying the boundary conditions on the PEC structure. However, the FDTD algorithm is

essentially a total field formulation and we must find a systematic way to separate the scattered

field and incident fields when hybridizing the DM method with the FDTD. There does exists a

scattered field formulation for the FDTD where an interior region calculates the total field and the

exterior region calculates the scattered field. In contrast, we are seeking the opposite of this

approach. Namely, we wish to know the incident field at the cell where the scatterer is, for which

the scattered field can be obtained by the DM method, and the total field at points away from the

scatterer. The reason for this approach is that, in general, the small scatterer may be in the

presence of a larger scatterer conventionally handled in the FDTD. In this case, the incident field

on the small scatterer will have contributions from both the source and scattered field of the larger

object. For convenience, we refer to this "total" incident field simply as just the incident field,

which must be calculated at points on the PEC scatterer in the DM formulation of (4.51). Since

the object of interest is small and usually contained within one or a few FDTD cells, the fields

vary little in this region. In FDTD, each field component has four nodal points with respect to the

center of a cell in the electric field grid (see Fig. 4.7). A simple bi-linear interpolation of these

fields at points where the scatterer is located can provide a good approximation to the incident

field and is given by (4.55).
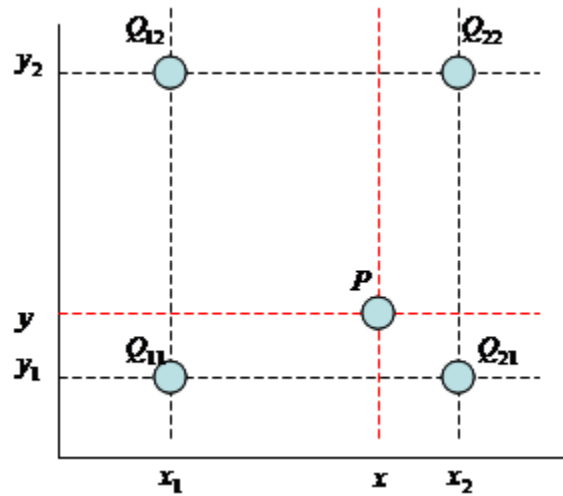
Fig. 4.7: Bilinear Interpolation.

$$f(x, y) \approx \frac{f(Q_{11})}{(x_2 - x_1)(y_2 - y_1)}(x_2 - x)(y_2 - y)$$

$$+ \frac{f(Q_{21})}{(x_2 - x_1)(y_2 - y_1)}(x - x_1)(y_2 - y)$$

$$+ \frac{f(Q_{12})}{(x_2 - x_1)(y_2 - y_1)}(x_2 - x)(y - y_1)$$

$$+ \frac{f(Q_{22})}{(x_2 - x_1)(y_2 - y_1)}(x - x_1)(y - y_1) \tag{4.55}$$

where Q_{ij} in this case would represent the E_z component and the subscripts relate to the position in the FDTD grid. A simple interchange of the coordinates yields the same interpolation scheme for the other electric field components.

Our next step is to find an appropriate updating scheme that will allow us to extract the incident field from the total field, which is calculated in the FDTD, in order to utilize it in the DM method. For the Electric Dipole Moment (EDM) located at cell (l, m, n), we seek to formulate a Total Field algorithm. For the *Total Field Formulation* (TFF) we need, for instance, $(Ez_{inc})^n_{l,m,n}$ to find $(Ez_{scat})^n_{l,m,n}$ and thus $(Ez_{total})^n_{l,m,n}$ to update $(Hy_{total})^{n+1/2}_{l+1/2,m,n+1/2}$. The steps involved in the implementation of this algorithm are presented below:

1) Assume we have found $(\vec{E}_{scat})^n_{l,m,n}$, $(\vec{E}_{total})^n_{l,m,n}$ and thus $(\vec{H}_{total})^{n+1/2}_{l+1/2,m,n+1/2}$.

2) Increment time to $n+1$.

3) *Update E field:*

If $(i, j, k) \neq (l, m, n)$

=>Update $\vec{E}^{n+1}_{total}$ conventional way

Else

$$\vec{E}_{inc}^{n+1} = \vec{E}_{total}^{n} - \vec{E}_{scatl}^{n} + \frac{\Delta t}{\varepsilon}\vec{\nabla}\times\vec{H}_{total}^{n+1/2} - \frac{\Delta t}{\varepsilon}\vec{\nabla}\times\vec{H}_{scat}^{n+1/2}$$

$$=> $$

$$= \vec{E}_{total}^{n} - \vec{E}_{scatl}^{n} + \frac{\Delta t}{\varepsilon}\vec{\nabla}\times\vec{H}_{total}^{n+1/2} - \left(\vec{E}_{scat}^{n+1} - \vec{E}_{scat}^{n}\right) \tag{4.56}$$

But near the EDM we know that $\dfrac{\partial\vec{E}_{scat}}{\partial t}\approx 0$, since the near-field has a quasi-static

behavior: consequently, the difference of the last two terms, appearing inside the parentheses in

the RHS of (4.56), can be neglected. Therefore, the update equation for the field at the cell

(l,m,n) becomes

$$\vec{E}_{inc}^{n+1} = \vec{E}_{total}^{n} - \vec{E}_{scatl}^{n} + \frac{\Delta t}{\varepsilon}\vec{\nabla}\times\vec{H}_{total}^{n+1/2} \tag{4.57}$$

     End If

4) Update $\left(\vec{E}_{scat}\right)_{l,m,n}^{n+1}$ and $\left(\vec{E}_{total}\right)_{l,m,n}^{n+1} = \left(\vec{E}_{incl}\right)_{l,m,n}^{n+1} + \left(\vec{E}_{scat}\right)_{l,m,n}^{n+1}$ using DM method for

    finding the EDM.

5) Increment time to $n + \dfrac{3}{2}$.

6) *Update H field:*

    Update as usual (no modification).

We now have a modified updating scheme that allows us to extract the incident field information

and only requires an updating of the total electric fields nearest the object contained within the

FDTD cell. Notice that this approach incorporates the known quasi-static scattered field, via the

DM method, and adds it to the incident field at the FDTD nodal points, thus avoiding any

complex contour path integration or the need to use auxiliary updating equations. Therein lies the

attractive feature of this proposed method and specifically, it is relatively simple to integrate into

existing FDTD codes.

4.4 Benchmark Examples

In this section we will present some tests that demonstrate how the FDTD can perform the analytic continuation of the quasi-static solution obtained for some simple geometries. Since many commercial codes are unable to handle features sizes that we are interested in, specifically objects with dimensions $<< \lambda/20$, we will compare the results with some analytical solutions. Our objective is, then, to gain confidence in the analytic continuation of the quasi-static fields performed by the FDTD, so that we may subsequently extend this hybrid technique to more complex geometries, which is the goal of our research.

4.4.1 Hybrid Method for Scattering by a small PEC sphere in a Lossless Dielectric Medium

For our first test case we simulated the scattering from a small PEC sphere with radius $a = \lambda_0/200$ in a lossless homogeneous dielectric medium with $\varepsilon_r = 4$. We excite the sphere with a time-harmonic, z-oriented point source operating at a frequency of 300 MHz. Although a plane wave excitation could have been used in this case, we take advantage of the fact that the wave front impinging on the sphere locally looks like a plane wave since the scatterer is small and we can avoid the complications presented by a plane-wave-source implementation in the FDTD. The point source was located $0.5\lambda_o$ away from the sphere and the backscattered field was calculated. The simulation setup is shown in Fig. 4.8 where the FDTD cell size was kept at the nominal value of $\lambda_d/20$, where λ_d is the wavelength in the dielectric medium. For comparison with the calculated results obtained by the hybrid method, we present the solution based on the Mie series and the equivalent electric dipole moment contribution.
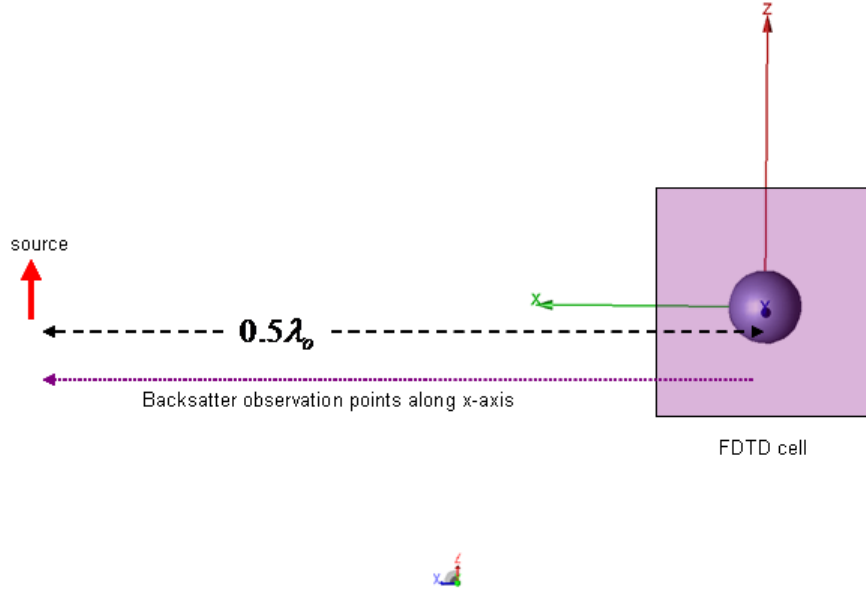
Fig. 4.8: Test geometry for calculating backscatter field from a PEC sphere in a lossless dielectric medium.

Figs. 4.9 and 4.10 clearly show that the results obtained with the hybrid method closely match those based on the Mie series. The results shown in Fig.4.9 show how the magnitude of the backscatter E_z component has taken the $1/r^3$ near field solution obtained from the DM solution for the PEC sphere and performed the analytic continuation of the near-fields into the region where the $1/r^2$ and $1/r$ terms dominate. Furthermore, the phase graphs shown in Fig. 4.10 demonstrate the dynamic behavior of the fields away from the sphere in the computational domain. In fact, we can conclude from these results that, given any dipole moment representation of an antenna in the transmit mode, we can construct the solution in the computational domain through a coupling of the quasi-static near fields to the FDTD grid.
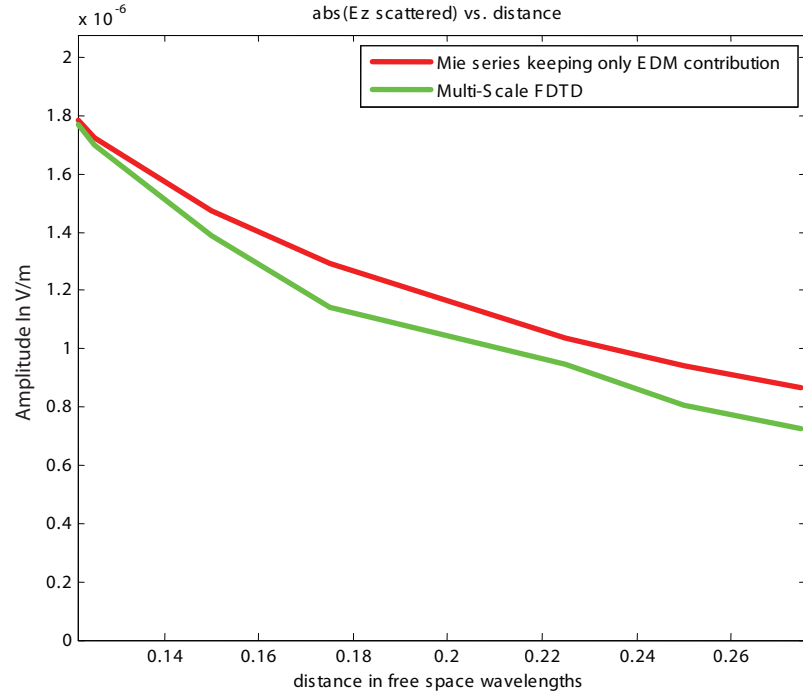
Fig. 4.9: Magnitude of the scattered E_z field versus distance for a PEC sphere in a lossless dielectric medium.
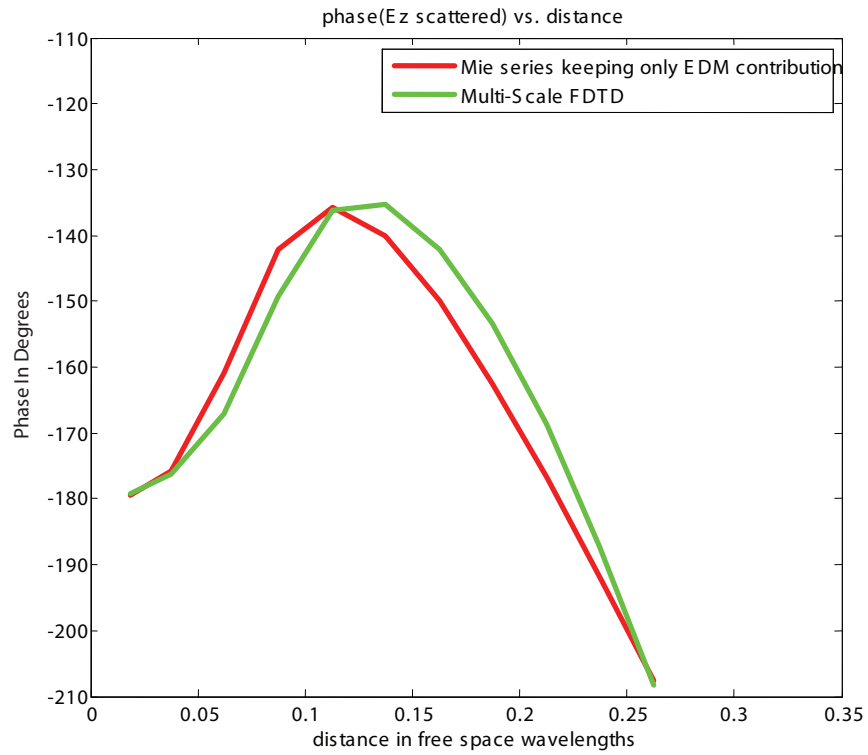
Fig. 4.10: Phase of the scattered E_z field versus distance for a PEC sphere in a lossless dielectric medium.

4.4.2 Hybrid Method for Scattering by a small PEC Sphere in a Lossy Dielectric Medium

One of the advantages of using the quasi-static results for small PEC sphere is that the solution for the scattered field is independent of the surrounding medium. This can be seen from (4.21) and (4.33) where the medium parameters cancel out in the expression for the scattered field. For this test case we choose the same setup as in Section 4.4.1, and consider a lossy medium whose parameters are $\varepsilon_r = 4$ and $\sigma = 0.5$. We again compare the results for this case with the Mie series solution for a plane wave incident on a sphere embedded in a lossy medium, and once again we only account for the electric dipole moment. As in the previous example for the lossless medium, we see an excellent agreement with the Mie series in Figs. 4.11 and 4.12 for the lossy medium case. The main difference in this result as compared to the lossless medium case can be seen in the graph for the phase variation of the backscattered E_z field.

Fig. 4.11: Magnitude of the scattered E_z field versus distance for a PEC sphere in a lossy dielectric medium.
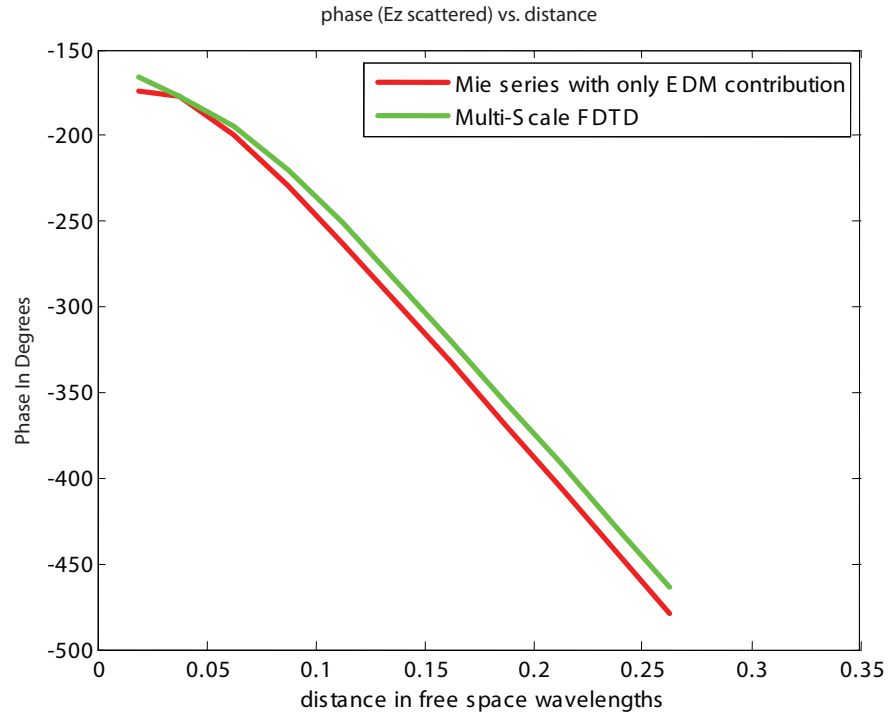
Fig. 4.12: Phase of the scattered E_z field versus distance for a PEC sphere in a lossy dielectric medium.

4.4.3 Hybrid Method for Scattering by Two Small Dielectric Spheres

For our next case, we consider the scattering from two dielectric spheres imbedded into the FDTD computational domain. Although our previous analyses were for PEC structures, and in particular PEC spheres, the dipole moment method can be generalized to dielectric structures equally well, using a methodology similar to the PEC case, and with little additional cost. The primary difference from the PEC case is that when dealing with dielectric structures we must remove the restriction imposed by a "preferred direction" and recognize that, in general, a dielectric sphere will contain three electric dipole moment representations, whose weights are determined by the polarization of the incident field. From the analytical solution (Mie series), it can be easily shown that for a dielectric sphere with arbitrary medium parameters we have both electric and magnetic dipole moment representations, given by

$$Il = E_o \frac{4\pi j}{\eta k^2} (ka)^3 \frac{\varepsilon_r - 1}{\varepsilon_r + 2} \tag{4.58}$$

$$kl = E_o \frac{4\pi j}{k^2} (ka)^3 \frac{\mu_r - 1}{\mu_r + 2}. \tag{4.59}$$

For the special case when $\mu_r = 1$ we have only the electric dipole moment present and the magnetic dipole moment contribution is exactly zero for all regions, near and far. Notice that the limits $\varepsilon_r \to \infty$ and $\mu_r \to 0$ yield the dipole moment representations for the small PEC sphere. Using this relationship we can go generalize the dipole moment method to composite structures, since the basic formulation for dielectric structures is a simple extension of the PEC case. The hybrid scheme for calculating the scattering by two dielectric spheres uses the relationship given in (4.58), although this time we must not assign a preferred direction since the incident field on each sphere will now be the summation of both the source contribution and the fields scattered by the other sphere. Furthermore, we must assign three electric dipole moments for each of the dielectric spheres. The simulation setup is shown in Fig. 4.13 where the source is the same as those in Sections 4.4.1-4.4.3, except it is now assumed to be y-polarized. The dielectric spheres have a radius of $\lambda_o/400$, where λ_o is the free space wavelength, and they are lossless with medium parameter $\varepsilon_r = 6$ .In this case the spheres were in adjacent FDTD cells and the backscattered electric field was once again computed by using the hybrid scheme.
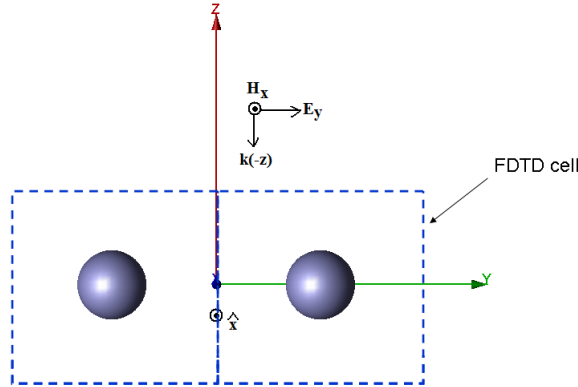
Fig. 4.13: The two dielectric spheres are λ/200 thick. They are placed at +/-λ/40 along Y. The fields are measured along Z passing through Y= - λ/40, from λ/20 to λ. Frequency of interest is 300 MHz. ε$_r$ = 6.

The results for the two sphere problem were compared with the T-matrix method (TMM) where the small radius approximation was made and thus it reduces to the DM method for separated dielectric spheres. The T-matrix method is a powerful tool that enables us to analyze several small discrete scatterers [38]. The results shown in Figs. 4.14 and 4.15 clearly demonstrate a close agreement with the TMM. Were we to try and model these spheres in a typical conformal FDTD (CFDTD) code the computational cost would be large. For example, in this case the computational domain was made to be $0.5\lambda \times 0.5\lambda \times 0.5\lambda$ (i.e., a relatively large domain size for the geometry of interest) but since no reduction in the FDTD cell size is required with the hybrid scheme the simulation time was less than 5 minutes. However, a simulation utilizing the conventional CFDTD for the same computational domain size and sphere radius would easily exceed 1 hour.
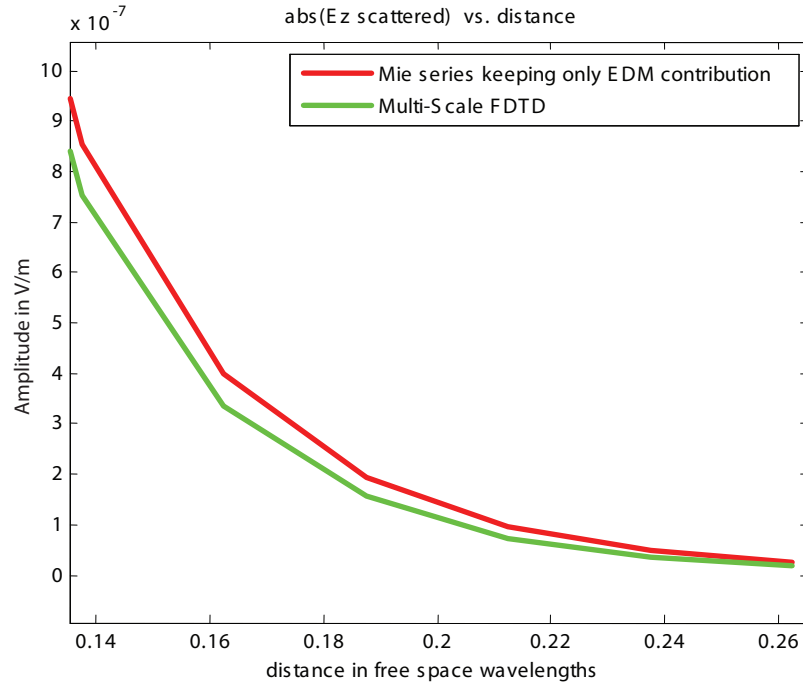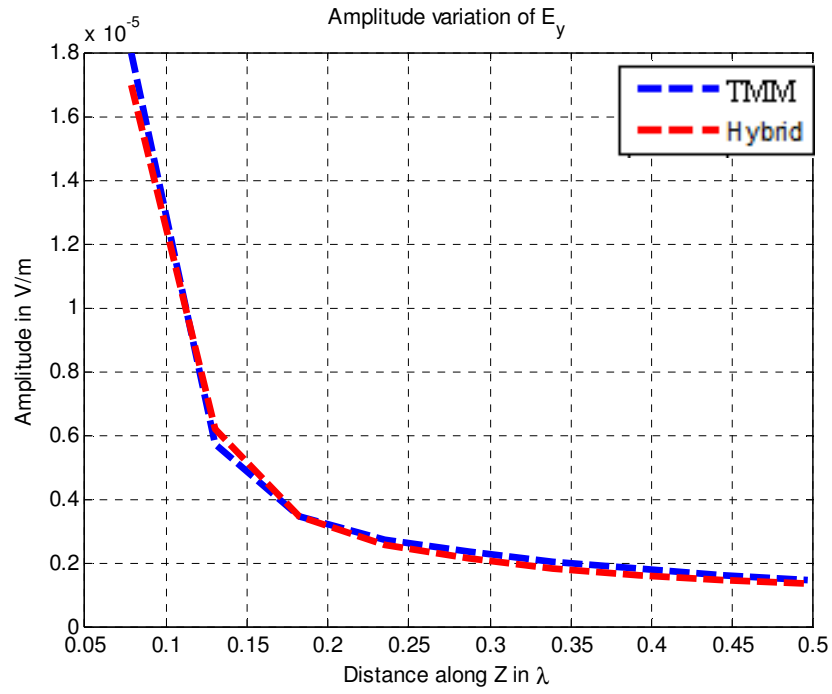
Fig. 4.14: Magnitude of the scattered E_y field versus distance for a two dielectric spheres.
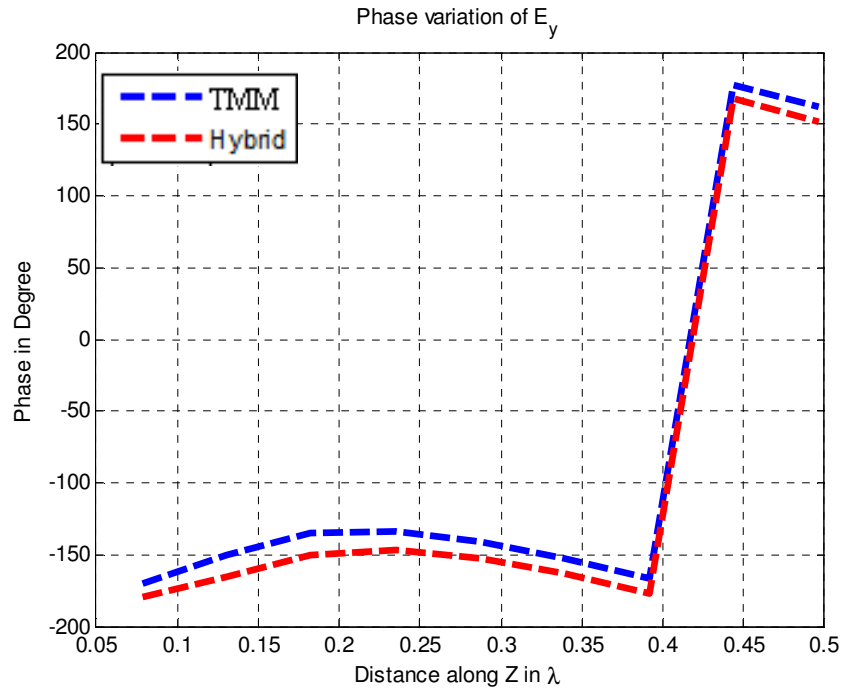
Fig: 4.15: Phase of the scattered E_y field versus distance for a two dielectric spheres.

4.4.4 Hybrid Method Applied to Slanted PEC Wire

The next example that we will consider is a small slanted PEC wire. The ability to model wire geometries that do not coincide with the FDTD mesh is an extremely beneficial feature of the hybrid method being proposed. For example, in BANs the human body model is fixed relative to the FDTD grid and any objects (e.g., antennas, sensors) that are desired to be conformal to the body must also conform to the FDTD mesh otherwise a crude staircase approximation must be made (see Fig. 4.16). This poses a severe restriction on the geometry of the simulation model for many types of configurations that are of practical interest. In Chapter 3 we used monopole antennas mounted on the human body phantom and we were forced to place the antennas where the body was locally planar so that the monopole conformed to the FDTD grid and to the surface of the phantom. In this section we show the results for the scattering by a small PEC $45°$ slanted wire with length $\lambda_o/30$ and wire radius $\lambda_o/200$ via the hybrid technique. The slanted wire confined to a single FDTD cell is shown in Fig. 4.17 and the source excitation is the same as that used in the previous sections.
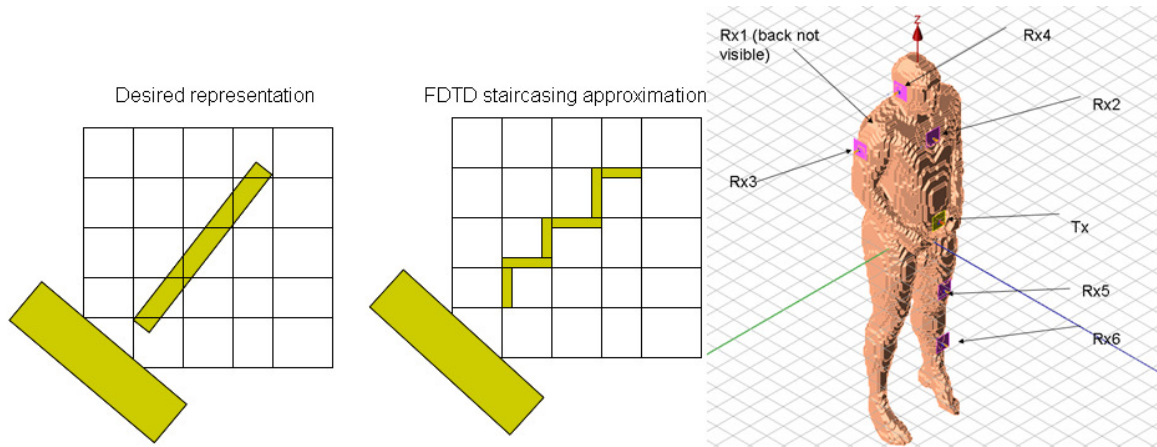
Fig. 4.16: Illustration of staircase approximation for slanted wires in FDTD.
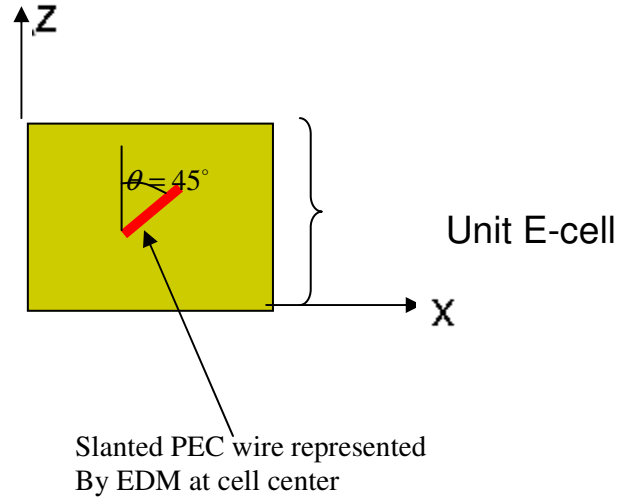
Fig. 4.17: A slanted PEC wire in a single FDTD cell.

In this case the full DM formulation was used to solve for the dipole moment distribution and the backscattered field was calculated. Since the wire length is smaller than the conventional segment size used in MoM (e.g., typically $\lambda_o/10$) the MoM matrix condition number was poor $(CN > O(10^3))$ and we are unable to compare directly with any available commercial codes suitable for thin wire structures. In any case, the main motivation here is to demonstrate the analytical continuation of the quasi-static field in FDTD and we will compare the validity of the DM method with MoM in later examples for which the matrix condition number was reasonable $(CN \approx O(10^2))$. To that extent we present the field patterns at $1.5\lambda_o$ for θ and ϕ cuts generated by the hybrid method (i.e., numerical results) and the DM method (i.e. analytical results including $1/r^3, 1/r^2, 1/r$ terms) directly as shown in Fig 4.18. Once again the results clearly demonstrate the analytic continuation of the quasi-static DM fields into the FDTD computational domain with the correct direction of maximum radiation for the tilted wire problem.

(a)

(b)
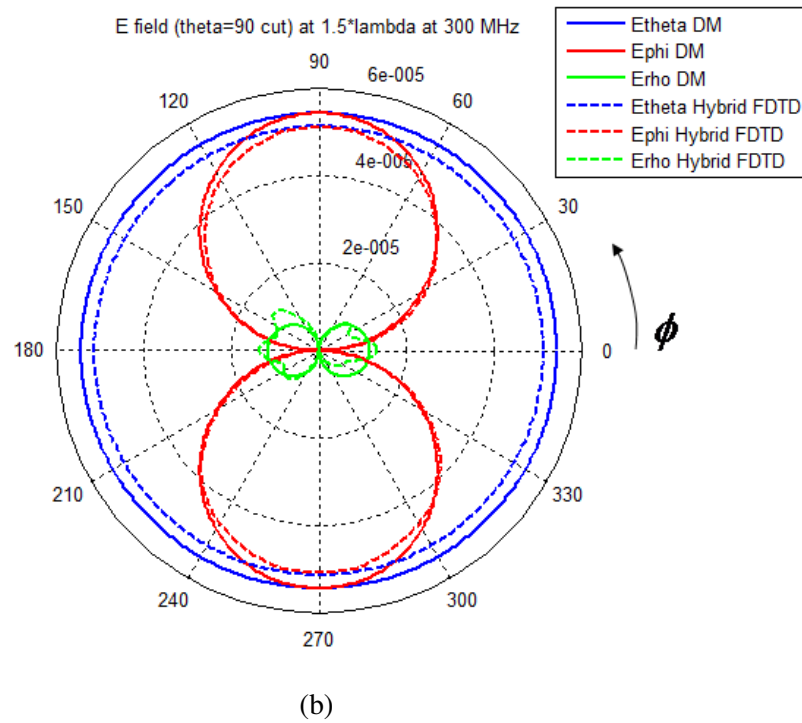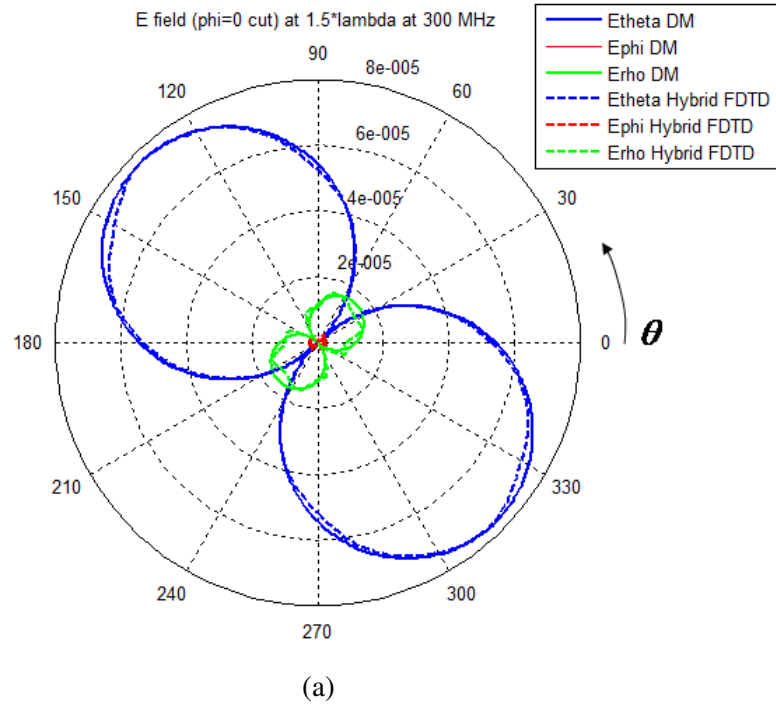
Fig. 4.18: Comparison of hybrid FDTD fields and the analytical DM solution for (a) E field $\phi = 0$ cut (b) E field $\theta = 90$ cut.

4.5 Hybrid Method for Complex Geometries

Thus far we have only considered simple test cases where the objects were confined within a single FDTD cell. However, the quasi-static approximation combined with the DM method can still be used for objects that penetrate multiple FDTD cells provided they continue to be small compared to the wavelength. In this section we will present some cases where the object is not confined to within a single FDTD cell and may extend to multiple cells as long as the quasi-static approximation is still accurate when we analyze the scattering from the object by using the DM approach. Furthermore, we have already seen that the FDTD can perform the analytic continuation given the near fields, and we wish to validate our results with some available commercial codes. To that extent, we have provided some comparisons with a popular commercial MoM code that is suitable for thin wire geometries.

4.5.1 Straight Wire in Multiple FDTD Cells

In this section we explain how to apply the hybrid technique to a straight PEC wire that is parallel with the z-axis and extends two FDTD cells. Once again the hybridization scheme requires us to solve for the dipole moment distribution for the entire wire structure. These dipole moments are then lumped together at the center of the FDTD cells where the aggregation depends on those portions of the wire that are contained within the respective cells, as shown in Fig. 4.19.
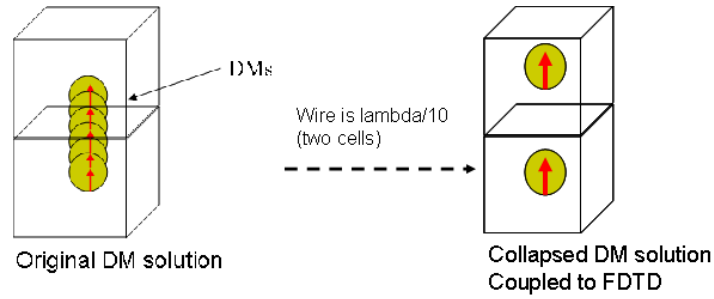
Fig. 4.19: The cell separation technique used to lump the DMs in the hybrid FDTD.

The source excitation, computational domain size, and cell size are the same as in previous sections. For this case, we have chosen a wire of length $\lambda_o/10$, with radius $a = \lambda_o/400$. Since the radius for this wire is very small, we have chosen to compare the computed hybrid results with MoM. The results for the backscattered field are shown in Figs. 4.20 and 4.21 where the agreement with MoM is within 10 percent even in the near to intermediate regions.
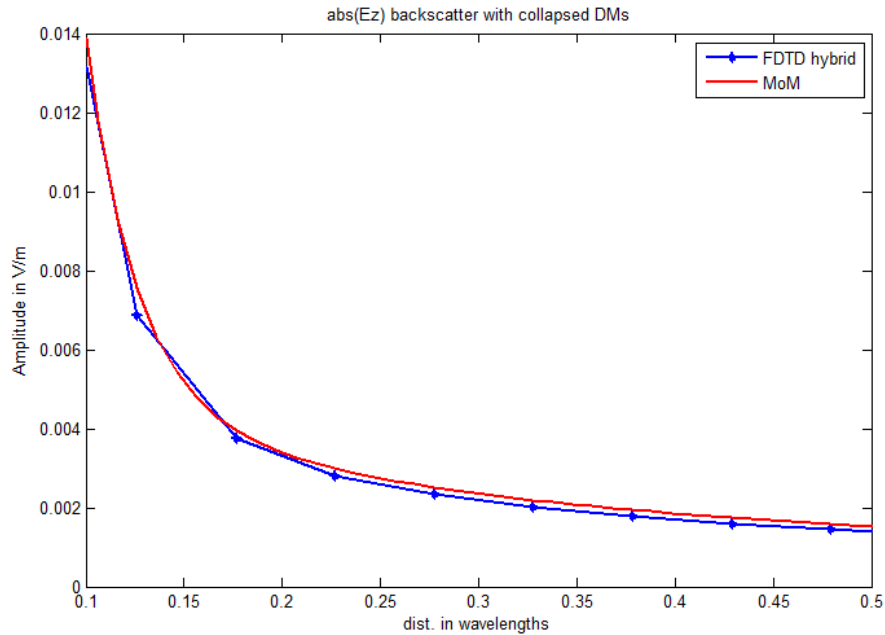
Fig. 4.20: Magnitude of the scattered E_z field versus distance for a $\lambda/10$ PEC wire at 300 MHz.
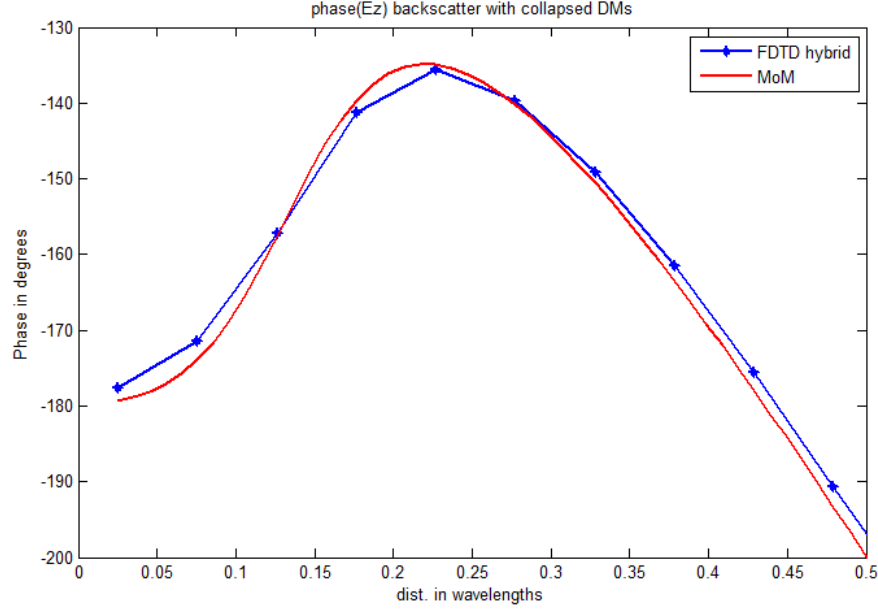
Fig. 4.21: Phase of the scattered E_z field versus distance for a $\lambda/10$ PEC wire at 300 MHz.

4.5.2 Helix Wire in Multiple FDTD Cells

In this section we extend the approach used for the straight wire passing through two FDTD cells to that of a helical wire scatterer. This geometry provides a good example for a case which is not amenable to accurate treatment in the conventional FDTD. The curved-wire helical scatterer is known to be problematic, even when we use the conformal FDTD method and accurate results are seldom reported for thin, curved wire geometries when Finite Methods are used. A typical wire helix scatterer is shown in Fig. 4.22, where the radius of the wire is $\lambda_o/1500$, and the radius of curvature is $\lambda_o/60$. The vertical length of the helix is $\lambda_o/12$ and it occupies two FDTD cells. The source excitation is a plane wave with the electric field z-polarized and traveling along the x-axis at 300 MHz. In contrast to all the previous examples we have looked at, the

helical scatterer will generally have dipole moments oriented along the three principal axes.

Therefore, its lumped representation will have $x-$, $y-$, and $z-$ oriented dipole moments.
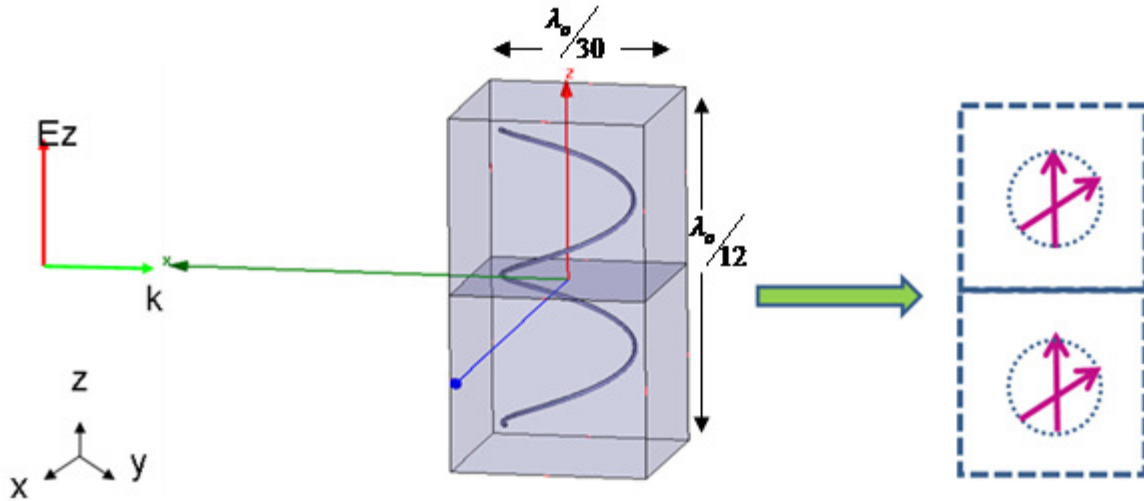
Fig. 4.22: A helical scatterer in two FDTD cells and its DM representation.

Using the DM method and the hybridization scheme we have computed the near fields on the radiation sphere at a distance of 0.5λ away from the scatterer and the backscatterer field variation versus distance. The reason for plotting the near fields is that many applications (e.g., medical sensors, implants) require knowledge of these quantities for analyzing sensing and coupling phenomena. The results using the hybrid DM FDTD and the regular DM method have been compared with simulations performed by using the standard MoM and are shown in Figs. 4.23 and 4.24. We note that there is close agreement between the results from the MoM solution and the hybrid scheme, though there are some slight differences as expected when two entirely different algorithms are used to solve the same problem. The important thing to realize is that the hybrid method is an approximation that allows us to model the helical scatterer, which cannot be handled by using the conventional FDTD, and this is a distinct improvement.
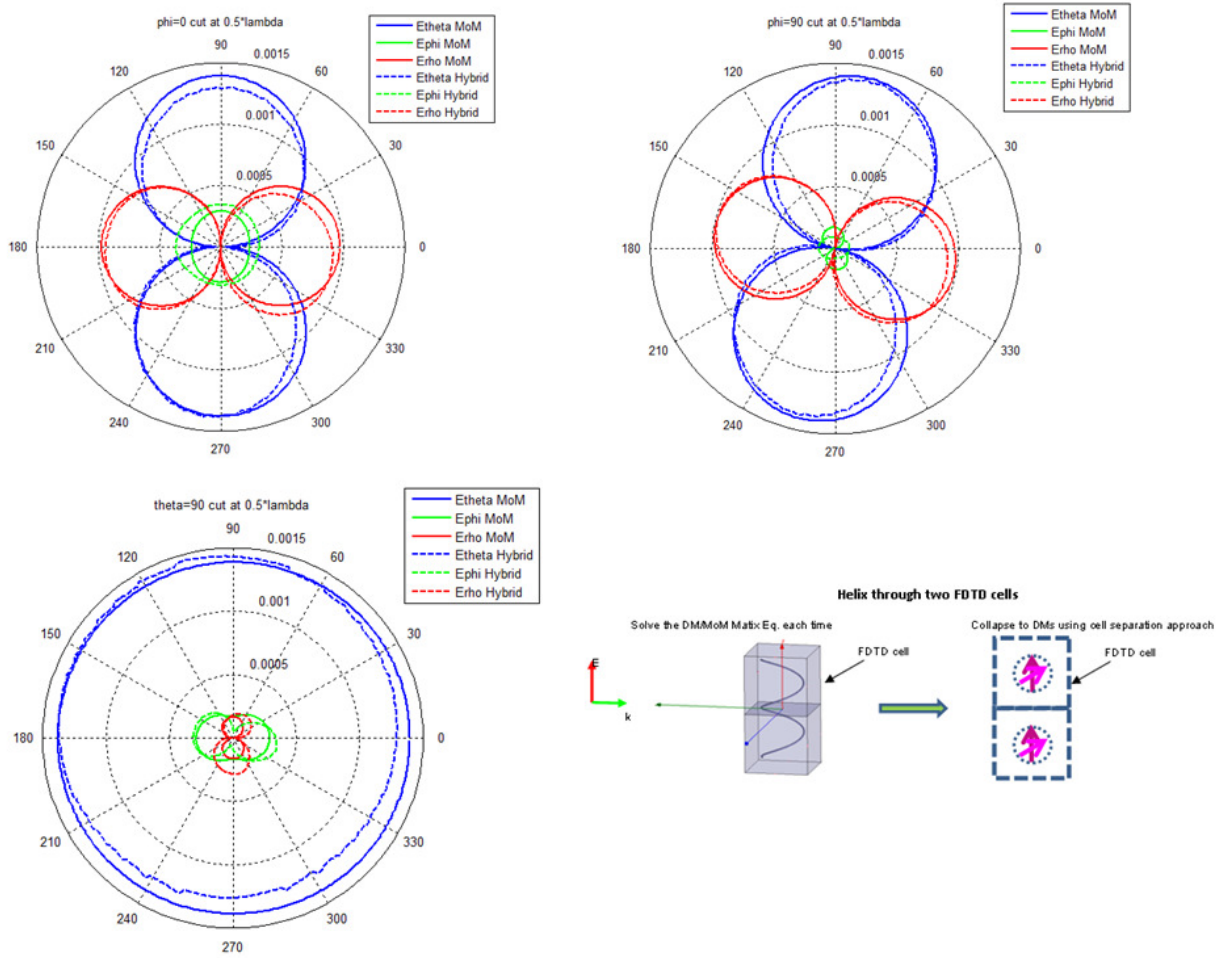
Fig. 4.23: E-field patterns for the principal plane cuts using hybrid FDTD and MoM.
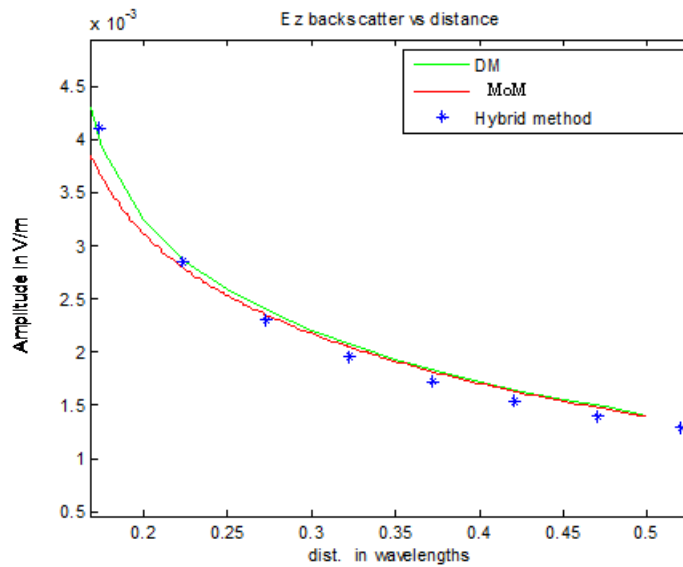
Fig. 4.24: Magnitude of the scattered E_z field versus distance for the helical scatterer using DM, MoM, and the hybrid FDTD at 300 MHz.

4.5.3 Short Dipole Antenna

In many cases, the small object of interest is a transmitting element rather than a scatterer. The dipole moment method for scattering by objects can be easily extended to the transmitting case by impressing a voltage source at the terminals of the antenna. This approach follows the same methodology as in conventional MoM formulations. Specifically, we discretized the wire geometry using the DM representation and define a voltage source along those elements that comprise the feed gap region. To illustrate the transmitting case we consider a dipole extending through four FDTD cells for a total length of $\lambda_o/5$ and aligned with the z-axis was considered. The wire radius of the dipole was $\lambda_o/400$ and it was located within the center of the FDTD cell, thus, making it a suitable test geometry for our multi-scale method. Notice that in this case the dipole penetrates several FDTD cells, and we must consider whether the quasi-static analysis is valid for this size geometry. It is known that the current distribution on the dipole is triangular for very short dipoles and becomes a sinusoidal distribution as the electrical length approaches $\lambda_o/2$, at which point the antenna becomes a resonant structure. It has been found that the quasi-static DM method can accurately calculate the current distribution when the antenna is smaller than its resonant length, and we can use this approach even for wire geometries extending several FDTD cells. A dipole antenna located in the FDTD mesh is shown pictorially in Fig. 4.25, along with the voltage gap excitation of 1 Volt at 300 MHz and its lumped DM representation required for the hybrid scheme.
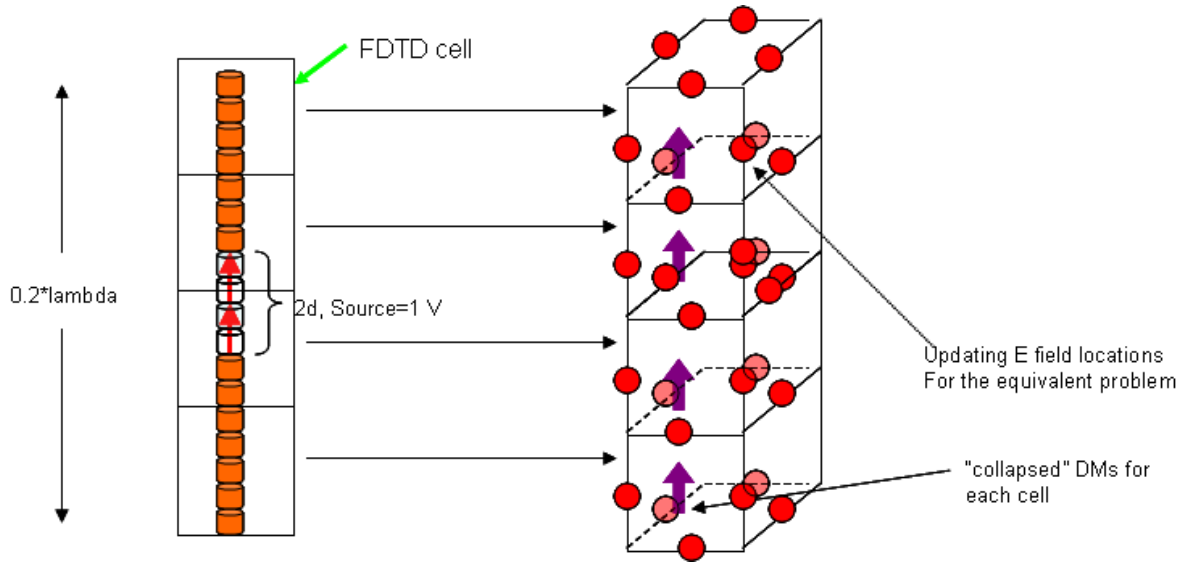
Fig. 4.25: The cell separation technique used to lump the DMs in the hybrid FDTD for a short dipole occupying four FDTD cells.

The hybrid FDTD was used for this dipole antenna and the near field pattern at 0.5λ was computed. In addition, it has been found that a calibration factor of 2 is necessary to couple the fields to the FDTD for transmitting cases when using the hybrid scheme. For comparison we simulated the same dipole antenna in MoM, and ensured that the defined voltage gap was the same as in the DM method. The results are shown in Fig. 4.26 for the $\phi=0$ cut and the other principal cuts are omitted due to the symmetry of the dipole antenna. Once again, we see that the hybrid FDTD matches the MoM results very well (within ten percent) with some slight differences for both components of the electric field.
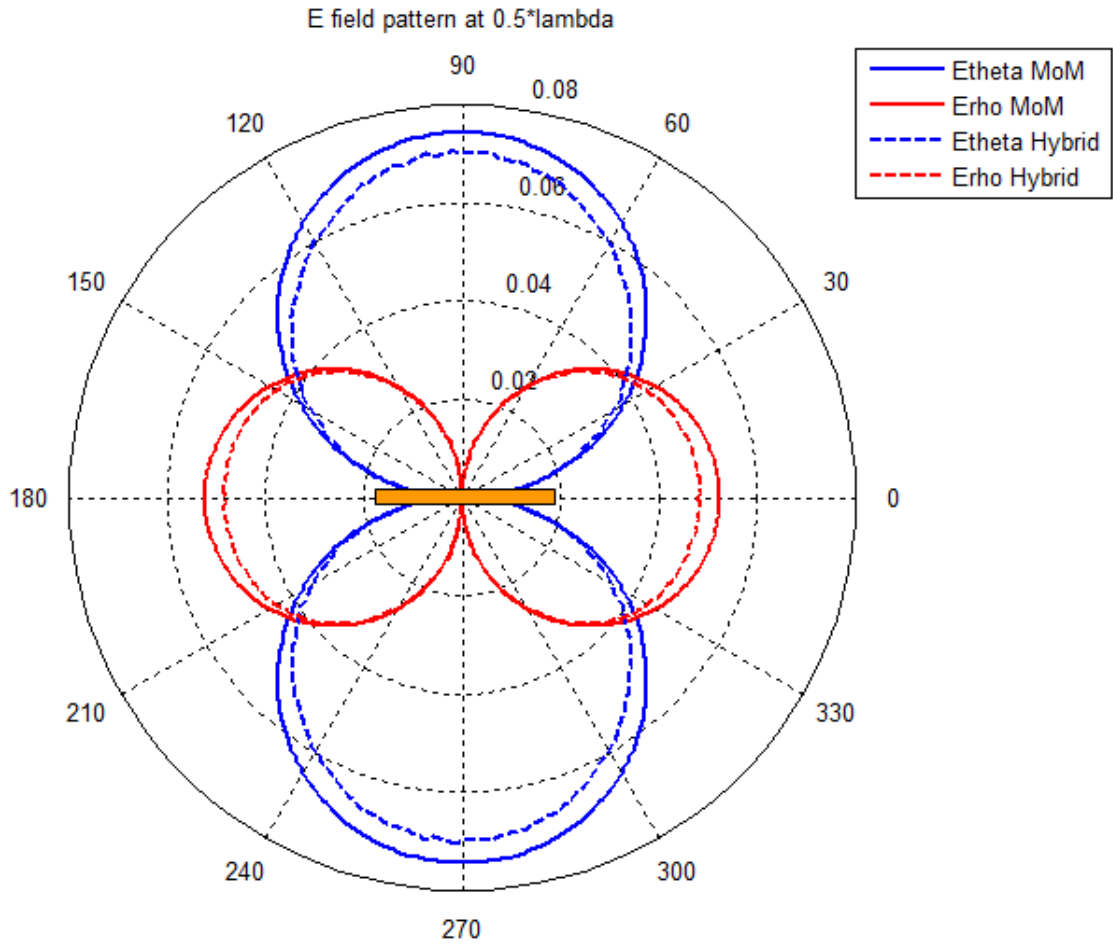
Fig. 4.26: E-field patterns for the $\phi = 0$ cut using hybrid FDTD and MoM.

4.5.4 Short Monopole Antenna

For the transmitting case we are often times interested in the input impedance of the antenna. We will now proceed to test if the DM formulation along with its hybridization in FDTD can accurately determine the terminal parameters. Towards this end, we have chosen to apply the hybrid technique to the case of a short monopole antenna operating in the transmit case. The

methodology follows that of the dipole case with some additional modifications. Specifically, since the monopole typically operates above a ground plane, this additional feature must be accounted for in the hybrid scheme. The approach taken to model this antenna utilizes the principle of images. In practice, the ground plane will be finite and the image theory will only provide an approximation to the correct solution. However, this approximation can be very accurate if the ground plane is sufficiently large. The approach we follow is then described as follows: 1) Solve for the DM distribution of the monopole using images, which is tantamount to solving the dipole problem: 2) Lump the DMs into their respective FDTD cell centers and only update the fields above the ground plane: 3) Let these DMs radiate in the presence of the ground plane which has been defined in the conventional FDTD algorithm. The procedure is shown pictorially in Fig. 4.27.
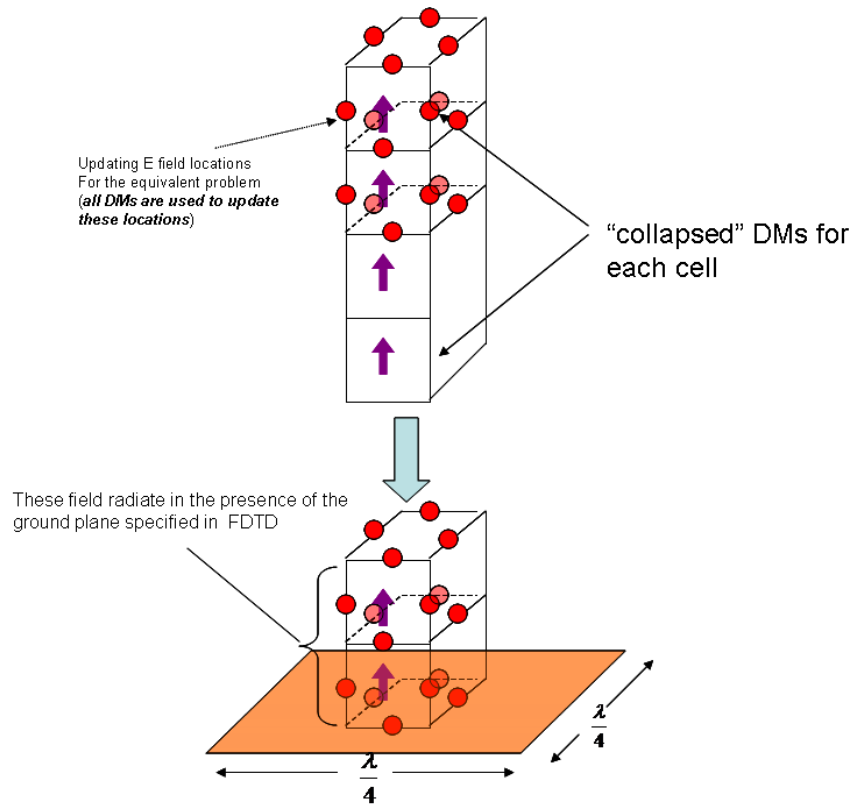
Fig. 4.27: DM representation in the hybrid FDTD for the monopole using image theory approximation.

The monopole geometry is shown in Fig. 4.28, where the monopole extends over two

FDTD cells (i.e., $\lambda_o/10$), and has a wire radius of $\lambda_o/400$. In addition, the source is 1 Volt at a

frequency of 300 MHz. For this case, we have chosen a square ground plane whose length is

$\lambda_o/4$ on each side.
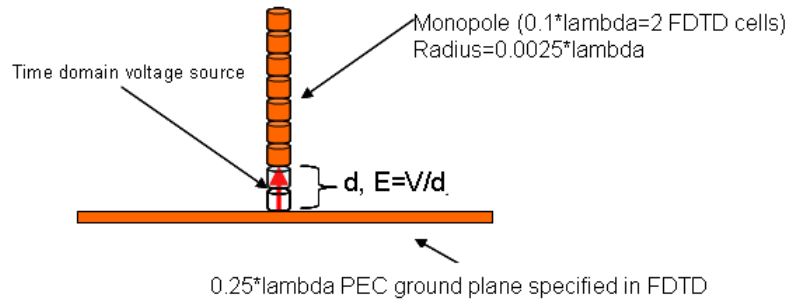
Fig. 4.28: Monopole geometry used in the hybrid FDTD.

For the geometry in Fig. 4.28 the current distribution obtained with the DM method is

compared with the results calculated from MoM, as shown in Fig. 4.29. It is evident that the DM

method is a novel technique for calculating the current distribution and results are in excellent

agreement with MoM.
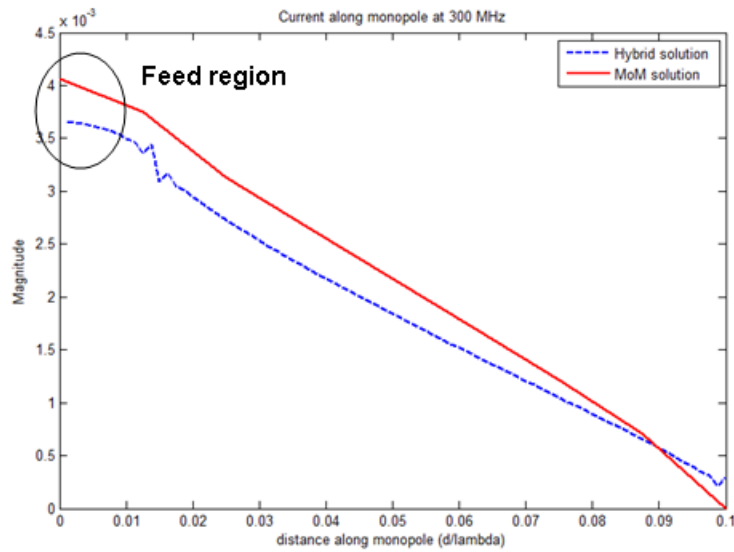
Fig. 4.29: Current distribution obtained by the DM method and MoM for the monopole.

As in previous examples, we have plotted the near fields in Fig. 4.30 at 0.5λ away from the monopole and the results are compared with those obtained from MoM. Similar to the dipole case, only the $\phi=0$ cut is shown due to the symmetry of the monopole and ground plane geometry. The results indicate that applying the image theory method to this configuration is a very good approximation and the effect of the finite ground plane is clearly visible in the backside radiation (i.e., $\theta=180°$).
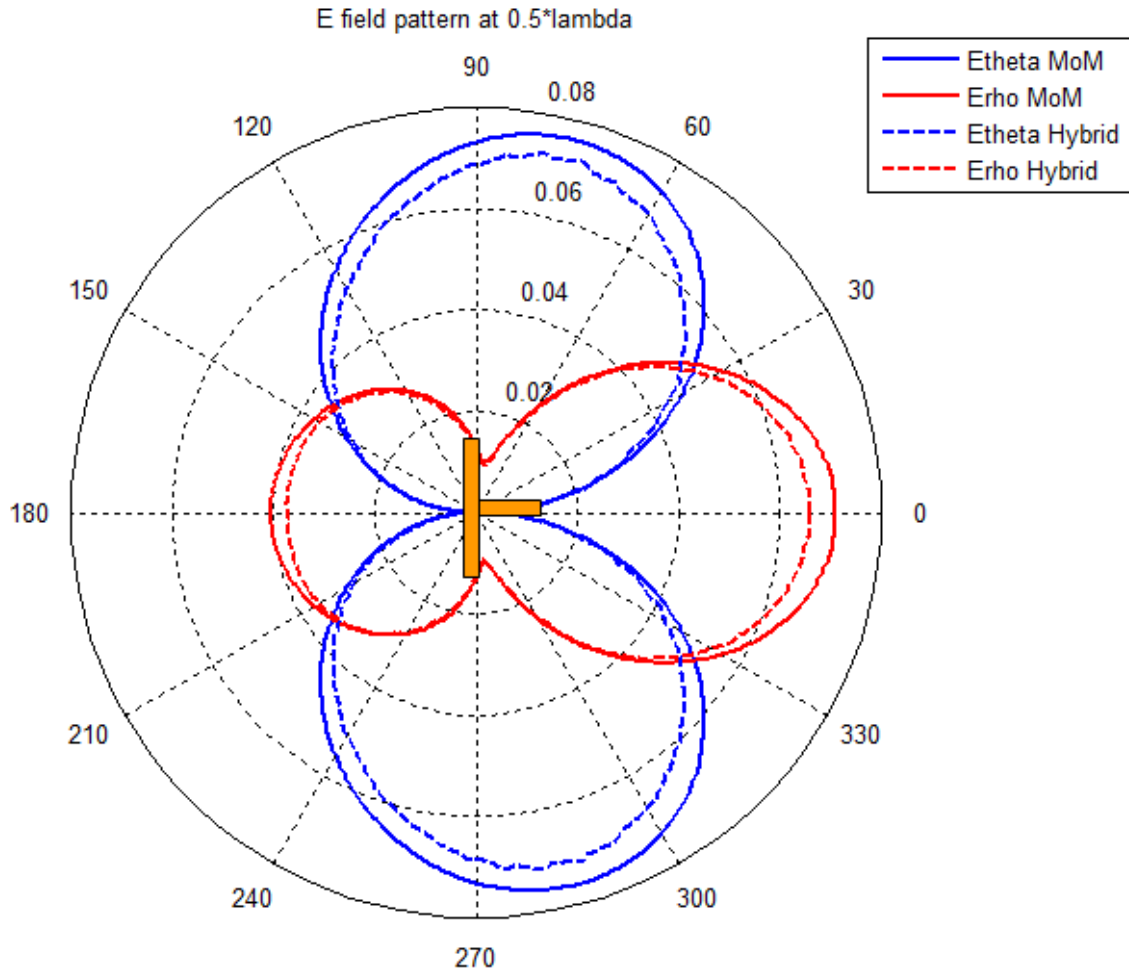
Fig. 4.30: E-field patterns for the $\phi=0$ cut using hybrid FDTD and MoM.

With the current distribution obtained from the DM method and the known source voltage, it is possible to calculate the input impedance of the short monopole antenna. However, we should mention that the feed model in different codes (i.e., MoM, FDTD, FEM) can give very different results, especially for the reactance calculation. This is primarily due to the nature of the feed structure with the numerical technique used. Furthermore, we should expect some differences between different numerical codes and, indeed, this has been reported in the literature [39]. In MoM the feed structure is typically a voltage feed gap feed and it becomes difficult to exactly relate this source model to other numerical approaches. A key point worth making is that we are dealing with electrically small geometries and as a result the MoM impedance matrix can become very ill-conditioned leading to comparisons that can be inconclusive. In any case, we have performed the impedance calculation from the DM solution obtained in the hybrid technique and compared the results to that of MoM, as shown in Figs. 4.31 and 4.32. The agreement between the DM method and MoM is seen to be good for the input impedance with some differences for both the real and imaginary parts.
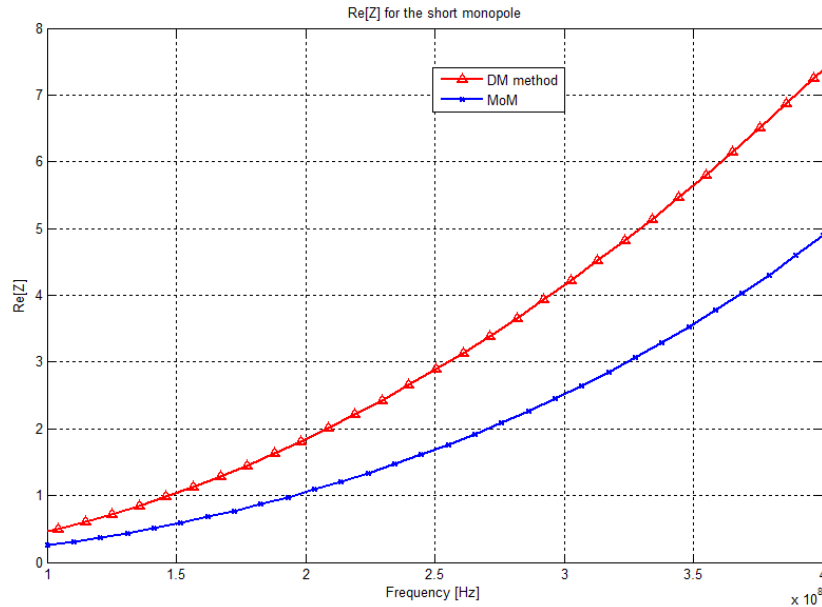
Fig. 4.31: Real part of the input impedance for the monopole.
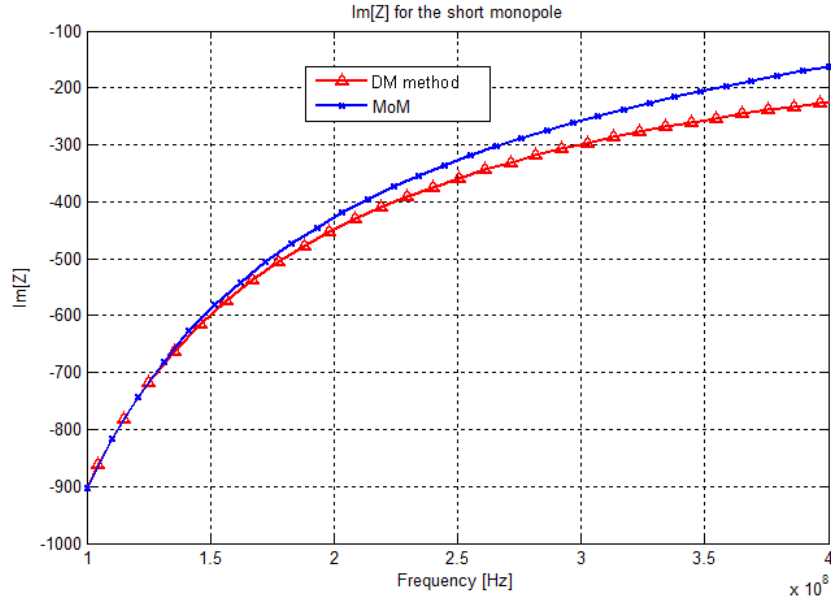
Fig. 4.32: Imaginary part of the input impedance for the monopole.

4.5.5 Thick Patch Antenna

The methodology used for the monopole antenna can also be applied to simple feed models for patch antennas. In this case the wire feeding element plays the role of a probe feed. This model is commonly used for numerical simulations because it is simple to implement in a variety of codes. Furthermore, it reduces the complexity of modeling the coaxial portion of the feeding structure and has been found to give reasonably accurate results [39]. Expanding on the approach for the monopole antenna we have modeled a thick patch antenna with the dielectric substrate material being that of air (i.e., $\varepsilon_r = 1$) for simplicity. The vertical thickness is two FDTD cells (i.e., $\lambda_o/10$) and the rectangular patch has dimensions of $0.5\lambda_o \times 0.25\lambda_o$ at 300 MHz. The pin feed is modeled via the hybrid FDTD method in the same fashion as the monopole case for a wire radius of $\lambda_o/400$ and is offset from the patch center by $0.075\lambda_o$. The geometry is pictorially shown in Fig. 4.33 with the square ground plane of length λ_o on each side.

rectangular patch 0.5*lambda
At 300 MHz

Pin feed: V=1 volt/m
(height=0.1*lambda -> 2 cells)

Square Gnd 1*lambda at 300 MHz
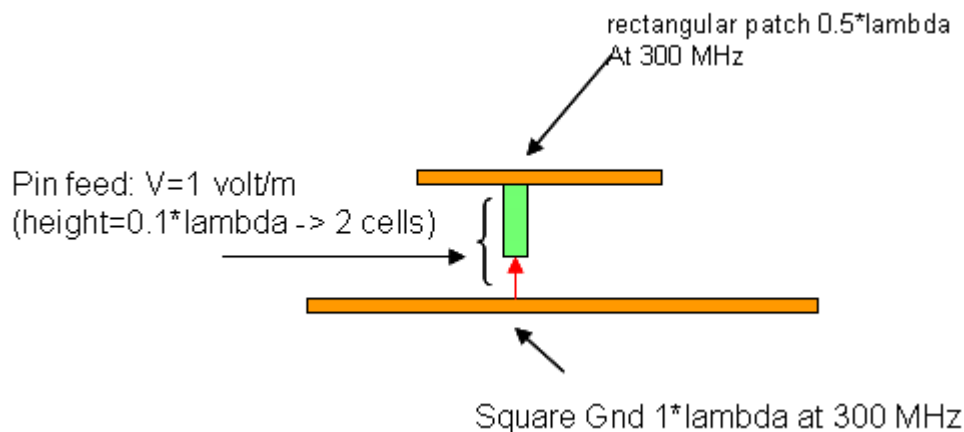
Fig. 4.33: A rectangular thick patch antenna and probe feed simulated using the hybrid FDTD.

The resonant behavior of the patch antenna is well understood and the fields underneath the patch can be approximated by an eigenmode analysis of a cavity with PMC walls. However, because the patch we have chosen to model is intentionally thick, there will be a loading effect on the input impedance from the wire feed and we can expect that the reactance will not go to zero at the frequency predicted by the cavity model. Indeed, this was verified and the results for the input impedance using the compensated feed-model hybrid FDTD was compared with those obtained by a commercially available MoM (Feko) , and FDTD (GEMS) codes and are shown in Figs. 4.34-4.35. It is evident that there is reasonably good agreement between all three approaches. Furthermore, as in many cases, the results from the various codes exhibit some differences due to the feed model. Finally, using the hybrid FDTD method results in considerable time-savings, provided the feed model compensation is made. The time-savings comes from the fact that in the hybrid method we are not required to mesh the fine feature of the probe feed whereas this must be done in GEMS to accurately model the fine features of the above feed.
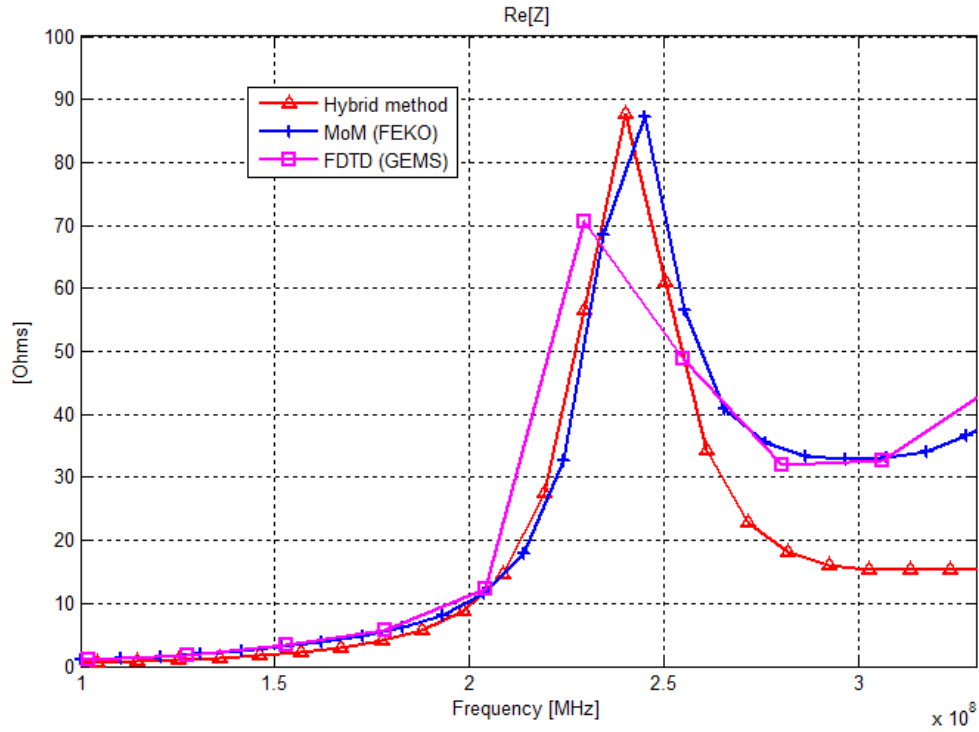
Fig. 4.34: Real part of the input impedance of the probe fed patch using the hybrid method, MoM (FEKO), and the conventional FDTD (GEMS).
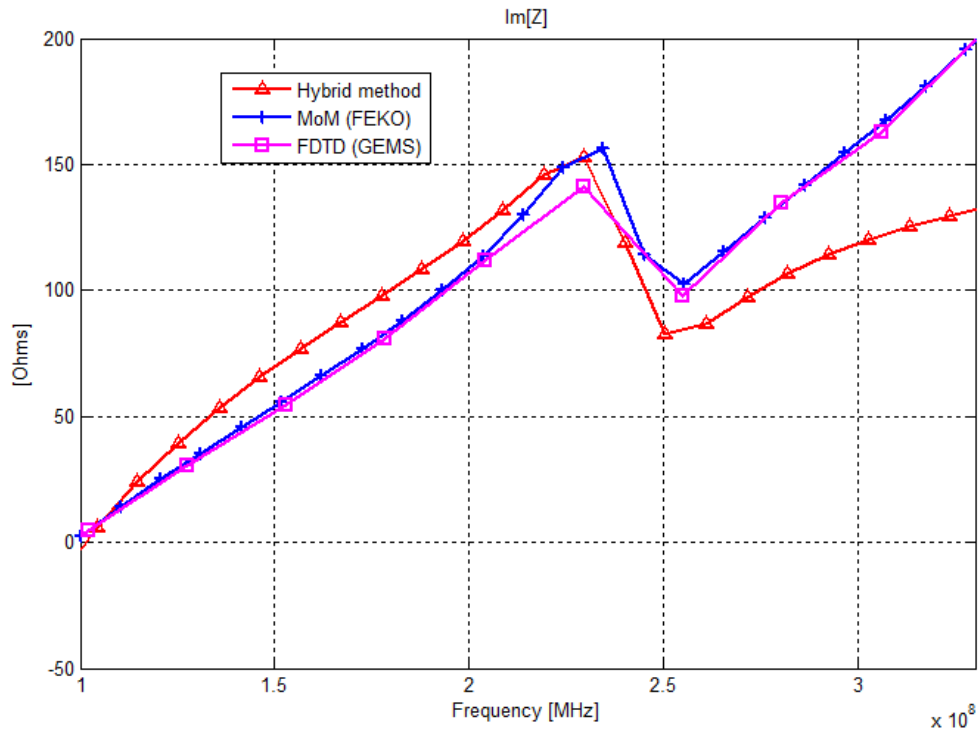
Fig. 4.35: Imaginary part of the input impedance of the probe fed patch using the hybrid method with feed model compensation, MoM (FEKO), and the conventional FDTD (GEMS).

4.5.6 Coated Wire

Thus far we have only hybridized the DM approach with the FDTD for PEC scatterers and antenna geometries. In many applications, such small geometries have the additional feature of thin dielectric coatings. This can be the case for medical implants where the dielectric coating plays the role of separating the radiating device from direct contact with human tissue. It is possible to formulate a DM approach for integrated structures containing both dielectric and PEC materials. However, a simpler approach is to reformulate the DM method from the scattering behavior of a small coated PEC sphere. The Mie series for a dielectric coated PEC sphere can be found in Appendix B and a parametric study of the spatial dependence of the near field at 1 GHz for various coating thicknesses and dielectric constants, given that the PEC spherical core has radius $\lambda_o/200$, was performed. The results for the backscattered field, which is E_θ in this case and corresponds to an x-polarized incident field, based on the Mie series is shown for three coating thicknesses and compared to the same sphere when the coating is occupied by PEC. The three cases are shown in Fig. 4.36a-c for coating thicknesses of $\delta = \lambda_o/100$, $\delta = \lambda_o/20$, and $\delta = \lambda_o/10$, respectively. Furthermore, the dielectric constant in each case was varied. It is known that the near field of the small PEC sphere varies as $1/r^3$, and one should expect that the dielectric coated sphere to exhibit a similar behavior. Indeed, this is exactly what is found to be the case, and the results presented in Figs. 4.36a-c suggest that the scattered near fields produced by a small dielectric coated PEC sphere can be modeled simply as a PEC sphere, but with a larger effective radius than the original spherical PEC core.
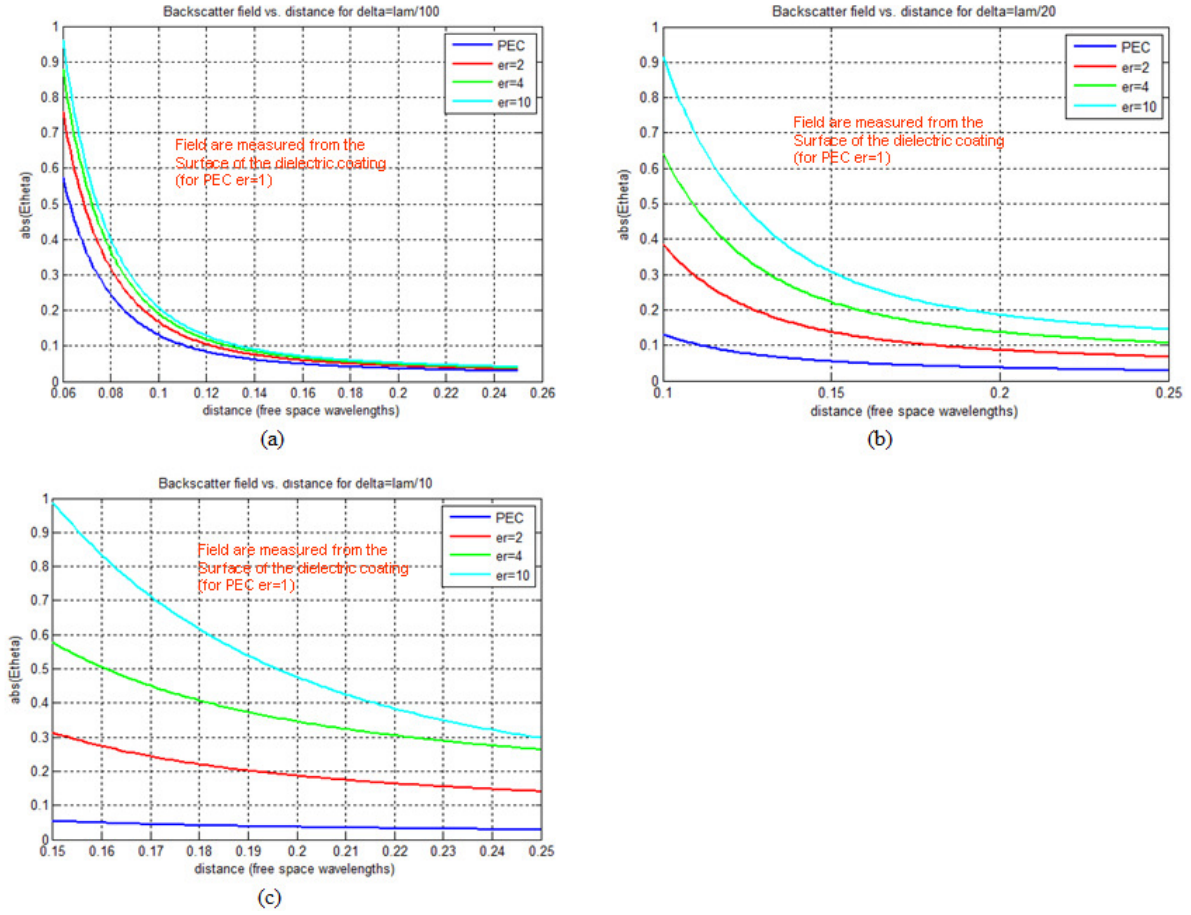
Fig. 4.36: Electric field in the near region for a coated PEC sphere with coating thickness (a) $\lambda_o/100$ (b) $\lambda_o/20$ and (c) $\lambda_o/10$.

In order to test our hypothesis regarding the effective radius concept we have performed a numerical experiment for a specific PEC spherical core and dielectric coating thickness. The frequency of interest is 1 GHz and the PEC core radius is again $\lambda_o/200$ with a dielectric coating of $\delta = \lambda_o/80$ and $\varepsilon_r = 4$. Notice that in this case the coating thickness is larger than the PEC core radius. The backscattered field, namely E_θ, was calculated from the Mie series solution and we hypothesize is that in the backscatter direction ($\theta = 0$) the near field can be written as

$$E_\theta = E_o \left(\frac{a_{eff}}{r} \right)^3 \qquad . \qquad (4.60)$$

The Mie series solution and the functional form of (4.60) was plotted versus distance R on a log-log graph in order to find the parameter a_{eff}. The results are shown in Fig. 4.37 from which it was determined that $a_{eff} = 0.014\lambda_o$.
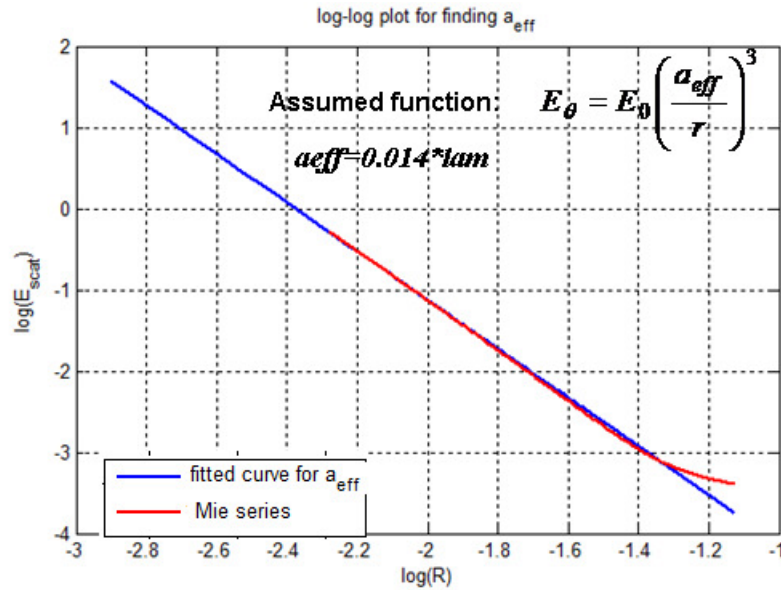
Fig. 4.37: Curve-fitting the electric near field of the coated PEC sphere based on the effective radius and DM concept.

The result for a_{eff} can now be simply used the DM formulation that we have already developed. To demonstrate this, we now proceed to simulate a simple coated wire using the hybrid FDTD method, where the PEC core and coating thickness are unchanged from the coated sphere previously considered. The geometry of the coated wire is shown in Fig. 4.38, and it has a length of $\lambda_o/10$ which extends across two FDTD cells and the discretization of the coated wire is

$\Delta = 0.8a_{eff}$. The test setup consists of a z-polarized plane wave incident on the wire and the backscattered field was computed. In order to compare our results using the hybrid FDTD, we have plotted it alongside data obtained from a commercially available MoM code (FEKO). The results are shown in Fig. 4.39 where the agreement is seen to be excellent.
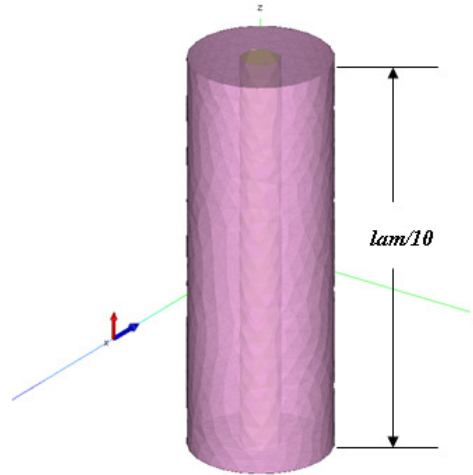
Fig. 4.38: A coated PEC wire simulated using the hybrid FDTD.
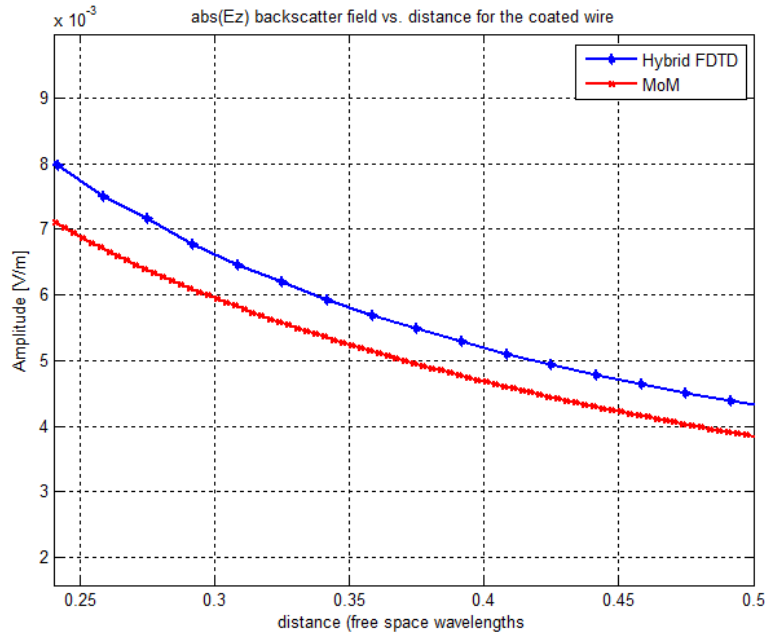
Fig. 4.39: Magnitude of the scattered E_z field versus distance for a $\lambda/10$ coated PEC wire at 1 GHz.

4.5.7 Scattering From A PEC Loop

The PEC loop is a special geometry that cannot be similarly handled by the previous approach used for hybridization with FDTD. The reason for this is due to the fact that the magnetic vector potential term is dominant for this structure and the near fields are in effect quasi-magnetostatic. Since the DM method previously described is useful for structures in which the near fields are primarily quasi-electrostatic, we must find an alternative approach for hybridizing small PEC loops in the FDTD. One way to circumvent this apparent obstacle is to observe the relationship between a small loop carrying an electric current and its magnetic dipole moment equivalent. Consider a small PEC loop with radius a carrying a current I. Then it is well known that the fields produced by this current carrying loop are equivalent to those from a magnetic dipole moment given by

$$kl = j\omega\mu IS .\tag{4.61}$$

where $S = \pi a^2$ (i.e., the area of the loop). It can be shown that using the relationship for the fields produced by magnetic dipole moments in accordance with (4.61) give rise to magnetic near fields that are quasi-static whereas the electric fields are not. In fact, if we consider the dual problem of the scattering from a PEC sphere, namely that of the scattering from a PMC sphere, it can be shown that the induced magnetic dipole moment is given by

$$kl = j\omega 4\pi\mu a^3 H_o\tag{4.62}$$

where H_o is the incident magnetic field. The difference between (4.61) and (4.62) is based on the nature of the problems analyzed. The result obtained in (4.61) is based on the assumption that the current I is known (i.e., the transmitting case). In contrast, the result given in (4.62) is based on the scattering properties of the PMC sphere. Since the result in (4.62) must represent some equivalent PEC loop where the current is induced by the incident magnetic field, there must exist

some effective radius a_{sphere} that relates (4.61) to (4.62). Therefore, a series of numerical

experiments were carried out to determine the relationship between the induced current I^{ind} and

the incident magnetic field H_o from which we can extract the relationship between a_{sphere}

and a_{loop}.

The numerical test setup consists of a circular PEC loop with radius a_{loop} in the x-y plane

excited by an incident plane wave with $H_o = 1$ A/m polarized perpendicular to the surface area

of the loop at 1 GHz. The simulation was performed using MoM and the induced current was

plotted versus loop radius (in wavelengths). The loop radius was restricted to be small relative to

the wavelength so that it would fit inside at most two FDTD cells. However, for very small loops

the MoM matrix condition number became poor (e.g., $O(10^3)$). Using these data we have

attempted to fit a linear relationship for the induced current as a function of the loop radius and

incident magnetic field. This functional relationship is given by

$$I^{ind} \approx \frac{2a_{loop}}{\pi} \vec{H}_o \cdot \hat{a}_{surface} \qquad (4.63)$$

where $\hat{a}_{surface}$ is the unit vector perpendicular to the loop. From this it can be shown that the

induced magnetic dipole moment equivalent is given by

$$kl = j\omega\mu I^{ind} S = j\omega\mu 2a_{loop}^3 H_o \quad . \qquad (4.64)$$

Comparing (4.64) with the PMC sphere magnetic dipole moment given in (4.62), we can

establish the equivalency: $a_{sphere} = (2\pi)^{-1/3} a_{loop} \approx 0.54 a_{loop}$. The results from MoM are plotted in

Fig. 4.40 along with the expression found in (4.63), which we have termed the PMC-sphere-

equivalent to an electric current loop. In addition, the MoM matrix condition numbers (given in

Fig. 4.40 as CN) are included to demonstrate where the numerical simulations fail to accurately

predict the current in the loop. Once the equivalent magnetic dipole moment is known as a

function of the incident magnetic field, it becomes straightforward to implement the scattering of

a small PEC loop into the hybrid FDTD scheme by applying duality to all the modified update

equations. Thus, it will be the scattered magnetic fields that will be updated in the FDTD and the

procedure is exactly the same as those for the electric dipole moments. Therefore, we have used

the hybrid FDTD method to calculate the backscattered electric field (only E_ϕ is present for a

loop in the x-y plane) from a small PEC loop with radius $a_{loop} = \lambda_o/20$ (i.e. the loop occupies

multiple FDTD cells) at 1 GHz, as shown in Fig. 4.41 (normalized with respect to the incident

electric field), and compared it to the theoretical expression given that we have already found the

current distribution in the loop using MoM. Clearly, the agreement in Fig. 4.41 suggests that

using the magnetic dipole moment approach is useful for simulating small PEC loop structures in

the hybridized FDTD algorithm.
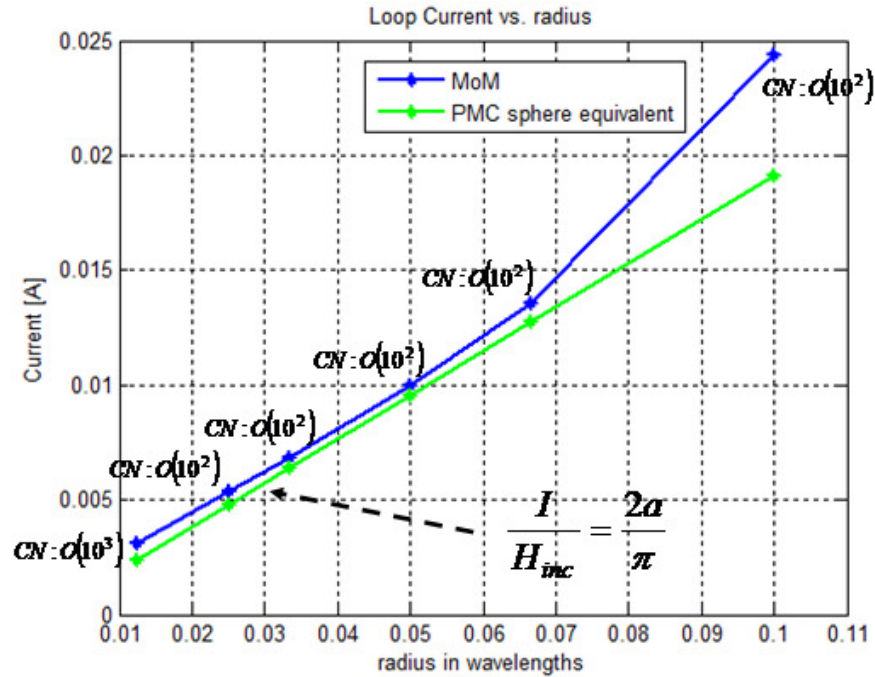
Fig. 4.40: Induced current on the loop versus radius of the loop for plane wave scattering at 1 GHz.
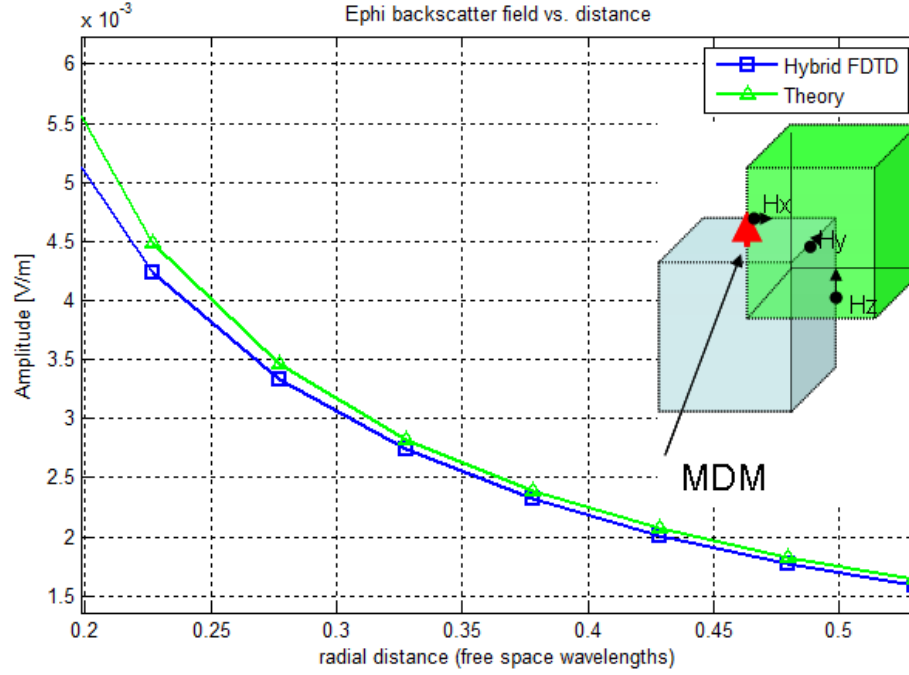
Fig. 4.41: Magnitude of the scattered E_ϕ field versus distance for a PEC loop with radius $\lambda/20$ at 1 GHz.

4.5.8 Plasmonic Sphere

The dipole moment concept can be extended to the hybrid FDTD for the case where the material parameters of the scatterer are frequency dependent, which is difficult to handle in the conventional FDTD. As an example, in this section we consider the problem of scattering by a plasmonic sphere whose relative permittivity is given by

$$\varepsilon_{DL} = \varepsilon_\infty - \frac{\omega_D^2}{\omega(\omega + i\gamma_D)} - \frac{\Delta\varepsilon \cdot \Omega_L^2}{(\omega^2 - \Omega_L^2) + i\Gamma_L\omega} \quad . \tag{4.65}$$

The expression in (4.65) is referred to as the Drude-Lorentz dispersion model. If we use the conventional FDTD algorithm to handle dispersive scatterers described by this model, it requires

extensive modifications to the basic update equations. However, dealing with plasmonic spheres is relatively straightforward in the hybrid approach we are proposing because, fortunately, many researchers have been interested in the scattering properties of small plasmonic spheres, and an equivalent dipole moment is readily available for this geometry. It is given by

$$Il = E_o \frac{4\pi j}{\eta k^2} (ka)^3 \frac{\varepsilon_{DL} - 1}{\varepsilon_{DL} + 2} \; . \qquad (4.66)$$

To model a small plasmonic sphere in a conformal FDTD that can handle Drude-Lorentz materials would considerably increase the simulation time. However, in the hybrid FDTD scheme the expression in (4.66) is treated like any other dipole moment. Furthermore, an important feature of the plasmonic sphere is the so called near-field enhancement. For conventional non-dispersive materials the polarization factor $\frac{\varepsilon_r - 1}{\varepsilon_r + 2}$ is always less than unity. As a result, the scattered field is always less than the incident field. The special property of the plasmonic sphere occurs due to the fact that the denominator of the polarization factor can approach zero and, thus, the scattered field will be "enhanced" relative to the incident field.

The plasmonic properties of gold are often used for near field enhancement of nanoparticles. In addition, it is often necessary to perform an optimization scheme to fit the Drude –Lorentz model. These optimizations for gold have been done in [41] for both Drude and Drude-Lorentz models and are shown in Table 4.1. Also, the results for the real and imaginary parts of ε_{DL} are displayed in Fig. 4.42 while the polarizability factor is shown in Fig. 4.43. It is evident from Fig. 4.43 that the frequencies at which the polarizability factor rises above unity corresponds to those at which near-field enhancement occurs.

Table 4.1: The values of parameters used for the optimization of the Drude and Drude-Lorentz models (source from [41]).

	ϵ_∞	$\omega_D/2\pi$ (THz)	$\gamma_D/2\pi$ (THz)	$\Omega_L/2\pi$ (THz)	$\Gamma_L/2\pi$ (THz)	$\Delta\epsilon$	Φ
Drude	9.0685	2155.6	18.36				431.46
Drude-Lorentz	5.9673	2113.6	15.92	650.07	104.86	1.09	14.521

$$\epsilon_{DL}(\omega) = \epsilon_\infty - \frac{\omega_D^2}{\omega(\omega + i\gamma_D)} - \frac{\Delta\epsilon \cdot \Omega_L^2}{(\omega^2 - \Omega_L^2) + i\Gamma_L\omega},$$
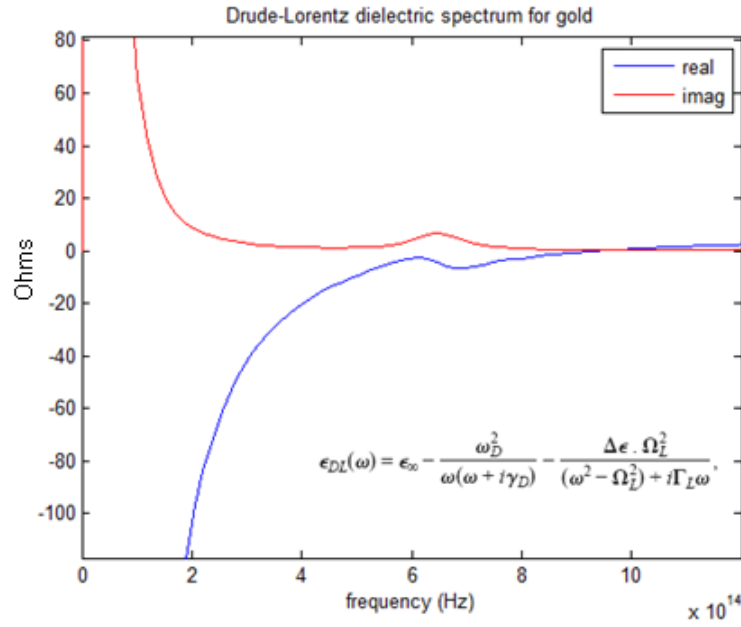
Fig. 4.42: Real and Imaginary parts of the Drude-Lorentz model for gold.

$$\frac{\varepsilon_{DL} - 1}{\varepsilon_{DL} + 2}$$
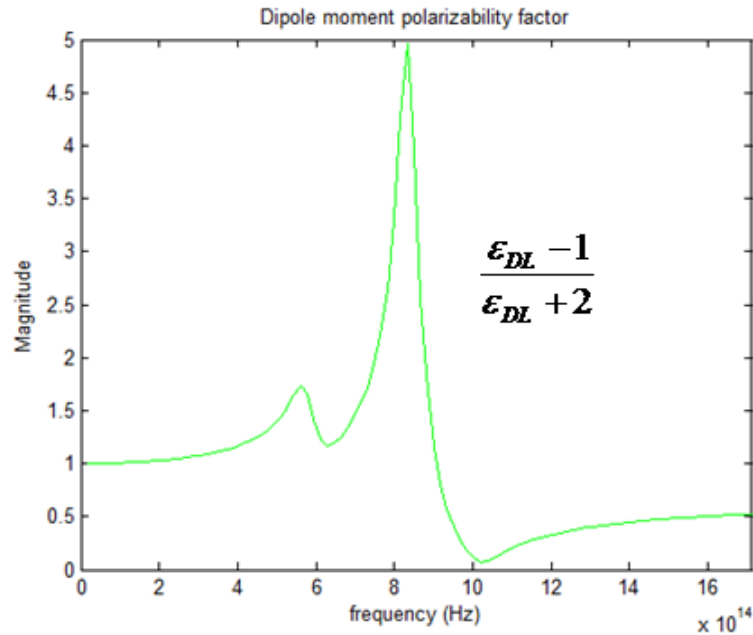
Fig. 4.43: Polarization factor spectrum for gold based on the Drude-Lorentz model.

As an example, a plane wave incident upon a small plasmonic gold nanosphere was simulated using the hybrid FDTD approach. The source was a modulated Gaussian pulse with $f_c = 200$ THz and $f_{-3dB} = 1000$ THz traveling along the x-axis with the incident electric field z-polarized. The sphere radius was $a = \dfrac{\lambda_{high}}{40}$, where λ_{high} is the wavelength at f_{-3dB}. The result for the time signature of the backscatter field at $0.5\lambda_c$ is shown in Fig. 4.44. The frequency spectrum of the near field using the hybrid FDTD is shown Fig. 4.45a and the results using a modified conformal FDTD are shown in Fig. 4.45b for comparison. It is worth noting that the near-field spectrum of both methods exhibit nearly the same behavior. However, the hybrid technique offers significant time and memory advantages over the conventional FDTD, because it does not require mesh refinement to handle the small sphere.
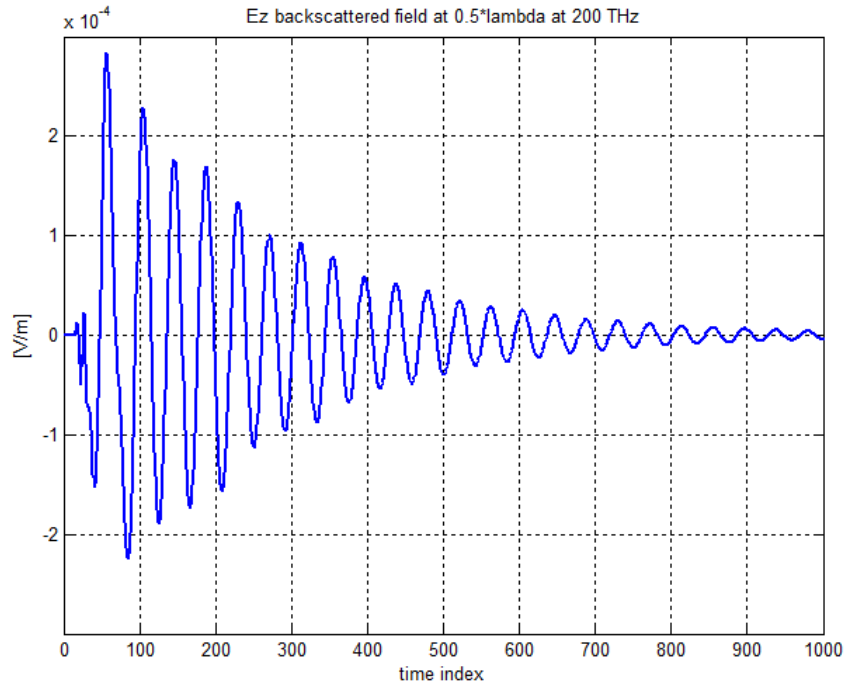
Fig. 4.44: Time domain response for plane wave scattering from of a small gold plasmonic sphere.

(a)

(b)
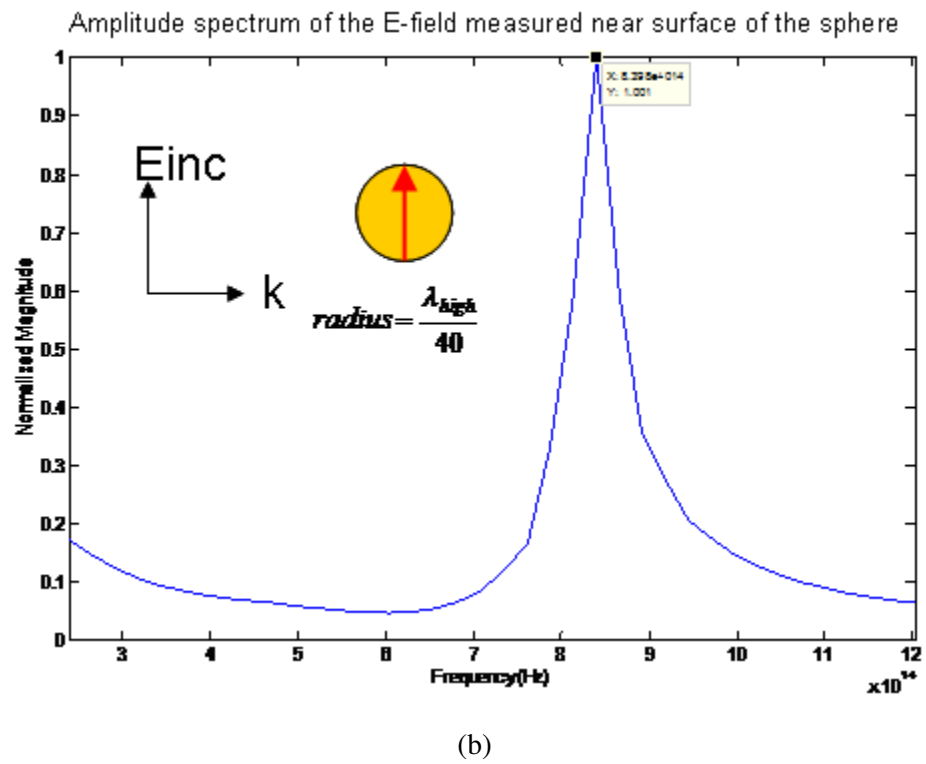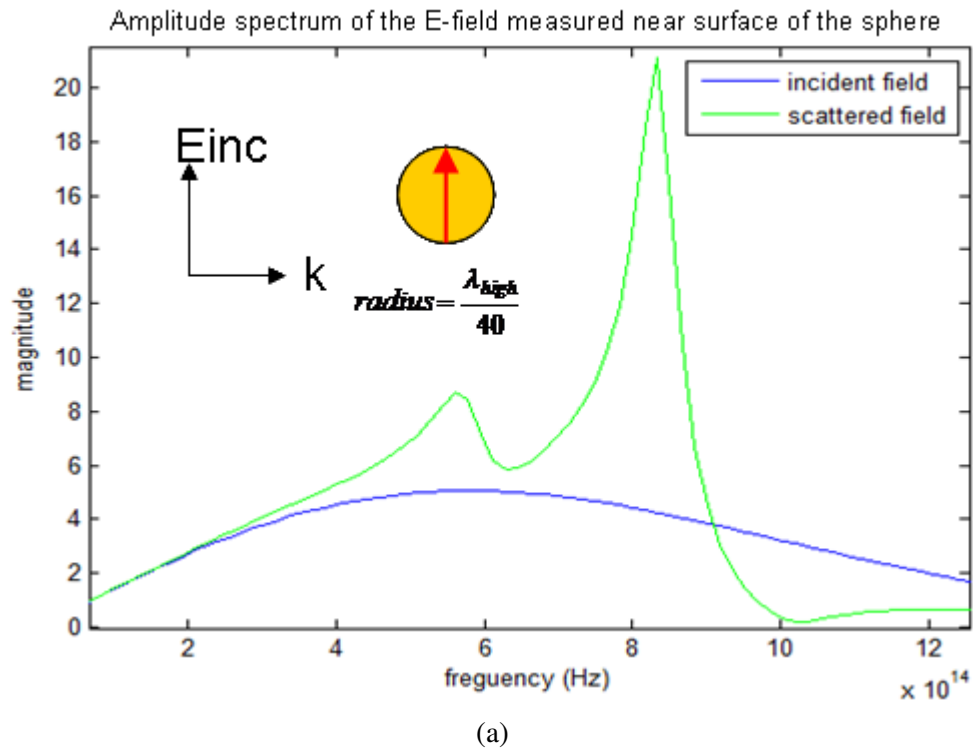
Fig. 4.45: Near field spectrum using the (a) hybrid FDTD (b) Modified FDTD for Drude-Lorentz materials (source from [42]).

4.6 Concluding Remarks

The methods developed in this chapter have been geared towards eliminating the need to generate a fine mesh in the FDTD computational domain when there are small features present. It is well known that if fine features are involved in the simulation they can exacerbate the problems of long runtimes and the need for extensive computational resources when the conventional FDTD algorithm is used. This problem has been circumvented by a hybrid FDTD scheme, presented herein, which is based on the dipole moment concept. Its implementation has been demonstrated for several canonical geometries as well as for more complex structures. And an important feature of the hybrid scheme is that it allows for the nominal cell size of $\lambda_{high}/20$ to remain unchanged. This, in turn, leads to significant savings in simulation time and memory. Lastly, the hybrid FDTD can solve many problems, such as the small, thin wire helix, with limited computing resources, whereas the conventional FDTD is often times unable to model these problems accurately.

Chapter 5

A New Time-Domain Electric Field Integral Equation Formulation Using A Closed Form Basis Function

In this chapter we describe a new formulation for the Time-Domain-Electric-Field-Integral Equation (TD-EFIE). The key feature of this new approach, which distinguishes it from other available TD-EFIE algorithms, is that it utilizes a unique set of basis functions. As will be detailed in the discussion that follows, we choose a basis function that has a known closed form representation, which is amenable to a simple time domain representation in terms of time delays. Furthermore, such a choice deviates from the conventional approach to modeling the unknown current distribution by using a separable basis function expansion in both temporal and spatial domains. Another important advantage of the new approach is that it leads to a tri-diagonal form of the matrix in the updating scheme, which is relatively easy to handle. Therefore, this approach leads to an algorithm which is simpler and computationally more efficient than conventional algorithms, especially when dealing with large number of unknowns.

5.1 Preliminary Analysis of the Basis Function for the TD-EFIE

In our formulation we exploit the fact that the induced current on a simple PEC wire whose dimension are less than the resonant length (i.e., $<< \lambda_o/2$) has a current distribution given by

$$I = jI_m \sin\left(k\left(H - |\xi|\right)\right) \quad , \quad |\xi| \leq H \tag{5.1}$$

where ξ extends the length of an arbitrarily oriented wire. In general, the wire does not need to

be straight and may indeed have bends. Next, we analyze the fields produced by such a wire

element. Consider the geometry in Fig. 5.1
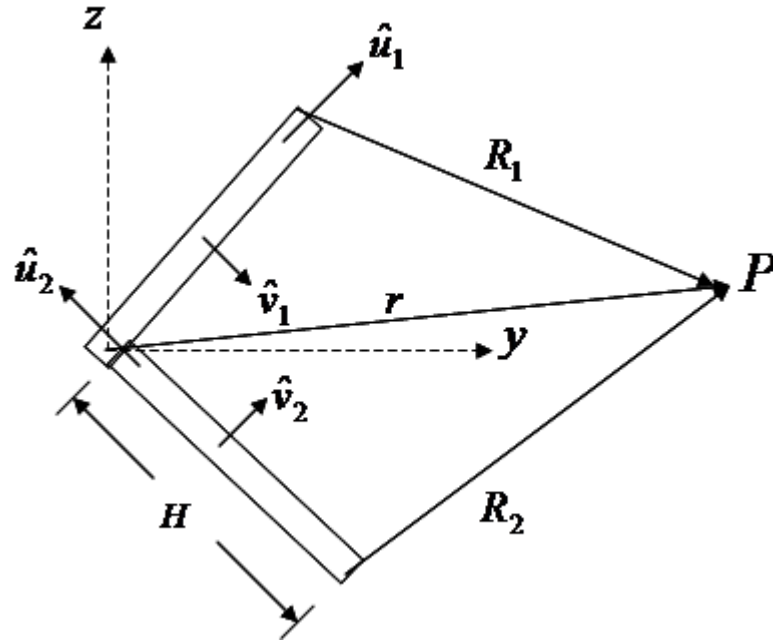
Fig. 5.1: A bent wire and the geometrical parameters used for the field analysis.

where $\hat{u}_1, \hat{v}_1, \hat{u}_2, \hat{v}_2$ are the tangential and normal unit vectors to the top and bottom portions of

the wire, respectively. The electric field produced by the electric current given in (5.1) can be

obtained from the equation given by

$$\bar{E} = -j\omega\mu\bar{A} + \frac{1}{j\omega\varepsilon}\nabla\left(\nabla \cdot \bar{A}\right) \tag{5.2}$$

where the magnetic vector potential $\bar{A}$ is given in terms of the integral

$$\bar{A} = \frac{1}{4\pi} \int_{l'} \frac{Ie^{-jk|\bar{r}-\bar{r}'|}}{|\bar{r}-\bar{r}'|} dl' \quad . \tag{5.3}$$

After some lengthy manipulations using (5.1)-(5.3), the total electric field from the contributions

of the current on both top and bottom portions can be written in closed form as

$$\bar{E} = E_{u_1}\hat{u}_1 + E_{v_1}\hat{v}_1 + E_{u_2}\hat{u}_2 + E_{v_2}\hat{v}_2 \tag{5.4}$$

where $E_{u_1}, E_{v_1}, E_{u_2}, E_{v_2}$ are given by

$$E_{u_1} = 30I_m \left\{ \frac{e^{-jkR_1}}{R_1} - \cos(kH)\frac{e^{-jkr}}{r} - ju_1 \sin(kH)\left(\frac{1}{r^2} + \frac{1}{jkr^3}\right)e^{-jkr} \right\} \tag{5.5}$$

$$E_{v_1} = -30\frac{I_m}{v_1} \left\{ (u_1 - H)\frac{e^{-jkR_1}}{R_1} - u_1 \cos(kH)\frac{e^{-jkr}}{r} - j\frac{\sin(kH)}{kr^3}\left(rku_1^2 + jv_1^2\right)e^{-jkr} \right\} \tag{5.6}$$

$$E_{u_2} = 30I_m \left\{ \frac{e^{-jkR_2}}{R_2} - \cos(kH)\frac{e^{-jkr}}{r} + ju_2 \sin(kH)\left(\frac{1}{r^2} + \frac{1}{jkr^3}\right)e^{-jkr} \right\} \tag{5.7}$$

$$E_{v_2} = -30\frac{I_m}{v_2} \left\{ (u_2 + H)\frac{e^{-jkR_2}}{R_2} - u_2 \cos(kH)\frac{e^{-jkr}}{r} + j\frac{\sin(kH)}{kr^3}\left(rku_2^2 + jv_2^2\right)e^{-jkr} \right\}. \tag{5.8}$$

In the time domain, the cosine and sine terms in (5.5)-(5.8) become problematic due to

the noncausality they produce in conjunction with the exponential factors. To circumvent this

problem we approximate these terms by their small argument (i.e., $kH \ll 1$) Taylor expansions.

Since this wire element will form a basis for the TD-EFIE, we will assume that its electrical

length is small and this justifies our use of the Taylor approximation. By applying this

approximation for the cosine and sine terms, namely, $\cos(kH) \approx 1 - (kH)^2/2$ and

$\sin(kH) \approx kH$ we get

$$E_{u_1} = 30I_m \left\{ \frac{e^{-jkR_1}}{R_1} + \left[\frac{H^2}{2rc^2}\omega^2 - \frac{u_1H}{r^2c}j\omega - \left(\frac{u_1H}{r^3} + \frac{1}{r}\right) \right]e^{-jkr} \right\} \tag{5.9}$$

$$E_{v_1} = -30\frac{I_m}{v_1}\left\{ (u_1 - H)\frac{e^{-jkR_1}}{R_1} + \left[\frac{u_1 H^2}{2rc^2}\omega^2 - \frac{u_1^2 H}{r^2 c}j\omega + \left(\frac{v_1^2 H}{r^3} - \frac{u_1}{r} \right) \right]e^{-jkr} \right\}$$ (5.10)

$$E_{u_2} = 30I_m\left\{ \frac{e^{-jkR_2}}{R_2} + \left[\frac{H^2}{2rc^2}\omega^2 + \frac{u_2 H}{r^2 c}j\omega + \left(\frac{u_2 H}{r^3} - \frac{1}{r} \right) \right]e^{-jkr} \right\}$$ (5.11)

$$E_{v_2} = -30\frac{I_m}{v_2}\left\{ (u_2 + H)\frac{e^{-jkR_2}}{R_2} + \left[\frac{u_2 H^2}{2rc^2}\omega^2 + \frac{u_2^2 H}{r^2 c}j\omega - \left(\frac{v_2^2 H}{r^3} + \frac{u_2}{r} \right) \right]e^{-jkr} \right\}.$$ (5.12)

It is important to recognize that the form of (5.9)-(5.12) have only terms with ω or ω^2 in the numerator and exponentials containing kR. Thus, it is straightforward to obtain a closed-form expression for the electric fields in the temporal domain, and this is the key to our new approach for formulating the TD-EFIE. Specifically, the exponential factors correspond to delays in the temporal domain and the time derivatives are approximated by difference operators which give rise to a marching on time (MOT) algorithm that will be presented in later sections.

If we define a global coordinate system, then we can express the electric fields for an arbitrarily oriented bent wire, given in (5.9)-(5.12) in a compact form as

$$\vec{E} = I_m\left[\underline{\underline{T_1}} \cdot \hat{u}_1 + \underline{\underline{T_2}} \cdot \hat{u}_2 \right]$$ (5.13)

where $\underline{\underline{T_1}}$ and $\underline{\underline{T_2}}$ are given by

$$\underline{\underline{T_1}} = 30\frac{e^{-jkR_1}}{R_1}\underline{\underline{G_{R_1}}} + 30e^{-jkr}\left(\omega^2\underline{\underline{G_2^1}} + j\omega\underline{\underline{G_1^1}} + \underline{\underline{G_0^1}} \right)$$ (5.14)

$$\underline{\underline{T_2}} = 30\frac{e^{-jkR_2}}{R_2}\underline{\underline{G_{R_2}}} + 30e^{-jkr}\left(\omega^2\underline{\underline{G_2^2}} + j\omega\underline{\underline{G_1^2}} + \underline{\underline{G_0^2}} \right).$$ (5.15)

and the matrix terms are explicitly written as follows:

$$\underline{\underline{G_{R_1}}} = \begin{bmatrix} 1 & \dfrac{-x(y-H)}{x^2+z^2} & \dfrac{-x(z-H)}{x^2+y^2} \\[3ex] \dfrac{-y(x-H)}{y^2+z^2} & 1 & \dfrac{-y(z-H)}{x^2+y^2} \\[3ex] \dfrac{-z(x-H)}{y^2+z^2} & \dfrac{-z(y-H)}{x^2+z^2} & 1 \end{bmatrix} \tag{5.16}$$

$$\underline{\underline{G_{R_1}}} = \begin{bmatrix} 1 & \dfrac{-x(y+H)}{x^2+z^2} & \dfrac{-x(z+H)}{x^2+y^2} \\[3ex] \dfrac{-y(x+H)}{y^2+z^2} & 1 & \dfrac{-y(z+H)}{x^2+y^2} \\[3ex] \dfrac{-z(x+H)}{y^2+z^2} & \dfrac{-z(y+H)}{x^2+z^2} & 1 \end{bmatrix} \tag{5.17}$$

$$\underline{\underline{G_2^1}} = \frac{H^2}{2rc^2} \begin{bmatrix} 1 & \dfrac{-yx}{x^2+z^2} & \dfrac{-zx}{x^2+y^2} \\[3ex] \dfrac{-xy}{y^2+z^2} & 1 & \dfrac{-zy}{x^2+y^2} \\[3ex] \dfrac{-xz}{y^2+z^2} & \dfrac{-yz}{x^2+z^2} & 1 \end{bmatrix} \tag{5.18}$$

$$\underline{\underline{G_1^1}} = \frac{H}{r^2c} \begin{bmatrix} -x & \dfrac{-y^2x}{x^2+z^2} & \dfrac{-z^2x}{x^2+y^2} \\[3ex] \dfrac{-x^2y}{y^2+z^2} & -y & \dfrac{-z^2y}{x^2+y^2} \\[3ex] \dfrac{-x^2z}{y^2+z^2} & \dfrac{-y^2z}{x^2+z^2} & -z \end{bmatrix} \tag{5.19}$$

$$\underline{\underline{G_0^1}} = \begin{bmatrix} -\left(\dfrac{xH}{r^3}+\dfrac{1}{r}\right) & -\left(\dfrac{(x^2+z^2)H}{r^3}-\dfrac{y}{r}\right)\dfrac{x}{x^2+z^2} & -\left(\dfrac{(x^2+y^2)H}{r^3}-\dfrac{z}{r}\right)\dfrac{x}{x^2+y^2} \\[3ex] -\left(\dfrac{(y^2+z^2)H}{r^3}-\dfrac{x}{r}\right)\dfrac{y}{y^2+z^2} & -\left(\dfrac{yH}{r^3}+\dfrac{1}{r}\right) & -\left(\dfrac{(x^2+y^2)H}{r^3}-\dfrac{z}{r}\right)\dfrac{y}{x^2+y^2} \\[3ex] -\left(\dfrac{(y^2+z^2)H}{r^3}-\dfrac{x}{r}\right)\dfrac{z}{y^2+z^2} & -\left(\dfrac{(x^2+z^2)H}{r^3}-\dfrac{y}{r}\right)\dfrac{z}{x^2+y^2} & -\left(\dfrac{zH}{r^3}+\dfrac{1}{r}\right) \end{bmatrix} \tag{5.20}$$

$$\underline{\underline{G_0^2}} = \begin{bmatrix} \left(\dfrac{xH}{r^3} - \dfrac{1}{r}\right) & \left(\dfrac{\left(x^2+z^2\right)H}{r^3} + \dfrac{y}{r}\right)\dfrac{x}{x^2+z^2} & \left(\dfrac{\left(x^2+y^2\right)H}{r^3} - \dfrac{z}{r}\right)\dfrac{x}{x^2+y^2} \\ \left(\dfrac{\left(y^2+z^2\right)H}{r^3} + \dfrac{x}{r}\right)\dfrac{y}{y^2+z^2} & \left(\dfrac{yH}{r^3} - \dfrac{1}{r}\right) & \left(\dfrac{\left(x^2+y^2\right)H}{r^3} + \dfrac{z}{r}\right)\dfrac{y}{x^2+y^2} \\ \left(\dfrac{\left(y^2+z^2\right)H}{r^3} + \dfrac{x}{r}\right)\dfrac{z}{y^2+z^2} & \left(\dfrac{\left(x^2+z^2\right)H}{r^3} + \dfrac{y}{r}\right)\dfrac{z}{x^2+y^2} & \left(\dfrac{zH}{r^3} - \dfrac{1}{r}\right) \end{bmatrix} \tag{5.21}$$

and it is possible to show that

$$\underline{\underline{G_2^2}} = \underline{\underline{G_2^1}} \tag{5.22}$$

$$\underline{\underline{G_1^2}} = -\underline{\underline{G_1^1}} \ . \tag{5.23}$$

The equations in (5.16)-(5.23) pertain to the geometry shown in Fig. 5.1, when the object is located at the global origin. If the object is located at some other point in space away from the global origin, it is a simple matter to translate the coordinate values with respect to the reference origin.

As a simple example, we consider the case when the wire has both segments collinear with the z-axis. For this example, we find that the electric field has the form

$$\bar{E} = 30I_m \left[\frac{e^{-jkR_1}}{R_1}\underline{\underline{G_{R_1}}} + \frac{e^{-jkR_2}}{R_2}\underline{\underline{G_{R_2}}} + \left(2\omega^2\underline{\underline{G_2^1}} + \underline{\underline{G_0^2}} + \underline{\underline{G_0^1}}\right)e^{-jkr} \right] \cdot \hat{a}_z \ . \tag{5.24}$$

For the E_z component (5.24) reduces to

$$E_z = \hat{a}_z \cdot \bar{E} = 30I_m \left[\frac{e^{-jkR_1}}{R_1} + \frac{e^{-jkR_2}}{R_2} + \left(\frac{2H^2}{rc^2}\omega^2 - \left(\frac{zH}{r^3} + \frac{1}{r}\right) + \left(\frac{zH}{r^3} - \frac{1}{r}\right)\right)e^{-jkr} \right] \tag{5.25}$$

$$E_z = 30I_m \left[\frac{e^{-jkR_1}}{R_1} + \frac{e^{-jkR_2}}{R_2} + \left(\frac{(kH)^2}{r} - \frac{2}{r}\right)e^{-jkr} \right] \ . \tag{5.26}$$

However, we recognize that the last term in (5.26) is our Taylor approximation for $-2\cos(kH)$ and the exact analytical result for the E_z component is

$$E_z = 30 I_m \left[\frac{e^{-jkR_1}}{R_1} + \frac{e^{-jkR_2}}{R_2} - \frac{2\cos(kH)}{r} e^{-jkr} \right], \tag{5.27}$$

which is the three-term expression often found in the literature [48].

5.2 Formulation

Before proceeding directly to the time domain, we expand upon our knowledge of the basis function in the frequency domain from the previous section to construct the matrix equation. When using a particular basis function it often becomes convenient to normalize it to unity. Thus the basis function for the current from the previous section will have the form

$$b(\xi) = \frac{\sin(k(H - |\xi|))}{-jkH} \quad , \quad |\xi| \leq H \tag{5.28}$$

so that $|b(0)| \approx 1$ for $kH \ll 1$. Now, for a general wire geometry each basis will be weighted by the unknown current values for which we seek a solution. Thus, the total field produced by all these contributions can be written as

$$\frac{1}{-jkH} \sum_{m=1}^{N} I_m \left(\underline{\underline{T_1}} \cdot \hat{u}_1 + \underline{\underline{T_2}} \cdot \hat{u}_2 \right)_{ij} = \bar{E}_n^s \tag{5.29}$$

where n and m are the source and observation points respectively. For the case of point matching the incident field at the source points we have

$$\left. \frac{(\hat{u}_1 + \hat{u}_2)}{|\hat{u}_1 + \hat{u}_2|} \right|_n \cdot \sum_{m=1}^{N} I_m \left(\underline{\underline{T_1}} \cdot \hat{u}_1 + \underline{\underline{T_2}} \cdot \hat{u}_2 \right)_{nm} = -jkH \left. \frac{(\hat{u}_1 + \hat{u}_2)}{|\hat{u}_1 + \hat{u}_2|} \right|_n \left(-\bar{E}_n^{inc} \right). \tag{5.30}$$

The term $\dfrac{(\hat{u}_1 + \hat{u}_2)}{|\hat{u}_1 + \hat{u}_2|}$ corresponds to the unit vector in the direction of the tangential electric field component at the observation points, and it is also applicable to the case when the basis function

straddles the two arms of a bent corner. By letting $\hat{v}_n = \dfrac{(\hat{u}_1 + \hat{u}_2)}{|\hat{u}_1 + \hat{u}_2|}\bigg|_n$, and using matrix algebra

notation, we can write

$$
\hat{v}_n^T \sum_{m=1}^{N} 30 I_m \left[\frac{e^{-jkR_1}}{R_1} \underline{\underline{G}}_{R_1} \hat{u}_1 + \frac{e^{-jkR_2}}{R_2} \underline{\underline{G}}_{R_2} \hat{u}_2 + \underline{\underline{G}}_2^1 (\hat{u}_1 + \hat{u}_2) \omega^2 e^{-jkr} \right.
$$
$$
\left. + \underline{\underline{G}}_1^1 (\hat{u}_1 - \hat{u}_2) j\omega + \left(\underline{\underline{G}}_0^1 \hat{u}_1 + \underline{\underline{G}}_0^2 \hat{u}_2 \right) e^{-jkr} \right]_{nm} = jkH\left(\hat{v}_n^T \vec{E}_n^{inc} \right)
$$
$$ \tag{5.31} $$

The above equation can be written in a more compact form as

$$
\hat{v}_n^T \sum_{m=1}^{N} I_m \left[\frac{e^{-jk(R_1)_{nm}}}{(R_1)_{nm}} \left(\underline{\underline{G}}_{R_1} \right)_{nm} (\hat{u}_1)_m + \frac{e^{-jk(R_2)_{nm}}}{(R_2)_{nm}} \left(\underline{\underline{G}}_{R_2} \right)_{nm} (\hat{u}_2)_m \right.
$$
$$
\left. + \bar{\alpha}_{nm} \omega^2 e^{-jk(r)_{nm}} + \bar{\kappa}_{nm} j\omega e^{-jk(r)_{nm}} + \bar{\gamma}_{nm} e^{-jk(r)_{nm}} \right] = \frac{jkH}{30} \left(\hat{v}_n^T \vec{E}_n^{inc} \right)
$$
$$ \tag{5.32} $$

where $\bar{\alpha}_{nm}, \bar{\kappa}_{nm}, \bar{\gamma}_{nm}$ are given by

$$
\bar{\alpha}_{nm} = \left(\underline{\underline{G}}_2 \right)_{nm} (\hat{u}_1 + \hat{u}_2)_m \tag{5.33}
$$

$$
\bar{\kappa}_{nm} = \left(\underline{\underline{G}}_1 \right)_{nm} (\hat{u}_1 - \hat{u}_2)_m \tag{5.34}
$$

$$
\bar{\gamma}_{nm} = \left[\left(\underline{\underline{G}}_0^1 \right)_{nm} (\hat{u}_1)_m + \left(\underline{\underline{G}}_0^2 \right)_{nm} (\hat{u}_2)_m \right] \tag{5.35}
$$

and $\underline{\underline{G}}_2 = \underline{\underline{G}}_2^1 = \underline{\underline{G}}_2^2$, $\underline{\underline{G}}_1 = \underline{\underline{G}}_1^1 = -\underline{\underline{G}}_1^2$.

The result in (5.32) constitutes a matrix equation in the frequency domain, where the

solution is obtained through point matching when enforcing the boundary condition. Furthermore,

it is apparent that (5.32) only contains complex exponential terms and this enables us to evaluate

the time-domain form relatively easily. By performing the inverse Fourier transform $\mathfrak{I}^{-1}\{\ \}$ on

(5.32), it can be shown that its time-domain representation is given by

$$\hat{v}_n^T \sum_{m=1}^N \left[\frac{1}{(R_1)_{nm}} \left(\underline{\underline{G_{R_1}}}\right)_{nm} (\hat{u}_1)_m I_m\left(t - \frac{(R_1)_{nm}}{c}\right) + \frac{1}{(R_2)_{nm}} \left(\underline{\underline{G_{R_2}}}\right)_{nm} (\hat{u}_2)_m I_m\left(t - \frac{(R_2)_{nm}}{c}\right) \right.$$
$$\left. - \bar{\alpha}_{nm} \frac{\partial^2}{\partial t^2} I_m\left(t - \frac{(r)_{nm}}{c}\right) + \bar{\kappa}_{nm} \frac{\partial}{\partial t} I_m\left(t - \frac{(r)_{nm}}{c}\right) + \bar{\gamma}_{nm} I_m\left(t - \frac{(r)_{nm}}{c}\right) \right] = \frac{H}{30c} \frac{\partial}{\partial t} \left(\hat{v}_n^T \bar{E}_n^{inc}\right) \tag{5.36}$$

In discrete time the substitution $t \to n\Delta t$ is made and the differential operators are replaced with backward differences. The resulting difference equation is written as

$$\hat{v}_i^T \sum_{j=1}^N \left[\frac{1}{(R_1)_{ij}} \left(\underline{\underline{G_{R_1}}}\right)_{ij} (\hat{u}_1)_j I_j^{n - \frac{(R_1)_{ij}}{c\Delta t}} + \frac{1}{(R_2)_{ij}} \left(\underline{\underline{G_{R_2}}}\right)_{ij} (\hat{u}_2)_j I_j^{n - \frac{(R_2)_{ij}}{c\Delta t}} \right.$$
$$- \frac{\bar{\alpha}_{ij}}{(\Delta t)^2} \left(I_j^{n - \frac{(r)_{ij}}{c\Delta t}} - 2 I_j^{n-1 - \frac{(r)_{ij}}{c\Delta t}} + I_j^{n-2 - \frac{(r)_{ij}}{c\Delta t}} \right) + \frac{\bar{\kappa}_{ij}}{\Delta t} \left(I_j^{n - \frac{(r)_{ij}}{c\Delta t}} - I_j^{n-1 - \frac{(r)_{ij}}{c\Delta t}} \right) + \left. \bar{\gamma}_{ij} I_j^{n - \frac{(r)_{ij}}{c\Delta t}} \right] \tag{5.37}$$
$$= \frac{H}{30c} \frac{\partial}{\partial t} \left(\hat{v}_i^T \bar{E}_n^{inc}\right)$$

where the subscripts have been changed to avoid confusion with the time index n. In addition, the right hand side of (5.37) contains the time derivative of the incident field and this quantity is assumed to be known *a priori*. Therefore, it becomes unnecessary to numerically compute this term and, in fact, doing so can lead to unstable results.

Returning to (5.37), we can see that a suitable time step has yet to be chosen. The choice of time step is not an obvious one and many TD-EFIE formulations rely on conservative estimates that provide the most stable results. However, the form of (5.37) provides some insight for the marching on time (MOT) scheme that is desired. If a straight wire is considered, then we note that for terms other than the self term the distance from the source to the observation points are integral multiples of the basis discretization, specifically the length H. Furthermore, the distance from the source to its nearest observation point will always be H regardless of the

geometry. In view of this, a suitable choice for the time step for this TD-EFIE scheme is $\Delta t = H/c$.

Using this prescribed time step, (5.37) can be rewritten as

$$
\hat{v}_i^T \sum_{j=1}^N \left[\frac{1}{(R_1)_{ij}} \left(\underline{\underline{G_{R_1}}} \right)_{ij} (\hat{u}_1)_j I_j^{n-\frac{(R_1)_{ij}}{H}} + \frac{1}{(R_2)_{ij}} \left(\underline{\underline{G_{R_2}}} \right)_{ij} (\hat{u}_2)_j I_j^{n-\frac{(R_2)_{ij}}{H}} \right.
$$
$$
\left. + \left(\bar{\gamma}_{ij} + \frac{\bar{\kappa}_{ij}}{\Delta t} - \frac{\bar{\alpha}_{ij}}{(\Delta t)^2} \right) I_j^{n-\frac{(r)_{ij}}{H}} + \left(\frac{2\bar{\alpha}_{ij}}{(\Delta t)^2} - \frac{\bar{\kappa}_{ij}}{\Delta t} \right) I_j^{n-1-\frac{(r)_{ij}}{H}} - \frac{\bar{\alpha}_{ij}}{(\Delta t)^2} I_j^{n-2-\frac{(r)_{ij}}{H}} \right]
$$
$$
= \frac{H}{30c} \frac{\partial}{\partial t} \left(\hat{v}_i^T \bar{E}_n^{inc} \right)
$$

(5.38)

Noting that $(r)_{ii} \equiv 0$, and collecting the terms without delays on the left hand side while the remaining terms are kept on the right hand side, yields the desired MOT scheme. It is given by

$$
\hat{v}_i^T \left(\frac{\underline{\underline{G_{R_1}}}}{R_1} \right)_{ii-1} (\hat{u}_1)_{i-1} I_{i-1}^n + \hat{v}_i^T \left(\frac{\underline{\underline{G_{R_2}}}}{R_2} \right)_{ii+1} (\hat{u}_2)_{i+1} I_{i+1}^n + \hat{v}_i^T \left(\bar{\gamma}_{ii} + \frac{\bar{\kappa}_{ii}}{\Delta t} - \frac{\bar{\alpha}_{ii}}{(\Delta t)^2} \right) I_i^n =
$$
$$
\frac{H}{30c} \frac{\partial}{\partial t} \left(\hat{v}_i^T \bar{E}_i^{inc} \right) - \sum_{\substack{j=1 \\ j \neq i-1}}^N \hat{v}_i^T \left(\frac{\underline{\underline{G_{R_1}}}}{R_1} \right)_{ij} (\hat{u}_1)_j I_j^{n-\frac{(R_1)_{ij}}{H}} - \sum_{\substack{j=1 \\ j \neq i+1}}^N \hat{v}_i^T \left(\frac{\underline{\underline{G_{R_2}}}}{R_2} \right)_{ij} (\hat{u}_2)_j I_j^{n-\frac{(R_2)_{ij}}{H}}
$$
$$
- \sum_{\substack{j=1 \\ j \neq i}}^N \hat{v}_i^T \left(\bar{\gamma}_{ij} + \frac{\bar{\kappa}_{ij}}{\Delta t} - \frac{\bar{\alpha}_{ij}}{(\Delta t)^2} \right) I_j^{n-\frac{(r)_{ij}}{H}} - \sum_{j=1}^N \hat{v}_i^T \left(\frac{2\bar{\alpha}_{ij}}{(\Delta t)^2} - \frac{\bar{\kappa}_{ij}}{\Delta t} \right) I_j^{n-1-\frac{(r)_{ij}}{H}}
$$
$$
+ \sum_{j=1}^N \hat{v}_i^T \frac{\bar{\alpha}_{ij}}{(\Delta t)^2} I_j^{n-2-\frac{(r)_{ij}}{H}}
$$

(5.39)

An important aspect of this MOT algorithm is that the resulting matrix is tri-diagonal in form. Therefore, even for large structures, (5.39) can be done relatively easily by well known matrix techniques. This is in contrast with many other TD-EFIE schemes where the matrix may be sparse but would still require sophisticated treatment for large problems. We should point out that, when using these basis functions, the terms on the right hand side of (5.39) must be given special consideration when the geometry is curved, or bent, as this is the general case with most

structures. For arbitrarily curved wires, the terms on the right hand side that contain the

associated time delays for $(R_1)_{ij}, (R_2)_{ij}, (r)_{ij}$ will in general not coincide with integral multiples of

the discretization length H. Therefore, a time domain interpolation scheme must be included to

accurately account for these delays and this has been done when implementing the algorithm.

The matrix equation given in (5.39) requires only point matching to satisfy the boundary

condition that the electric field vanishes at these points. Consequentially, the boundary condition

may or may not be satisfied at points other than those that were chosen to construct the matrix

equation. It is therefore necessary to perform a smoothing operation in the form of a testing

function over the geometry so that on average the boundary condition will be satisfied. This

approach is often designated as the Method of Moments (MoM). However, in the MoM

formulation the basis and testing functions are often chosen to be identical and this is referred to

as Galerkin's method. In the MOT formulation that has been derived here Galerkin's method

cannot be easily applied. The reason for this lies in the fact that we have chosen a basis function

that is frequency dependent and therefore testing (5.39) with the inverse Fourier transform of this

function will lead to numerous complications. Fortunately, the imposed constraint of identical

basis and testing functions is often unnecessary and an alternative testing function may be used.

In fact, a suitable testing function for the MOT algorithm is just a pulse. This function is simple

and the result of testing with it leads to a simple extension of (5.39). A graphical illustration of

pulse testing with the basis function of (5.28) is shown in Fig. 5.2.
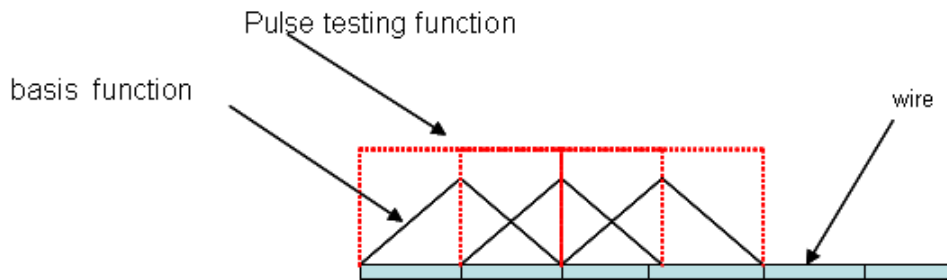

Fig. 5.2: The basis and testing functions used for the TD-EFIE.

Using this pulse testing function w_i the resulting TD-EFIE algorithm can be derived

from (5.39) and is given by

$$
\left\langle w_i, \hat{v}_i^T \left(\frac{\overline{\overline{G_{R_1}}}}{R_1} \right)_{ii-1} (\hat{u}_1)_{i-1} \right\rangle I_{i-1}^n + \left\langle w_i, \hat{v}_i^T \left(\frac{\overline{\overline{G_{R_2}}}}{R_2} \right)_{ii+1} (\hat{u}_2)_{i+1} \right\rangle I_{i+1}^n + \left\langle w_i, \hat{v}_i^T \left(\bar{\gamma}_{ii} + \frac{\bar{\kappa}_{ii}}{\Delta t} - \frac{\bar{\alpha}_{ii}}{(\Delta t)^2} \right) \right\rangle I_i^n =
$$

$$
\left\langle w_i, \frac{H}{30c} \frac{\partial}{\partial t} \left(\hat{v}_i^T \bar{E}_i^{inc} \right) \right\rangle - \sum_{\substack{j=1 \\ j \neq i-1}}^N \left\langle w_i, \hat{v}_i^T \left(\frac{\overline{\overline{G_{R_1}}}}{R_1} \right)_{ij} (\hat{u}_1)_j \right\rangle I_j^{n-\frac{(R_1)_{ij}}{H}} - \sum_{\substack{j=1 \\ j \neq i+1}}^N \left\langle w_i, \hat{v}_i^T \left(\frac{\overline{\overline{G_{R_2}}}}{R_2} \right)_{ij} (\hat{u}_2)_j \right\rangle I_j^{n-\frac{(R_2)_{ij}}{H}}
$$

(5.40)

$$
- \sum_{\substack{j=1 \\ j \neq i}}^N \left\langle w_i, \hat{v}_i^T \left(\bar{\gamma}_{ij} + \frac{\bar{\kappa}_{ij}}{\Delta t} - \frac{\bar{\alpha}_{ij}}{(\Delta t)^2} \right) \right\rangle I_j^{n-\frac{(r)_{ij}}{H}} - \sum_{j=1}^N \left\langle w_i, \hat{v}_i^T \left(\frac{2\bar{\alpha}_{ij}}{(\Delta t)^2} - \frac{\bar{\kappa}_{ij}}{\Delta t} \right) \right\rangle I_j^{n-1-\frac{(r)_{ij}}{H}}
$$

$$
+ \sum_{j=1}^N \left\langle w_i, \hat{v}_i^T \frac{\bar{\alpha}_{ij}}{(\Delta t)^2} \right\rangle I_j^{n-2-\frac{(r)_{ij}}{H}} .
$$

The above equation is the final form of the MOT TD-EFIE algorithm that has been implemented

for some simple cases as shown in the next section.

5.3 Numerical Results

In this section the formulation of (5.40) has been used to simulate the transient behavior

of the induced current on some simple benchmark geometries. The first case is that of scattering

by a long straight wire for a normally incident plane wave. For the second example we consider

the problem of scattering by a square loop when the propagation vector is normal to the loop area.

In the final case, we present the results for the transmitting case of the same square loop, where

we compute the Fourier transform of the current distribution and compare it to the corresponding

results obtained from MoM.

5.3.1 Scattering From a Straight Wire

The scattering from a long straight wire serves as a good benchmark test for the new TD-EFIE method that we have introduced. The geometry of the wire, which is 1 meter in length and is collinear with the z-axis, is shown in Fig. 5.3. Furthermore, the incident electric field is z-polarized, has a Gaussian time signature, with $f_c = 300\,\text{MHz}$ $f_{-3dB} = 800\,\text{MHz}$, and travels along the x-axis.
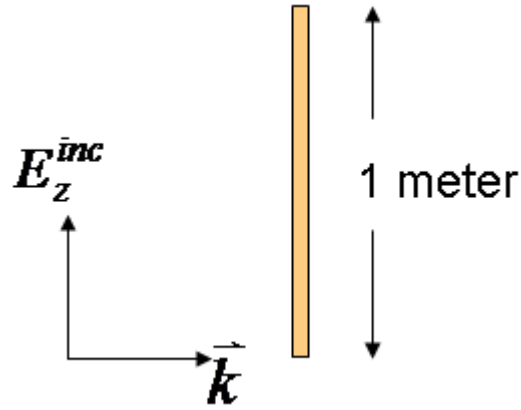
Fig. 5.3: Plane wave scattering of a 1 meter PEC wire.

The radius of the wire was chosen to be $a = 5e - 4$ meters, which is in accordance with the thin wire approximation often made in MoM. In addition, the basis function discretization parameter was chosen to be $H = 0.025$ meters, which corresponds to $\lambda_o/40$ at 300 MHz. Of interest are the current distributions and far-field plots at 300 MHz and 600 MHz. In the time domain the current undergoes reflections by the presence of the discontinuity at the ends of the wire and this in turn sets up standing wave distributions in the frequency domain. In the time domain this process is not so easy to visualize, and we must compute the Fourier transform from the time histories of the solution vector $\bar{I}$ to compare with other existing codes. Therefore, the

TD-EFIE algorithm was used and the computed current distributions and far-fields at 300 MHz and 600 MHz are shown as well as compared with MoM in Figs. 5.4-5.7.

Fig. 5.4: The induced current distribution at 300 MHz using Fourier transform of the TD-EFIE solution and MoM.

Fig. 5.5: The induced current distribution at 600 MHz using Fourier transform of the TD-EFIE solution and MoM.
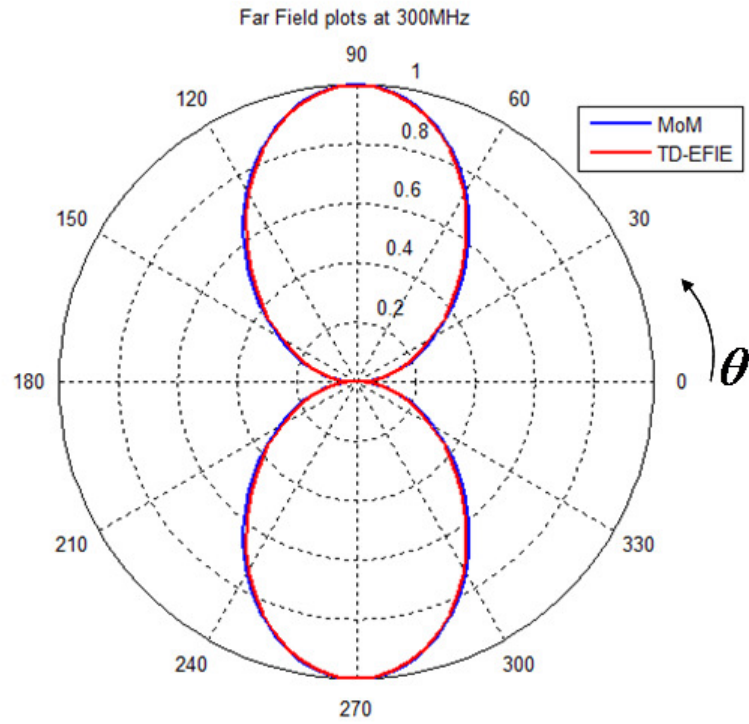
Fig. 5.6: Normalized far-fields for $\phi = 0$ at 300 MHz using Fourier transform of the TD-EFIE solution and MoM.
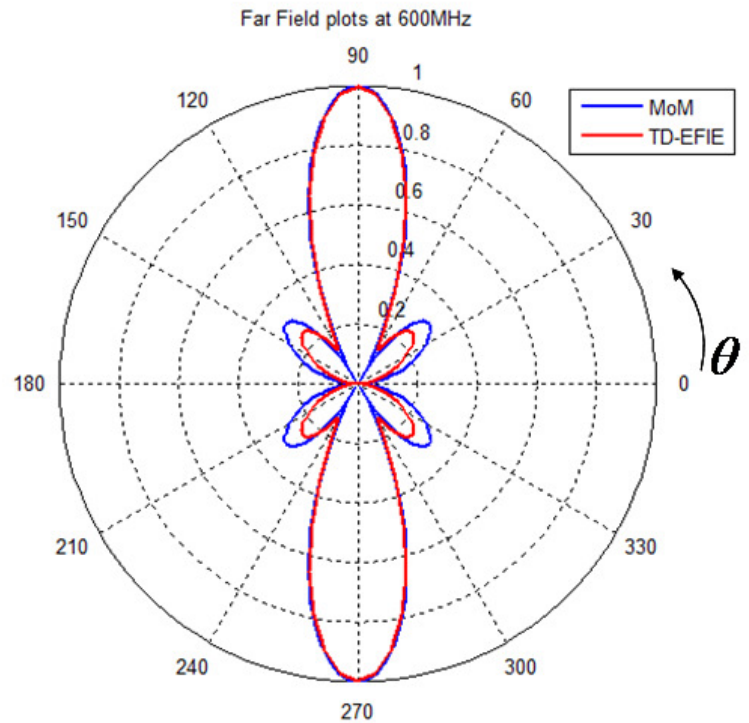
Fig. 5.7: Normalized far-fields for $\phi = 0$ at 600 MHz using Fourier transform of the TD-EFIE solution and MoM.

5.3.2 Scattering From a Square Loop

A more complicated example is the scattering from a square loop. The wire radius and incident field time signature were kept the same as in Section 5.3.1, and the total length of the loop was chosen to be 0.5 meters. In this case, the incident electric field is z-polarized and it travels along the y-axis, while the loop lies in the xz-plane (see Fig. 5.8). Furthermore, a sample of the time signature of the current on one of the basis segments is shown in Fig. 5.9.
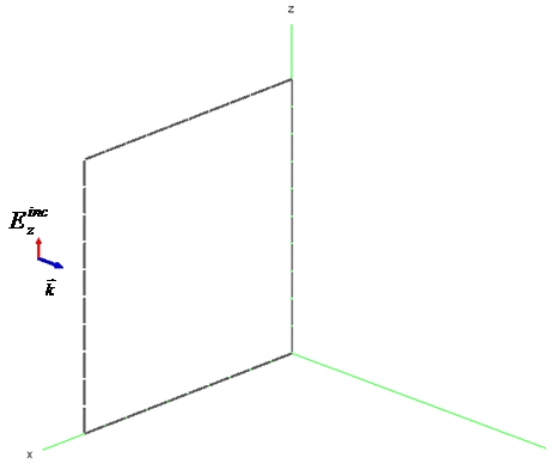
Fig. 5.8: Geometry for plane wave scattering from a square loop.
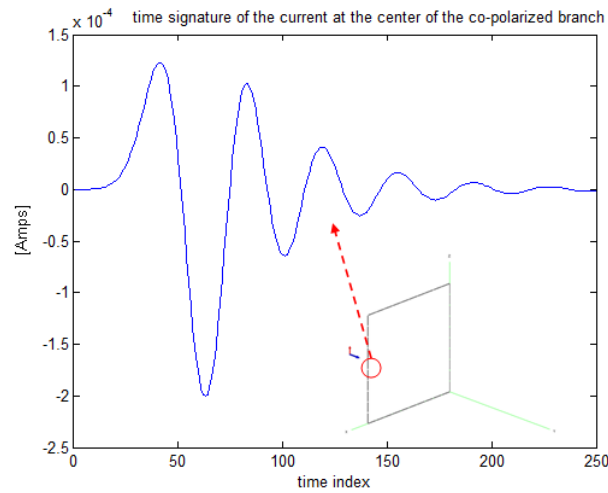
Fig. 5.9: Time signature of the current on a co-polarized basis element.

For the loop case, the corner elements required special treatment in the way the testing function was applied. The formulation previously described generalizes the case for bent wire geometries where the unit vector on the corner is computed as the vector sum of the orientations of each arm of the basis function chosen. Thus, a right angle bend is accounted for by testing the field at an angle of $45°$ where the basis function straddles the corner element. The results for the current distribution at 300 MHz using the results of the TD-EFIE and MoM are shown in Fig. 5.10.
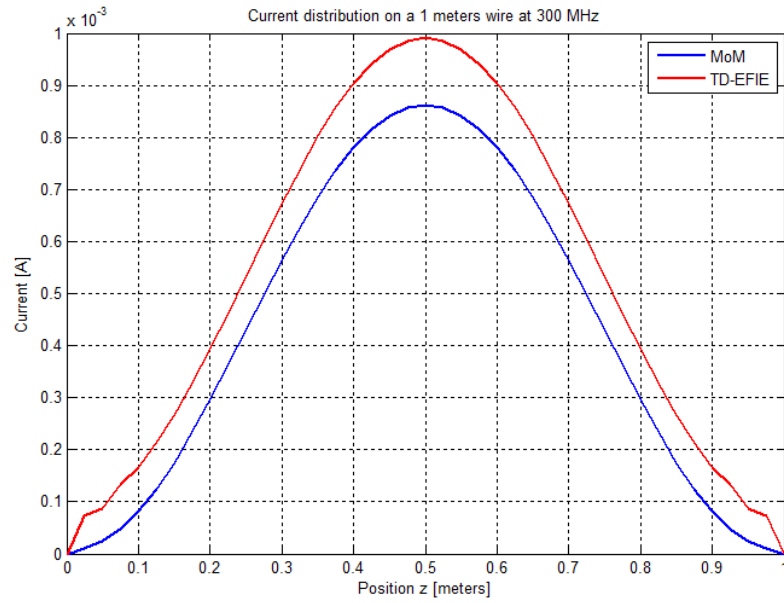

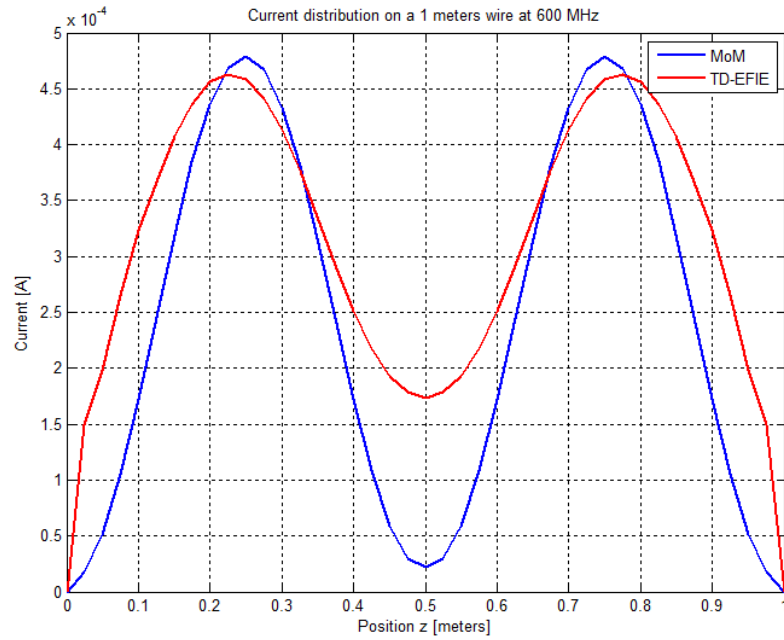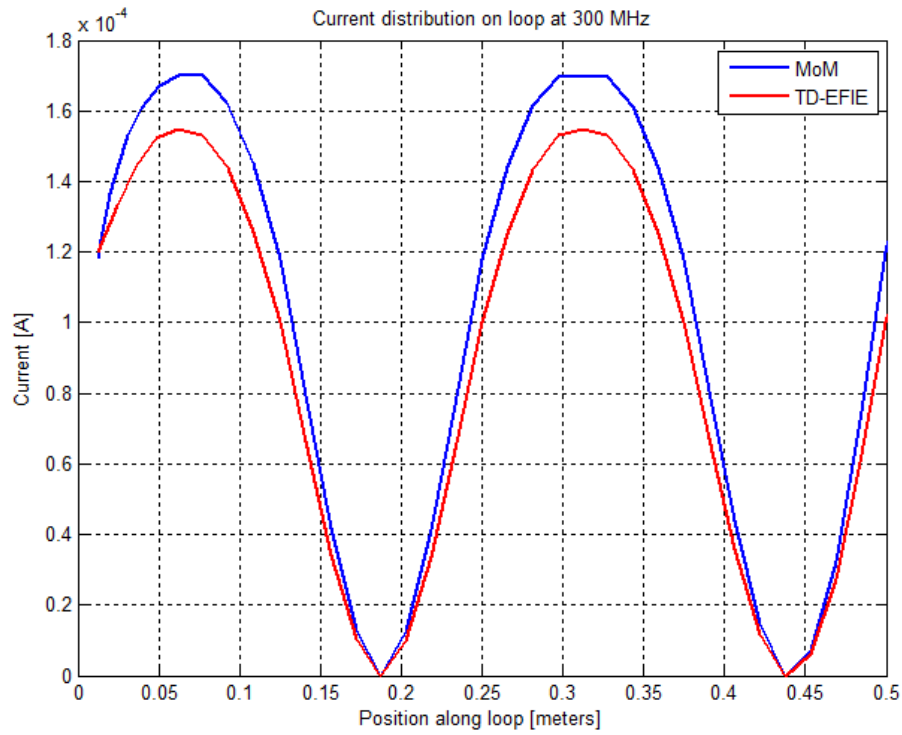Fig. 5.10: The induced current distribution at 300 MHz using Fourier transform of the TD-EFIE solution and MoM.

5.3.3 Transmitting Square Loop

In some cases, it is often desirable to simulate the antenna in transmit mode. Many

formulations for the TD-EFIE have been put forth in recent years, but often times the results

presented are for the scattering cases only. This can be attributed to the choice of the feed model,

which can lead to spurious or even unstable results. In the frequency domain, the delta gap feed

model is used almost universally for wire type structures. However, for our new TD-EFIE

formulation, we have found that this model in the time domain leads to spurious results at the

feed point. An alternative feed model is that of a frill type source where the electric field

excitation is distributed along the geometry. It has been found that this model eliminates the

spurious effects of the delta gap model. To that extent, the square loop of Section 5.3.2 was

analyzed in the transmit mode using the new TD-EFIE algorithm. The frill source was centered

along one of the arms of the loop, and the current distribution was computed by taking the Fourier

transform of the time domain solution. The resulting current distribution is plotted in Figs. 5.11

and 5.12 for 300 and 600 MHz, respectively.
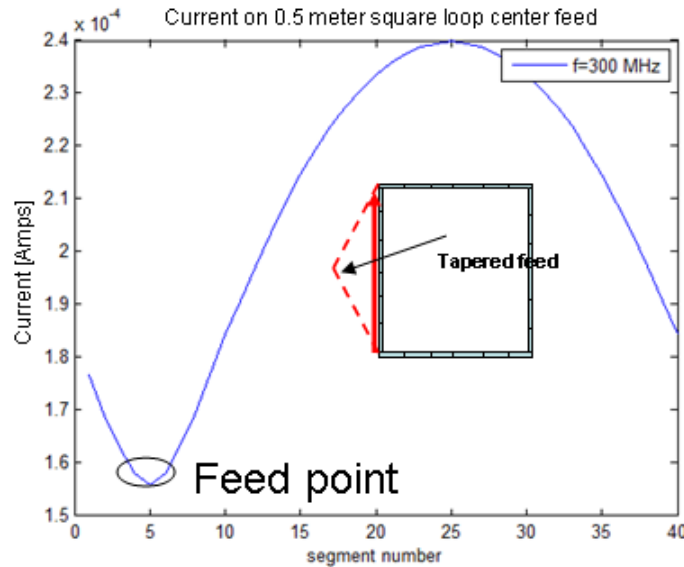
Fig. 5.11: Current distribution on the square loop in transmit mode at 300 MHz using the Fourier transform of the TD-EFIE solution.
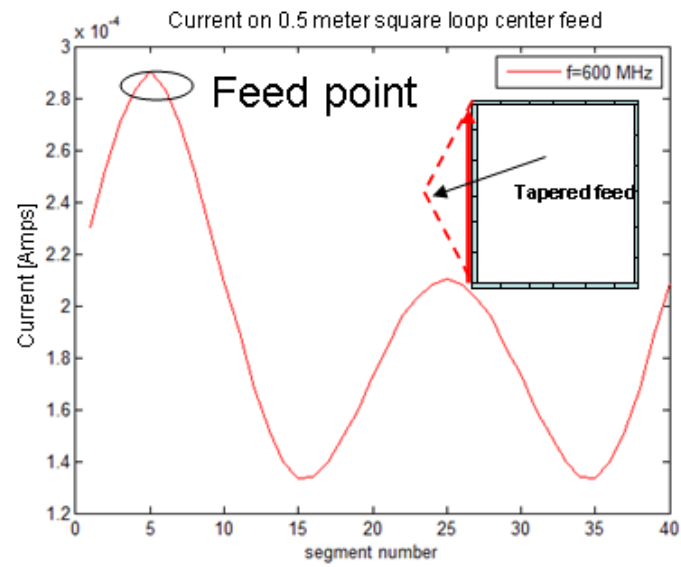
Fig. 5.12: Current distribution on the square loop in transmit mode at 600 MHz using the Fourier transform of the TD-EFIE solution.

Chapter 6

Conclusion and Future Work

The overall theme of thesis has been the solution of multi-scale problems that often occur in computational electromagnetics, and are being encountered, more and more frequently, as engineers continue to attempt modeling realistic systems. The approach presented in chapter two can be applied when large separation distances are involved on planar surfaces and meshing the entire computational domain in FDTD becomes costly. Often the geometrical features are far too complex to use any approximation schemes and it becomes necessary to rigorously apply the FDTD to the entire domain. This has been done for a realistic human body phantom in Chapter 3 in attempt to model realistic communication channel parameters in BANs.

The hybrid scheme presented in Chapter 4 attempts to solve the problem when fine features are included in a large computational domain, and it is desired to maintain a relatively course global cell size. This approach has been successfully demonstrated for some sample geometries and amounts to large simulation time savings. However, the DM hybrid FDTD method makes exclusive use of the fact that for small geometries a quasi-static analysis can be made, provided that the features are small and occupy less than typically four FDTD cells.

In many cases, the wire geometries may extend several FDTD cells and the quasi-static approach is invalid if the retardation effect must be included. The new TD-EFEI algorithm presented in Chapter 5 has been shown to compare well to the MoM results in the frequency domain. The results using this new approach have some promising applications for hybridization with other time domain codes when the wire geometries are not small. In particular, future work can focus on a hybridization with the novel TD-EFIE algorithm and the FDTD. The approach would entail a different methodology that the DM hybrid FDTD since the retardation effect must

be included. Therefore, additional work can be directed toward expanding on the range of geometries that can be included in the FDTD and some further improvements into the new TD-EFIE approach would also be desirable.

As a final note, the introduction of the dipole moment concept, and its hybridization with the FDTD, can be adapted to other existing techniques which require meshing the computational domain. A particular case is a novel frequency domain version of the FDTD algorithm called the recursive update frequency domain (RUFD) method. This computational approach makes use of existing FDTD concepts, except that it is performed in the frequency domain. The advantage of this approach is that no matrix inversion is required. However, the RUFD still requires meshing the computational domain, and, as a result, fine features can still greatly increase the computational resources needed. Fortunately, the hybrid FDTD method, based on the dipole moment concept presented in this thesis, is easily adaptable to the RUFD. Furthermore, due to the fact that the RUFD is a frequency domain algorithm, we are not restricted by the quasi-static approximation, which is required in time domain, and it may be possible to extend this approach to larger geometries for which the retardation effect is not negligible. To that end, further work is required to demonstrate that the dipole moment concept can be incorporated into to the RUFD method.

Bibliography

[1] M.I. Aksun, R. Mittra, "Closed-Form Green's Function and Their Use in The Method of Moments," Chapter 1 in *Electromagnetic Wave Interaction*, A. Guran, R. Mittra, P. J. Moser (Ed.), World Scientific Publishing Co., New Jersey, 1996.

[2] M. I. Aksun, G. Dural, "Clarification of Issues on the Closed-Form Green's Functions in Stratified Media," *IEEE Trans. on Antennas and Propagation*, Vol. 53, No. 11, Nov. 2005.

[3] R. W. Hamming, *Numerical Methods for Scientists and Engineers*, 2nd ed., Dover Publications, 1986.

[4] W. Yu, R. Mittra, T. Su, Y. Liu, X. Yang, *Parallel Finite-Difference-Time-Domain Method*, Artech House, Inc., Massachussetts, 2006.

[5] R. F. Harrington, *Time Harmonic Electromagnetic Fields*, IEEE-Wiley Press, 2001

[6] Y. Zhao, Y. Hao, A. Alomainy, C. Parini, "UWB On-Body Radio Channel Modeling Using Ray Theory and Subband FDTD Method," *IEEE Trans. Microwave Theory Tech.*, Vol 54, No. 4, pg. 1827-1835, April 2006.

[7] P. S. Hall *et al,* "Antennas and Propagation for On-Body Communication Systems," *IEEE Antennas and Propagation Magazine*, Vol. 49, No.3, June 2007.

[8] A. Alomainy, Y. Hao, X. Hu, C.G. Parini, P.S. Hall "UWB on-body radio propagation and system modelling for wireless body-centric networks," *IEE Proc.-Commun*, Vol 153 No. 1, February 2006

[9] M.R. Kamarudan, Y.I. Nechayev, P.S. Hall "Performance of antennas in the on-body environment," *Second International Symposium*, Year:19-20 Oct. 1998, Page(s):116-122

[10] Jaehoon Kim, Yahya Rahmat-Samii "Implanted antennas inside a human body: simulations design, and characterization," *IEEE MTT*, Vol.52, No. 8, August 2004

[11] R. Mittra, J. Bringuier, J. Wiart, K. Yoo "Modeling of Interaction Between Body-Mounted Antennas," *EuCAP* ,2006.

[12] W.G. Scanlon, N.E Evans, "Body-Surface Mounted Antenna Modelling for Biotelemetry Using FDTD with Homogeneous, Two- and Three-Layer Phantoms," *10th International Conference on Antennas and Propagation*, 14-17 April 1997, Conference Publication No. 436 IEE 1997.

[13] T. Zasowski, F. Althaus, M. Stager, A. Wittneben, and G**.** Troster, "UWAB for Noninvasive Wireless Body Area Networks: Channel Measurements and Results," *IEEE Conference on Ultra Wideband Systems and Technologies*, Reston, Virginia, USA**,** 2003**.**

[14] . J**.** Ryckaert, P. De Doncker, R. Meys, A**.** de Le Hoye, and S**.** Donnay, "Channel Model for Wireless Communication Around Human Body," *Electronics Letters,* 40, 9**,** April 29**,** 2004, pp**.** *543*-544.

[15] A. Alomainy, Y. Hao, A. Owadally, C. Parini, Y. I. Nechayev, P. S. Hall, and C. C. Constantinou, "Statistical Analysis and Performance Evaluation for On-body Radio Propagation with Microstrip Patch Antennas," *IEEE Transactions on Antennas and Propagation,* 2007.

[16] Y. P. Zhang, Q. Li, "Performance of UWB Impulse Radio With Planar Monopoles Over On-Human-Body Propagation Channel for Wireless Body Area Networks," *IEEE Transactions on Antennas and Propagation*, Vol. 55, No. 10, pg. 2907-2914 Oct 2007

[17] A. Fort, C. Desset, J. Ryckaert, P. De Doncker, L. Van Biesen, and S. Donnay, "Ultra wide-band body area channel model," in *Proc. IEEE Int. Conf. Commun.*, Korea, May 16–20, 2005, vol. 4, pp. 2840–1844.

[18] Y. Hao, A. Alomainy, W. Song, C. G. Parini, P. Hall, Y. Nechayev, and C. Constantinou, "Numerical modeling of on-body radio propagation channel," *presented at the IEEE AP-S Int. Symp.*,Washington, DC, Jul. 3–8, 2005.

[19] A. Alomainy, Y. Hao, C. Parini, and P. Hall, "Comparison between two different antennas for UWB on-body propagation measurements," *IEEE Antennas Wireless Propag. Lett.*, vol. 4, pp. 31–34, 2005.

[20] M. Kamarudin, Y. Nechayev, and P. Hall, "Antennas for on-body communication systems," in *Proc. IEEE Int. Workshop Antenna Technol.*, Singapore, Mar. 7–9, 2005, pp. 17–20.

[21] Y. I. Nechayev, P. S. Hall, C. C. Constantinou, Y. Hao, A. Alomainy, R. Dubrovka, and C. Parini, "Antennas and Propagation for On-Body Communication Systems," *11th International Symposium. on Antenna Technology and Applied Electromagnetics ANTEM*, June 15-17, 2005, Saint Malo, France.

[22] Y. I. Nechayev, P. S. Hall, C. C. Constantinou, *Y.* Hao, A. Alomainy, R. Dubrovka, and C. Parini, "On-Body Path Gain Variations with Changing Body Posture and Antenna Position," *IEEE International Symposium on Antennas and Propagation*,Washington, USA, July 2005.

[23] M. R. Kamarudin, Y. 1. Nechayev, and P. S. Hall, 'Performance of Antennas in the On Body Environment," *IEEE International Symposium on Antennas and Propagation*, Washington, USA, July 2005.

[24] P. S. Hall and Y. Hao, *Antennas and Propagation for Body Centric Communications Systems*, Norwood, MA, Artech House, 2006, pg. 241-255.

[25] C. M. Furse, J.-Y. Chen, O. P. Gandhi, "The Use of the Frequency-Dependent Finite-Difference Time-Domain Method for Induced Current and SAR Calculations for a Heterogeneous Model of the Human Body," *IEEE Trans. on Electromagnetic Compatibility*, Vol. 36, No. 2, MAY 1994

[26] O. P. Gandhi, B.-Q. Gao, J.-Y. Chen, "A Frequency-Dependent Finite-Difference Time-Domain Formulation for General Dispersive Media," *IEEE Trans. Microwave Theory Tech.,* Vol. 41, No. 4, APRIL 1993.

[27] S. Gabriel, R. W. Lau, C. Gabriel, "The Dielectric Properties of Biological Tissues: III Parametric Models For the Dielectric Spectrum of Tissues," *Physics in Medicine and Biology*, Vol. 41, Issue 11, pp. 2271-2293, 1996.

[28] W. Yu, R. Mittra, "A Conformal FDTD Software Package Modeling Antennas and Microstrip Circuit Components," *IEEE Antennas and Propagation Magazine*, Vol. 42, No. 5, Oct. 2000.

[29] A. Taflove, K. R. Umanshankar, B. Beker, F. Harfoush, K. S. Yee, "Detailed FD-TD Analysis of Electromagnetic Field Penetrating Narrow Slots and Lapped Joints in Thick Conducting Screens," *IEEE. Trans. on Antennas and Propagation*, Vol 36, No. 2, Feb. 2008.

[30] A. Taflove, S. C. Hagness, *Computational Electrodynamic—The Finite Difference Time-Domain Method*, 3rd ed., pgs. 415-417, Artech House, Inc., MA 2005.

[31] R. Holland, L. Simpson, "Finite-Difference Analysis of EMP Coupling to Thin Struts and Wires," *IEEE Trans. on Electromagnetic Compatibility*, Vol. EMC-23, No. 2, May 1981.

[32] K. Ren, C. Railton, "Modelling of Microstrip Circuit Using a Hybrid PEEC/FDTD Approach," *IEEE Trans. on Antennas and Propagation*, Vol. 56, No. 10, Oct. 2008.

[33] F. Edelvik, "A New Technique for Accurate and Stable Modelling of Arbitrarily Oriented Thin Wire in the FDTD Method," *IEEE Trans. on Electromagnetic Compatibility*, Vol.45, No. 2, 2003.

[34] Dr. Cynthia Furse, *private communication*.

[35] R. E. Kleinman, T. B. A. Senior, "Low Frequency Scattering by Space Objects," *IEEE Trans. on Aerospace and Electronic Systems*, Vol. AES-11, July 1975.

[36] J. G. Van Bladel, *Electromagnetic Fields*, Wiley-IEEE Press, 2nd ed., 2007.

[37] K. Panayappan, J. N. Bringuier, R. Mittra, K. Yoo, N. Mehta, "A New-Dipole-Moment-based MoM Approach for Solving Electromagnetic Radiation and Scattering Problems," *IEEE International APS and USNC/URSI National Radio Science Meeting*, 2009.

[38] L. Zhao, K. L. Kelly, G. C. Schatz, "The Extinction Spectra of Silver Nanoparticle Arrays: Influence of Array Structure on Plasmon Resonance Wavelength and Width," *J. Phys. Chem. B*, Vol. 107, No. 30, 2003.

[39] H. E. Abd El-Raouf, V. V. S. Prakash, J. Yeo, R. Mittra, "FDTD Simulation of a Microstrip Phased Array with a Coaxial Feed," *IEE Proc.-Microw. Antennas Propag.*, Vol. 151, No. 3, 2004.

[40] H. Sharfman, "Scattering from Dielectric Coated Spheres in the Region of the First Resonance," *J. Appl. Phys.,* Vol. 25, No. 11, Nov. 1954.

[41] A. Vial, *et. al.*, "Improved Analytical Fit of Gold Dispersion: Application to the Modeling of Extinction Spectra with a Finite-Difference-Time-Domain Method," *Physical Review B*, Feb. 2005.

[42] Dr. Iftikhar Ahmed, *private communication*.

[43] Z. Ji, T. K. Sarkar, B. H. Jung, Y.- S. Chung, M. Salazar-Palma, M. Yuan, "A Stable Solution of the Time Domain Electric Field Integral Equation for Thin-Wire Antennas Using Laguerre Polynomials," *IEEE Trans. on Antennas and Propagation*, Vol. 52, No. 10, Oct. 2004.

[44] B. H. Jung, T. K. Sarkar, "Time-Domain Electric-Field Integral Equation with Central Finite Differences," *Microw. and Opt. Tech. Letters*, Vol. 31, No. 6, Dec. 2001.

[45] A. Mohan, D. S. Weile, "A Hybrid Method of Moments-Marching on in Time Method for Solution of Electromagnetic Scattering Problems," *IEEE Trans. on Antennas and Propagation*, Vol. 53, No. 3, March 2005.

[46] R. Mittra, H. Abd-El-Raouf, N. Huang, "A Serial-Parallel FDTD Approach for Modeling the Coupling Problem Between Two Large Arrays," *Journal of Applied Computational Electromagnetics Society*, Vol. 21, No. 3, 2006.

[47] J. P. Berenger, "A Perfectly Matched Layer for the Absorption of Electromagnetic Waves," *J. Comp. Phys.*, 1994.

[48] E. C. Jordan, K. G. Balmain, *Electromagnetic Waves and Radiating Systems*, 2nd ed., Prentice-Hall, Inc., 1968.

[49] J. B. Keller, "Geometrical Theory of Diffraction," *J. Opt. Soc. Amer.*, Vol. 53, No. 2, Feb. 1962.

[50] M. Zhai, H. Uberall, "Scattering of an Obliquely Incident Plane Wave by Conducting Prolate Spheroids," *IEEE International Symposium on Electromagnetic Compatibility*, 1991.

[51] W. L. Stutzman, G. A. Thiele, *Antenna Theory and Design*, 2nd ed., John Wiley & Sons, Inc., 1998.

Appendix A

Prony's Method

In Chapter 2 we found it necessary to approximate the fields by a sum of complex exponentials. Prony's method is a useful technique which can be used to determine the corresponding weights and exponents of each individual term. The fact that we are able to obtain these parameters is satisfying because in many engineering problems the quantities of interest behave exponentially. The algorithm below is a typical derivation of Prony's method and can be found in [3]. Initially, we will assume that the function can be approximated by the form

$$f(x) = A_0 e^{\alpha_0 x} + A_1 e^{\alpha_2 x} + \cdots\cdots + A_{k-1} e^{\alpha_{k-1} x} \tag{A.1}$$

where the data points are sampled at $x = x_j \, (j = 1,2,....,n)$. For convenience we can chose $x_j = j - 1$ without loss of generality. A simple variable substitution can be performed if the data are taken at non-integer points. Furthermore, we will require that the function of interest is sampled uniformly (i.e., equally spaced). The key to Prony's method is the fact that each of the exponential terms

$$e^{\alpha_i j} = \left(e^{\alpha_i}\right)^j \equiv \rho_i^j \qquad i = 0,1,....,k-1 \tag{A.2}$$

is a solution to some homogeneous, *kth*-order, linear difference equation with constant coefficients. In general, the coefficients may be complex. In any case, the difference equation can be written as

$$y(j+k) + C_{k-1} y(j+k-1) + C_{k-2} y(j+k-2) + ... + C_0 y(j) = 0 . \tag{A.3}$$

The solutions can be determined by solving for the roots of the characteristic equation given by

$$\rho^k + C_{k-1}\rho^{k-1} + C_{k-2}\rho^{k-2} + ... + C_0 = 0 . \tag{A.4}$$

Note that each exponential satisfies (A.3), so it must be the case that the linear combination of these terms will also satisfy (A.3). Specifically, the function of (A.1) satisfies (A.3) and we have the equation given by

$$f(j+k)+C_{k-1}f(j+k-1)+.....+C_0f(j)=0 \qquad j=1,2,.....,n-k \ . \qquad (A.5)$$

In order to obtain a unique solution for the $2k$ unknowns in the assumed function we must require that we know *a priori* the values of the function at $n=2k$ sample points. If this information is available then we can setup k equations and uniquely determine the C_i's. Advanced matrix techniques can be used in other cases when we do not have exactly $n=2k$ samples of data. It is noted in [3] that the C_i's can only be found if the persymmetric determinant

$$\Delta = |f(j+k)| \qquad (A.6)$$

does not vanish. The exponents α_i's are found from the characteristic equation given in (A.4) for which we have already found the corresponding C_i's. We note that when the roots are positive then the α_i's will be real. However, in Chapter 2 the data was necessarily composed of complex data, and, in general, the roots can consist of both real and imaginary parts. Lastly, to determine the A_j's we can use the calculated α_i's and evaluate (A.1) at points were the function value is already known.

Appendix B

Plane Wave Scattering by a Coated PEC Sphere

In Chapter 4 we made use of the scattering properties by a coated PEC sphere. Here we briefly list the results for the Mie series representation as given in [40]. Consider the problem of plane wave scattering by a coated PEC sphere as shown in Fig. B.1.
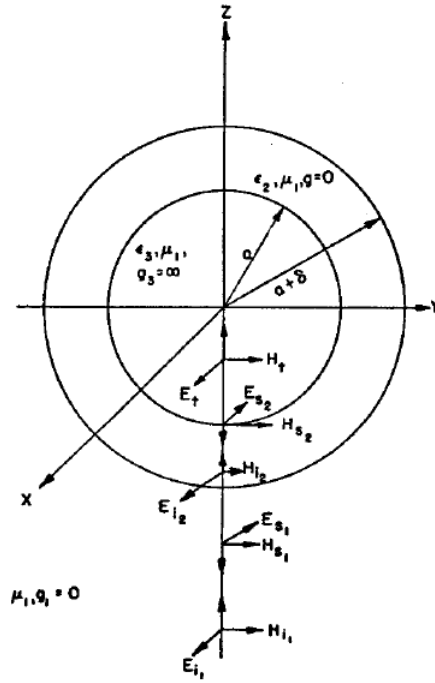
Fig. B.1: Geometry for plane wave scattering by a coated PEC sphere (source from [40]).

The incident electric and magnetic fields with an $e^{-i\omega t}$ time dependence are given by:

$$E_i = E_0 e^{-i\omega t} \sum_{n=1}^{\infty} i^n \frac{2n+1}{n(n+1)} \left[\overline{m}_{oln}^{(1)} - i\overline{n}_{eln}^{(1)} \right]$$
(B.1)

$$H_i = \frac{-k_1 E_0}{\omega \mu_1} e^{-i\omega t} \sum_{n=1}^{\infty} i^n \frac{2n+1}{n(n+1)} \left[\overline{m}_{eln}^{(1)} + i\overline{n}_{oln}^{(1)} \right]$$
(B.2)

and the scattered fields outside the sphere (i.e. $r > (a + \delta)$) can be written as:

$$E_s = E_0 e^{-i\omega t} \sum_{n=1}^{\infty} i^n \frac{2n+1}{n(n+1)} \left[a_n^s \overline{m}_{o1n}^{(3)} - ib_n^s \overline{n}_{e1n}^{(3)} \right] \tag{B.3}$$

$$H_s = \frac{-k_1 E_0}{\omega \mu_1} e^{-i\omega t} \sum_{n=1}^{\infty} i^n \frac{2n+1}{n(n+1)} \left[b_n^s \overline{m}_{e1n}^{(3)} + ia_n^s \overline{n}_{o1n}^{(3)} \right] \tag{B.4}$$

where $\overline{m}_{(o,e)1n}^{(1)}$ and $\overline{n}_{(o,e)1n}^{(1)}$ are given by:

$$\begin{aligned}
\overline{m}_{(o,e)1n}^{(1)} = &\pm \frac{1}{\sin\theta} j_n(k_1 r) P_n^1(\cos\theta) \begin{pmatrix} \cos\phi \\ \sin\phi \end{pmatrix} \hat{a}_\theta \\
&- j_n(k_1 r) \frac{d}{d\theta} P_n^1(\cos\theta) \begin{pmatrix} \sin\phi \\ \cos\phi \end{pmatrix} \hat{a}_\phi
\end{aligned} \tag{B.5}$$

$$\begin{aligned}
\overline{n}_{(o,e)1n}^{(1)} = &\frac{n(n+1)}{k_1 r} j_n(k_1 r) P_n^1(\cos\theta) \begin{pmatrix} \sin\phi \\ \cos\phi \end{pmatrix} \hat{a}_r \\
&+ \frac{1}{k_1 r} \left[k_1 r j_n(k_1 r) \right]' \frac{d}{d\theta} P_n^1(\cos\theta) \begin{pmatrix} \sin\phi \\ \cos\phi \end{pmatrix} \hat{a}_\theta \\
&\pm \frac{1}{k_1 r \sin\theta} \left[k_1 r j_n(k_1 r) \right]' P_n^1(\cos\theta) \begin{pmatrix} \cos\phi \\ \sin\phi \end{pmatrix} \hat{a}_\phi
\end{aligned} \tag{B.6}$$

The primes at the square brackets indicate differentiation with respect to the argument $k_1 r$. In addition, j_n is the spherical Bessel function of the first kind, and $P_n^1(\cos\theta)$ is the associated Legendre polynomial of the first kind, first order, and *nth* degree. Furthermore, the expressions for $\overline{m}_{(o,e)1n}^{(3)}$ and $\overline{n}_{(o,e)1n}^{(3)}$ are obtained by replacing j_n in (B.5) and (B.6) with the spherical Hankel function of the first kind, $h_n^{(1)}$. By solving the boundary value problem the scattering coefficients become:

$$a_n^s = \frac{- j_n(A) \left\{ h_n^{(1)}(C) \left[B j_n(B) \right]' - j_n(C) \left[B h_n^{(1)}(B) \right]' \right\} + \left[A j_n(A) \right]' \left\{ j_n(B) h_n^{(1)}(C) - j_n(C) h_n^{(1)}(B) \right\}}{h_n^{(1)}(A) \left\{ h_n^{(1)}(C) \left[B j_n(B) \right]' - j_n(C) \left[B h_n^{(1)}(B) \right]' \right\} - \left[A h_n^{(1)}(A) \right]' \left\{ j_n(B) h_n^{(1)}(C) - j_n(C) h_n^{(1)}(B) \right\}} \tag{B.7}$$

$$b_n^s = \frac{-j_n(A)\left\{\left[Bh_n^{(1)}(B)\right]\left[Cj_n(C)\right]' - \left[Bj_n(B)\right]'\left[Ch_n^{(1)}(C)\right]\right\} + \left(\frac{\varepsilon_2}{\varepsilon_1}\right)\left[Aj_n(A)\right]'\left\{h_n^{(1)}(B)\left[Cj_n(C)\right]' - j_n(B)\left[Ch_n^{(1)}(C)\right]'\right\}}{h_n^{(1)}(A)\left\{\left[Bh_n^{(1)}(B)\right]\left[Cj_n(C)\right]' - \left[Bj_n(B)\right]'\left[Ch_n^{(1)}(C)\right]\right\} - \left(\frac{\varepsilon_2}{\varepsilon_1}\right)\left[Ah_n^{(1)}(A)\right]'\left\{h_n^{(1)}(B)\left[Cj_n(C)\right]' - j_n(B)\left[Ch_n^{(1)}(C)\right]'\right\}}$$
(B.8)

where

$$k_1 = \frac{2\pi}{\lambda}$$
(B.9)

$$k_2 = \frac{2\pi}{\lambda}\left(\frac{\varepsilon_2}{\varepsilon_1}\right)^{\frac{1}{2}}$$
(B.10)

$$A = k_1(a + \delta)$$
(B.11)

$$B = k_2(a + \delta)$$
(B.12)

$$C = k_2 a$$
(B.13)

VITA

Jonathan Neil Bringuier was born in Los Angeles, California on June 2, 1981. He attended Granada Hills High School where he lettered 4 years in baseball and graduated as a scholar athlete in 1999. After high school, he enrolled at the California Polytechnic State University-San Luis Obispo (Cal Poly-SLO), and was awarded a Bachelor of Science degree in Electrical Engineering in December 2004. While at Cal Poly he researched the design of negative resistance oscillators at microwave frequencies and completed an undergraduate thesis on that topic. Subsequently, he attended The Pennsylvania State University as a graduate student in the Electromagnetic Communications Laboratory where he completed his Master of Science degree in Electrical Engineering in August, 2006. Following the completion of his M.S. degree, he continued his graduate studies on multi-scale techniques in computational electromagnetics, and received his Ph.D. in Electrical Engineering in May, 2010.